Synthesis of low-wear and high strength nano-scale leucite glass-ceramics for Dentistry

Antonios Theocharopoulos
BSc, MSc

A thesis submitted in fulfilment of the requirements for the degree of Doctor of Philosophy in the Institute of Dentistry, Queen Mary, University of London

January 2011

Centre of Adult Oral Health
Barts and The London School of Medicine and Dentistry
Queen Mary University of London
London, United Kingdom

ABSTRACT

Leucite glass-ceramics serve Restorative Dentistry needs for aesthetic replacement of lost or removed teeth or tooth substance. Their brittle fracture and the wear of the antagonistic enamel are however their main disadvantages. The aim of this thesis was to synthesize high strength, low-wear nano-sized leucite glass-ceramics for dental applications. Aluminosilicate glasses were experimentally synthesized using Appen models, characterised (DSC, CTE, XRD) and milled to powders using various milling routes. Leucite glass-ceramic materials were produced from the milled glass powders. Microstructural and physico-mechanical property control was pursued via compositional modifications, processing and heat treatment optimisation. All final materials where characterised using SEM and XRD. The experimental materials were tested using the biaxial flexural strength (BFS) test against commercial leucite glass-ceramic materials. A wear testing protocol was adapted on an MTS-Bionix 858 system. Human enamel pins were wear tested against disc samples of two experimental and one commercial material. Wear quantification was performed by superimposition of digitised test surfaces before and after wear testing by white light profilometry and the dedicated software using a novel protocol. All results were processed by applying appropriate statistics. Nanoscale tetragonal leucite median (Q1,Q3) crystal areas of up to 0.048 (0.030, 0.070) μm^2 were achieved for the experimentally synthesized materials. Microstructural control was achieved with varying morphologies (sphere-shaped, fibres) and minimal or no microcracking in all glass-ceramics. The BFS results showed that the experimental groups tested were significantly ($p < 0.05$) stronger than the commercial materials. The mean (SD) BFS of the experimental materials ranged from 192.5 (44.0) to 255.0 (35.0) MPa compared to a range of values of 75.7 (6.8) - 165.5 (30.6) MPa for commercial leucite glass-ceramic products. The experimental glass-ceramic groups tested in wear produced significantly ($p < 0.05$) lower antagonistic enamel wear than the commercial material, quantified both as tooth volume and mean-height loss. Further development and optimisation of the high strength nanosized materials synthesized may therefore help to address problems with brittle fracture of dental all-ceramic restorations and support their use to achieve reduced rates of enamel loss.

Dedicated to my beloved wife,

daughter

and son..

Table of Contents

List of Figures

List of Tables

Appendices

List of Abbreviations

AM	Attritor Milling
ANOVA	Analysis Of Variance
BFS	Biaxial Flexural Strength
CN	Coordination Number
CAD	Computer Aided Designing
CAM	Computer Assisted Manufacturing
CTE	Coefficient of Thermal Expansion
DSC	Differential Scanning Calorimetry
EDS	Energy Dispersive X-ray Spectroscopy
FDA	Federal Dental Association
FTIR	Fourier Transform Infrared Spectroscopy
HF	Hydrofluoric Acid
HP	Heat Pressed
HTXRD	High Temperature X-ray Diffraction
ICDD	International Centre for Diffraction Data
IEC	Ion-exchange Chromatography
MAS-NMR	Magic Angle Spinning – Nuclear Magnetic Resonance
MTS	Mechanical Testing System
PEEK	Polyether Ether Ketone
PM	Planetary Milling
PTFE	Polytetrafluoroethylene
Q1,Q3	25th and 75th percentiles (Quartile 1, Quartile 3)
SD	Standard Deviation
SEI	Secondary Electron Imaging
SEM	Scanning Electron Microscopy
SV	Specific Volume
XRD	X-ray Diffraction
YTZ	Yttria Tetragonal stabilized Zirconia

Acknowledgements

I would like to specially acknowledge the funding from St Bartholomew's and The Royal London Charitable Foundation (RAB05/PJ/06) and from the State Scholarships Foundation (IKY) of Greece that generously ensured the unimpeded materialisation of this study.

I would also like to express my sincere thanks to the following people whose help and support have been invaluable:

- My supervisor and mentor Dr Michael Cattell, for his enthusiasm, inspiration, personal dedication to my work, and constant support. His input has always been most constructive and has elicited the best possible out of me. He has undoubtedly helped me overcome all the insuperable difficulties setting a concrete foundation for my potential future as a scientist.
- My second supervisor, Prof Robert Hill for his most useful commentary and teachings in glass making and thermal analysis and the fruitful discussions on the wear testing and ion-exchange experiments.
- The examination committees of my transfer to PhD exam, (Prof Elizabeth Tanner, University of Glasgow and Prof D.Y.D. Samarawickrama, Barts and The London School of Medicine and Dentistry) and my final PhD exam (Dr Gary Fleming, Dublin Dental School and Prof Mike Reece, QMUL) for their most useful suggestions and commentary on this work.
- My colleague Xiaohui Chen for always been by my side providing fruitful comments and most useful information, but also relieving the pressure whenever the work intensity was increasingly demanding. Her paradigm in experimental protocol has been unique.
- Mr. Bill Godwin (QMUL) for his inspired contribution and adaptation of the wear testing device, his tireless, selfless guidance and assistance in the experimental procedure which rendered this piece of my work possible against all the odds. Special thanks to Mr. Vince Ford (QMUL) for making the wear testing jigs and Mr. Ted Heath (MTS Systems UK Ltd.) for his assistance in tuning of the MTS 858 used in this study.

- Dr Tom Chadwick (Denmat Corporation, USA) for the truly enlightening discussions and comments on the ion-exchange experiment but also for his wise personal advice.
- Dr Zofia Luklinska and Mr. Mick Willis (QMUL) for their huge support, advice and guidance in using the scanning electron and optical microscopes.
- Dr Isaac Abrahams (QMUL) for the most fruitful discussions and advice on all chemistry related issues that I faced that helped me target to the right direction.
- Nanoforce Technology Ltd. (QMUL) and all their staff for their great support and for allowing me to use their high speed milling facilities.
- Dr Laura Shotbolt and Mr. Simon Dobinson (QMUL) for their support, advice and guidance in the Ion-exchange chromatography.
- Mr. Tim Tuckey, Mr. Adam Henwood and Mr. Paul Adams (Scantron Industrial Products Ltd., Taunton, UK) for their continuous telephone support for the Proscan 2000 Profilometer.
- My colleague Ms Jamila Almuhamadi, MSc Dental Technology student for her assistance with part of the experimental work in glasses B1 – B3.

Special thanks to all my family, friends and colleagues for their continuous moral support. A huge thanks to my mother in law for her selfless and tireless support in my family.

1. INTRODUCTION

1. Introduction

Human teeth are functionally graded organs with a highly hierarchical structure that fulfil both functional (mastication, speech) and aesthetic needs (Nanci, 2003). Leucite glass-ceramics are utilised amongst other materials in Restorative Dentistry to replace teeth or tooth substance lost or removed due to disease, trauma and/or aesthetic reasons (Kelly, 1997, Zhou and Zheng, 2008). To adequately serve this purpose, these materials must be equipped with properties such as high flexural strength, modulus and toughness to ensure they resist failure during function in the oral environment but also restore lost aesthetics (Kelly et al., 1996).

A variety of processing routes exists for the production of several prostheses types (inlays, onlays, veneers, crowns and bridges) with leucite glass-ceramics. When used in all-ceramic restorations, brittle fracture and wear of the opposing teeth are the main disadvantages (Qualtrough and Piddock, 1997). Bilayer combinations of high strength alumina or zirconia cores with glasses are also available but the increased core opacity significantly limits the aesthetics and veneering with thermally compatible glasses is necessary. Susceptibility to interfacial failure (Kelly et al., 1995) or failure of the low flexural strength and toughness veneering glass (Carrier and Kelly, 1995, Studart et al., 2007) however, results in reduced reliability of such bilayer restorations. Targeted synthesis of leucite glass-ceramic formulations and their careful processing have previously led to strength and reliability optimisation (Cattell et al., 2001, 2006, Chen, 2009). The synthesis of leucite glass-ceramics that will combine high strength with low antagonistic enamel wear

is pursued in the current study. These new materials if coupled with good aesthetics would be useful in the Dental field. The fit surface modification and adhesive cementation of leucite glass-ceramics using etching and silane bonding to etched tooth structure (Simonsen and Calamia,1983, Calamia and Simonsen, 1984) can further increase their overall clinical performance (Nathanson, 1994).

Glass-ceramic technology enables tailoring of various properties of leucite glass-ceramics using established methodologies (Schairer and Bowen, 1955). Typical commercial production methods produce dental glass-ceramics with a 17-45% leucite content (Piche et al., 1994, Mackert and Russell, 1996), with large leucite crystal sizes (~10 μm) and irregular morphologies (Barreiro et al., 1989, Shareef et al., 1994). Leucite ($KAlSi_2O_6$) undergoes a reversible temperature dependent cubic to tetragonal phase transformation around 605 to 625°C (Mackert, 1988) which results in a 1.2% discontinuous volume change (Mackert et al., 1986) and a subsequent change in thermal expansion, from 11.7 - 12.8x10^{-6}/°C [25-600°C] for cubic leucite to 20 - 25x10^{-6}/°C [20-800 °C] for tetragonal leucite (Hermansson and Carlsson, 1976, Rouf et al., 1978). The reduced mechanical properties of some commercial leucite glass-ceramics have been linked to microcracking around larger non uniform leucite crystals and clusters (Cattell et al., 1999). This microcracking develops during the leucite cubic to tetragonal transformation on cooling after firing, as a result of the thermal expansion mismatch between the tetragonal leucite crystals and the glass matrix (Mackert et al., 2001). By carefully controlling this mismatch however, elimination of microcracking (Cattell et al., 2006) and generation

of tangential compressive stresses around leucite crystals can lead to significant strength improvements (Denry et al., 1996). Synthesis of new and/or modification of existing glass compositions using Appen factors in an attempt to optimise their thermal properties (e.g. CTE) and their relationship with the leucite crystals can thus be key to mechanical property optimisation (Lee et al., 1997).

A mean leucite crystal diameter of less than 4 μm has also been suggested to minimize or eliminate microcracking (Mackert et al., 2001). Rouf et al., (1978) have used nucleating agents to crystallise fine tetragonal leucite crystals (0.1-1 μm) in white-ware alumino-silicate glasses with high modulus of rupture values (200 to 300 MPa). The formulations by Rouf et al., (1978) however had both high viscosity and opacity that would complicate processing and limit aesthetics when considered for dental applications. Cattell et al., (2001, 2005) and Chen (2009) have used glass powder size reduction processing and controlled heat treatments for surface nucleating and growing aesthetic, fine-grained tetragonal leucite crystals with minimal matrix micro-cracking. An *in vitro* wear study of glass-ceramic materials against human enamel suggests that a reduced leucite crystal size and crystallinity produces a smaller amount of enamel and glass-ceramic wear (Metzler et al., 1999). *In vitro* wear testing carried out in the current thesis explores the effect of crystal size graduation down to nanoscale level on antagonistic enamel and glass-ceramic wear in newly synthesized leucite glass-ceramics.

While glass particle size-dependant bulk leucite crystallisation has been identified in certain aluminosilicate glass formulations (Tošić et al., 2000), controlled

surface crystallisation of leucite has also been demonstrated (Höland et al., 1995). A reactive ball milling route could enable increased glass-grain surface potassium content via ion-exchange. This could increase the availability of potassium close to nucleation sites such as interfacial boundaries between glass grains, enhancing glass powder reactivity and thus surface crystallisation. If stabilized at room temperature, low-expansion cubic leucite containing porcelains that may be thermally matched with zirconia cores may be produced. This stabilization is shown to be possible by a molten-salt bath method for ion exchanging potassium ions in the leucite structure with caesium (Denry et al., 1996) or rubidium ions (Denry et al., 1998). A reactive ball milling method where glass-ceramic ion exchanging may take place could therefore also be beneficial.

Microstructural and physico-mechanical property optimisation of dental leucite glass-ceramics may be thus be possible via synthesis and processing optimisation of new and/or compositional modifications of existing aluminosilicate glasses (Ibsen et al., 1991, Denry et al., 1996, 1998, Cattell et al., 2001, 2005, 2006, Chen, 2009). The methodologies described in the current thesis suggest that further control over tetragonal leucite crystal size, morphology and volume fraction to produce new high strength, low-wear nano-sized leucite glass-ceramics is possible. These new materials may help to address problems with brittle fracture of dental all-ceramic restorations and support their use to achieve reduced rates of enamel loss.

2. LITERATURE REVIEW

2.1 Historical perspective on dental ceramics

Porcelain as a Dental Restorative material was first proposed by Fauchard (1728) for artificial teeth (van Noort, 2002). Later, in 1789, a Parisian dentist called Dubois de Chemant and a pharmacist called Duchâteau patented an improved version of “mineral paste” porcelain teeth (de Chemant, 1804). Land (1893) later introduced the porcelain jacket crown constructed using gas furnaces. Although the porcelain used at the time presented good aesthetics, due to its very low flexural strength and toughness, it could still not be used in dental bridges. The reinforcement of porcelain using porcelain fused to metal systems (Weinstein et al., 1962) allowed this to be overcome. The first aluminous core dental ceramic was introduced by McLean and Hughes (1965) who effectively reinforced the traditional feldspathic porcelain utilizing 40 - 50% alumina grains. This material had a limited application in bridges. Sadoun (1988) further extended the applications of aluminous cores by using glass to infiltrate partially sintered cores of greater than 80% fine grain alumina content. These cores were subsequently veneered with aesthetic porcelains.

Adair and Grossman (1984) developed the first castable glass-ceramic. This material was initially cast in a mould as a glass and was then given a special heat treatment, so that fluoromica crystals would nucleate and grow to reinforce the glassy matrix. A similar castable material was developed by Hobo and Itawa (1985) with a hydroxyapatite crystal phase. Leucite glass-ceramics in combination with a heat pressing process were later introduced (Wohlwend et al., 1990, Beham, 1990). Heat pressing has also been used for lithium disilicate glass-ceramics (Schweiger et

al., 1999) and these systems find applications as inlays, onlays, veneers and crowns.

Computer Aided Designing (CAD) and Computer Assisted Manufacturing (CAM) are the latest advances in the fabrication of all-ceramic restorations. CAD methods are used first to scan the abutment teeth either directly or from a die and then the prosthesis is designed in a computer. The CAM devices then utilize blocks of the latest glass-ceramics, alumina and stabilized zirconia materials to machine high strength cores or finished restorations. High strength cores are veneered with appropriate heat pressed or sintered porcelains to finalise the restoration (Rekow et al., 1991, Rekow and Thompson, 2005, 2007).

2.2 Glass

According to the American Society for Testing and Materials (ASTM, 2005), glass can be defined as a fusion derived inorganic product which has cooled and solidified without crystallising. This definition however, can be rather restrictive as it excludes glasses that are of organic origin or that are products of processes other than melt cooling (McMillan, 1979, Varshneya and Seward, 2001). A broader definition of glass that groups materials with similar molecular structure and properties can be that of an amorphous or non-crystalline solid (Kingery, 1976, Zarzycki, 1991) that exhibits a glass transition (Elliott, 1983).

2.2.1 Glass transition

Two phenomena are expected to occur when a liquid at an elevated temperature reaches the point of solidification (or freezing) T_f (Figure 2.1) (Zarzycki, 1991):

1. The liquid crystallises with an associated discontinuity in the temperature (T)-specific volume (SV) curve (ΔV_f, usually a reduction) or
2. The liquid is cooled below its freezing point (supercooled) avoiding crystallisation.

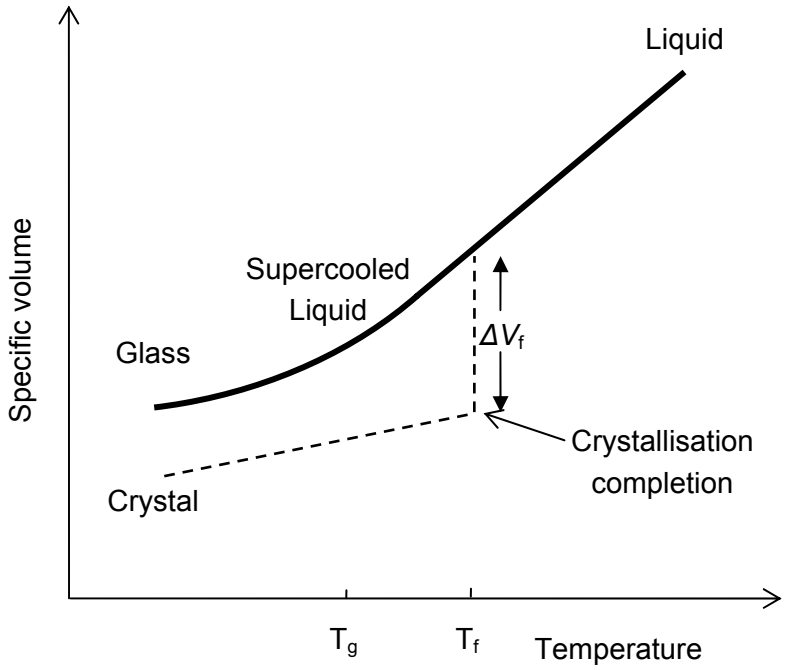

Figure 2.1: Variation of specific volume with temperature. T_g: Glass transition, T_f: Solidification point, ΔV_f: Change in specific volume.

In the first case, after crystallisation completion, the crystalline solid contracts again with a T-SV curve slope reduction compared to the initial liquid until complete solidification. In the second case, the supercooled liquid at first contracts as a result of the temperature drop with no change in the T-SV curve slope. The slope then decreases at the temperature defined as the glass transition (T_g) to approach that of the crystalline solid. The transition from a supercooled liquid to a glass is thus marked by this curve break at the T_g. Glass transition is cooling rate dependant and shifts to higher temperatures as this rate increases. Faster cooling rate also results in an increase in specific volume and conductivity and a decrease in viscosity and refractive index (Zarzycki, 1991).

The opposite transition between a (non-crystalline) solid and the corresponding intermediate phase or liquid, is also defined as T_g (Wunderlich, 1994). The glass transition is generally agreed to be a well defined phenomenon amongst glass forming materials which, although may not strictly be regarded as a phase transition, is relatively “sharp” in comparison to other progressive thermal effects (e.g. the temperature - drop associated viscosity increase of a supercooled liquid) (Hoare and Barker, 1977).

2.3 Structure of oxide glasses

Zachariasen (1932) created the continuous random network model that applies to the atomic arrangement of inorganic pure and multi-component oxide glasses. In his model, the building blocks in the glass structure are polyhedra comprising of cations surrounded by oxygen atoms. The determinant difference between glasses and

crystalline bodies is the way these polyhedra are bonded together in terms of bond angles and bond distance. In crystals, these angles are fixed and repeated in an orderly manner; this creates a highly ordered structure (three dimensional network) of periodically repeated identical structural units termed unit cells. Glasses also present extended three dimensional networks but lack both periodicity and symmetry. The degree of order present in the atomic arrangement of a material, ultimately distinguishes between crystalline and amorphous bodies. The lack of periodicity and symmetry found in glasses, is due to the broader distribution of the polyhedra bond angles (Zachariasen, 1932).

Zachariasen formulated the following rules for pure oxide glasses of the formula A_xO_y that have to be satisfied:

1. An oxygen atom must not be linked to more than two cations (A).
2. The number of oxygen atoms surrounding cations (coordination number, CN) must be small.
3. The oxygen polyhedra must share only corners and not edges or faces with each other.
4. At least three corners in each oxygen polyhedron must be shared in order for the resultant network to be three dimensional (Figure 2.2).

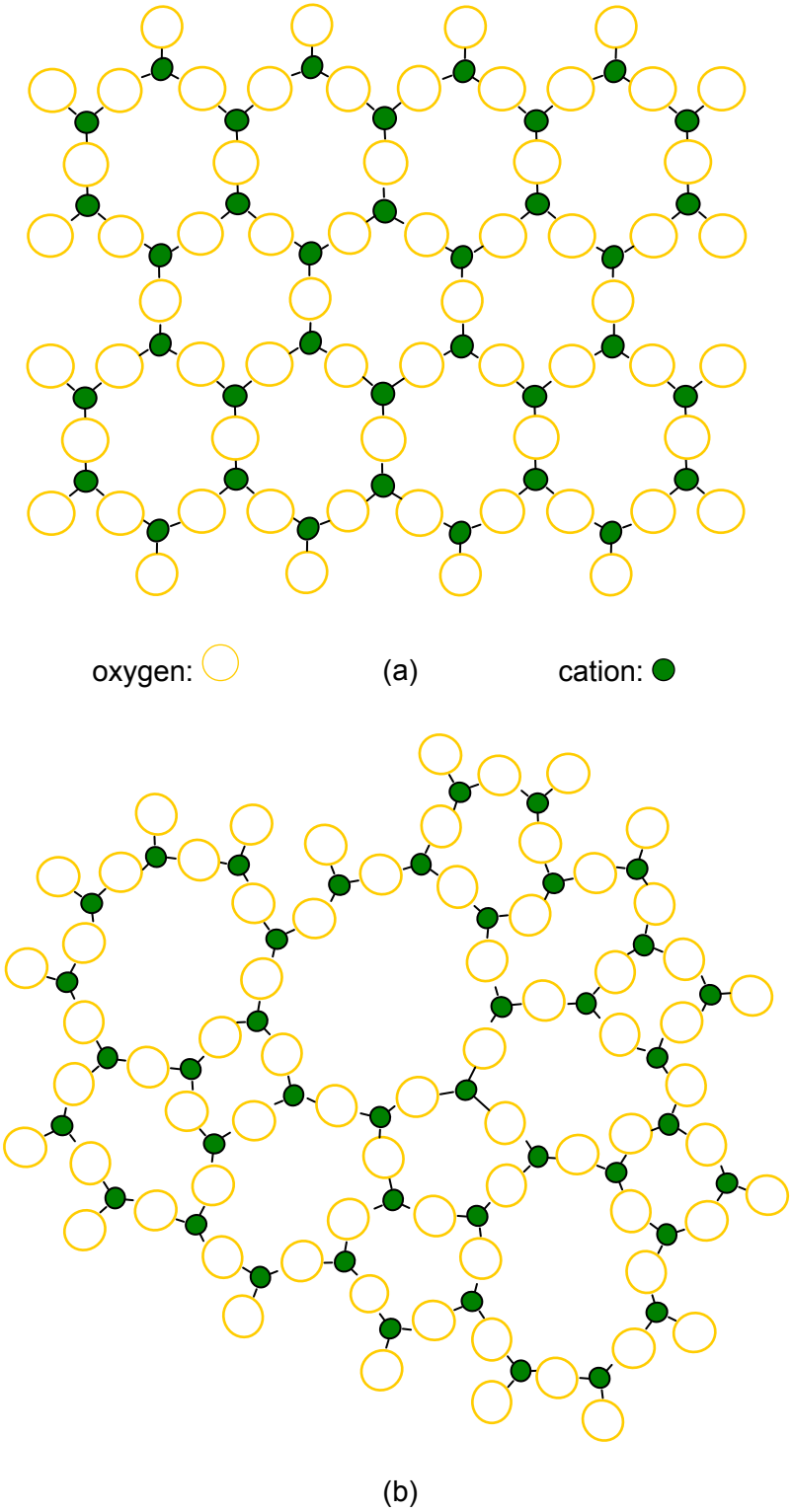

Figure 2.2: Network schematics for (a) an A_2O_3 crystal and (b) an A_2O_3 glass.

According to Pauling's (1929) first packing rule, the ionic radius ratio (R) of the cation and the anion (in this case oxygen) taking place in the formation of a stable polyhedron, determines the coordination number of the cation and thus the nature of the polyhedron. Table 2.1 shows the coordination number of the cation and the preferred polyhedral arrangement for different cation/anion radii ratios, as calculated taking into account purely geometrical considerations (Goldschmidt, 1926, Pauling, 1927, 1929). This rule applies to small cations with large charges (e.g. +3, +4) and large univalent or divalent anions (e.g. oxygen).

Table 2.1: The relationship of cation/anion radii ratios (r_c/r_a) with cation CN and the obtained polyhedron type.

$R = r_c/r_a$	**CN**	**Polyhedron type**
R< 0.155	2	Linear
0.155 <R< 0.225	3	Triangle
0.225 <R< 0.414	4	Tetrahedron
0.414 <R< 0.732	6	Octahedron
0.732 <R< 1	8	Cubic
R = 1	12	Hexagonal or cubic close packed

Data rearranged from Zarzycki (1965)

When combining Zachariasen's rules with this rule, from simple calculations it is obvious that A_2O and AO oxides (e.g. Na_2O, MgO, CaO) cannot form glasses (e.g. for MgO, $r(Mg^{+2})/r(O^{-2}) \approx 0.51$ thus, according to Table 2.1, octahedral bonding is preferred. This violates Zachariasen's rule 2. Boric oxide (B_2O_3) in contrast can form a glass where the oxygen atoms can be arranged in triangles around each B^{3+}. In a similar manner, AO_2 and A_2O_5 oxides can form glasses, where the cation of each building block is balanced in the centre of a tetrahedron whose corners are occupied by 4 oxygen atoms (e.g. silica [SiO_2], germania [GeO_2] and phosphorus pentoxide [P_2O_5] glasses). A_2O_3, AO_2 and A_2O_5 oxides are known as network formers due to the fact that they can produce extended three dimensional continuous random networks (McMillan, 1979). There are however exceptions to these rules like Al_2O_3, whose role is explained later.

For multi-component oxide glasses, Zachariasen (1932) modified his rules as follows:

1. The sample must contain a high percentage of cations surrounded either by oxygen tetrahedra or oxygen triangles.
2. The tetrahedra/ triangles must share only corners with each other.
3. Oxygen atoms must be linked to only two such cations and must not form further bonds with any other cations.

These modified rules further lead to the classification of oxides according to their role in the resultant network, apart from network formers, into modifiers and intermediate oxides, discussed later. Zachariasen's model was strongly supported by Fourier analysis of X-ray studies carried out by Warren et al., (1936). This analysis provided average radial distributions of atoms surrounding each atom, demonstrating the tetrahedral or triangular arrangement of oxygen atoms around silicon and boron cations. The similar but broader distribution of bond angles present in glasses in comparison to crystals was thus verified.

Zachariasen's structural model cannot be applied universally for all types of glasses. For non-oxide glasses for example, like $GeSe_2$ which is similar to SiO_2, his rules are largely inapplicable, as extensive edge sharing of the polyhedra takes place (Rao, 2002). The type of bonding is very important in determining the structure, as well as the melting temperature and the rheological properties of the melts (Rao, 2002). Zachariasen did not take this into account when designing his model, assuming only ionic bonding being present, for the convenience of applying the established principles of ionic crystals. The bonding type that is found in oxide glasses is of mixed covalent polar type (more covalent than ionic). This implies the presence of covalent links with a partial non-directional character (Smekal, 1951) as dictated by the electronegativity differences (Pauling, 1960). This type of bonding is necessary for glass formation, as both pure ionic or pure covalent bonding would induce ordering and thus crystallisation as noted by Smekal (1951).

2.3.1 Theories on the atomic arrangement in inorganic oxide glasses

Other models have also been employed, either in parallel or in opposition to Zachariasen's model. Lebedev (1921) had earlier introduced the crystalline theory based on primary X-ray diffraction studies of oxide glasses, that gave diffuse halos in areas that coincided with sharp Bragg peaks of the respective crystalline materials. This structural model, first conceptualized by Frankenheim (1835), described glass as an aggregate of randomly packed ultra-microcrystalline particles. This model was employed in an attempt to explain abrupt changes in properties as a result of gradual compositional changes (Vogel, 1985a). Valenkov and Poray-Koshitz (1936) further developed Lebedev's model by hypothesizing the presence of a highly disordered interlayer surrounding the crystallites. The degree of order in the crystallites was supposed to gradually increase from their periphery towards their centre, the latter being very close to the crystalline state. Lebedev later revisited his original ideas and referred to defined chemical compounds being present in glass in the form of both ordered and disordered regions (Vogel, 1985a).

Smekal's model (1951) treated glasses as polymer chains forming rigid irregular networks with mixed bonding. This model was intended to supplement and correct Zachariasen's model taking into consideration the type of bonding discussed earlier, which is mainly considered as mixed covalent-ionic. This model classified families of glasses according to the network connectivity where all member glasses are derived from a parent network (e.g. silicate glasses can be considered to originate from the polymer network in amorphous silica). Ray (1978) defined the connectivity of the

parent network as the number of network bonds that link each repeat unit in the network. For pure silica glass this translates to a connectivity of 4. Ray suggested that this type of classification is advantageous in that it groups glasses with similar physical and mechanical characteristics in classes with the same network connectivity.

2.3.1.1 Modifiers

Modifiers can be highly ionic oxides (uni or divalent) that disrupt the glass network producing structural gaps. The bridging oxygen atoms of shared tetrahedra corners are transformed into non-bridging oxygen atoms with a pair of terminated oxygen links (Figure 2.3). These links are charge balanced with modifier cations, one for each pair if they are divalent, and two if they are univalent (McMillan, 1979). As the network is being formed in this way, the modifier cations are seated in holes or interstices. The size of these sites is determined by the cation's size. This process is essentially the expression of rule 3 of the modified Zachariasen's rules. (Zachariasen, 1932).

The resultant network's properties are influenced by the modification, with the most significant effects being reduction of the glass viscosity and alteration of the thermal expansion coefficient and chemical resistance. This is also explained by Ray's polymer network model as the modifiers reduce the network connectivity of the glass and thus the cross link density (Ray, 1978). Modification effects depend on the percentage of the modifier used. Examples of modifiers that can be added to

glass compositions are Na_2O, K_2O, Li_2O, CaO, MgO and BaO. The K_2O and Li_2O modifiers are mostly used to increase the working range of the glass, Li_2O being more active in reducing the viscosity of the glass thus increasing its tendency to crystallise. Na_2O is mostly added to silica glasses to lower the viscosity and increase the thermal expansion coefficient. It also reduces their chemical resistance making them water soluble. CaO can be used to significantly reduce this solubility (Zarzycki, 1991).

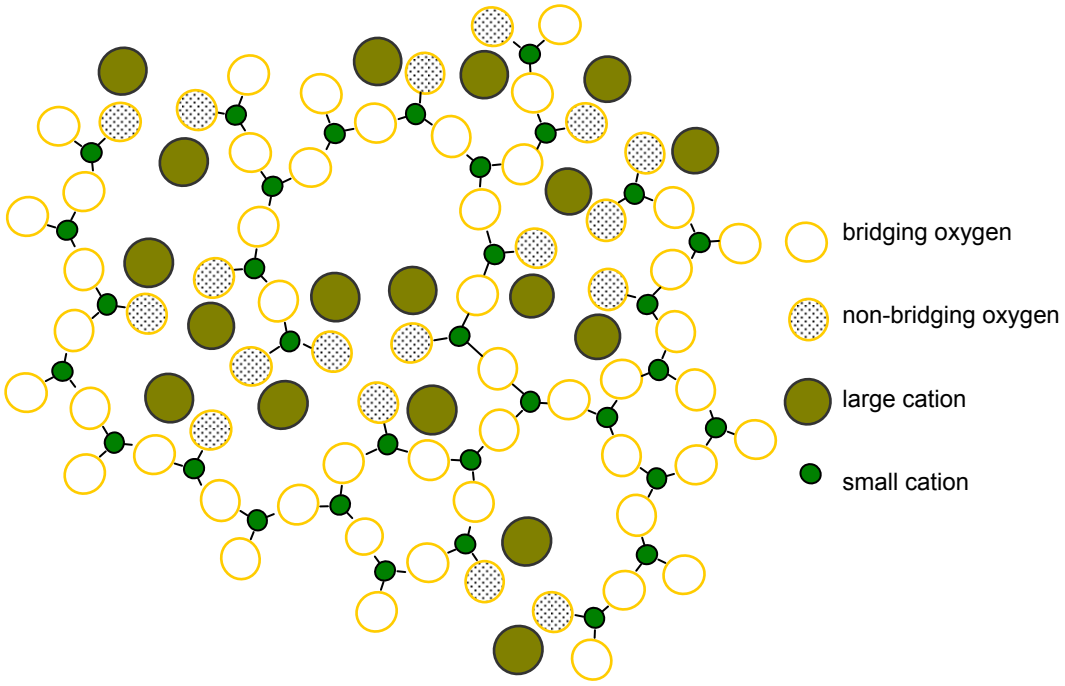

Figure 2.3: Network schematic of a bi – component glass.

2.3.1.2 Intermediate oxides

Intermediate oxides are oxides that may replace structural units in the random network (Zachariasen, 1932). They cannot however form a glass on their own. A good example is the aluminium oxide (Al_2O_3) substitution in silica glass which is expected to occur in a manner similar to the corresponding crystalline configuration.

In the latter state, aluminium tetrahedra may take the place of silicon tetrahedra in the crystal lattice. The charge of each aluminium ion however is +3 as opposed to silicon ions, which have a +4 charge and must be charge balanced by a modifying ion, so that electroneutrality is preserved. In the composition of many aluminosilicate glasses, each gram-molecule quantity of aluminium oxide present, must have the equivalent alkali or alkaline earth oxides added (McMillan, 1979). The presence of Al - O - Al and Si - O - Si linkages in aluminosilicate glasses has been experimentally demonstrated using nuclear magnetic resonance techniques (Lee and Stebbins, 2000).

Other common intermediate oxides are ZnO, CdO, PbO, TiO_2 and ZrO_2. TiO_2 and ZrO_2 promote phase separation and are both used as nucleating agents for their ability to induce crystallisation. Furthermore, TiO_2 increases the refractive index and the resistance to acids (Zarzycki, 1991).

2.3.2 Classification of cations

The classification of cations as network formers, modifiers and intermediate oxides has been attempted utilizing various criteria. Pauling's (1932) relative electronegativity of atoms can be used to determine the degree of ionic character of the covalent oxygen-cation bond. Stanworth (1946, 1948A, 1948B) classified cations according to their electronegativity difference in relation to oxygen. The smaller the electronegativity difference, the more covalent the bond character, the less likely is the oxide to vitrify. His classification agreed with Zachariasen's

observations, however his criterion in many cases did not hold true, both within and especially outside the oxide glasses field (Zarzycki, 1991). Sun (1947) calculated the single bond strengths of each different oxide glass component with oxygen and found that they are correlated to the ability of glass forming in a descending manner: network formers, intermediate oxides and modifiers. Rawson (1956) further correlated this ability with the melting temperature of the glass, suggesting that the latter indicates the amount of available thermal energy for the disruption of the component's bond. Rawson's improved classification was based on the fraction of the single bond energy divided by the melting temperature (K) for each component and gave a better insight into the ranking of glass formers. For example, a 4 coordinated Zr cation (as in ZrO_2) according to Sun may form a glass due to high bond strength, while due to its high melting point, Rawson suggests that the thermal energy availability is not adequate for glass formation (Zarzycki, 1991).

Dietzel (1942, 1983) used Coulomb's law to explain the tendency of a cation to form a bond with an anion in regards to their electrostatic interacting forces (K) and obtained:

$$K = (Z_c e \times Z_a e)/(r_c + r_a)^2 = (Z_c Z_a e^2)/a^2 \qquad \text{(Eq. 1)}$$

where Z_c and Z_a are the valencies of the cation and the anion respectively; e is the elementary charge; r_c,r_a are the radii of the cation and the anion respectively and their sum is replaced by a. In order to characterize the ability of only the cation to attract an oxygen anion during glass formation, Dietzel introduced the term field strength (F), given in Equation 2:

$$F = Z_c/a^2 \qquad \text{(Eq. 2)}$$

where *a* is the sum of the ionic radii of the oxygen anion and the cation measured in Angstroms (10^{-10} m). For non-oxide glasses, different values of *a* must be used. According to Dietzel, the higher the field strength, the more likely the cation to coordinate with oxygen at low coordination numbers (3 – 4) and thus network formers have the highest field strengths while intermediate oxides and modifiers follow in a descending manner. According to Equation 2, high field strength is obtained when the valence is high and the cation radius small. Important cations can be classified as follows according to their field strengths, as well as the other criteria mentioned: Network formers (B^{3+}, Si^{4+}), Intermediates (Ti^{4+}, Al^{3+}, Zr^{4+}) and Modifiers (Mg^{2+}, Ca^{2+}, Li^{1+}, Na^{1+}, K^{1+}, Rb^{1+}, Cs^{1+}).

In multi-component glasses, the difference in the field strength explains the role of each component. In a binary melt where both components have equally high field strengths (up to 0.3) (e.g. Si and B), oxygen will be almost equally attracted and thus densely coordinated around the cations forming a two-phase system. If the difference in the field strengths is between 0.3 and 1.33, the cation with the lower field strength tends to crystallise and precipitate in the glass formed by the high field strength cation, while for differences higher than 1.33, a binary glass is usually formed (Dietzel, 1942, Vogel, 1985a).

Dietzel's criterion considers ions to behave as hard spheres. This however is not strictly true as, in some cases, ions are deformable (large ions of low charge or non-noble gas ions)(McMillan, 1979). The classification it provides us with, is

nevertheless satisfactory and thus has often been applied in glass technology for various glass designing purposes (Vogel, 1985a). Greene et al., (2003) induced linear property variation (density, molar volume, hardness, thermal expansion and glass transition temperature) dependant on the field strength of the modifying rare earth used in a glass system. Thermal and dielectric property manipulation as a result of the varying field strength of network modifying ion chosen, has been employed in a zinc borosilicate glass system (An et al., 2006). Crystal microstructure and fracture toughness control in dental fluorcanasite glass-ceramics has also shown to be possible, by alteration of the relatively lower field strength Al_2O_3 content so as to reduce network interconnectivity (Zhang and Anusavice, 1999).

2.3.3 Glass property prediction

Properties of glasses are of two principal types: those related to the structure and those that depend upon the composition (Zarzycki, 1991). The importance of achieving a practical predictive method for glass properties lies in the potential of significantly simplifying the search of glasses with a desired set of properties (Priven, 2004). Structural-chemical and thermodynamic predictive glass property models exist (Maslyuk et al., 2001, Vedishcheva et al., 1996). They however, are generally of limited practical importance as they require verified structural or thermodynamic data for the predictive process to function. The current lack of availability of such data for anything but the simplest glass forming substances, attributes mainly theoretical significance to these models (Priven, 2004).

Winkelmann and Schott (1894b) were the first to attempt the prediction of specific properties of glass based on its chemical composition. Since then, numerous attempts have been undertaken (Gilard and Dubrul, 1937, Huggins and Sun, 1943, Appen, 1961, Hormadaly, 1986) and to date there has been no complete solution, especially for multi-component systems (Priven, 2004).

Winkelmann and Schott's (1894b) methodology was the first of a series of additive methods that relate oxide glass composition to a property α where:

$$\alpha = \sum_i \alpha i \, Pi$$

where α_i is a numerical constant characteristic of each oxide constituent and Pi is the weight or mole percent / fraction of the oxide constituent. Numerous oxides can be included in the calculation (Hormadaly, 1986). These methods may need correction in their calculation algorithm due to the fact that the property of interest is not always a linear function of the composition as the formula implies (Priven, 2004). The coefficient of thermal expansion (CTE) may nevertheless be accurately predicted to relatively narrow ranges using such additive methods. Appen's (1961) method is one of the most reliable additive methods (Priven and Mazurin, 2003) for CTE determination. Appen based his approach on the thermodynamic concept of glass as a solution of components, each of which independently contributes to the property of interest, in proportion to its molar content. In order to acquire the partial oxide properties, Appen utilized the arithmetic mean property values, retrieved from a very large number (1500) of investigated glasses. He also significantly improved the accuracy of calculations by introducing corrections for some oxides, mainly the

network forming oxides (e.g. SiO_2) and also for oxides that may experience coordination number changes like TiO_2 (Volf, 1988).

Databases of empirically acquired glass properties have been compiled in the SciGlass information system that applies computerized algorithms to provide predictions over a variety of properties and a relatively wide range of glass compositions. The empirical character of the most usable predictive methods signifies the need of including known structural information to potentially increase the precision of the calculations. Links between structure, composition and properties may then be possible (Priven, 2004). Nevertheless, until more structural information is experimentally established, these methods can provide a useful practical tool in glass designing.

2.4 Crystallisation

Crystallisation is the process by which the disordered liquid structure re-organizes itself generating an ordered crystal lattice. Crystallisation occurs as a nucleation and growth process.

2.4.1 Nucleation

Nucleation is the process where nuclei of a new phase are stabilised within and at the expense of an amorphous parent phase. The precursors of nuclei are termed embryos and are unstable (McMillan, 1979, Kingery, 1976). Nucleation is characterised as, either homogeneous (also known as volume or bulk) or

heterogeneous (also known as surface), depending on whether nuclei form spontaneously and with equal probability within the melt (Kingery, 1976) or on a pre-existing surface (e.g. impurities present, crucible walls) (Turnbull, 1969).

2.4.1.1 Homogeneous nucleation

Becker (1940) studied the spontaneous formation of embryos in supercooled melts and obtained the following expression for the local free energy change ΔG_i associated with the formation of a β phase embryo in a parent phase α:

$$\Delta G_i = - 4/3\pi r^3 \Delta G_v + 4\pi r^2 \Delta G_s \quad \text{(Eq. 3)}$$

where r is the radius of a generated spherical embryo consisting of i adjacent atoms (or molecules). ΔG_v is the volume free energy change per unit volume while ΔG_s is the interfacial free energy change per unit area. The negative term ($- 4/3\pi r^3 \Delta G_v$) in Equation 3 represents the reduction of free energy per unit volume of the system (hence proportional to r^3), associated to the transition from the less ordered phase α to the more ordered phase β. It can be measured as the difference between the volume free energies (ΔG_v) of phases α and β in the absence of stress and surfaces (Becker, 1940, Fisher et al., 1948). The positive term in Equation 3 ($4\pi r^2 \Delta G_s$) represents the gain in free energy (ΔG_s) per unit area (hence proportional to r^2); this is due to the melt-embryo (α-β) interface formed. Fisher et al., (1948) includes another positive term in the calculation of ΔG_i, the strain energy factor ($\Delta \Gamma_i$) or

elastic distortion energy. This is generated due to specific volume (1/ρ, ρ: density) difference between phases α and β. Fisher considers it indispensable in condensed (liquid-solid or solid-solid) systems, however other authors note that it may be excluded in liquid-liquid or vapour-liquid systems (Kingery, 1976, McMillan, 1979, Höland et al., 2003).

Figure 2.4 is a graphical representation of how the terms in Equation 3 change as a function of *r*. It can be observed that ΔG_i initially increases for small values of *r*, as a result of the prevalence of the positive interfacial term in Equation 3. ΔG_i reaches a maximum (ΔG_i^*) when the embryo obtains a critical size r^* determined by the number i^* of atoms (or molecules) it consists of (Kingery, 1976).

Beyond this point, the volume term of Equation 3 predominates, resulting in gradually decreasing ΔG_i. The embryo with radius r^* is termed as a critical nucleus. The energy needed to form a critical nucleus is ΔG_i^* and is defined as the thermodynamic barrier to nucleation. For values of ΔG_i less than ΔG_i^*, the embryo will re-dissolve into the parent phase. For values greater than ΔG_i^*, the embryo will form a stable nucleus which can further grow with decreasing free energy (Turnbull and Fisher, 1949). In order to calculate r^* we need to differentiate Equation 3. This gives us $r^* = 2\,\Delta G_s/\Delta G_v$ and by substituting this in Equation 3, we obtain (McMillan, 1979):

$$\Delta G_i^* = 16\pi\,(\Delta G_s)^3/3\,(\Delta G_v)^2 \qquad \text{(Eq. 4)}$$

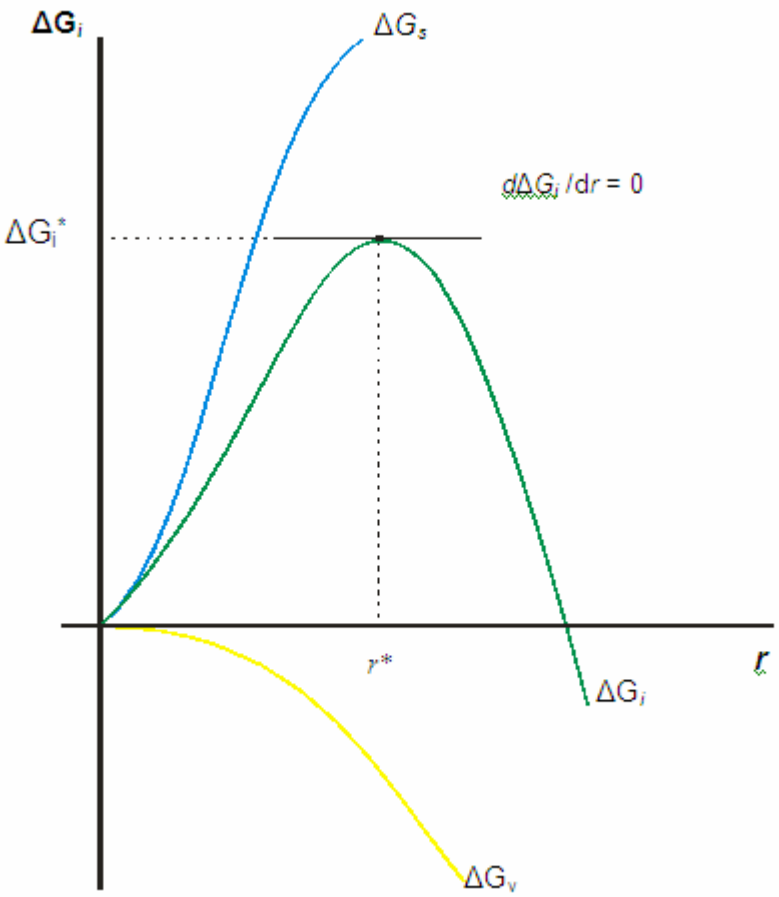

Figure 2.4: Changes in free energy as a function of nucleus radius *r.*

The volume free energy term Δ*Gv* is expressed by:

$$\Delta G_v = L\Delta T/VT_m \qquad \text{(Eq. 5)}$$

where *L* is the energy per mol evolved for the α→β transition (latent heat of fusion), Δ*T* is equal to the temperature difference between the liquidus (T_m) and the undercooled temperature and *V* is the gram-atomic volume of the critical nucleus. Thus we can estimate the thermodynamic barrier by using Equations 4 and 5 as:

$$\Delta G_i^* = 16\pi (\Delta G_s)^3 (V T_m)^2/3 (L\Delta T)^2 \qquad \text{(Eq. 6)}$$

For a critical nucleus to form spontaneously within the bulk of a cooling glass melt, a second barrier must also be overcome termed the kinetic barrier (ΔG_D), or free energy of activation (Turnbull and Cohen, 1958). This barrier is determined by the rate at which atoms (or molecules) are transported (or diffused, denoted by D) to the nucleating site (α-β interface). This rate must be sufficient as a feed for the new ordered phase to form. The transport of atoms (or molecules) across the α-β interface is characterized by a diffusion coefficient D^*, exponentially related to the kinetic barrier by (McMillan, 1979):

$$D^* = \alpha_o^2 \, v \exp(-\Delta G_D / kT)$$

which solving for v gives: $v = D^* / \alpha_o^2 \exp(-\Delta G_D / kT)$ (Eq. 7)

where α_o is the inter-atomic distance, v is the vibration frequency at the α-β interface and *k* is Boltzmann's constant.

The nucleation rate *I* (i.e. the number of nuclei per unit volume formed per unit time) is proven to exhibit an exponential relationship with both the thermodynamic and the kinetic barriers (Becker, 1940, Fisher et al., 1948, Turnbull and Cohen, 1958). Various expressions of *I* have been proposed. The general form of these expressions is an Arrhenius type formula that approximately expresses *I* as a function of the barriers and the absolute temperature T (°K) as follows (Fisher et al., 1948):

$$I = A \exp[-(\Delta G_{i^*} + \Delta G_D) / kT] \quad \text{(Eq. 8)}$$

where *A* is the pre-exponential factor (or rate coefficient). *A* is approximately equated to $n_o v$ where n_o is the number of atoms (or molecules) of nucleating phase

β per unit volume of parent phase α. By substituting the expressions for the thermodynamic barrier (Equation 6) and for $A = n_o v$ (calculated from Equation 7) into Equation 8, the temperature dependence of nucleation is obtained (McMillan, 1979):

$$I = [n_o D^* / \alpha_o^2] \exp [-16\pi (\Delta G_s)^3 V^2 T_m^2 / 3 L^2 \Delta T^2 kT] \quad \text{(Eq. 9)}$$

Equation 9 is one of the various expressions developed to enable approximation of nucleation rates using measurable parameters. Kingery (1976) notes that the temperature dependence of the nucleation rate is so sharp, that for a given melt, the temperature at which homogeneous nucleation takes place may constitute a material property. The diffusion co-efficient in Equation 9 is usually expressed by the Stokes-Einstein relation (Einstein, 1926) ($D=kT/3\pi\eta\alpha_o$) that relates diffusion D to viscosity η (McMillan, 1979, Zarzycki, 1991); it is however a matter of debate whether this relation holds true for the case of supercooled liquids, due to lack of systematic experimental data to support the underpinning theoretical assumptions (Tarjus and Kivelson, 1995, Granazy and James, 1999).

2.4.1.2 Heterogeneous nucleation

The first barrier (thermodynamic) for a nucleus to be formed is partially overcome when the surface onto which a nucleus can form is pre-existent in the melt (heterogeneity). That is because the surface free energy term in Equation 3 is reduced resulting in a decrease in the maxima of the ΔG_i curve in Figure 2.4. The amount of reduction is dictated by the ability of the nucleating phase to wet the

heterogeneity, thus depending upon their interfacial contact angle θ formed (Figure 2.5) (McMillan, 1979). Assuming a flat heterogeneity, at equilibrium, the contact angle θ is given by (Turnbull, 1950):

$$\gamma_{mh} = \gamma_{nh} + \gamma_{nm}\cos\theta \qquad \text{(Eq. 10)}$$

where γ is the interfacial tension present in each case between the melt (m), the heterogeneity (h) and a forming spherical cap shaped nucleus (n) in Figure 2.5.

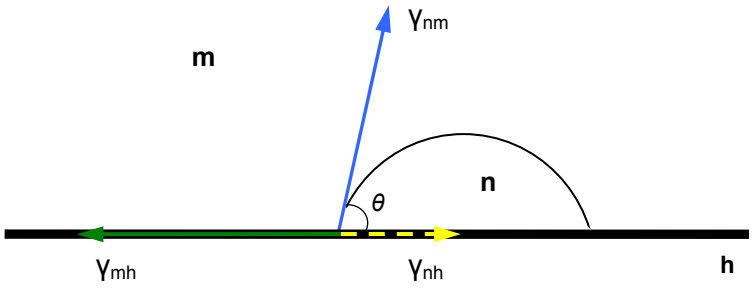

Figure 2.5: Heterogeneous formation of a nucleus on a flat substrate.

Turnbull and Vonnegut (1952) used Volmer's (1929) expression for the thermodynamic barrier $\Delta G_{i\varepsilon^*}$ of heterogeneous nucleation [$\Delta G_{i\varepsilon^*} = \Delta G_{i^*} f(\theta)$] to express the heterogeneous nucleation rate I_ε. They obtained a modified expression of Equation 8 which can be rewritten as:

$$I_\varepsilon = A_\varepsilon \exp\left[-\left(\Delta G_{i^*} f(\theta) + \Delta G_D\right) / kT\right] \qquad \text{(Eq. 11)}$$

where $f(\theta)$ is related to the contact angle θ by:

$$f(\theta) = (2 + \cos\theta)(1 - \cos\theta)^2/4 \qquad \text{(Eq. 12)}$$

This is valid when a spherical cap shaped nucleus is assumed to form on a flat heterogeneity larger than the nucleus (McMillan, 1979). According to this function, the greater the wetting ability of the nucleus, the less the energy that is needed for its formation, since $\Delta G_{i\varepsilon^*} \rightarrow 0$ as $\theta \rightarrow 0$ (Zarzycki, 1991). The constant A_ε in Equation 11 can approximately be equated to $n_{o\varepsilon}v$, where $n_{o\varepsilon}$ is the number of atoms (or molecules) of nucleating phase β in contact with the heterogeneity per unit area of contact (Kingery, 1976).

More complicated systems such as conical and cylindrical cavities have also been approached by Turnbull (1950), to obtain the work needed to form nuclei based on the model of flat heterogeneities described. Further complications of the basic model arise, by the fact that the concentration of pre-existing heterogeneous sites in the melt affects the nucleation rate (Zarzycki, 1991).

Nucleation, as described by the classical nucleation theory, utilises the model of a spherical nucleus that presents bulk properties, until it reaches a sharply defined interface (Kelton, 1991). This simplified model however, has been sceptically reviewed (Broughton and Gilmer, 1983, Laird and Haymet, 1992, Ohnesorge et al., 1994) and it is suggested that interfacial widths of multiple molecular layers, may better describe melt – nuclei transitional zones. Granasy and James (1998) further suggest that nuclei may almost completely consist of the melt – nuclei interface; therefore classical nucleation theory based predictions should always be looked at with caution.

2.4.1.3 Nucleating agents

One of the key parameters in producing fine-grained glass-ceramics, is to provide a high density of nucleation sites (McMillan, 1979). Nucleating agents are bodies that can catalyze the formation of nuclei of the newly developed phase (Turnbull and Vonnegut, 1952). Dispersion of nucleating agents in the form of colloidal sized particles within the glass is necessary for this catalysis to be efficient (McMillan, 1979).

The mechanisms of nucleation catalysis that have mainly been proposed are catalyst crystallisation, interfacial tension reduction and phase separation (Doremus, 1973). In catalyst crystallisation, it is suggested that the nucleation agent precipitates in the form of fine crystals that subsequently provide the sites for the main crystal phase to grow (epitaxial growth). It becomes obvious from the analyses on heterogeneous nucleation, that reduction of interfacial tension is a significant factor for promoting nuclei formation. Barry et al., (1969) supported the idea that high field strength ions may lower interfacial tension by acting as “surface active agents”. In their study, Ti^{4+} ions were proposed to attract and redistribute non-bridging oxygens to the surface of otherwise bridged network domains, thus creating potential growth sites.

Various nucleating agents are used in the glass-ceramic art, mainly metals, metal oxides and fluorides. The most widely used nucleating agent is titanium dioxide (TiO_2). Titanium dioxide is quite soluble in many glasses (Doremus, 1973). It has been shown to effect nucleation in amounts of 2 – 20% wt in many glass

systems (Stookey, 1960). Weyl (1951) suggested that coordination changes of 4 to 6 may lead to structural compatibility of the titanium-oxygen groups with tetrahedral silicate networks. When the glass melt is cooled, the coordination state reverts to the low-temperature configuration of 6 and the Ti ions are displaced from the network forming sites. In the presence of certain divalent metal oxides, Maurer (1962) suggested that Ti ions may form separate phases that can act as nucleation sites. This may be explained, as the interfacial energy for forming a crystal nucleus at the diffusion zone between the different phases, is expected to be lower (Tomozawa, 1972), thus fulfilling the criterion for heterogeneous nucleation.

In aluminosilicate systems, ZrO_2 and TiO_2 and P_2O_5 have successfully been used as nucleating agents for crystallising leucite in white-wares and TiO_2 was regarded as the most effective (Rouf et al., 1978). Fine grained dental aluminosilicate glasses that utilize TiO_2 as nucleating agents for leucite crystallisation have successfully been developed by Cattell et al., (2005, 2006). Cattell et al., (2009) also witnessed a secondary phase in a leucite containing frit that was Ca and Ti rich. The potential synergy of these elements in promoting leucite nucleation is attempted to be elucidated in a part of the present study.

2.4.2 Growth

Growth is the kinetic process of crystal development, during which atoms are deposited in an orderly manner onto a stabilized nucleus. This kinetic process may be governed by the rate at which the disordered network is rearranged to precipitate

an ordered crystal lattice and/or by the energy removal (heat flow) from the crystal – melt interface front (McMillan, 1979). Various expressions of crystal growth have been developed.

According to Turnbull (1956), a crystal of phase β may grow when atoms from the parent phase α cross the α-β interface by acquiring an activation free energy $\Delta G_D'$ (kinetic barrier). The difference in free energy between the two states is $\Delta G_v = G_\beta - G_\alpha < 0$ (Figure 2.6). The frequency by which this crossing occurs is given by:

$$v_{\alpha\beta} = v \exp[- \Delta G_D'/kT] \qquad \text{(Eq. 13)}$$

while for traversing the interface in the reverse direction (β→α) the frequency is given by:

$$v_{\beta\alpha} = v \exp[- (\Delta G_D' - |\Delta G_v|)/kT] \qquad \text{(Eq. 14)}$$

The velocity *u* of this migration (crystal growth rate) is given by the product of the inter-atomic distance α_o across the α-β interface multiplied by the net vibrational frequency v'. Since the latter is equal to $v_{\alpha\beta} - v_{\beta\alpha}$, *u* is given by:

$$u = \alpha_o v' = \alpha_o v \exp (- \Delta G_D'/kT)[1 - \exp (\Delta G_v/kT)] \qquad \text{(Eq. 15)}$$

It is questioned whether this expression of crystal growth rate can find direct application in most cases, as the activation energy $\Delta G_D'$ for an atom to cross the interface is unknown (Zarzycki, 1991). Turnbull (1956) stresses the fact that $\Delta G_D'$ and ΔG_D (the kinetic barrier to nucleation) are not necessarily equal or even of the same order of magnitude. This difference is larger for the cases where the crystal is compositionally different from the parent glass, as bonds between atoms must be broken (Turnbull and Cohen, 1958). The different types of diffusion governing

nucleation (short range diffusion) and growth (long range diffusion) seem to be responsible for this phenomenon (Zarzycki, 1991).

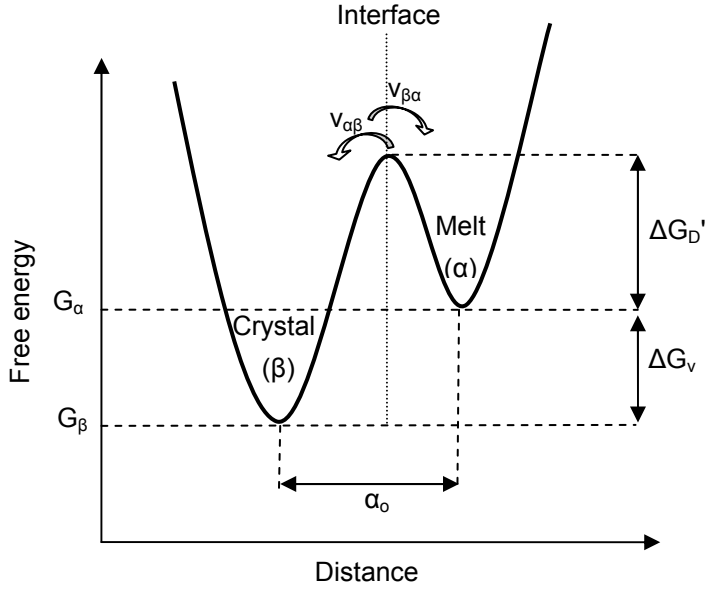

Figure 2.6: Free energy relations during the crystal growth process.

(redrawn and edited from Zarzycki, 1991)

The diffusion coefficient *D'* for the transport across the α-β interface during crystal growth can be expressed as an exponential function of the kinetic barrier $\Delta G_D'$ by (Doremus, 1973):

$$D' = \alpha_o^2 \, v \exp(-\Delta G_D'/kT) \quad \text{(Eq. 16)}$$

and thus Equation 15 can be further written as:

$$u = \alpha_o \, D' [1 - \exp(\Delta G_v/kT)] \quad \text{(Eq. 17)}$$

where D' can be also expressed by the Stokes-Einstein relation (Einstein, 1926) ($D=kT/3\pi\eta\alpha_o$) taken it is valid for supercooled melts.

Significant effort has been expended in simulating phase transformation phenomena (Levi and Kotrla, 1997, Rak et al., 2001) by incorporating nucleation and growth theories in numerical models. These models would aid the better

understanding of nucleation and growth processes and the development of new materials (Kotrla, 1996).

2.5 Glass - ceramics

A glass-ceramic is a polycrystalline solid that is initially formed as an amorphous glass and subsequently heat treated in a controlled manner, so that crystals nucleate (I) and grow (U) before cooling (Figure 2.7) (McMillan, 1979). This process can be enhanced by the presence of nucleating agents. In Dentistry, glass-ceramics find applications as monolithic systems for inlays, onlays veneers or crowns. They can also serve as veneering materials for metal or ceramic cores and also as bioactive bone replacement materials (Höland et al., 2006).

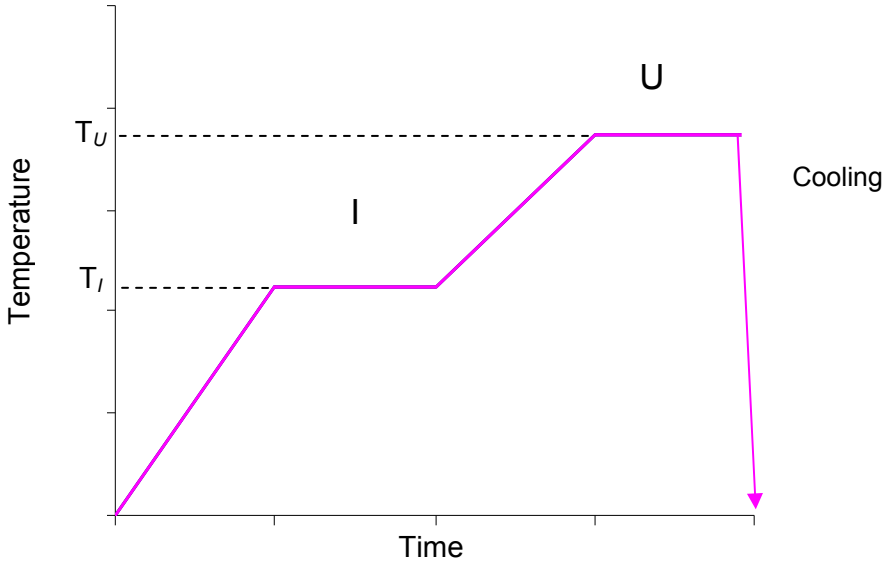

Figure 2.7: Diagram of crystal nucleation (I) and growth (U) as a function of time and temperature.

Studies on the crystallisation kinetics and the glass transition temperature of the starting glass material are necessary prior to choosing the optimum nucleation and growth temperatures. The crystallisation kinetics studies provide the information of the major crystalline phase/ phases that can be grown in the chosen glass system and determine the temperatures at which these phenomena occur. Differential Scanning Calorimetry and X-ray diffraction are relevant and complementary experimental techniques for these studies (Basudeb et al., 2002). A temperature of 30°C above the determined T_g is generally selected as the nucleation temperature (McMillan, 1979), unless indicated otherwise from pilot nucleation experiments. The sample is ramped to the nucleation temperature and typically held for 1-2 hours to allow nuclei formation. The growth of the major crystalline phase of interest is achieved by further heating of the nucleated glass to the chosen growth temperature. Control of the growth kinetics is achieved, by both the chosen temperature linked with the crystallisation of the phase of interest and the time allowed for the phase to grow. The initial glass composition and the crystalline phase stoichiometry further determine this process. Sample deformation and redissolution of the phase / phases of interest must be taken into account when choosing the growth temperature. Yielding of a fine grained microstructure ideally requires a high nucleation rate and low growth rate. A plethora of nucleation sites can be thus formed whose growth will be restricted by the low growth rate (Kingery, 1976).

Crystallisation yields improved and controllable properties in dental glass-ceramics. Wear properties (Metzler et al., 1999), elastic modulus and strength are enhanced (McMillan, 1979). In addition, the crystals created serve as a toughening mechanism due to the fact that cracks in the glassy matrix are either stopped or deflected by them, thus increasing the amount of energy needed for cracks to propagate. The resulting increase in the mechanical properties can also be attributed to the absence of pores due to the fabrication process (McMillan, 1979), which also contributes significantly to their increased translucency (McLean, 2001). A fine grained microstructure is desirable to further enhance strength and wear properties (Cattell et al., 2006).

2.6 Structure of Leucite

Leucite ($KAlSi_2O_6$) is a rock forming alumino-silicate mineral. Rings of four and six corner linked SiO_4 tetrahedra form a (Si, Al)-O framework silicate structure. Structural channels are formed by axial arrangement of the six membered rings. The centre of these channels is occupied by mono-valent cations of K, Cs and Rb. Tetragonal and cubic leucite configurations exist that both contain 16 ($KAlSi_2O_6$) in the unit cell. The tetragonal phase of leucite is stable at room temperature where the K cations are too small to fill the large cavities within the channels. This results in a shift from their central position in the channels causing the framework to collapse. The high temperature configuration of leucite (above 625°C) is cubic and the K cations reside in their central position (Deer et al., 1969). The cubic to tetragonal phase transformation of the unit cell is reversible (Mackert, 1988), being

temperature dependant (605 to 625°C) and results in a 1.2% discontinuous volume change (Mackert et al., 1986). There is also a subsequent change in thermal expansion from 11.7 to 12.8x10^{-6}/°C [25-600°C] for cubic leucite, to 20 to 25x10^{-6}/°C [20-800°C] for tetragonal leucite (Hermansson and Carlsson, 1976, Rouf et al., 1978). During the tetragonal to cubic transformation, the unit cell of tetragonal leucite contracts along the c-axis (Figure 2.8) and expands along the a-axis. This results in a characteristic twinning of crystallographic planes which has been verified by X-ray diffraction studies (Mazzi et al., 1976, Palmer et al., 1988).

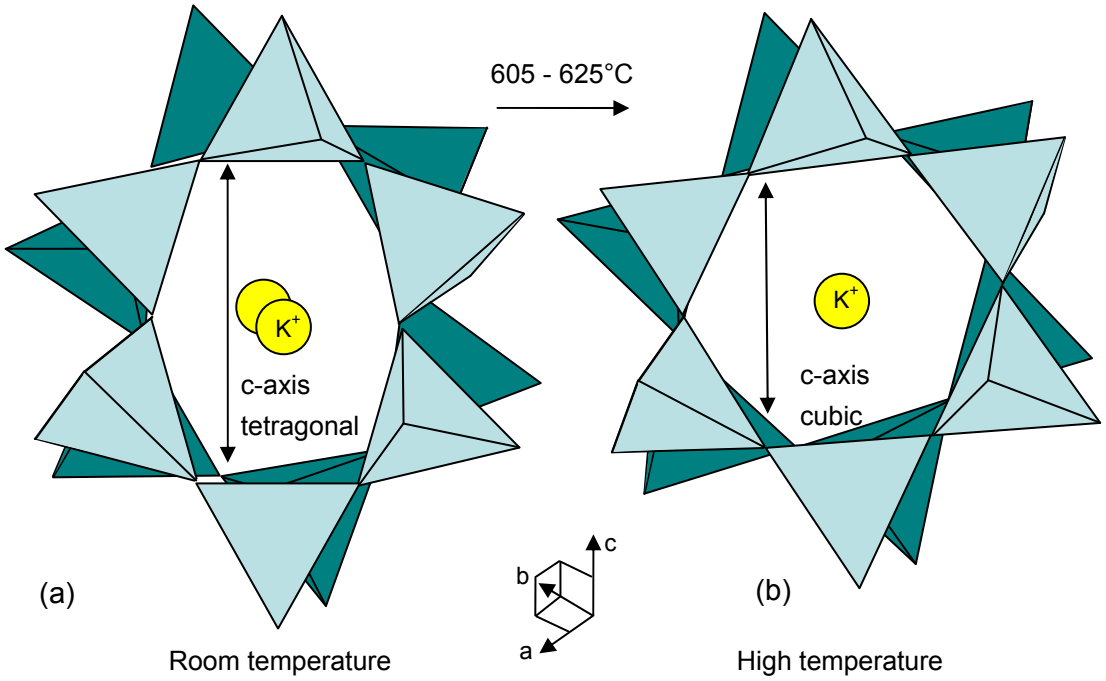

Figure 2.8: Six membered SiO_4 tetrahedra rings forming channel structures of (a) tetragonal leucite (b) cubic leucite (redrawn and edited from Palmer et al., 1997).

2.6.1 Leucite in dental porcelains

Leucite was first introduced in dental porcelains to enable metal-ceramic coefficient of thermal expansion (CTE) matching for dental restorations. Leucite incorporation in a base glass was achieved either by blending low and high expansion powdered feldspar frits (Weinstein et al., 1962), or by dispersion (Burk and Burnett, 1978). The mismatch of the CTE between the base glass and the leucite crystals also results in development of tangential compressive stresses around the latter which is thought to enhance the strength of feldspathic dental porcelain (Denry et al., 1996). The extent of this mismatch however may be responsible for microcracking in and around the leucite crystals. Microcracks can either reduce strength by acting as stress raisers, or reduce the CTE of the bulk porcelain by reducing the crystal – matrix coupling (Binns, 1983). Reduction of leucite crystal size may however limit this microcracking (Mackert et al., 2001); Cattell et al., (2006) have successfully synthesized fine grained leucite glass-ceramics with minimal matrix microcracking and improved mechanical properties. Tailoring the crystal-matrix CTE mismatch by stabilizing cubic leucite at room temperature in an attempt to avoid microcracking, has been shown to be possible by ion exchanging potassium ions in the leucite structure with larger ions such as caesium (Denry et al., 1996) or rubidium (Denry et al., 1998) (Figure 2.8). Nevertheless, while the crystal-matrix mismatch was successfully reduced by Denry et al., (1998) the accompanying residual stresses were also reduced. This was associated with a reduction in strength values (Denry et al., 1996). It may be that the exchange process has not yet been optimized

and/or the presence of composition related limitations. Rasmussen et al., (2004) used caesium stabilised leucite particulate dispersion in a caesium - free dental glass matrix and noticed a caesium dependant increase in toughness of the final product as a result of transformation toughening. The modulus of rupture of the toughest combinations was however low and was attributed to internal flaws and crystal-matrix decoupling.

Höland et al., (1995) demonstrated the surface crystallisation mechanism for leucite. Tošić et al., (2000) found a glass particle size dependant mechanism switch from bulk to surface for glass particle sizes below 75 μm. Glass particle size is therefore key to the control over leucite crystallisation in dental glass-ceramics (Cattell et al., 2006, Chen, 2009).

2.7 Mechanical milling

Mechanical milling is a form of powder processing that can be employed to reduce the particle size of a powder (Suryanarayana, 2001). Various types of mills exist in terms of design, operating conditions and milling efficiency that can be used for this task. The simplest design involves a rotating jar that is charged with a mix of balls (media) and the powder to be milled. As the jar is rotated, the balls collide with each other and with the jar walls. These collisions crush and grind the powder to finer sizes. The speed of rotation is the limiting parameter of this design in terms of minimum achievable particle size. At speeds where the centrifugal force acting on the media becomes higher than gravity, the media are pinned to the walls and no milling can take place (Suryanarayana, 2004).

Attritor mills consist of vertical drums that are filled with media and equipped with a series of impellers. The impellers are rotated by a powerful motor effecting the development of a variety of forces (impact, shear, tumbling) amongst the impeller-agitated media and consequently on the powder particles. Attritor mills can be very efficient in terms of energy transfer, thus they can easily produce powder sizes that are in the micrometer range (He and Schoenung, 2002). Another high-energy design is that of a planetary ball mill. Cylindrical vials (milling stations) that are capable of rotating around their own axes are attached to a rotating support disc or encased in a rotating support cylinder. The rotation of the support effects planet-like movement to the vials and the resultant mixed centrifugal forces transferred to their contents (ball media and material to be ground) lead to high impact energy (Mio et al., 2002). Nanometre range particle sizes have been reported to have been

achieved in planetary mills (Chinnasamy et al., 2001).

The intensity of milling (or milling energy) E_w has a direct impact on the efficiency of milling and for a planetary mill has been defined as (Kano et al., 1999):

$$E_W = \sum_{j=1}^{n} \frac{1}{2W} m v_j^2 \qquad \text{(Eq. 18)}$$

where v_j is the relative velocity between a ball colliding against the mill wall or two colliding balls, m is the mass of a media ball and W is the sample mass charged into the mill. The number of collisions of a ball against other balls or the mill wall within a second is denoted by n.

Reducing glasses to a fine powder provides a plethora of nucleation sites on the glass particles' surface. Increasing nucleation sites can significantly improve the resultant microstructure of the end glass-ceramic and reduce the obtained crystal size (McMillan, 1979). It has been suggested that reactive surfaces of small glass particles are highly probable to initiate the crystallisation of leucite in certain glass compositions (Höland et al., 1995).

The energy developed in high energy mills has also been extensively exploited for driving various chemical reactions, mechanical alloying (Boldyrev and Tkácová, 2000, Suryanarayana, 2001) and for ion-exchanging experiments (Christian and Mao, 2002). Particle size reduction and ion-exchange experiments exploiting high energy milling have been performed for the purposes of the current thesis.

2.8 Processing of glass-ceramic dental restorations

2.8.1 Condensation and firing

In order to form a porcelain restoration, the ceramic powder is first mixed with a binder (usually water or any organic binder), shaped using instruments and then the binder is removed (Gill, 1932). The process of binder removal and subsequent compaction is termed condensation. The goal of condensation is to achieve maximum compaction of the ceramic grains. Therefore both the particle size distribution, as well as the process employed for condensation, have an effect on the final packing density. The benefits of good condensation are less shrinkage (30 – 38% vol.) and porosity during firing (Kingery, 1976, Binns, 1983).

Condensation relies on the effect of surface tension of the binder, which effectively while being removed, brings the particles closer together. Condensation can be achieved by applying mild vibration, so that the binder emerges on the surface where it can be absorbed with a tissue or wiped with a brush (Binns, 1983).

After shaping and condensing porcelain, the next stage is firing. This includes drying and sintering in a furnace. Drying occurs at a low temperature where the remainder of the binder is evaporated, along with any organic colouring agents usually added to porcelain to distinguish the various layers. Sintering occurs in three stages called low, medium and high biscuit (Cheung and Darvell, 2002). In the low biscuit stage, bridges are formed between adjacent particles. This occurs as a result of the thermodynamic principle where, in order for them to decrease their excess energy provided by the heat, their total surface is decreased by bridging (Kuczynski

and Zaplatynskyj, 1956). At this stage no perceivable reduction in volume occurs. In the medium biscuit stage, the grains start to melt and fuse. Shrinkage is evident at this stage, while the porcelain surface is rough and full of pores. In the high biscuit stage, where the temperature is at the highest point, the fusing is completed. No more shrinkage occurs after this point while the porcelain surface becomes more even and relatively pore free (Cheung and Darvell, 2002). When vacuum firing is used and not air firing, porosity is virtually eliminated (Vines et al., 1958) and the resulting porcelain becomes more translucent (Binns, 1983).

The surface pores after firing are sealed through the final process termed glazing. The aim of glazing is to provide a hygienic surface. Glazing can be achieved after the adequate shape adjustments through grinding have taken place. A glazing method consists of application of a low fusing glass paste on the fired surface and firing of the restoration at a lower temperature than the porcelain maturing temperature. Alternatively, a special firing cycle is performed where the superficial surface layer fuses and self-glazes the surface (van Noort, 2002).

2.8.2 Heat pressing

Heat pressing is a ceramic manufacturing process, that exploits the application of an external pressure at high temperature for driving the densification of the ceramic article (Coble, 1970). This process is advantageous over condensation and firing, as porosity and shrinkage are largely reduced. The elimination of porosity may enhance mechanical and optical properties of the pressed component. The temperature of pressing may be chosen so that extensive grain growth is avoided,

thus enabling microstructural control (Kingery, 1976). In leucite dental glass-ceramics, significant biaxial flexural strength and reliability increases have been achieved as a result of heat pressing (Cattell et al., 2001).

Heat pressing for dental glass-ceramics is intended either for monolithic or core materials. The restoration is made in a wax pattern and subsequently invested in a refractory die material so that a lost wax process will follow. The refractory is burnt out and then placed into a special pressing furnace, where a glass-ceramic ingot is heated and then extruded by a plunger, so that it flows into the empty space of the refractory. After divesting and shaping with appropriate rotary tools, the article can be further layered with thermally compatible sintered porcelain, or directly finished with appropriate stains and glaze (Wohlwend et al., 1990, Beham, 1990).

2.9 Human enamel

2.9.1 Enamel structure

Enamel is the most mineralised (>96% wt) known body tissue, containing less than 4% wt organic matter and water. Enamel presents a highly hierarchical structure. The smallest building blocks of enamel are long carbonatoapatite (hydroxyapatite substituted with carbonate atoms) crystals of 25 – 30nm thickness closely packed together into two structures, namely rod and interrod enamel. Rods (4 μm thick) are almost cylindrical structures with longitudinal axes that run from the amelo-dentinal junction towards the tooth surface. The long axes of the crystallites in the rods run, for the most part, parallel to the longitudinal rod axis. The rods are embedded into

the interrod enamel (Nanci, 2003). The crystallites' long axes in the interrod enamel run at about 60° angle to the rods longitudinal axis (White et al., 2001). Between the rod and interrod enamel structures lies organic material known as the rod sheath (Nanci, 2003). Proteins (Nanci, 2003) and collagen (Açil et al., 2005) present in this organic material and also between the crystallites, maintain this highly hierarchical enamel structure (He and Swain, 2007a). The enamel layer at the tooth surface where unimpeded enamel growth has occurred, is characterised by the lack of rods and crystallites (Boyde, 1967) and is known as aprismatic enamel (Whittaker, 1982). The thickness of the aprismatic enamel surface layer varies (20 – 100 μm) with tooth type, tooth surface (Whittaker, 1982) and age (Nanci, 2003). Aprismatic enamel is potentially more wear resistant than prismatic (Krejci et al., 1999). As aprismatic enamel is the superficial tooth zone however, it is also the first to wear. Enamel rods reaching the surface, or complex surfaces formed by both aprismatic enamel and rod-interrod enamel, are the two other two main types of surface found (Whittaker, 1982).

2.9.2 Properties of enamel

Being the outmost tooth layer, enamel protectively covers its anatomic crown. Although due to its high mineral content enamel is usually described as a natural bio-ceramic material (Robinson et al., 2004), He and Swain (2007a) describe its stress-strain response properties as that of a metallic-like biocomposite. He and Swain (2007b) further suggest, that macro - mechanical responses of enamel may

be regulated nano-mechanically by the inherent nano-mechanical properties (e.g. inelastic stress redistribution) of proteins between the enamel crystallites. This is also confirmed by the study of Baldassarri et al., (2008). Anisotropy of elastic modulus has been predicted in a finite element model of enamel, that shows differences in calculated modulus along (higher *E*) and across (lower *E*) the rods' longitudinal axis orientation, with the along axis values in agreement with experimental values. This anisotropy becomes less pronounced with increasing enamel to organic ratio in the model (Spears, 1997). Resistance to crack propagation is proposed to be moderately anisotropic, with enamel possessing higher toughness across than along the rods' longitudinal axis orientation (White et al., 2001). The toughness values are also found to increase from the surface to the amelodentinal junction, attributing rising R-curve behaviour to enamel and values up to 4.0 MPa $m^{0.5}$/mm (Bajaj and Arola, 2009).

2.10 Tooth wear

Tooth wear is the surface material net loss of a tooth under function. Tooth wear may incorporate different processes, frequently occurring in combination, that lead to material loss such as erosion, attrition and abrasion (Bartlett and Smith, 2000). Erosion is a material removal process occurring due to acidic attack (e.g. gastric fluids) excluding acids generated by bacterial activity. When material removal is caused by the physical wearing action of one tooth against another, the phenomenon is defined as attrition. When something other than tooth tissue causes that physical wear, the material removal process is described as abrasion (Addy and Shellis, 2006). Distinguishing amongst these processes, especially when there is insufficient evidence for the prevalence of one in particular, becomes difficult in practice and for this reason the term wear is preferred to describe material loss (Smith et al., 1997).

Wear can be encouraged and/or accelerated by various factors. These include types of food chewed, tooth brushing, medical conditions like bulimia and anorexia nervosa, acidic beverages, abrasive dust inhalation and parafunctional habits like bruxism (Smith et al., 1997).

One of the most important factors is the nature of the antagonistic surfaces in contact. In the case of dissimilar antagonistic surfaces, as is the case for natural teeth against dental ceramic restorative materials, the wearing process is greatly dependant upon physical (hardness, fracture toughness, frictional resistance), microstructural (porosity, crystallinity and crystal size/morphology) and compositional parameters. Chemical (acidic/ alkalic liquids) and surface finish

factors also affect the wearing process (Oh et al., 2002). Different ceramic restorative materials possess different sets of properties, that will affect the wear of the opposing dentition differently as shown by *in vivo* (Etman et al., 2006, Esquivel-Upshaw et al., 2006) and *in vitro* wear studies (Magne et al., 1999, Heintze et al., 2008). An *in vitro* wear study of glass-ceramic materials against human enamel, suggests that a reduced leucite crystal size and crystallinity, produces a smaller amount of enamel and glass-ceramic loss (Metzler et al., 1999). As far as enamel's material removal process, enamel seems to behave similar to some ceramic materials (e.g. alumina, zirconia and silicon carbide) with development of subsurface microcracks and delaminations (Arsecularatne and Hoffman, 2010).

2.10.1 Wear testing

The multi-factorial nature of wear complicates its study and assessment. Clinical studies of wear are generally time-consuming and complicated (Heintze, 2006). Laboratory simulation of wear is thus desirable (DeLong and Douglas, 1991). Numerous examples can be found in the literature, where different devices and protocols have been employed to reproduce and assess the wear effects on a wide range of dental materials (DeLong and Douglas, 1991, Ramp et al., 1997, Hu et al., 1999). Approaches with several levels of complexity are adopted. One challenging approach adopted is to mimic as closely as possible the intra-oral environment, by simultaneously considering variables such as contact force variability, three-dimensional movement of the specimen and the counter-sample, counter-sample

standardisation and environmental variability (saliva, humidity, temperature, aeration) (DeLong and Douglas, 1991, Krejci et al., 1999). Attempts also exist that limit the variables, so that simulation focuses in specific aspects of intraoral conditions mainly for material comparison (Hacker et al., 1996, Metzler et al., 1999) or specified variable effect purposes (Shortall et al., 2002). The lack of standardization amongst different studies further complicates the issue. Heintze (2006) reviewed *in vitro* wear simulators taking into account the FDA Good Laboratory Practice guidelines. He concluded that, the only simulator to fulfil the criteria and thus fall within the first approach mentioned earlier, is the MTS wear simulator developed by DeLong and Douglas (1983). In this method, the physiological relative movements of antagonistic members are simulated by using servo-hydraulic actuators, to control the force and lateral excursion of an axial and a horizontal actuator, closely mimicking the jaw motion under function. The load profile achieved (positive half of a sine wave) correlates well with *in vivo* measurements (Nyquist and Owall, 1968, Munakata et al., 1991, Kohyama et al., 2004). As a semi-qualified alternative, Heintze (2006) reports the Willytec wear simulator (Kern et al., 1999, Heintze et al., 2008), where the applied load on teeth specimens is delivered by weights and the relative movements of antagonistic members are controlled by stepping motors to complete the desired mastication cycle. In the Willytec wear simulator, no force sensor is integrated; however the resultant load waveform is established (sine wave with an initial impulse) using external force sensors. These examples can serve as the best to date for identifying

the limitations of any custom made wear testing machine. Simplistic designs that may have no correlation to *in vivo* wear effects, yet may potentially serve the purpose of material comparison under the individual design-specified parameters, are also found in the literature. Metzler's design (1999) incorporated drilled enamel cylinder specimens (pins), swept back and forth onto porcelain blocks by means of an offset CAM and a motor. Seghi et al., (1991) modified a polisher and its precision thinning attachment, so that enamel pins could be continuously loaded over a rotating disc of the tested ceramic.

When studying wear of dental materials *in vitro,* many important issues must be considered which will determine the significance of the results and the potential of *in vivo* correlation including: The device that will be used to simulate the wear and its limitations (Heintze, 2006). The type of specimens to be used (i.e. discs, fully anatomic crowns etc (Heintze et al., 2008)) and the standardization procedure for surface finish to be followed. The type of antagonistic material to be used (i.e. human enamel or substitute) (Shortall et al., 2002) and their standardized or non-standardized shape (Krejci et al., 1999, Heintze et al., 2008). The experimental settings to be chosen (i.e. applied load and its profile, contact time, number of cycles, environment) (Heintze, 2006) and the design of the wear assessment protocol by appropriate profilometric techniques (Mehl et al., 1997).

2.10.2 Wear quantification

Interest in quantification of the material loss (wear quantification) of dental materials and dental hard tissues is evident by a plethora of studies in the literature (Wiskott et al., 2000, Heintze et al., 2006, Zou et al., 2009). Wear quantification methods for measuring material loss after *in vivo* or *in vitro* wear tests include measuring weight (Kaidonis et al., 1998), height (Etman et al., 2008), mean-height, (Mehl et al., 1997, Kramer et al., 2006) and volume (Metzler et al., 1999, Mehl et al., 1997) material loss parameters. Volume and mean-height parameters provide the most clinically relevant information as they can be linked to cuspal structure loss and, ultimately, to facial height loss (Pintado et al., 1997). Wear quantification methodologies that can provide reliable and repeatable results are thus essential. The *in vitro* wear quantification process usually requires the employment of a method that can make an accurate topographical representation of the surfaces of interest before and after wear testing. Methods that have been employed for *in vitro* wear quantification include mainly three types of sensors for scanning and subsequent digitisation of surfaces. These include mechanical sensors (contact) (Magne et al., 1999), and non-contact sensors such as laser (Mehl et al., 1997) and white light (Vieira et al., 2006). All three sensor types have been found to be suitable for the quantification of wear facets in a systematic study by Heintze et al., (2006). Many studies have used white light non contact profilometric techniques for quantification of dental wear related phenomena such as erosion (Hara and Zero, 2008) and/or abrasion (Vieira et al., 2006, Moore and Addy, 2005, Heintze et al., 2006). The information provided

in most of the studies is usually limited to sample type and testing method while parameters used for the scanning (e.g. sensor, sampling rate) and the rationale behind the choice are not discussed. While surface matching and difference detection software are commercially available for *in vitro* wear quantification, algorithms have also experimentally been developed (Mitchell and Chadwick, 1998) and applied in quantification of erosive wear *in vivo* (Chadwick and Mitchell, 2001). Ongoing research highlights that these resources need to be tested and understood before application in dental studies, as their infallibility should not be taken for granted (Mitchell and Chadwick, 1998). White light profilometry is the technique of choice for the current study and a discussion on a novel designed wear quantification protocol and the scanning parameters selected therein (Theocharopoulos et al., 2010) is presented.

2.10.3 White Light Profilometry

White light profilometry is a profilometric technique that exploits the optical phenomenon of longitudinal chromatic aberration for obtaining accurate distance measuring sensors (Litwin et al., 2006). This phenomenon is expressed by special lenses that can split the light beam of a polychromatic (white) light source into its constituent wavelengths. Each wavelength can only be sharply focused on a point that lies at a specific distance from the sensor, thus creating a continuum of monochromatic imaging points. The distance sensing ability of the sensor is enabled by routing the reflected focused monochromatic beam through a pinhole

filter to a spectrometer. The spectrometer matches the central wavelength of the beam to the exact height of the focused point. A microtopographic image is then constituted by raster scanning across the desired specimen surface (Cohen-Sabban et al., 2001, Litwin et al., 2006) (Figure 2.9). Applications of white light sensors include industrial process control, reverse engineering and as high precision research tools. These non-contact sensors can provide analysis of shape and texture, microtopography and microform as well as roughness measurements. The 3-D microtopographic images constructed using white light Profilometry data, can be used in conjunction with specialised software for wear quantification of human enamel and dental materials (Moore and Addy, 2005, Vieira et al., 2006, Heintze et al., 2006, Hara and Zero, 2008, Theocharopoulos et al., 2010).

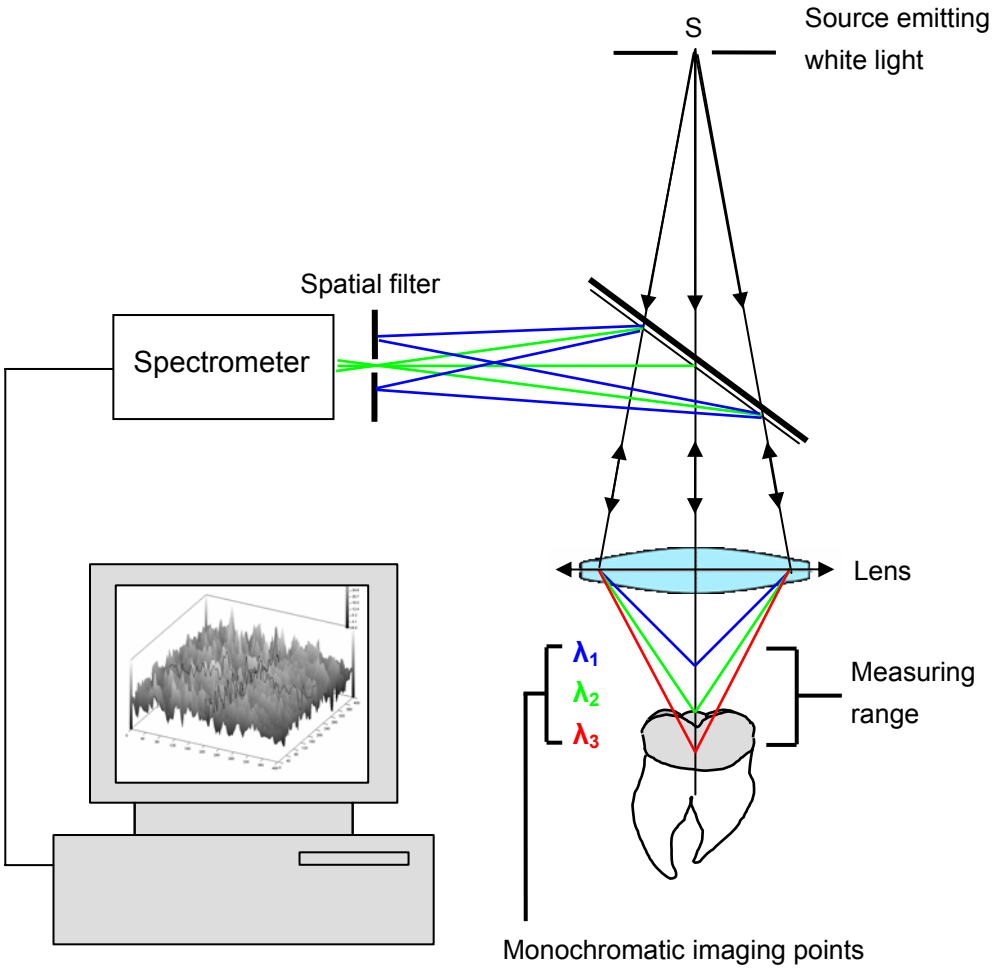

Figure 2.9 Schematic of the operation of a non contact white light sensor as part of a profilometer (redrawn and edited from Cohen-Sabban et al., 2001).

2.11 Experimental techniques

2.11.1 Differential Scanning Calorimetry

Differential Scanning Calorimetry (DSC) is a technique that measures the change of the difference in heat flow rate to the sample of interest and to a reference sample, that are simultaneously subjected to the same controlled thermal treatment (Höhne et al., 2003). Heat flow is the result of heat transfer between a system and its surroundings, as a consequence of a state change (solid ↔ liquid ↔ gas), a phase change or transformation, or a chemical reaction within the studied system (Price, 1998). The heat flow rate (DSC trace) is plotted against temperature and the resultant plot provides information of endothermic (valleys) or exothermic (peaks) events in the tested sample (Höhne et al., 2003). DSC finds applications in glass-ceramic technology to enable identification of various thermal events (Baricco et al., 2001, Yu et al., 2007) including: the glass transition temperature (T_g), crystallisation peak/s (T_p) and melting temperature of a glass sample (Höhne et al., 2003). The technique is complementary to SEM and XRD in the study of crystallisation kinetics in a glass system (Basudeb et al., 2002).

Different granulation range in powder samples tested by DSC may provide information on the mechanism of crystallisation (surface or bulk). Tošić et al., (2000) investigated this effect in a leucite glass-ceramic and found that, the larger the sample powder size, the higher the peak crystallisation temperature and the sharper the peak and *vice versa*. At very fine sizes (below 75 μm) the mechanism shifted from bulk to surface. Bulk crystallisation is typically expressed as a sharp peak while

surface crystallisation as a broad peak (Marotta et al., 1980, Laudisio et al., 1998).

2.11.1.1 Activation Energy determination

The information acquired from DSC results can be exploited to determine the crystallisation activation energy of glasses. The rate law for a generic chemical reaction mA + nB → Γ links its rate r with the concentrations of reactants A and B by:

$$r = k[A]^m[B]^n \qquad \text{(Eq. 19)}$$

where m, n are the partial reaction orders of the reactant concentrations [A] and [B] and k is a constant known as the rate constant (Muller, 1994). Arrhenius (1889) expressed k as a function of absolute temperature (T) and activation energy (E_a) (minimum energy required for the reaction to begin) by:

$$k = A \exp(-E_a/RT) \qquad \text{(Eq. 20)}$$

where A is a pre-exponential factor and R is the gas constant. Glass crystallisation kinetics under isothermal conditions have commonly been analysed using the Johnson-Mehl-Avrami equation which incorporates *k* to express the volume fraction x crystallised in time *t* as:

$$x = 1 - \exp[-(kt)^n] \qquad \text{(Eq. 21)}$$

where n is a factor known as the Avrami exponent and is dependant on the mechanism of crystallisation and takes various values (e.g. for surface crystallisation n=1, for bulk crystallisation n=3). By taking the double natural logarithm of Eq. 21 and substituting *k* from Eq. 20, we derive:

$$\ln[-\ln(1-x)] = -nE_a/RT + n\ln tA \quad \text{(Eq. 22)}$$

This expression can be used to plot ln[-ln(1-x)] as a function of the inverse absolute temperature at crystallisation (1/T, in this case a DSC determined T_p) as a straight line. The factor nlntA can be regarded a constant and gives the line x-axis intersect while the slope nE_a/R of the resultant line is used to calculate the activation energy (E_a) for crystallisation (Matusita et al., 1975, Xu et al., 1991). The double logarithm function however, is generally not very sensitive to subtle changes and may not apply to different kinetic models other than the Johnson-Mehl-Avrami, thus should be carefully examined (Málek, 1995).

For nucleation to commence and proceed in a glass, a certain period of incubation is necessary. By applying increasing heating rates during different DSC runs, the period to reach the desired temperature is shortened. This leads to a time lag for crystallisation shifting T_p to progressively higher temperatures (Kaidatzis et al., 2008). Kissinger (1956) exploited the varying peak position as a result of varying heating rate φ to introduce a different approach to activation energy determination:

$$\ln (\varphi/T_p^2) = -E_a/RT_p + \text{constant} \quad \text{(Eq. 23)}$$

The Kissinger equation is generally accurate for cases where surface crystallisation is predominant (Kaidatzis et al., 2008). It has however been criticised in various ways as it does not take into account the Avrami approach (dependence of nucleation mechanism) and the possibility of nuclei formation during the DSC measurements especially in non-isothermal conditions (Matusita et al., 1975, Matusita and Sakka, 1980, 1981) as well as heat conduction occurring in the DSC

(Yi et al., 2008). As a result modifications have been proposed. Nevertheless, when the crystallisation mechanism is not categorically discerned, activation energy calculations based on Kissinger plots of ln (φ/T_p^2) versus $1/T_p$ may provide some insight in respect to the ease of a glass system to crystallise in comparison to glasses of similar composition.

2.11.2 X-ray Diffraction

X-ray diffraction is a structural characterization technique for solid and powder substances and can be used to identify crystalline and amorphous phases in the sample tested.

According to Bragg (1928), a beam of parallel x rays (e.g. AB and A'B') (Figure 2.10) incident on a net of lattice planes (h,k,l) at an angle θ can be scattered so that the resultant reflections coincide and constitute a reinforced reflection. This reflection can be regarded as the diffracted beam. The law dictates that the length sum of AB and BC must be less than the sum of A'B' and B'C' by an integer number (n) of wave lengths (λ), thus the two X-rays must be in phase. This holds true for AB + BC = $2d_{hkl} \sin\theta$, where d_{hkl} is the distance between successive lattice planes (unique for each hkl family of atomic planes) and θ is the unique value of the angle of the incident beam with the lattice planes at which diffraction occurs. The mathematical representation of the law is:

$$2d_{hkl} \sin\theta = n\lambda \qquad \text{(Eq. 19)}$$

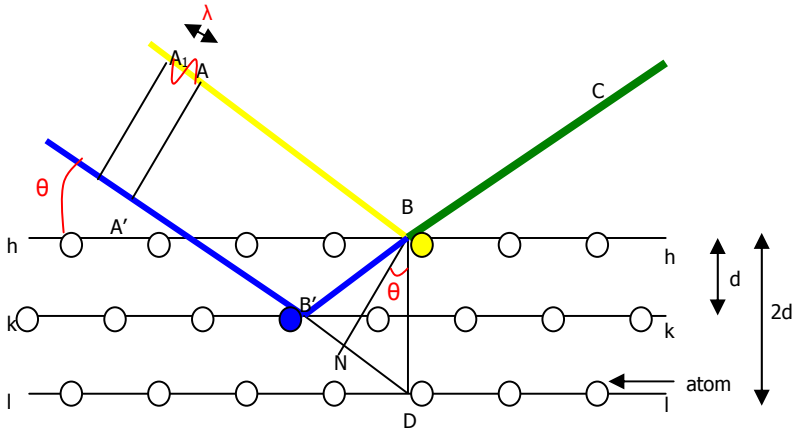

Figure 2.10: Successive lattice planes reflecting a beam of x rays (redrawn and edited from Bragg, 1928).

In the cubic system, d_{hkl} is related to the Miller indices and the lattice parameter α (distance between successive unit cells in a crystal lattice) by:

$$d_{hkl} = \alpha / \sqrt{(h^2 + k^2 + l^2)} \qquad \text{(Eq. 20)}$$

By combining Equation 20 with Bragg's law (Equation 19) we obtain:

$$(\lambda / 2\alpha)^2 = \sin^2\theta / (h^2 + k^2 + l^2) \qquad \text{(Eq. 21)}$$

which solved for $\sin^2\theta$ gives:

$$\sin^2\theta = (h^2 + k^2 + l^2) \times (\lambda / 2\alpha)^2 \qquad \text{(Eq. 22)}$$

Equation 20 predicts all the possible Bragg angles at which diffraction can occur for a given λ and a particular cubic crystal with lattice parameter α. A cubic crystal is the simplest crystal unit cell model where the unit cell volume is equal to α^3. For different crystal systems, Equation 20 is restructured for the relevant lattice parameters accordingly. By measuring the directions of diffracted X-rays from an unknown crystal, we can determine the size and shape of its unit cell (Cullity and

Stock, 2001).

What Bragg's law implies is that a practical method must be devised to ensure that the X-rays will be diffracted in the way described previously. One of the methods devised to achieve diffraction, is the powder method. The concept for this method is to set up the experiment in a way so that λ or θ will be continuously varied in a controlled manner and thus n will take different integer values. In powder diffraction λ is kept fixed and θ is variable. The material to be examined must be in powder form of a very fine scale, so that the condition for diffraction for all lattice planes within the material's structure can be satisfied. The different intensities of diffracted beams are reinforced and plotted against their respective 2θ values in a graph and the pattern is used for identification of the different phases present. The peak positions in the plot are determined by the space d_{hkl} between diffracting atom planes hkl. The intensity of each peak is determined by the type of atoms present in the plane. Crystalline solids produce intensity/2θ patterns with almost zero intensity everywhere apart from certain diffraction angles where distinct maxima occur. This pattern is the fingerprint of the examined crystalline body. Amorphous solids, due to the lack of periodicity, produce curves with one or two broad maxima (amorphous humps) (Cullity and Stock, 2001).

2.11.3 Scanning Electron Microscopy

Electron microscopy is a technique that utilizes an electron beam to constitute magnified images of specimens. The use of an electron beam in scanning electron microscopy (SEM) is analogous to the use of a light beam in optical microscopy and for this reason their principals are quite similar (Flegler et al., 1993).

Thermoionically emitted electrons (electron beam) are produced from a hot filament (electron gun) and attracted from an anode. The electron beam is reduced in diameter (condensed) and finely focused onto the specimen surface by a set of successive electromagnets (lenses) after being filtered (condensed and refined from stray electrons) by an aperture. Within the objective lens there is a set of small wire coils (scan coils). A scan generator produces a varying voltage which energizes the scan coils. This process results in the formation of a controlled magnetic field that is utilized to scan the electron beam across the specimen surface in two opposite directions in a repetitive and controlled manner (raster scanning). The focused beam interacts with the sample surface in various ways so long as electrical conductivity of the latter is ensured. Non-conductive samples are surface coated with an electrically conductive thin film (either gold or carbon in the order of 20 nm thickness) to enable their imaging. Different types of interactions provide different information (Nixon, 1969).

Production of secondary or low energy electrons is one of the main interactions and originates from only a thin surface layer of the specimen up to 50 nm deep. Backscattered electrons are high energy electrons originating by interactions deeper

into the specimen (~100 nm) and provide atomic contrast images; the higher the atomic number of the element receiving the incident electron beam, the brighter it appears (Flegler et al., 1993). X-rays and Auger electrons are also emitted and can give us elemental analyses information (Nixon, 1969).

The Secondary Electron Imaging (SEI) mode utilizes inelastically scattered incident secondary electrons from weakly bound electrons of the sample's atoms. The same varying voltage is applied through the scan generator to the set of deflection coils of a cathode ray tube screen, thus precisely replicating the raster scanning of the electron beam with a spot of light on the back of the cathode ray tube screen surface. Projections or depressions on the specimen surface result into high and low numbers of secondary electrons produced respectively and thus high and low voltages. This is translated as brighter or darker spots on the cathode ray tube screen. The resulting image acquired, which is the collection of these spots, is therefore a fine topographical representation of the specimen surface (Rochow and Tucker, 1994).

2.11.4 Ion-exchange Chromatography

Ion-exchange chromatography belongs to the family of analytical techniques termed chromatographic. Chromatographic techniques are used to separate and determine various types of solutes. In the case of ion-exchange chromatography, ionic solutes are analysed (Sarzanini, 1999). The principle of operation of ion-exchange chromatography is as follows:

A cylindrical column constructed of a rigid polymer (e.g. PEEK) is filled with a suitable stationary phase. The stationary phase may comprise of packed solid resin particles, with a viscous resin surface layer containing covalently bonded anions. Porous frits located at both ends of the column hold the stationary phase in place. A suitable solvent (e.g. methanesulfonic acid) known as the mobile phase, is run in a continuous flow through the column. The sample in the form of an ionic solution is introduced to the mobile phase before entering the column. The mobile phase and the dissolved sample (together constitute the eluent) are then passed through the column and the cations present interact with the covalently attached anions of the stationary phase. According to the strength of this interaction, different cation species spend different times in the column being held electro-statically close to the anions and as a result exit the column at different time intervals. These intervals are characteristic of each cation type. This process (termed elution) essentially separates the sample into its cationic constituents (Harris, 2007). This separated extract from the column (termed eluate), is then passed through a detector that records conductivity (Sarzanini, 1999). The concentrations of the different cations in the sample of interest, are determined by comparing the detected amount of the element/s against a calibration curve formed by at least 4 samples (standards) of known scaled concentration of the element/s of interest (Harris, 2007).

2.11.5 Biaxial Flexural Strength testing for dental ceramics

Clinical trials of dental ceramic materials can provide important information about the performance of a specific material under stress *in vivo*. It may however be difficult to assess and distinguish between the performances of different materials, as clinical stress situations and restoration geometry can largely vary. A relevant *in vitro* test for the evaluation of dental ceramics is thus desirable (Cattell et al., 1997b). Flexural strength testing has the advantage of pure tension being applied on one surface of the specimen (Berenbaum and Brodie, 1959). Tensile stress is a common cause of failure in dental ceramic restorations due to their brittle nature (Anusavice et al., 2007). Biaxial flexure is generally preferred over uni-axial flexure, since the former ensures establishment of the maximum tensile stress centrally within the loading area and eliminates spurious edge failures (Ban and Anusavice, 1990). Ban and Anusavice (1990) also suggest that biaxial flexural strength testing is a method relatively insensitive to test conditions such as loading rates. Greater tolerances of crosshead speed (0.2 – 5 mm/min) and specimen thickness (1-2 mm) are permitted by this type of testing (Dorsch et al., 1994, Cheng et al., 2003). Various loading arrangements for the biaxial flexural strength test have been proposed in the literature for brittle materials including: piston-on-three-ball test (Kirstein and Woolley, 1967), piston-on-ring (Wilshaw, 1968), ball-on-ring (McKinney and Herbert, 1970), ring-on-ring (Kao et al., 1971) and ring-on-ball (Shetty et al., 1983). The ball-on-ring setup (McKinney and Herbert, 1970) is when the tested disc is supported by a continuous knife-edge support (ring) and the load is transferred

via a ball bearing (Figure 2.11). Disc specimens can be a close representation of crowns in terms of surface to volume ratio (Piddock et al., 1987), thus minimizing the effects of specimen geometry to acquired strength measurements (Cattell et al., 1997a).

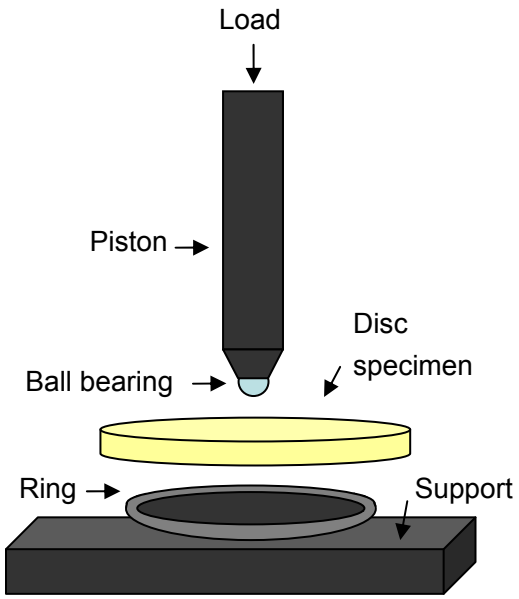

Figure 2.11: Ball-on-ring test schematic.

2.11.5.1 Weibull analysis of Biaxial Flexural Strength data

The results of biaxial flexural strength (BFS) testing, when analysed using appropriate statistics, may provide useful information on strength reliability and variability of materials. This can be quite important for dental ceramic materials where a statistical distribution of failure stresses as a function of flaw size distribution is expected (Della Bona et al., 2003). Weibull analysis is commonly the statistical approach to strength reliability (Weibull, 1951). This analysis describes

the probability of failure (P_f) as a function of fracture stress (σ) by the Weibull two-parameter equation:

$$P_f = 1 - \exp [- (\sigma/\sigma_0)^m] \quad \text{(Eq. 23)}$$

where the two parameters are σ_0 (characteristic strength) and m (Weibull modulus). Weibull analysis of data usually requires plotting the ranked data based on the rearranging of Eq. 23 as follows:

$$1- P_f = \exp [- (\sigma/\sigma_0)^m]$$

$$1/(1- P_f) = 1/\exp [- (\sigma/\sigma_0)^m]$$

$$\ln[1/(1- P_f)] = (\sigma/\sigma_0)^m$$

$$\ln\ln[1/(1- P_f)] = m\ln\sigma – m\ln\sigma_0 \quad \text{(Eq. 24)}$$

where the probability of failure P_f of the n^{th} ranked sample of N amount of samples is given by:

$$P_f = n / (N+1) \quad \text{(Eq.25)}$$

On the ranked data plot of $\ln\ln[1/(1- P_f)]$ versus $m\ln\sigma$ based on Eq. 24, a line is fitted through the data (e.g. using least squares fit). The slope of the line provides m, while σ_0 is given by the intercept with $m\ln\sigma$ (Creyke et al., 1982). This intercept occurs at the 63.2% median rank value therefore the characteristic strength expresses the stress level at which 63.2% of the specimens failed. The Weibull modulus m (shape parameter) demonstrates data scatter and material homogeneity (McCabe and Carrick, 1986). The higher the Weibull modulus, the more structurally reliable is the tested material (Della Bona et al., 2003).

Weibull statistics have extensively been used in dentistry to describe dental

ceramics' brittle failure (Cattell et al., 1997a, Fleming and Narayan, 2003, Addison et al., 2007). Cheng et al., (2003) formulated specific statistical analysis models for the piston-on-three-ball test data and proved the applicability of the Weibull treatment even under different loading conditions. The Weibull parameters proved to be characteristic of the surface defects' population. Weibull statistics may however not apply to complex geometries such as crowns (Ban and Anusavice, 1990) therefore generalisation of results from biaxial flexural strength testing on discs may not be advisable. Furthermore, it is recommended that strength data for brittle materials are modelled utilising more than one distribution function (e.g. log-normal) as more appropriate (Basu et al., 2009).

3. AIMS

1 To design and synthesize new aluminosilicate glass/ leucite glass-ceramic formulations.

2 To synthesize new nanosized leucite glass-ceramics.

3 To ion-exchange selected glass and glass-ceramic powders.

4 To test the flexural strength of the experimental and commercial glass-ceramic materials.

5 To test the wear properties of the experimental and commercial leucite glass-ceramics.

4. MATERIALS AND METHODS

4.1 Glass synthesis and crystallisation

4.1.1 Glass prediction

Appen factors (Appendix 1) were used to design glass compositions (Tables 4.1, 4.2, 4.3) according to a desired Coefficient of Thermal Expansion (CTE). The properties were predicted based on the contribution of each oxide according to the additive method of Appen (1961) factors using:

$$CTE = \sum_i \alpha_i P_i$$

where α_i is the characteristic Appen factor of each oxide constituent and *Pi* is the mole percentage of the respective oxide constituent. Fusion temperature contribution of each oxide was also taken into account to provide an estimate of the processing temperatures (Winkelmann and Schott, 1894a).

Glasses A, B and C were designed to attain scaled CTE's ranging from 8.5 to 10.5 x 10^{-6}/ K (Table 4.1). In the presence of certain divalent metal oxides, Mauer (1962) suggested that Ti^{4+} ions may form separate phases that can act as crystal nucleation sites. The B composition was selected and further systematically modified to investigate the potential synergistic effect of TiO_2 and CaO of equal molar % quantities in leucite nucleation previously witnessed by Cattell et al., (2009) (Table 4.2). A synergy of Ca and Ti in the intended 1:1 fashion would be expected to form a Calcium titanate, e.g. $CaTiO_3$. The starting glass B composition was also modified to investigate the effect of reduced Al_2O_3 content on the morphology/ volume fraction of leucite in the glass-ceramics (Table 4.3).

Table 4.1: Starting glass compositions in mole percentage.

	SiO_2	Al_2O_3	K_2O	CaO	TiO_2	Na_2O	LiO_2	MgO	B_2O_3
Glass A	72.6	10.7	7.9	2.1	0.3	4.7	1.1	0.5	-
Glass B	69.3	10.1	12.5	2.1	0.5	4.0	1.1	0.5	-
Glass C	69.7	10.6	12.8	1.5	1.3	1.9	1.6	-	0.7

Table 4.2: Systematic Ca/Ti addition to the starting glass B composition (mole %).

	SiO_2	Al_2O_3	K_2O	CaO	TiO_2	Na_2O	LiO_2	MgO
Glass B1	69.6	10.2	12.5	1.0	1.0	4.0	1.1	0.5
Glass B2	68.2	10.0	12.3	2.0	2.0	3.9	1.1	0.5
Glass B3	66.8	9.7	12.0	3.0	3.0	3.8	1.1	0.5

Table 4.3: Systematic Al content reduction in starting glass B composition (mole %).

	SiO_2	Al_2O_3	K_2O	CaO	TiO_2	Na_2O	LiO_2	MgO
Glass B4	69.5	9.8	12.5	2.1	0.5	4.0	1.1	0.5
Glass B5	70.6	8.5	12.7	2.1	0.5	4.0	1.1	0.5

4.1.2 Glass making

4.1.2.1 Glass A preparation

Glass A with composition shown in Table 4.1 was commercially produced by Den-Mat Holdings LLC, California, USA. Powder reagents (details in Ibsen *et al.,* 2008) were mixed into a baffle jar and agitated on a jar roll for 2 hours. Batches were packed into square cordierite saggers (25 x 25 x 8.5cm) previously coated with a 3 mm layer of tabular alumina (Mean PS: 50 μm). The saggers were then stacked into an electric furnace (Fredrickson Kiln Co. New York, USA), fired at a rate of 10°C/min to 1316° C and held for 7 hours. The furnace was then switched off and was allowed to cool to room temperature over 2 days. The glass was then removed from the saggers as intact blocks. The alumina oxide was removed from the glass blocks by sandblasting. The glass blocks were then crushed to 1-5 cm chips and was then wet ground with 5 mm diameter yttria tetragonal stabilized zirconia (YTZ) media and screened through a 125 μm nylon screen to attain a powdered glass with an average particle size of 11.4 μm (Ibsen *et al.,* 2008, Chen, 2009).

Starting glass A powder was further wet milled (distilled water) in an Attritor mill (Model 1-S Lab Attritor, Union Process, Ohio, USA) for 2 hours with 5 mm YTZ milling media at a rate of 400 rpm. A sample was withdrawn at 90 min and the resultant glass powder was designated as A-AM (Attritor Milling) 1.5. The 2 hour milled slurry was then further milled for 2 hours with 2 mm YTZ milling media at a rate of 400 rpm (Chen, 2009). The resultant glass powder was designated as glass A-AM4.

4.1.2.2 Glasses B and C preparation

Glasses B, B1-B5 and C compositions (Tables 4.1, 4.2 and 4.3) were selected using Appen factors. Weighed high purity powder reagents (details in Appendix 2) were ball milled with 26.4 mm diameter alumina grinding media for 2 hours in a ball mill (Pascal Engineering Ltd, London, UK). The batches were then sequentially transferred to a 90% Pt – 10% Rh crucible and heated in a high temperature chamber furnace (Lenton UAF16/10, Hope Valley, UK) by ramping at 10°C/min from room temperature to 1550°C and holding for 5 hours (B series glasses) or 6 hours (C glass). The crucible was taken out of the furnace, and annealed at 500°C for 1 hour (Tris burnout furnace, Dentalfarm, Torino, Italy). Glasses were then crushed and ground to a powder for 2 hours in a ball mill (Pascal Engineering Ltd, London, UK) using 26.4 mm diameter alumina grinding media. The glass powders were rehomogenised by remelting for 2 hours at 1550°C, air quenching for 1 min, annealing for 2 hours at 500°C and furnace cooling to room temperature. The glasses were then crushed and ground to a fine powder for 2 hours in a ball mill (Pascal Engineering Ltd, London, UK) using a mix of 19.0 mm and 26.4 mm diameter alumina grinding media. Powders were then screened on a sieve shaker (Retsch, VS1000, Haan, Germany) (1 hour, 60 Hz) through a 125 μm sieve (Endecotts Ltd, London, UK).

Repeat batches of all experimental starting glasses were produced as previously described to obtain sufficient amounts of powders for further tests.

4.2 High speed milling of starting glasses

Glass A, B, B5 and C powder samples (20 g) were mixed with 40 mL of purified water (Direct-Q™, Millipore, Molsheim, France) and 100 g of 1 mm YTZ grinding media (LOT 52600590100, Tosoh, Tokyo, Japan) into 80 mL zirconia lined milling bowls (Fritsch, Idar-Oberstein, Germany). Samples were milled in a high speed planetary mill (Pulverisette P7, Fritsch, Idar-Oberstein, Germany) at 1000 rpm for: 4 h (glass A), 2 h (glass B) and 0.5 h (glass B5 and glass C). For glass A, samples (1.5 mL) were retrieved and collected in glass vials at 2, 6, 10, 16, 30, 46, 60, 120 and 240 minutes, for glass B at 30, 60 and 120 minutes and for glasses B5 and C at 30 min milling time. Samples were designated under the original glass name, the suffix PM (Planetary Milling) and the milling time. All milled slurry samples were separately sieved through 500 µm sieves by washing the remaining powder off the media with purified water and were subsequently freeze dried using a Virtis Advantage Freeze Drier (VirTis, Gardiner, New York, USA). Sublimation was carried out by freezing to -40°C for 360 minutes (200 Torr vacuum) followed by primary drying first at 35°C for 60 minutes (100 Torr vacuum) and secondary drying at 25°C for 24 hours.

Repeat batches of all experimental high speed milled glasses were produced as previously described to obtain sufficient amounts of powders for further tests.

4.2.1 Particle Size Analysis

Particle size analysis was performed on the freeze dried samples of Glass APM 2 – 240 min using a Beckman Coulter Laser Diffraction analyser (LS13320, Beckman Coulter, High Wycombe, UK). Before the measurements, samples were dispersed in an aqueous solution of sodium hexametaphosphate and anhydrous sodium carbonate mixed in the ratio of 5:0.7 wt (Rowell, 1994) and an on stage ultrasonic probe was used for 45 minutes per sample in a 40 mL glass beaker. Background measurement was performed before each sample. The average of 3 runs per sample was evaluated. Obscuration was set to 41% (PIDS) and the pump speed was at 60%. The run length was 90 seconds and the wait between runs was set to 2 seconds.

4.3 Crystallisation studies

In order to identify the effect of nucleation and growth heat treatments on the experimental starting and the freeze dried high speed milled glass powders, the following regimes were employed.

The starting glass powders B, B1-B5 and C were prepared as powder compacts by mixing 3 g powder with 0.5 mL modelling liquid (VITA, C.H.B 24066, Vita Zahnfabrik, Bad Sackingen, Germany) into slurry. The slurry was then transferred to a steel mould (27 x 6 mm cross section) with a plunger where it was condensed by manual vibration and tissue dried for to 30 seconds to remove excess moisture. The slurry was then pressed in a hydraulic press (Quayle Dental, Worthing, UK) for 1

minute at 150 x 10^3 Pa pressure. The powder compacts were removed from the mould, sequentially placed on platinum foils and inserted (25°C) into a high temperature chamber furnace (Lenton UAF16/10, Hope Valley, UK). The compacts were subjected to two step heat treatments (Table 4.4) and subsequently air quenched. A temperature of 30°C above the determined T_g was selected as the nucleation temperature (McMillan, 1979). Differential Scanning Calorimetry (DSC) (4.6.3) and High Temperature X-ray diffraction (HTXRD) (4.6.1) data were used to determine the ideal heat treatments in order to ensure the controlled crystallisation of tetragonal leucite in the glasses.

For the freeze dried powders, samples (0.25 g) of the high speed milled glasses APM 0.5-1-2-4, BPM 0.5-1-2, B5PM0.5 and CPM0.5 (see 4.2) and samples (0.25 g) of glass A and glass A-AM4 (section 4.1.2.1) were separately mixed with deionised water (0.45 mL) to a thick paste consistency and condensed by hand vibration and tissue drying (30 seconds) to form compacts. The powder compacts were placed onto platinum foils and subjected to two step heat treatments (Table 4.4). At the end of the growth holds the powder compacts were quenched in air and allowed to cool to room temperature.

In order to prepare glass-ceramic powders in sufficient quantities for ion-exchange/ flexural strength / wear testing, experimental glass powders (glasses A-AM1.5, A-AM4, APM2, APM4, B, BPM2, B5PM0.5, C) were weighed, placed on custom made investment trays (IPS Press Vest investment material, Ivoclar-Vivadent, Schaan, Liectenstein), and heat treated using two step heat treatments

according to Table 4.4. At the end of the treatments the trays were quenched in air and left to cool to room temperature. The resultant glass-ceramics were surface cleaned from investment material using 50 μm glass beads (SG4017 Bracon Ltd, Etchingham, UK) and were separately crushed and ground to fine powders for 2 hours in a ball mill (Pascal Engineering Ltd, London, UK) using a mix of 19.0 mm and 26.4 mm alumina grinding media. The glass-ceramic powders were then screened through a 125 μm sieve.

Table 4.4: The two step heat treatments for the glass-ceramics preparation.

Glass powder	**Nucleation (°C)**	**Hold (h)**	**Growth (°C)**	**Hold (h)**	**Ramp rates (°C/min)**	**Furnace**
A-AM1.5, 4	610	1	1050	1	10†	RHF1600*
APM series	610	1	1050	1	10†	RHF1600
B	610	1	804	1	20	UAF16/10#
BPM series	610	1	804	1	20	UAF16/10
B1	606	1	868	1	20	UAF16/10
B2	613	1	903	1	20	UAF16/10
B3	618	1	916	1	20	UAF16/10
B4	597	1	924	1	20	UAF16/10
B5	588	1	820	1	20	UAF16/10
B5PM0.5	588	1	820	1	20	UAF16/10
C	618	1	1040	0.5	10†	UAF16/10
CPM0.5	618	1	1040	0.5	10†	UAF16/10

* Carbolite RHF 1600, Carbolite, Bamford, UK, # Lenton UAF16/10, Hope Valley, UK

† Rates based on crystallisation studies.

4.4 Ion-exchange of starting glass A with KNO_3

In order to effect ion-exchange using a reactive ball milling route, glass A powder (14 g) was mixed with 40 mL 1M KNO_3 solution (Glass A/KNO_3 sample). The KNO_3 had been prepared by dissolving 25.5299 g KNO_3 (99% Alpha Aesar, Lot: FAO32574, Johnson Matthey, Lancashire, UK) in 250 mL purified water (Direct-Q™, Millipore, Molsheim, France). The A control sample (Glass A/H_2O) was also prepared by mixing glass A powder (14 g) with 40 mL of purified water (Direct-Q™, Millipore, Molsheim, France). Samples were mixed with 5 mm YTZ grinding media (NIKKATO corporation, Tokyo, Japan) and placed into 80 mL zirconia lined milling bowls (Fritsch, Idar-Oberstein, Germany). Samples were then milled in a high speed planetary mill (Pulverisette P7, Fritsch, Idar-Oberstein, Germany) at 1000 rpm for 4 hours.

The milled slurry samples were sieved through 500 μm sieves by washing the remaining powder off the media with purified water and were next decanted into acid washed plastic centrifuge flasks (250 mL). The powders were washed 7 times by topping the flasks with deionised water, centrifugating at 4000 rpm for 10 minutes (Centrifuge 5804, Eppendorf AG, Hamburg, Germany) and decanting the supernatants. In between the centrifugation runs, sedimented samples were re-suspended by using a flask shaker (Stuart Scientific, Staffordshire, UK) for 5 minutes at 700 oscillations/min. Samples were then placed into two acid washed glass trays and freeze dried as in section 4.2.

The washing efficiency in terms of KNO_3 removal was verified by Fourier Transform Infrared Spectroscopy (FTIR). Samples of the freeze dried glass A/KNO_3 powder and the freeze dried glass A/H_2O powder were mixed with deionised water and placed on the transmission stage of a Perkin Elmer GX Near infrared - FTIR instrument (Perkin Elmer Instruments, Cambridge, UK). A sample of the 1M aqueous KNO_3 solution was also analysed. Spectra were collected for the glass A/KNO_3 powder, the glass A/H_2O powder and the 1M KNO_3 solution from 4000-600 cm^{-1} in the transmission mode.

4.4.1 Glass acid digestion

Samples (0.5 g) of glass A, glass A/H_2O and glass A/KNO_3 were weighed and placed into acid washed Teflon beakers. Powders were suspended by adding 5 mL concentrated HNO_3 (Analytical reagent grade, S.G. 1.42, 70%, Batch 1094183, Fisher Scientific, Leicestershire, UK) in each beaker. The beakers were put into a fume cupboard on a hotplate at room temperature overnight (22 hours). Five mL of hydrofluoric acid (Laboratory reagent grade, HF 40%, Batch 0618194, Fisher Scientific, Leicestershire, UK) and 3 mL perchloric acid (AnalaR®, $HClO_3$ 70%, Lot B251573 248, BDH Laboratory supplies, Poole, England) were next added and the hotplate temperature raised to 100°C for 4 hours. The samples were next left to cool to room temperature (23°C) overnight (16 hours). The hotplate was then raised to 100°C for 30 minutes and then to 150°C to evaporate the $HClO_3$ fumes. After cooling to room temperature, 2 mL of concentrated HNO_3 and 48 mL of purified

water (18.2 MΩ·cm at 25°C) were added to re-suspend the decomposed samples. Samples were quantitatively transferred to 100 mL acid washed volumetric flasks (Class A) and purified water was added up to the 100 mL mark.

4.4.2 Ion-exchange Chromatography

The digested samples of glass A, glass A/H_2O and glass A/KNO_3 were quantitatively analysed for potassium (K^+) and sodium (Na^+) using an Ion-exchange Chromatographer (Dionex-ICS 2500 Modular System, Sunnyvale, USA) fitted with an Ion Pac CS16 column (Column temperature 30°C). Methane sulfonic acid (MSA) was used as the eluent. Standards of 100, 200, 400 and 800 ppm K^+ and 50, 100, 200 and 400 ppm Na^+ were prepared in 100 mL Class A glass volumetric flasks using purified water (18.2 MΩ·cm at 25 ^oC) and the respective concentrated standards (10000 ppm Nitrate cation solutions in 2% HNO_3, Aristar Plasma Emission Standards, BDH Laboratory supplies, Pode, UK). The acidity of the standards was adjusted using 2 mL of concentrated HNO_3 to match that of the samples to be analysed. The Ion Chromatographer was programmed to automatically create calibration curves for both K^+ and Na^+ cations using the standards inserted to compare the concentrations of the tested samples.

4.5 Ion-exchange of a glass-ceramic A-AM1.5 with $RbNO_3$

Glass A-AM1.5 powder was heat treated in a two step heat treatment (Table 4.4), milled to powder and sieved through 125 μm sieve according to the protocol in section 4.3 to produce the glass-ceramic A-AM1.5 powder. In order to effect ion-exchange using a reactive ball milling route, glass-ceramic A-AM1.5 powder (15 g) was mixed with 30 mL purified water (Direct-Q™, Millipore, Molsheim, France) and 11.172 g $RbNO_3$ (Glass-ceramic A/$RbNO_3$ sample). This would result in a non-saturated $RbNO_3$ solution of 2.5M above 60°C. A control sample (Glass-ceramic A/H_2O) was also prepared by mixing glass-ceramic A-AM1.5 powder (15 g) with 38 mL of purified water. Samples were mixed with 10 mm YTZ grinding media (NIKKATO corporation, Tokyo, Japan) and placed into 80 mL zirconia lined milling bowls (Fritsch, Idar-Oberstein, Germany). Samples were then milled in a high speed planetary mill (Pulverisette P7, Fritsch, Idar-Oberstein, Germany) at 850 rpm for 4 hours.

Both milled slurry samples were separated from the milling media, washed 7 times (section 4.4) and freeze dried (section 4.2).

One powder compact disc specimen of each glass-ceramic powder (A-AM1.5, A/H_2O, A/$RbNO_3$) was made according to the protocol in section 4.7.1, pg 110 and sintered using the firing cycles (A series) in Table 4.5, pg 111.

4.6 Characterisation

4.6.1 X-ray powder diffraction

In order to establish the phases present in the investigated glasses and glass-ceramics, X-ray powder diffraction (XRD) was performed. Samples of prepared experimental glasses and glass-ceramics were processed into fine powders. The samples were placed in the holder of an X'Pert-PRO diffractometer (PANalytical B.V., Almelo, The Netherlands) using Bragg-Brentano flat plate geometry. Cu Kα radiation (λ_1=1.54059 Å and λ_2=1.54442 Å) was used. Data were collected (no monochromator, fixed divergence slit) from 5° to 120° 2 θ, with the X'Celerator in continuous mode giving data equivalent to a count time of 200 seconds and an interval of 0.0334^o 2θ on a normal diffractometer. Phase analysis was carried out with the PANalytical X'Pert HighScore Plus software using the International Centre for Diffraction PDF-4 database. The model of tetragonal leucite used for identifying its presence in the samples was that of Mazzi et al., (1976), (ICDD: 00-038-1423). The reference model for cubic leucite used was that of Hermansson and Carlsson (1978) (ICDD: 00-031-0967).

Glass powders were also subjected to a High Temperature XRD regime. Powders were placed on a platinum heat strip (Anton Paar HTK-16 sample stage, Anton Paar Ltd, Hertford, UK) of the X'Pert-PRO diffractometer (PANalytical B.V., Almelo, The Netherlands). Data collection settings were the same as previously. An XRD pattern was retrieved at room temperature (25°C) and then patterns were retrieved every 20°C in a temperature range from 500-1200°C. For the high

temperature work, the exact surface temperature of the strip had previously been calibrated by known melting points of high purity calibration materials (Appendix 4). The resulting straight line plot had the formula T(Meas)=0.9211T(Corr) + 9.6218 over a range of 129 to 1076°C with a correlation coefficient of R^2=0.9999.

4.6.2 Differential Thermal Expansion

Glass frit from all glasses were cut into blocks of 6 mm width x 6 mm depth x 25 mm length using a diamond saw (Accutom-Z, Struers, Rotherham, UK) under water lubrication. Specimens were finished to final dimensions on wet P320 SiC papers (Figure 4.1) on a polishing machine with a rotating table (KENT 4, Kemet International Ltd., Maidstone UK) at 250 rpm using light finger pressure, cleaned in water and air dried.

Figure 4.1: A finished thermal expansion glass specimen.

The Coefficient of Thermal Expansion (CTE) of the glass specimens was measured using a differential dilatometer (DIL 402 PC, Netzsch Instruments, Selb, Germany).

A calibration cycle was first run using a standard alumina rod ramping from 25°C to 1200°C at 3°C/min in a nitrogen gas atmosphere. The glass specimens were run using the same cycle and softening point detection was enabled. The results were corrected against the calibration plot of specimen change in length against temperature to enable the glass transition temperature (T_g) and dilatometric softening point (D_{sp}) to be determined. The CTE was measured over the 100 - 400°C temperature range using the dedicated Netzsch Proteous Thermal Analyses software (ver. 4.8.2, 2006, Netzsch Instruments, Selb, Germany) according to the formula:

$$CTE(T_0 - T) = 1/L_0 \times \Delta L/\Delta T = (L_T - L_0) / L_0 (T - T_0)$$

where T_0 is the start temperature, T is the end temperature, L_0 is the start value of specimen length, L_T is the end value of specimen length, ΔT is the change in temperature and ΔL is the change in specimen length.

4.6.3 Differential Scanning Calorimetry

Differential Scanning Calorimetry (DSC) was carried out using a Stanton Redcroft DSC 1500 (Rheometric Scientific, Epsom, UK) to study the crystallisation kinetics of the glass powders. The instrument was calibrated for the 20 – 1300°C temperature range. Weighed glass powder samples (0.05 g) were placed into a platinum crucible on the DSC stage next to a matched platinum crucible with alumina powder (0.05

g). Glass powders were sieved through 300, 125 and 45 μm sieves (Endecotts Ltd., London, UK) to provide powder grades of 125 – 300, 45 – 125 and of less than 45 μm. Samples were ramped from 30°C to 1200°C at 20°C/min under a nitrogen atmosphere. For activation energy determination, four rates of 5, 10, 20 and 40°C/min were run using the bulk glass powders (through 125 μm) and the Kissinger (1956) equation was used (see 2.11.1.1):

$$\ln (\varphi/T_p^2) = -E_a/RT_p + \text{constant}$$

where T_p is the peak crystallisation at the respective heating rate φ and R is the gas constant. All DSC results were processed using the dedicated Infinity PRO Software (ver. 4.2.140, Instrument Specialists Inc, Wisconsin, USA) to enable glass transition temperature (T_g) and peak crystallisation temperature (T_p) determination.

4.6.4 Secondary Electron Imaging

Specimens from crystallisation studies on all experimental glasses, and specimens from the wear testing (teeth and glass-ceramic discs) (see section 4.9, pg 117) were prepared for secondary electron imaging (SEI).

Specimens from the crystallisation studies were embedded in epoxy resin (Epofix, Struers, Copenhagen, Denmark), wet polished on successive SiC papers (P320, P600, P800, P1000, P2400, P4000) and then with 1 μm and 0.3 μm alumina micropolish solutions (Deagglomerated Alpha Alumina, Buehler, Lake Bluff, USA)

on polishing cloths using a rotating table polishing machine (KENT 4, Kemet International Ltd., Maidstone UK) at 400 rpm using moderate finger pressure. Specimens were cleaned in an ultrasonic bath for 10 minutes with detergent and were washed with water. The polished surface of the specimens was etched with a 0.1% HF solution for 60 seconds then washed with water and cleaned with ethanol.

Specimens from the wear testing (teeth and glass-ceramic discs) were surface cleaned with ethanol and mounted on special SEM disc stages.

All specimens were gold coated in a sputter coater (Model 108A, Agar Scientific Ltd, Stansted, England) at 40 mA for 100 seconds. Specimens were viewed in a Scanning Electron Microscope (SEM) (FEI Inspect F., Europe NanoPort, Eindhoven, The Netherlands) in the SEI mode at a 10 mm working distance using 10 KV accelerating voltage and a 3.5 spot size.

4.6.5 Energy Dispersive X-ray Spectroscopy

Specimens were carbon coated in a sputter coater (Balzers/CED030 carbon evaporator, Bal-Tec Gmbh, Rüdinghausen, Germany). Energy Dispersive X-ray Spectroscopy (EDS) spectra (Oxford Instruments, High Wycombe, UK) were acquired using spot analyses in an SEM (FEI Inspect F., Europe NanoPort, Eindhoven, The Netherlands) using 10KV or 30KV for a count time of 30 seconds. Spectra were analysed using the dedicated software (INCA, Oxford Instruments, High Wycombe, UK).

4.7 Glass - ceramic disc specimen fabrication

4.7.1 Sintered specimen fabrication

Sintered glass-ceramic disc specimens were prepared from experimental glass-ceramic materials and from the commercial reference group Ceramco 3 dentine material (Batch No 02111576, Dentsply, Ceramco, New Jersey, USA). Specimens were made by mixing glass-ceramic powder (1.1 g) with modelling liquid (0.4 mL) (VITA, C.H.B 24066, Vita Zahnfabrik, Bad Sackingen, Germany) and transferring to a hollow cylinder steel mould (16 mm inner diameter) with a plunger. The slurry was condensed by manual vibration and tissue drying to remove excess moisture for 30 seconds. The powder slurry was pressed in a hydraulic press (Quayle Dental, Worthing, UK) at 50 x 10^3 Pa pressure for 1 minute and the disc was then removed from the mould. The disc specimens were sintered in dental porcelain furnaces (Multimat MCII, Dentsply, Weybridge, UK / Multimat 2 Touch + Press, Dentsply, Weybridge, UK) according to the disc firing cycles in Tables 4.5 and 4.7. Ceramco 3 specimens also received one simulated glaze firing cycle to reflect clinical practice in terms of thermal history (Table 4.7). Sintered specimen groups were further prepared by following protocols dependant on subsequent testing as described in sections 4.8 and 4.9.1.

Table 4.5: Firing cycles for the sintered glass-ceramic groups.

Firing cycles	A series	B series	B5 PM0.5	C
Standby Temp. (°C)	538	538	538	538
Drying time (min)	5	2	5	2
Preheat (min)	5	2	5	2
Heating rate (°C/min)	38	38	38	38
Vacuum (hPa)	55	55	55	55
Vacuum release (°C)	1025	1099	1049	1059
Firing Temp. (°C)	1040	1100	1050	1060
Holding time (min)	2	2	1	2
Cooling Program	3	1	1	1
Furnace	MCII*	M2#	M2	M2

*Multimat MCII and #Multimat 2 Touch+Press, Dentsply, Weybridge, UK

Table 4.6: Ingot, Stain and Glaze firing cycles for the glass-ceramics A series.

Firing cycles	Ingot firing	Stain firing	Glaze firing
Standby Temp. (°C)	538	538	538
Drying time (min)	5	1	1
Preheat (min)	5	2	2
Heating rate (°C/min)	38	55	55
Vacuum (hPa)	55	N/A	N/A
Vacuum release (°C)	1025	N/A	N/A
Firing Temp. (°C)	1040	780	860
Holding time (min)	2	0	0.3
Cooling Program	3	3	3
Furnace	MCII	MCII	MCII

Table 4.7: Firing cycles for the Ceramco 3 glass-ceramic.

Firing Cycle	Dentine firing	Glaze Firing
Firing Temp. (°C)	930	920
Heating rate (°C/min)	45	45
Standby Temp. (°C)	650	650
Holding time (min)	1	0.5
Drying time (min)	5	3
Preheat (min)	5	3
Vacuum (mbar)	50	N/A
Vacuum release (°C)	930	N/A

4.7.2 Heat pressed specimen fabrication

Heat pressed glass-ceramic disc specimens were prepared from the experimental A-AM4 / APM2 glass-ceramic materials. Glass-ceramic powder samples (1.6 g) (section 4.3) were transferred to a special hollow cylinder steel mould (13 mm inner diameter) with a plunger. The plunger was inserted and the mould was pressed to 0.5 x 10^3 kg for 30 seconds in a hydraulic press. The dry powder ingots (Figure 4.2a) were sintered (Figure 4.2b) in a dental porcelain furnace (Multimat MCII, Dentsply, Weybridge,UK) according to the ingot firing cycles in Table 4.6.

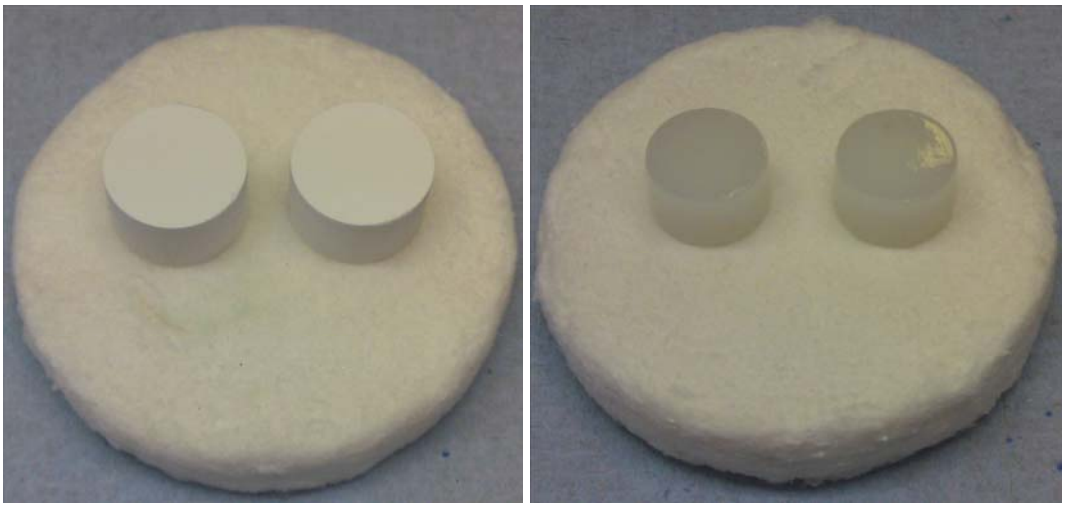

Figure 4.2: (a) Dry and (b) sintered powder compacts of the experimental APM2 glass-ceramic.

Perspex® discs (ICI Plastics, UK) (14mm diameter x 2mm thickness) were sprued using 3 mm diameter wax sprues attached to large investment ring bases fitted with surrounding silicone cylinders. Specimens were then invested using 200 g of investment material (IPS Press Vest Speed powder, Ivoclar-Vivadent, Schaan, Liechtenstein) mixed with 32 mL of investment liquid (IPS Press Vest Speed liquid, Ivoclar-Vivadent, Schaan, Liechtenstein) and 22 mL of distilled water in a vacuum mixer (Multivac compact, Degudent, Hanau, Germany) for 90 seconds and vibrated

on a lab vibrator (Export 2, Dentalfarm, Torino, Italy) into the investment cylinders. Muffle gauges were then placed on top of the cylinders to ensure a flat surface for the top of the investment material. After setting for 45 minutes the refractory investment cylinders were transferred to a preheated burnout furnace (5365, KaVo EWL, Leutkirch, Germany) at 850°C and held for 45 minutes. The preheated cylinders were removed from the furnace and room temperature A-AM4 / APM2 experimental glass-ceramic ingots and alumina plungers (850°C) were inserted into the refractory muffles. The refractories were next transferred to preheated (700°C) pressing furnaces. The A- AM4 experimental glass-ceramic was heat pressed in a Cerampress Ney (Jeneric Pentron, Wallington, USA) pressing furnace and the APM2 experimental glass-ceramic in a EP3000 (Ivoclar-Vivadent, Schaan, Liechtenstein) furnace. The glass-ceramic ingots were extruded into the refractories using the heat pressing parameters in Table 4.8. The refractories were then allowed to cool to room temperature.

The pressed components were divested using 50 μm glass beads (SG4017 Bracon Ltd, Etchingham, UK) at 50 x 10^3 Pa pressure in a sand blasting machine (Renfert Basic Quattro IS, Renfert Gmbh, Hilzingen, Germany). After water rinsing for 1 minute, the specimens were separated from the sprues at low speed (15000 rpm) under water lubrication with a diamond disc (006, Bracon Ltd., Etchingham, UK) followed by a sintered diamond bur (9907, Bracon Ltd., Etchingham, UK). The heat pressed specimen groups were then further prepared by following protocols dependant on subsequent testing as described in sections 4.8 and 4.9.1.

Table 4.8: Pressing parameters for the experimental glass-ceramics A-AM4 HP and APM2 HP.

Pressing Parameters	A-AM4 HP glass-ceramic	APM2 HP glass-ceramic
Start temperature (^{o}C)	700	700
Pressing temperature (^{o}C)	1040	1040
Rate of climb (^{o}C/min)	40	40
Vacuum (%)	101	N/A
Hold before pressing (min)	15	15
Pressing time (min)	10	*
Press (Absorption speed) (µm/min)	N/A	300
Pressure (Pa)	5×10^{5}	*

*Parameters automatically controlled and adjusted by the pressing furnace during pressing.

4.8 Biaxial Flexural Strength studies

4.8.1 BFS specimen preparation

The sintered disc specimen groups (APM2, APM4, B, BPM2, B5PM0.5, C and Ceramco 3) were manufactured as in section 4.7.1. The heat pressed group APM2 (designated as APM2 HP) was manufactured in accordance with section 4.7.2. The sintered disc specimen groups were wet lapped on both sides on successive SiC papers (P320, P600, P800 and P1000) on a lapping unit (KENT 4, Kemet International Ltd., Maidstone UK) to 2 mm thickness using a hollow steel mould (14 mm inner diameter) fitted with a thin fabric pad. The heat pressed group (APM2 HP) was lapped only on one surface using the same regime, the other surface left as divested. All specimens were then cleaned in an ultrasonic bath with detergent for 10 minutes and then washed with water. The disc specimens for groups APM2, APM4 and APM2 HP received one stain and one glaze simulated firing cycle (Table 4.6) to reflect clinical practice in terms of thermal history. Sintering / pressing parameters for glass A series were previously optimised by Chen (2009) based on the work of Cattell et al., (2006). Groups B, BPM2, B5PM0.5, C and Ceramco 3 were put in a desiccator overnight (16h).

4.8.2 BFS testing

Biaxial Flexural strength testing was carried out using the ball-on-ring test setup (McKinney and Herbert, 1970). Disc specimens (n=30, 14 mm diameter, 2 mm thickness) were supported on a 10 mm diameter knife-edge support and centrally loaded with a 4 mm diameter ball indenter. A thin plastic sheet (0.03 mm) was inserted between the disc surface and the indenter to distribute the applied load evenly (Ban and Anusavice, 1990). Specimens were loaded using a tensile testing machine (5567/H1580, Instron, Buckinghamshire, UK) fitted with a 1 kN load cell and the specimens were loaded until failure at a crosshead speed of 1 mm/min. The biaxial flexural strength was then calculated using the following formula (Timoshenko and Woinowsky-Krieger, 1959):

$$\sigma_{max} = P / h^2 \{ (1+v) [0.485 \times \ln (a / h) + 0.52] + 0.48 \}$$

where σ_{max} was the maximum tensile stress, P was the recorded load at fracture, h was the specimen thickness (average of one measurement in the middle and three equidistant measurements at the edges of the disc), *a* was the radius of the knife-edge support ring and v the Poisson's ratio, set at 0.25 (ISO 6872). Both non parametric and Weibull statistics were used to analyse the strength data.

4.9 Wear studies

Ethical approval was gained for the following study (Medical Ethics REC: 06/Q0603/98).The wear properties of two experimental glass-ceramics (A-AM4 HP, APM2 HP) and one commercial reference glass-ceramic (Ceramco 3) against human enamel were determined.

4.9.1 Wear specimen fabrication

Freshly extracted human adult molar teeth were collected from the Department of Oral and Maxillofacial Surgery (Institute of Dentistry, Barts and The London, School of Medicine and Dentistry) and stored in a 30% water / 70% ethanol solution in a tissue bank. The teeth were visually screened by the same operator under a microscope (Wild M3B, Heerbrug, Switzerland) to exclude those with pointed configurations, demineralisations or surface defects (Heintze et al., 2008). Individual cusps were sectioned in the form of cylinders using a 2.75 mm inner diameter core drill (UKAM Industrial Superhard Tools, California, USA) under water lubrication. The selected tooth cylinders were embedded in photo-curing resin using a custom made hollow cylinder PTFE mould (6 mm inner diameter x 14.5 mm height) (Figure 4.3a). Three reference marks were made on the top surface of the resin stub with the embedded tooth (Figure 4.3a) by pressing a wax tool tip against the uncured resin. The reference marks acted as reference points for initial alignment of the surfaces that were to be digitised before and after wear testing. The stub was then irradiated for 5 minutes at 3 equidistant points around the circumference (3M ESPE Elipar™

Freelight™, Seefeld, Germany). Glass-ceramic disc specimens (n=12) were manufactured as in sections 4.7.1 (Ceramco 3) and 4.7.2 (A-AM4 HP, APM2 HP). They were then wet lapped on one side with P600 SiC papers (as in section 4.8.1) to achieve flatness and standardize the test surface at a thickness of 2 mm. Glass-ceramic A-AM4 HP and APM2 HP specimens were subjected to one stain and one glaze simulated firing cycles (Tables 4.6 and 4.7) to reflect clinical practice in terms of thermal history. Three hemispherical reference marks forming the points of a triangular area in which the wear test was to be carried out were made on the glass-ceramic disc surfaces, using a pointed dental stone followed by a dental rubber bur (Figure 4.3b). Specimens were then cleaned in an ultrasonic bath with detergent for 10 minutes and then washed with water.

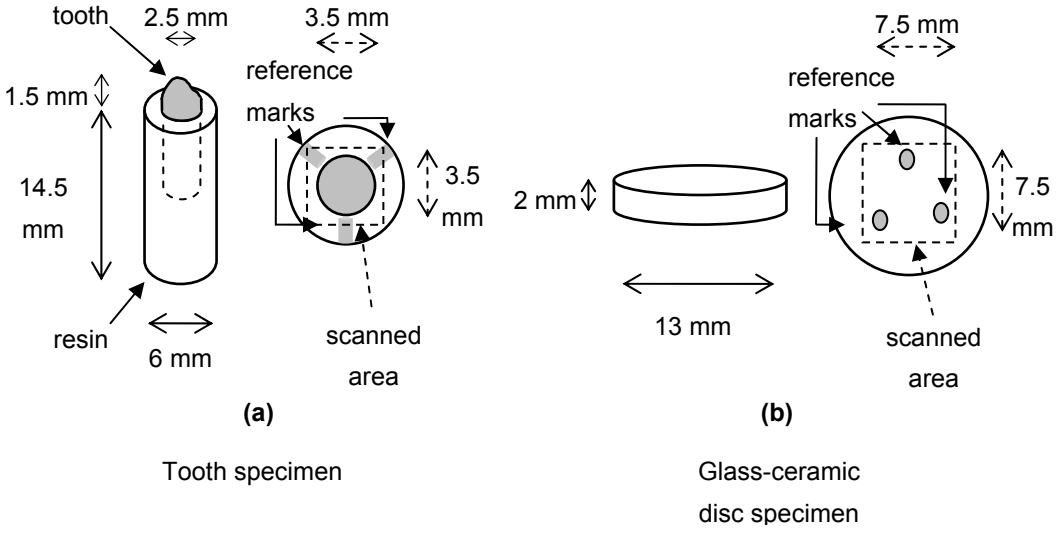

Figure 4.3 : Schematics of the (a) tooth and (b) glass-ceramic disc specimens.

4.9.2 Wear testing

Glass-ceramic disc specimens were stored in deionised water and enamel specimens were stored in a 30% water / 70% ethanol solution for 1 week before testing. Glass-ceramic discs and enamel specimens were then fixed into specially designed holders (Figure 4.4, Appendix 5) on the upper and lower members of a servo-hydraulic test frame (Bionix 858, MTS, Minnesota, USA). The opposing glass-ceramic disc and enamel specimens were subjected to 300,000 simulated masticatory cycles at a rate of 2Hz. Specimens were loaded with a load of 13.5 N each, by operating the axial shaft under displacement control on the axial plane. This was followed by a lateral excursion movement exerted by rotating the axial shaft under displacement control by 1.5 degrees. A controlled cuspal contact time (0.25 seconds) to complete a cycle was achieved after experimentation by combined phasing of a square wave for the load and of a sine wave for the lateral (torsional) displacement. The oscilloscope trace of the wave form was monitored as created by a 2.5 x 10^3 N load cell placed under the disc specimens and set to its low (10%) calibration range (250 N). A continuous flow of deionised water (37°C) was directed on the tested surfaces during testing for wear debris removal and surface conditioning.

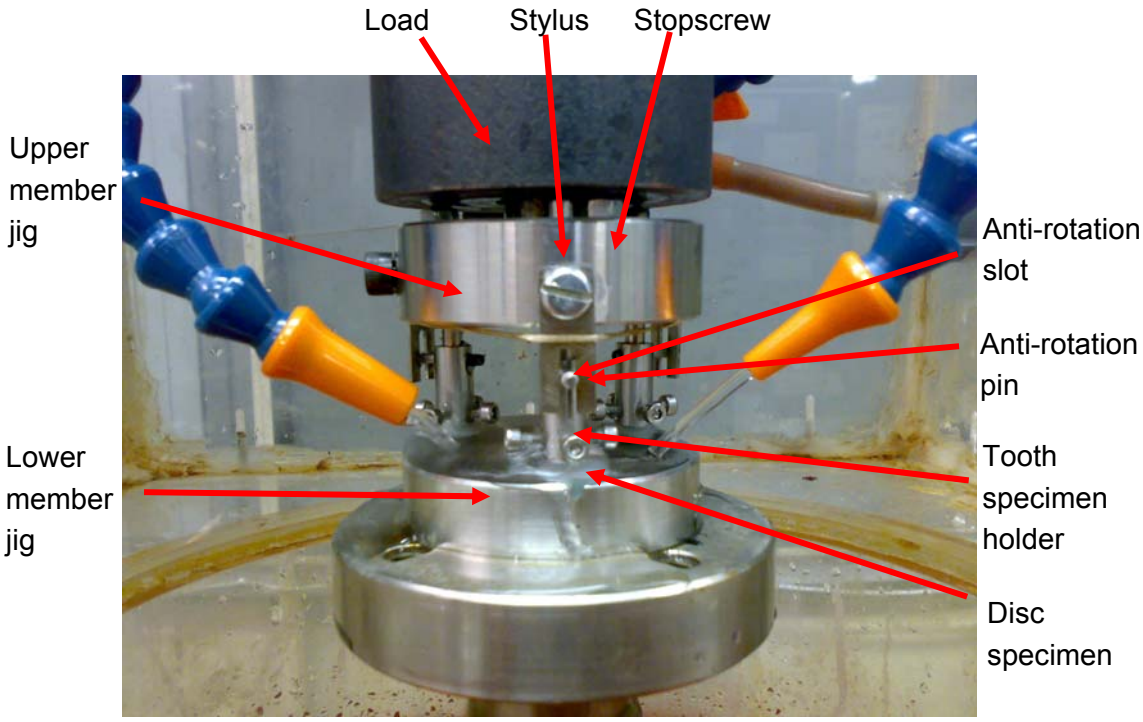

Figure 4.4 : Wear Testing apparatus.

4.9.3 Wear quantification method development

4.9.3.1 Scanning equipment and parameters

A non-contact 3D profilometer (Proscan 2000, Scantron, Taunton, UK) and the dedicated software (Proscan 2000, ver. 2.1.8.8+ software, Proform version 1.41 software, Scantron Industrial Products Ltd, Taunton, UK) were used for the tooth and glass-ceramic surface digitisation and the subsequent image analysis. A custom made jig was constructed to fit on the Proscan 2000 stage which allowed the repositioning of wear specimens before and after testing. The S16 /3.5 Chromatic sensor (STIL S.A., Aix-en-Provence, France) was used for all scans operated at 30 Hz frequency (low scanning speed) through a CHR-150 controller (STIL S.A., Aix-en-Provence, France) that was connected to the Proscan 2000 profilometer. This sensor has a 3.5 mm

measuring range and a 75 nm axial resolution. Dark background measurement was performed prior to each scanning session to ensure maximum sensor sensitivity to reflected light. The step size for the scans was selected after scanning a disc and a tooth specimen before and after a pilot wear test using five step sizes (10, 20, 30, 50 and 100 μm, Appendix 6). according to Theocharopoulos et al., (2010). (Publication pg 293).

4.9.3.2 Wear quantification method and measurement improvement test

All tooth and glass-ceramic disc specimen test surfaces were scanned before and after wear testing using the optimal step sizes (teeth: 20 μm, glass-ceramic discs: 30 μm) selected previously. Filters were applied to all tooth (warpage 2) and glass-ceramic disc (warpage 3) digitised surfaces. This was performed to separate the long wavelength (low frequency) shape associated information from the short wavelength (high frequency) roughness associated information prior to the superimpositions. The digitised test surfaces before and after wear testing were next superimposed (Proform ver.1.41, Proscan 2000 version 2.1.8.8+ software, Scantron, Taunton, UK) to quantify the total volume, height and mean-height loss. In order to evaluate the wear quantification method to be applied, wear quantification data of 8 Ceramco 3 glass-ceramic discs / tooth pairs were evaluated as follows.

The series of steps followed for the wear quantification of the glass-ceramic disc specimens is shown in Figures 4.5 - 4.7. The shading in all figures illustrates the height gradient. The three reference marks made on the disc surface (Figure 4.5 a, b) were used for initial alignment of the surfaces before and after testing. The

surfaces were superimposed (Figure 4.6 a,b) and the region with the volume difference was cropped to a 3 x 3 mm^2 area. At this stage automated measurements are provided from the software for the volume and mean-height loss and these were recorded as the “Automated” set of data. The superimposed file (difference view) was then saved and opened in the Proscan software where the volume tool was used to measure the values. The difference view was then further processed in Proscan software to isolate the worn area (Figure 4.7 a,b). The file (x,y,z data) was then exported in Excel format and the height values (z values) were averaged to generate the mean-height loss for each specimen. These values were recorded as the “Experimental” data set. For the tooth specimens (Figures 4.8 - 4.9), the difference view from the Proform software was cropped as closely as possible to the worn area (Figure 4.10) and the volume / mean-height loss measurements provided by the software were recorded as the “Automated” set of data. It was then further processed in the Proscan software to delete unwanted areas around the worn area that interfered with volume calculation (Figures 4.9 b, 4.10). The deleted areas were then replaced with a zero height area (Figure 4.11 a) to enable the final volume loss determination by the Proscan software. Mean-height calculation was then performed as for the disc specimens (Figure 4.11 b). The values recorded at this stage were recorded as the “Experimental” set of data. The “Automated” and “Experimental” data sets created for volume and mean-height loss of human enamel and glass-ceramic were then compared using individual t-tests to evaluate statistical differences ($p < 0.05$).

The Experimental methodology was then used to retrieve wear quantification

data for all wear tested specimens. Height loss values were also acquired for all glass-ceramic discs (Figure 4.7a) and teeth (Figure 4.11a) using the software tool “highest point” (indicated by crosshair - lines) followed by the measuring tool that measures height at that point in respect to zero height. The results were statistically analysed to describe the data and to identify statistically significant differences (Sigma Stat ver. 2.03, SPSS Inc., Chicago, USA).

4.9.3.3 Operator uncertainty and scanning repeatability tests

Five superimpositions were carried out following the developed protocol on a tooth / Ceramco 3 glass-ceramic disc pair, before and after wear testing to evaluate the wear quantification testing process and the operator introduced uncertainty. The volume loss values from the individual scans (1 to 5) were then subtracted in all possible combinations (1-2, 1-3, 1-4, 1-5, 2-3, 2-4, 2-5, 3-4, 3-5, 4-5) and the differences averaged. Scanning repeatability was also evaluated by repeated (x 5) scanning of a tooth and a Ceramco 3 glass-ceramic specimen. The volume differences between the scans was measured by superimposing scans in all possible combinations (1-2, 1-3, 1-4, 1-5, 2-3, 2-4, 2-5, 3-4, 3-5, 4-5).

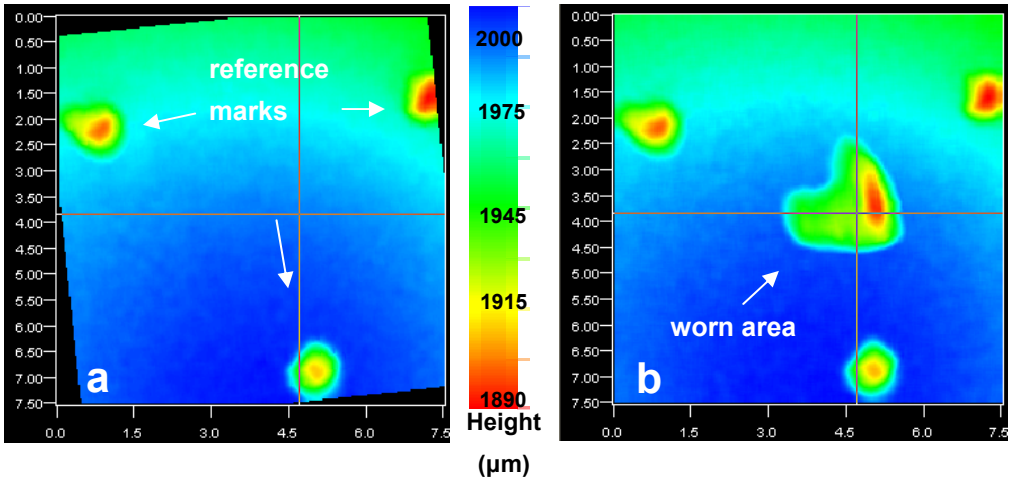

Figure 4.5: Digitised glass-ceramic disc surfaces (a) before and (b) after wear testing.

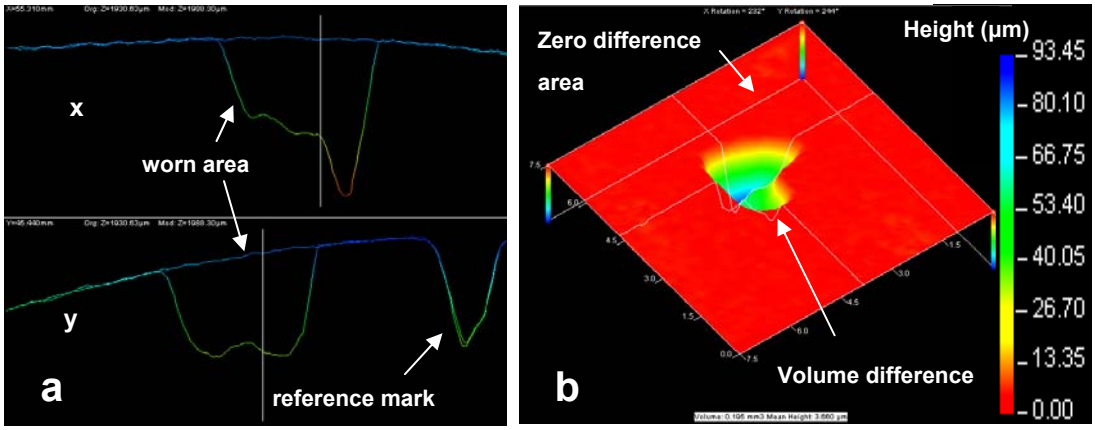

Figure 4.6: (a) Digitised glass-ceramic disc cross sectional (x,y) fit overview and (b) superimposed 3D difference view.

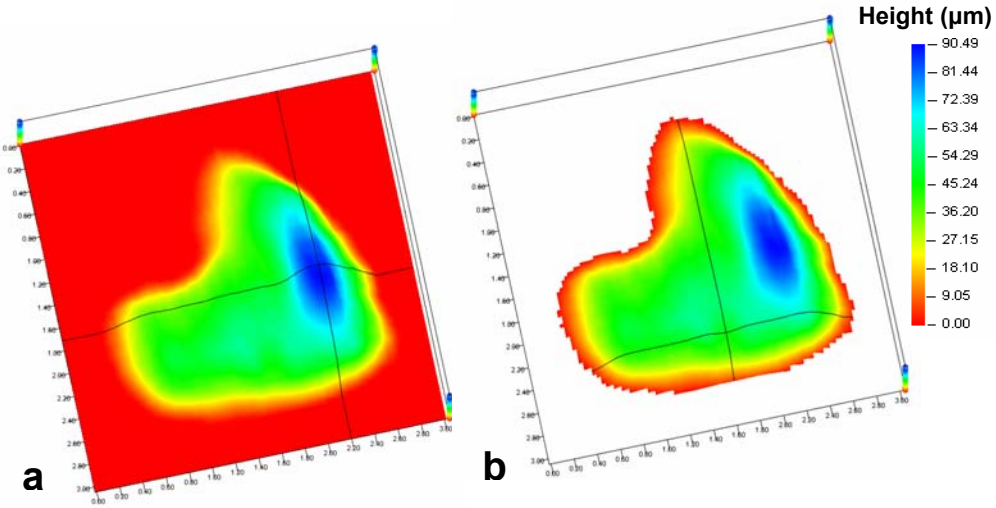

Figure 4.7: (a) Cropped difference view for glass-ceramic disc volume and height calculation. (b) Isolated glass-ceramic disc worn area for mean-height calculation.

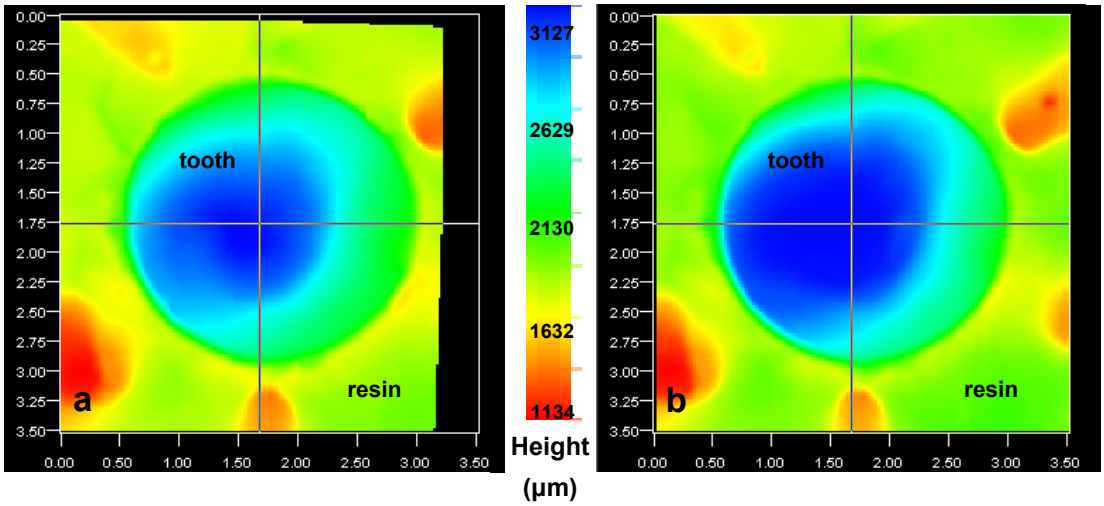

Figure 4.8: Digitised tooth surfaces (a) before and (b) after wear testing.

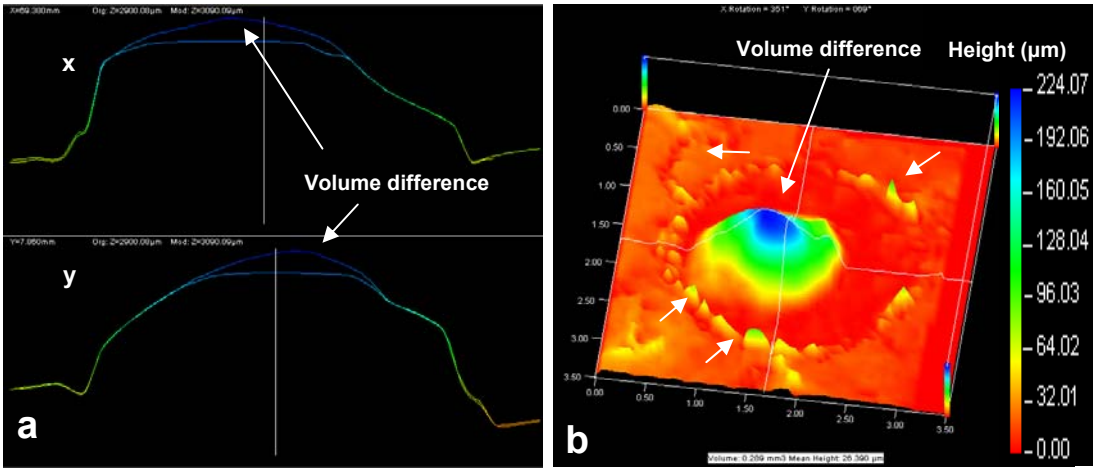

Figure 4.9: (a) Tooth cross sectional (x,y) fit overview and (b) superimposed 3D difference view showing irregularities and peaks (arrows) interfering in the volume/ mean-height loss calculation.

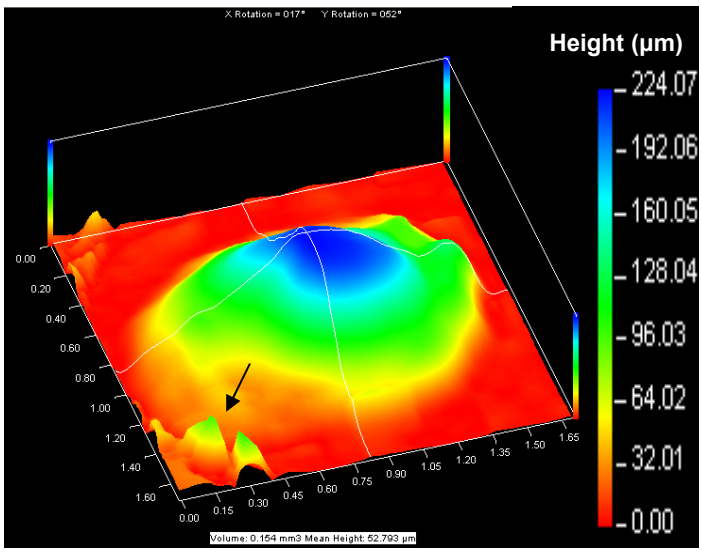

Figure 4.10: Cropping of the digitised tooth specimen area with unwanted peaks still included.

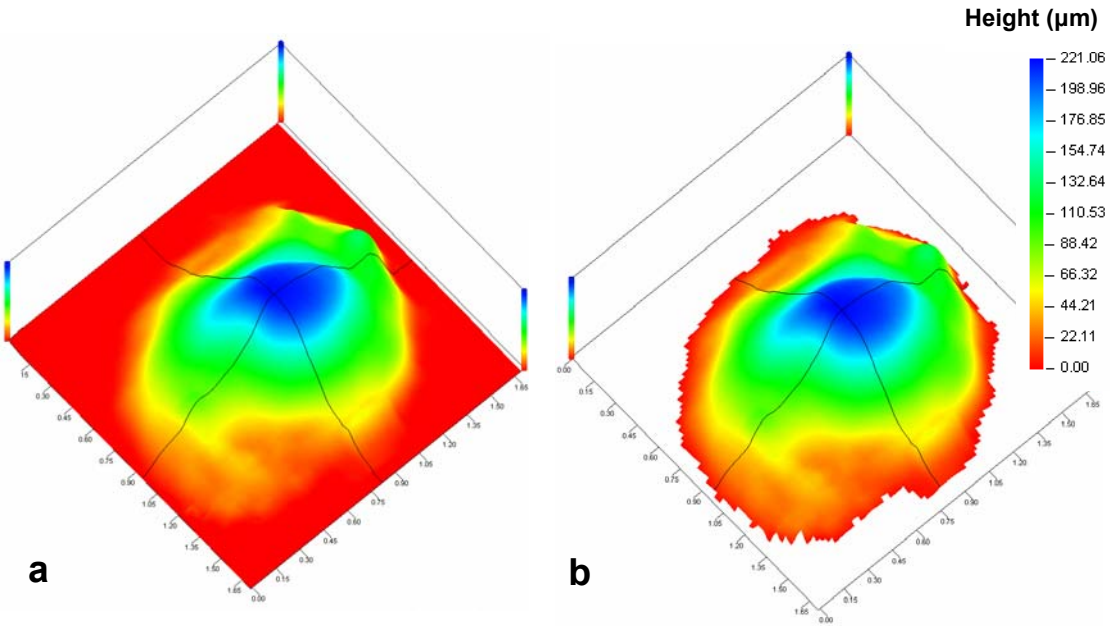

Figure 4.11: (a) Peaks eliminated and a zero area inserted around the difference view for tooth volume and height loss calculation. (b) Isolation of the worn area for tooth mean-height loss calculation.

4.9.4 Surface topography and roughness

Surface topography images were acquired from a glass-ceramic disc from each test group (Ceramco, A-AM4 HP, APM2 HP) and the opposing antagonistic tooth cylinder after wear using a non-contact 3D profilometer (Proscan 2000, Scantron, Taunton, UK) and SEM (FEI Inspect F., Europe NanoPort, Eindhoven, The Netherlands) in SEI mode (section 4.6.4). A set of images was acquired to include the whole wear pattern of surfaces (2.5 x 2.5 mm) using 501 profiles at 5 μm (x, y) step size. A set of images was also acquired from inside the wear patterns of the same specimens (0.5 x 0.5 mm) using 501 profiles at 1 μm (x, y) step size. The raw data from the 1 μm step size acquired profilometric images (501 x and y lines) were analysed for surface roughness (R_a) and wave height calculation (Proscan 2000, Scantron, Taunton, UK), for quantitative comparison purposes. A surface filter (100) (Appendix 7) was applied to all surfaces to separate the surface roughness associated information from the shape associated information.

5. RESULTS

5.1 Glass characterization

5.1.1 Dilatometry results

The dilatometry results for the selected glasses can be seen in Table 5.1. Predicted and measured coefficient of thermal expansion (CTE) values were correlated by an r^2 = 0.9137 (Figure 5.4). The line of equality is drawn to represent the collection of points where predicted and measured values would coincide. A root mean squared error of 0.36 x 10^{-6}/ K was calculated. The dilatometry plots are shown in Figures 5.1 - 5.3. Coefficient of thermal expansion calculations took place between 100-400 ^{o}C as the plots were linear at that range for all the glasses.

Table 5.1: Dilatometry results for the selected glass compositions.

Glass	**Predicted CTE** (x 10^{-6}/ K)	**Measured CTE (100-400^{o}C)** (x 10^{-6}/ K)	**Difference** (x 10^{-6}/ K)	**DSP** (^{o}C)	**T_g** (^{o}C)
Glass A	8.60	8.47	0.13	683	585
Glass B	10.35	10.06	0.29	670	580
Glass B1	10.32	9.93	0.39	664	576
Glass B2	10.35	10.01	0.34	675	583
Glass B3	10.37	10.06	0.31	675	588
Glass B4	10.38	10.16	0.22	665	567
Glass B5	10.55	10.48	0.07	639	558
Glass C	9.73	9.01	0.72	679	584

DSP: Dilatometric softening point T_g: glass transition temperature

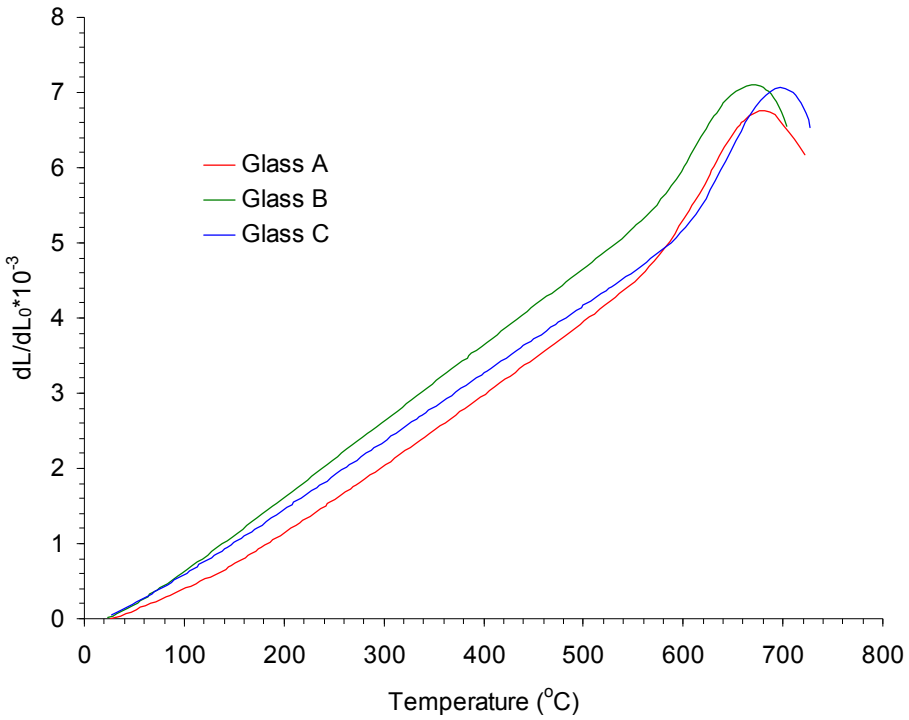

Figure 5.1: Dilatometry plots for the starting glasses.

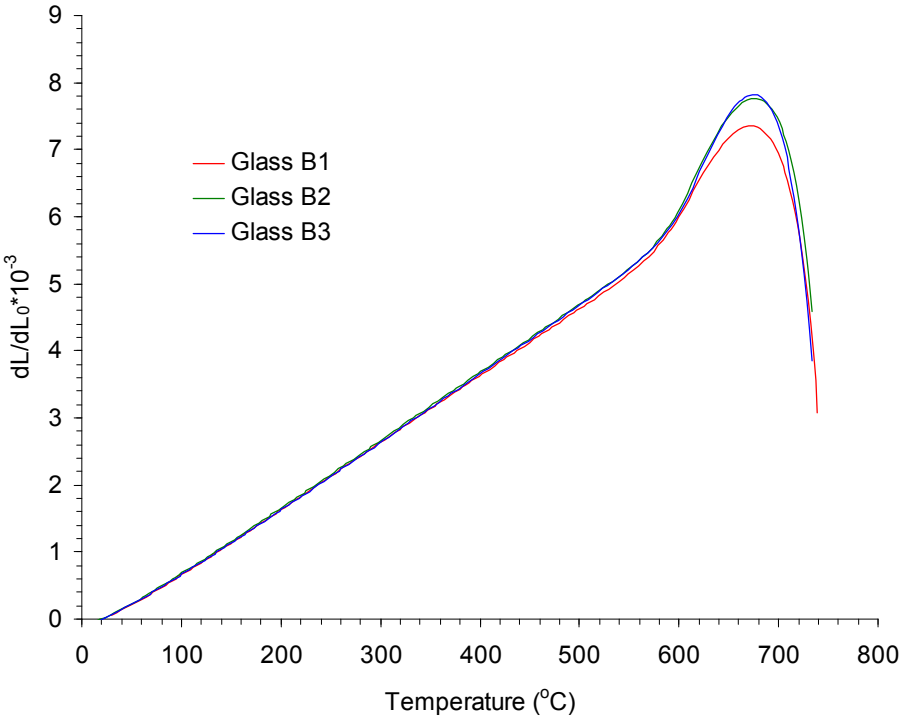

Figure 5.2 : Dilatometry plots for the glasses B1, B2 and B3.

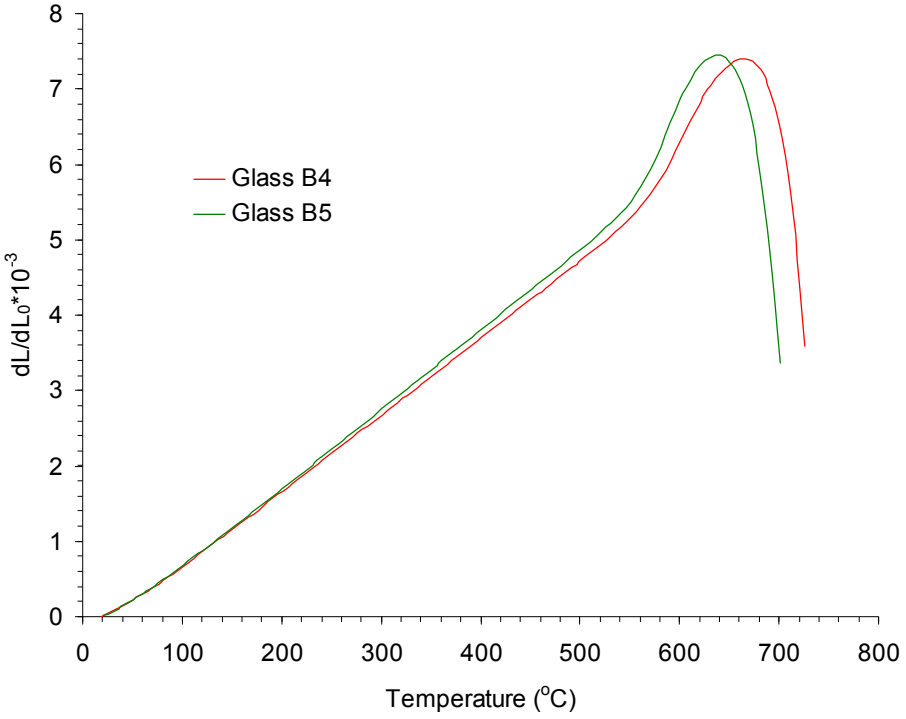

Figure 5.3 : Dilatometry plots for the glasses B4 and B5.

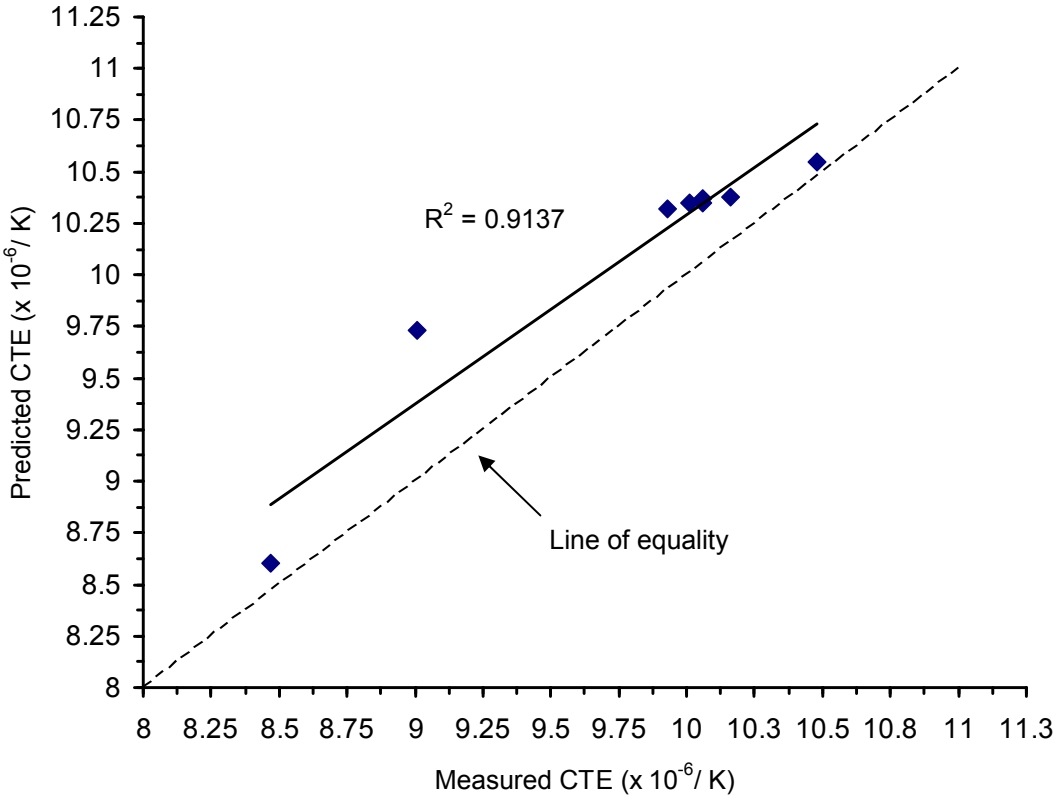

Figure 5.4: Relation of Measured and Predicted CTE values for the experimental glasses.

5.1.2 Differential Thermal Analyses results

5.1.2.1 Glass A series

The results of the differential thermal analyses of bulk powder samples of the glasses A, AMP2 and APM4 at a rate of 20°C/min are shown in Figure 5.5. There is a positive shift (rise) of the crystallisation peak noticed starting from the glass A to the planetary milled glasses APM2 and APM4. The crystallisation peak for the glass A appears quite broad while it becomes narrower and more pointed as the milling progresses.

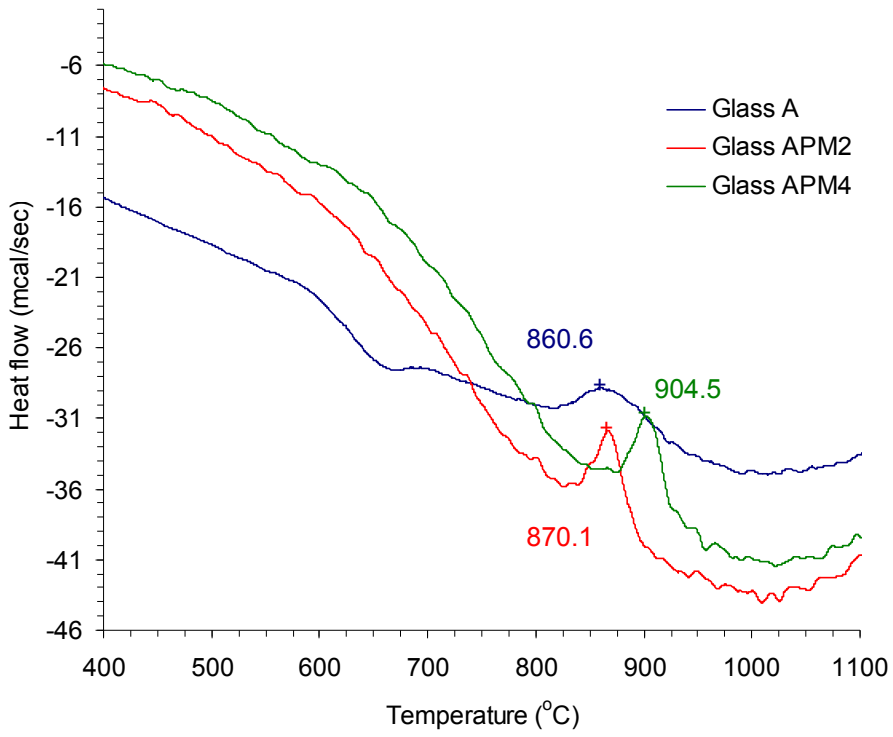

Figure 5.5: DSC plots for the glasses A, APM2 and APM4.

5.1.2.2 Glass B series

The results of the differential thermal analyses of the glass B at three particle sizes (PS) and at a rate of 20°C/min are shown in Figure 5.6. There is a positive shift of the crystallisation peak noticed when the particle size analysed is below 45 µm in respect to the two other larger particle sizes.

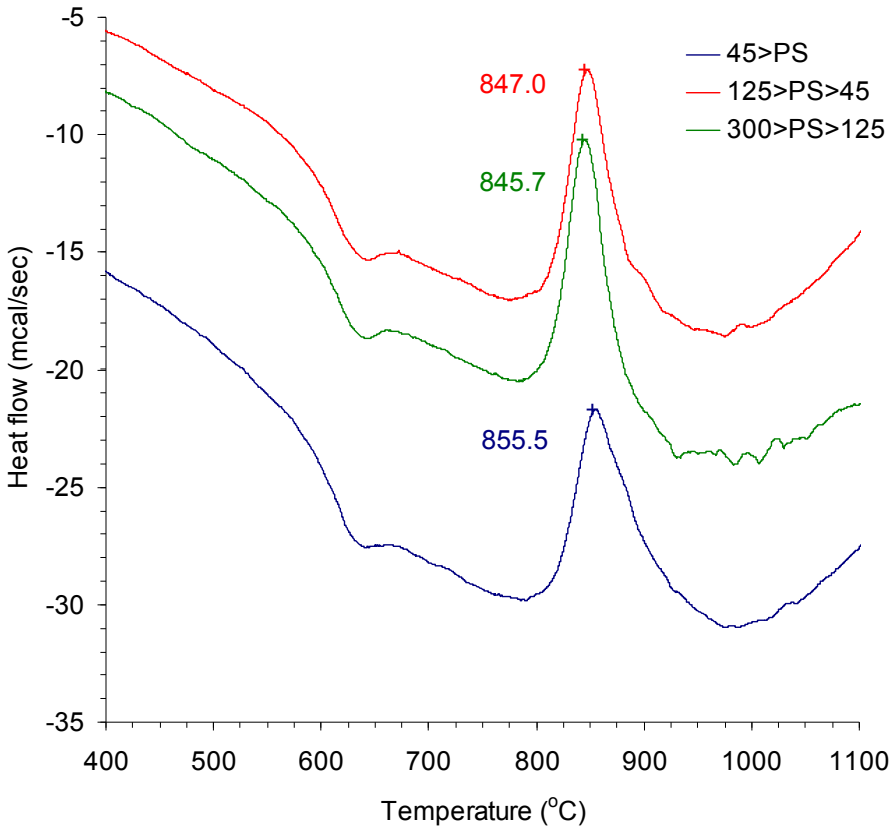

Figure 5.6: DSC plots for the glass B at three particle sizes.

The results of the differential thermal analyses of the glasses B1, B2 and B3 (PS<125 μm) at a rate of 20°C/min are shown in Figure 5.7. There is a positive shift (rise) of the crystallisation peak noticed as the content of Ca and Ti increases (B1→B2→B3).

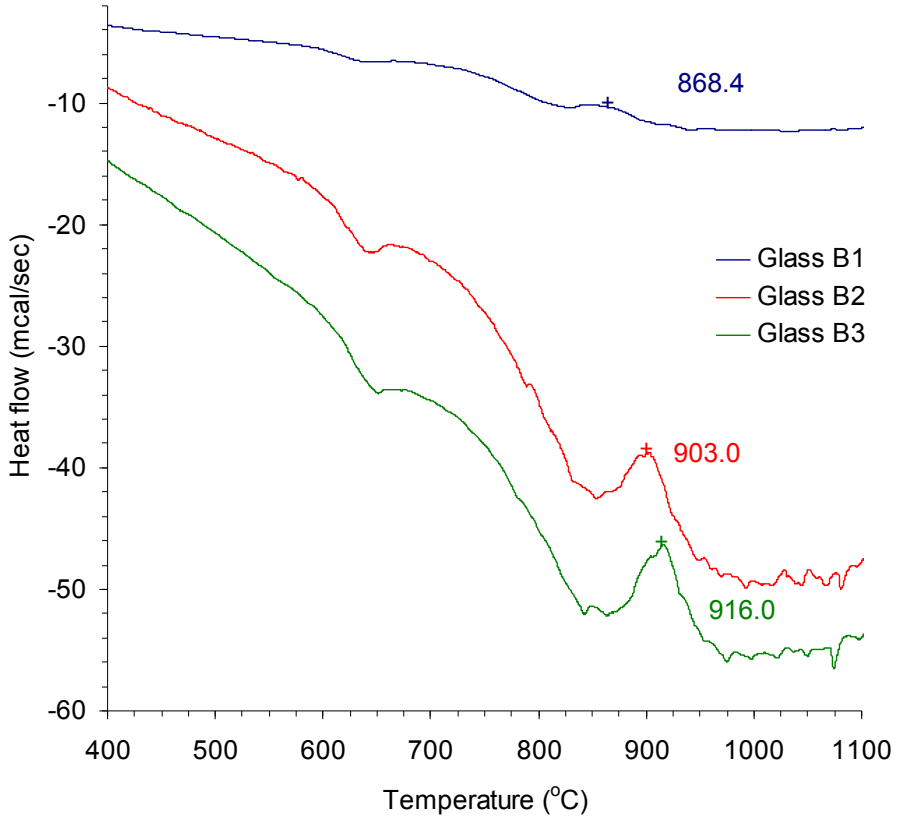

Figure 5.7: DSC plots for the glasses B1, B2 and B3.

The results of the differential thermal analyses of the glass B4 at three particle sizes (PS) at a rate of 20°C/min are shown in Figure 5.8. The T_p exotherms are generally broad with a positive shift noticed for glass particle size between 125 and 45 μm.

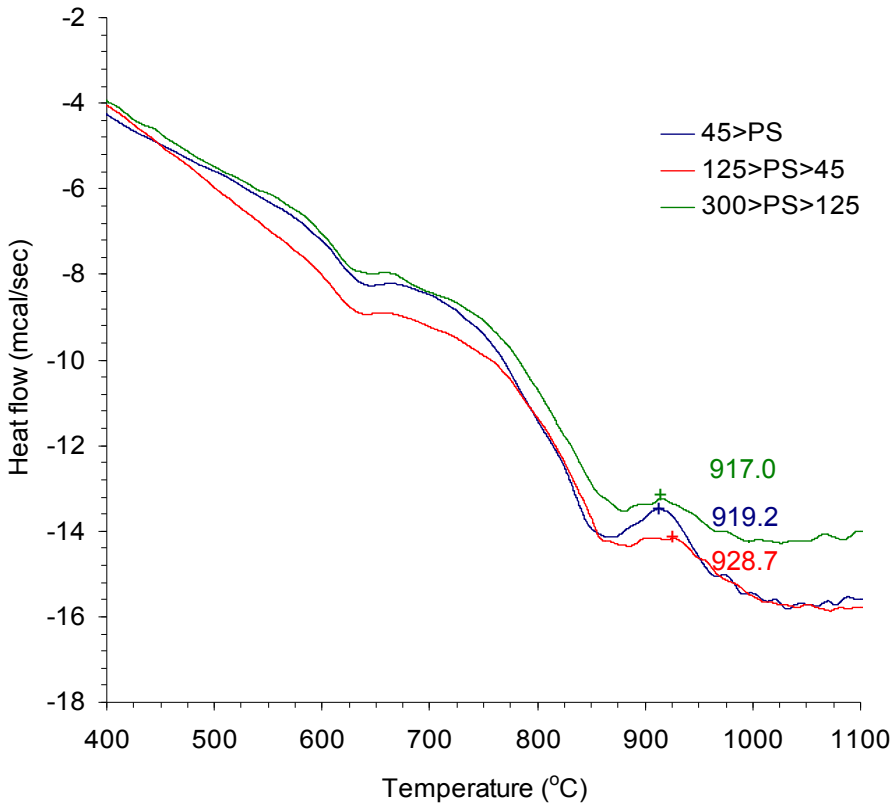

Figure 5.8: DSC plots for the glass B4 at three particle sizes.

The results of the differential thermal analyses of glass B4 at three particle sizes (PS) at a rate of 20°C/min are shown in Figure 5.9. Accurate T_p determination was not facilitated for these plots.

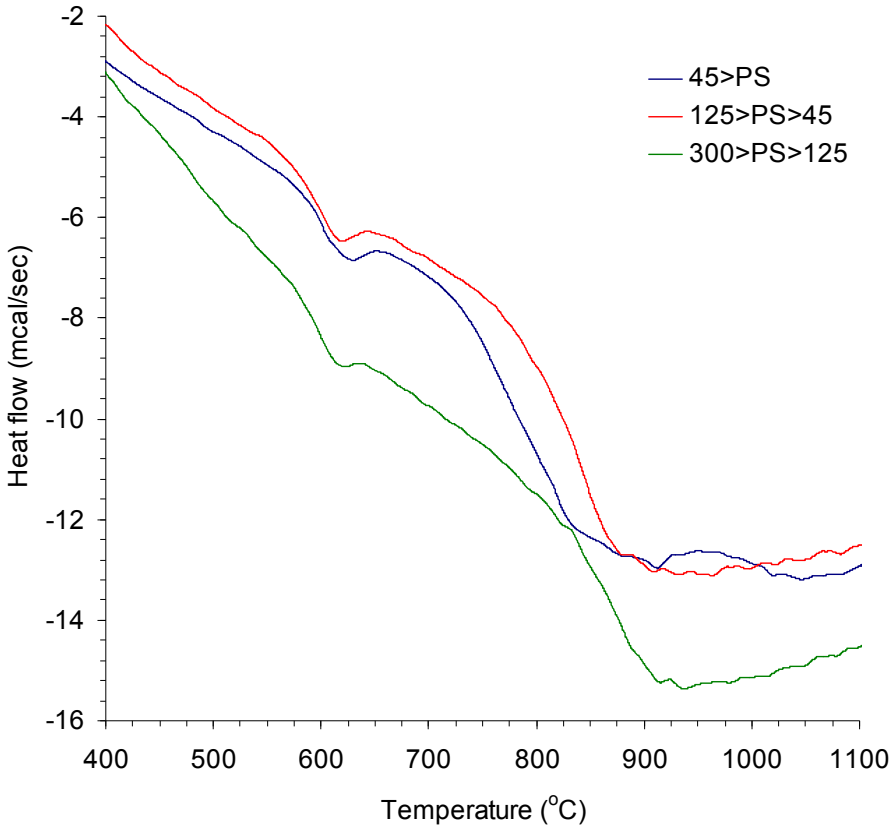

Figure 5.9: DSC plots for the glass B5 at three particle sizes.

5.1.2.3 Glass C series

The results of the differential thermal analyses of the glass C at three particle sizes (PS) at a rate of 20°C/min are shown in Figure 5.10. There is a positive shift (rise) of the crystallisation peak noticed when the particle size analysed is below 45 μm in respect to the two other larger particle sizes.

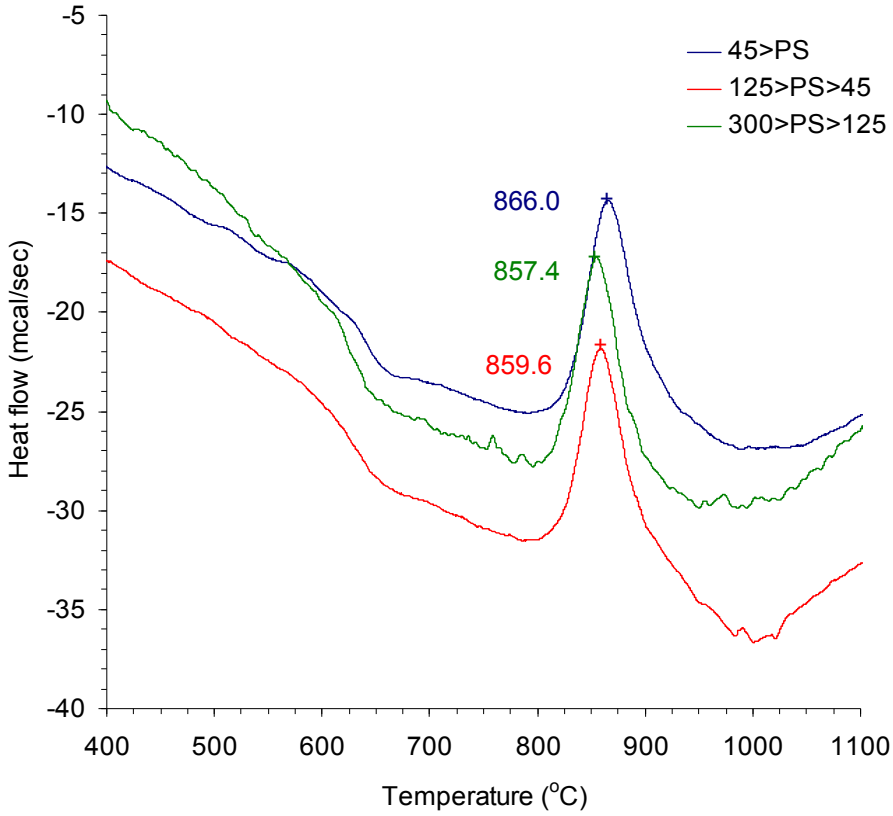

Figure 5.10: DSC plots for the glass C at three particle sizes.

5.1.3 Activation energy of crystallisation

The activation energy for the glasses B, B1-B3 and B4 was calculated using the Kissinger (1956) equation (see 2.11.1.1). Plots of ln (φ/T_p^2) versus $1000/T_p$ were plotted for the different rates run (Figures 5.11, 5.12) and a line was fitted through the data points. The lines' slope, fit (r^2) and the activation energies are given in Table 5.2.

Table 5.2: Activation energies

Glass	Slope	r^2	Activation energy ($KJ \cdot mol^{-1}$)
B	- 25.65	0.9931	213.3
B1	- 22.34	0.9619	185.7
B2	- 23.19	0.9938	192.8
B3	- 23.71	0.9969	197.1
B4	- 21.25	0.9999	176.6

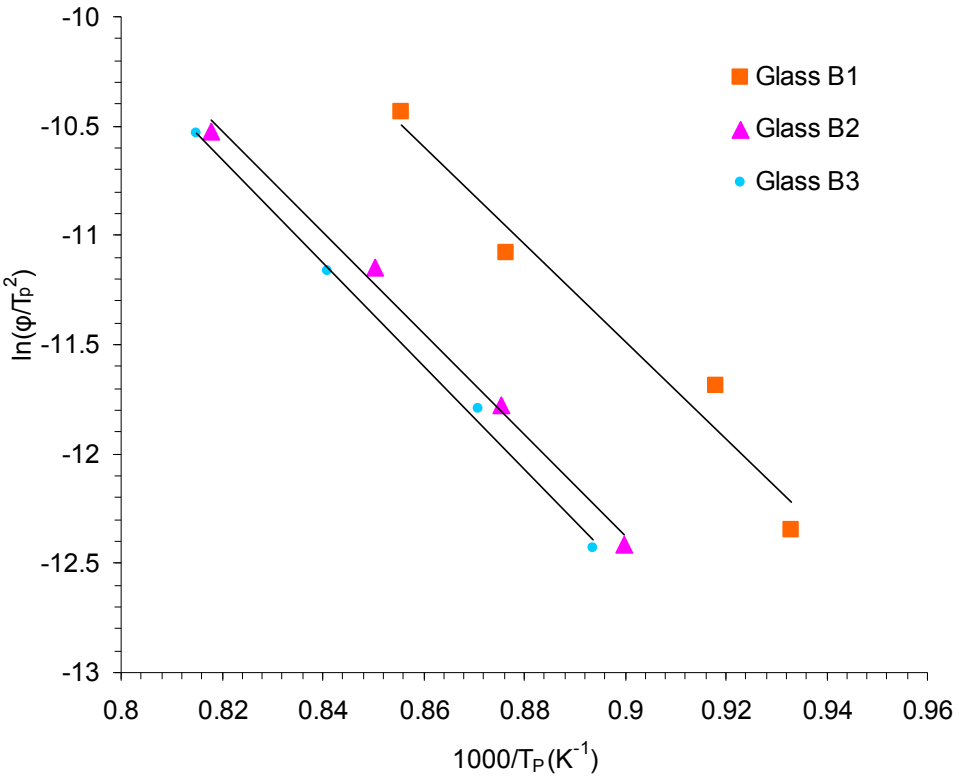

Figure 5.11: Kissinger plots for the glasses B1, B2 and B3.

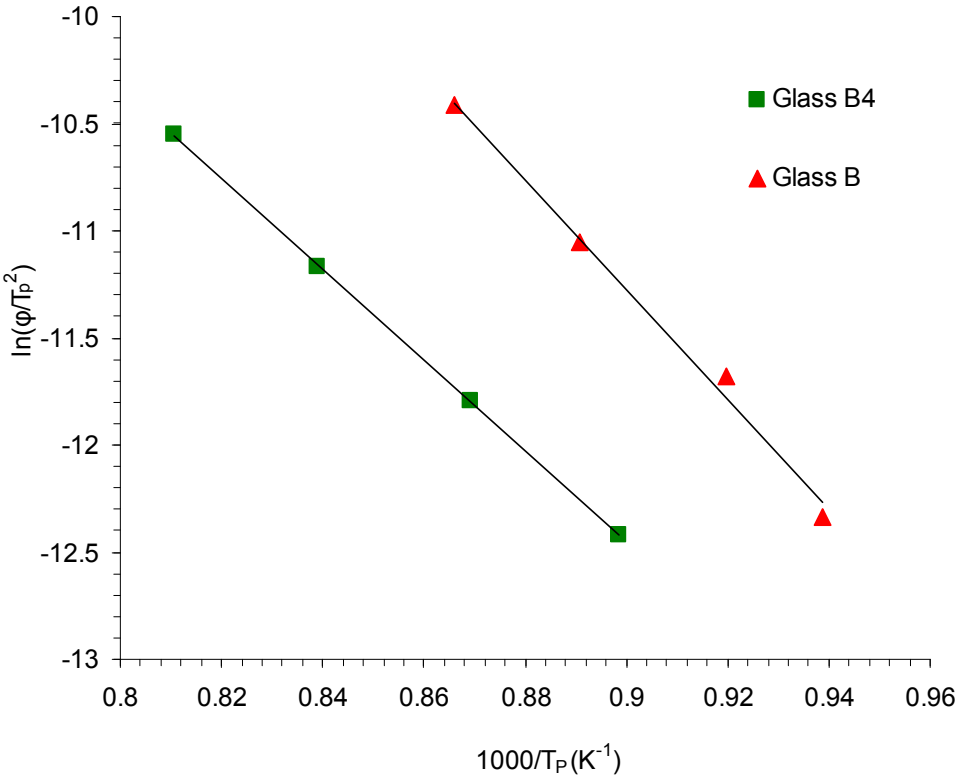

Figure 5.12: Kissinger plots for the glasses B and B4.

5.1.4 X-ray powder diffraction results

5.1.4.1 XRD Results for the experimental glasses

All starting (A, B, B1-B5 and C) and high speed milled (APM4, BPM2, B5PM0.5 and CPM0.5) glasses were characterised as amorphous and the patterns are shown in Figures 5.13 – 5.16.

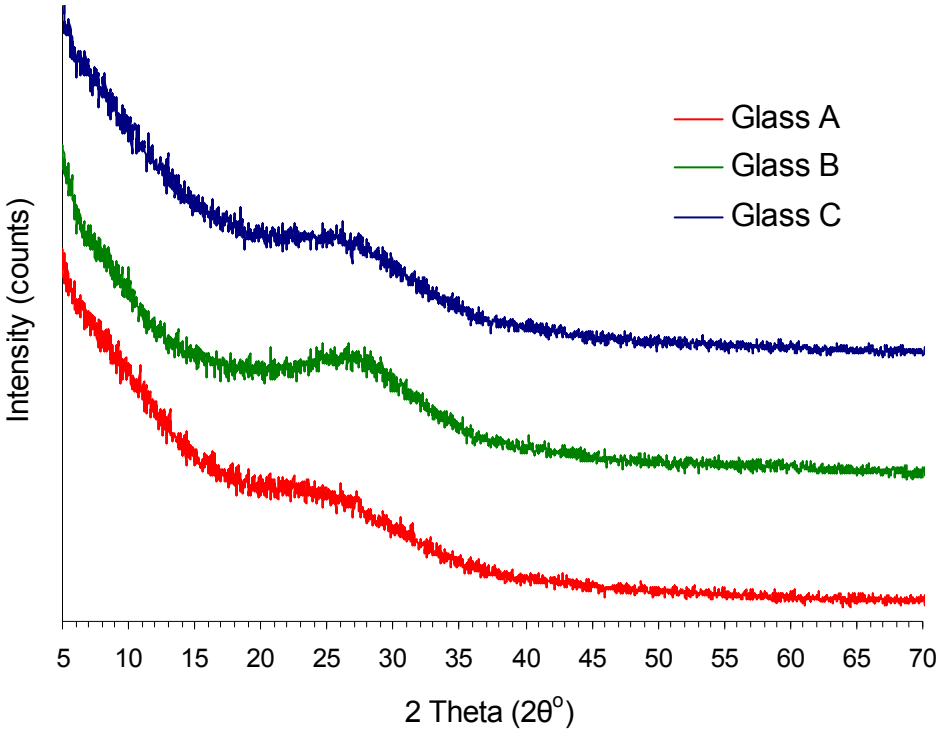

Figure 5.13: XRD patterns of the starting glasses.

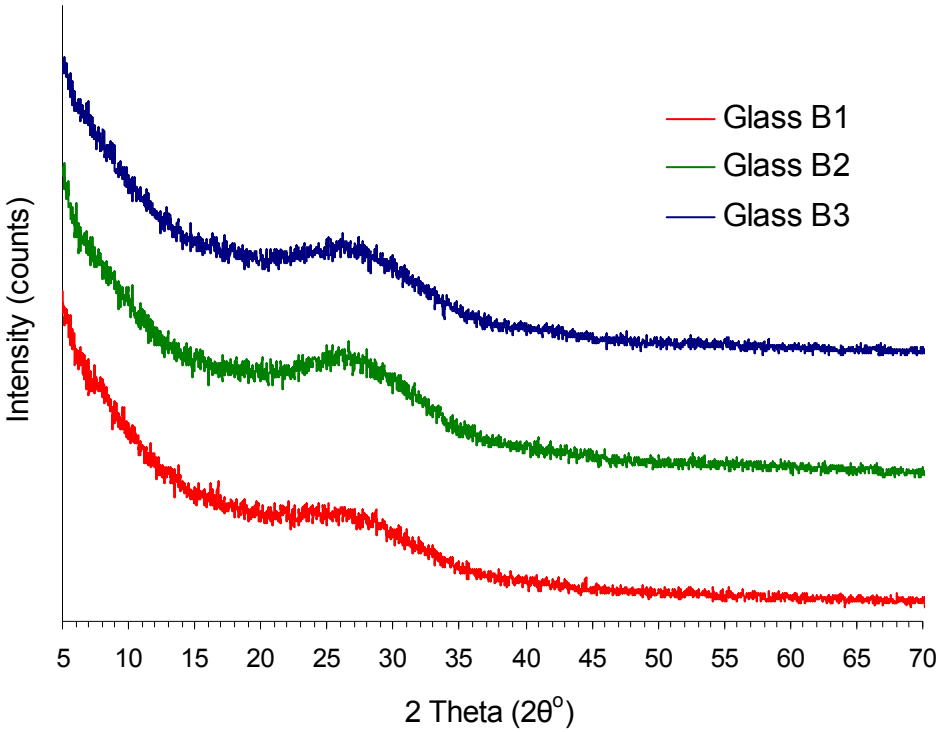

Figure 5.14: XRD patterns of the glasses B1, B2 and B3.

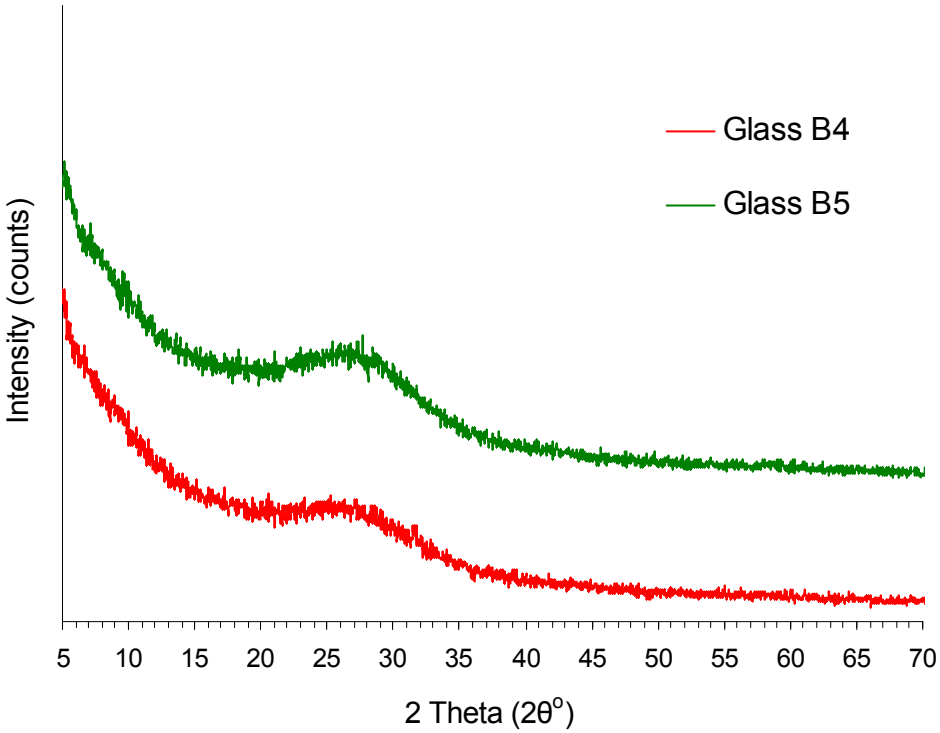

Figure 5.15: XRD patterns of the glasses B4 and B5.

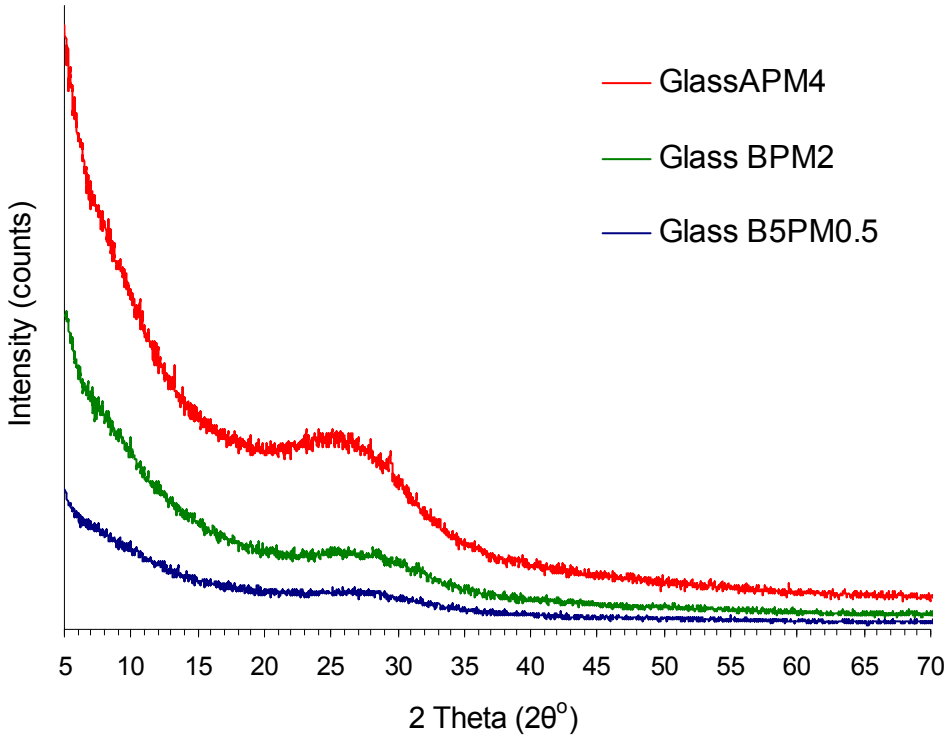

Figure 5.16: XRD patterns of the high speed milled glasses APM4, BPM2 and B5PM0.5.

5.1.4.2 High Temperature XRD results for the experimental glasses

The results of the High Temperature XRD (HTXRD) for the experimental glasses B, B1 – B5 and C are shown in Table 5.3. All glasses were amorphous at room temperature and the first crystalline peaks appear in the range 663 - 771°C. The peaks for all glasses then increased in intensity until they reached their maxima in the range of 793 – 902°C. The peaks then decreased gradually in intensity until they were no longer detectable (glasses B1 – B5) or were still present at low intensities (glasses B and C) (Table 5.3). For the glasses B and B1 – B5, all peak positions at all temperatures were confirmed to be cubic leucite (ICDD: 00-031-0967).

For the glass C, cubic leucite was confirmed to be present at all temperatures above 700°C. Some new crystalline peaks appeared from 836°C to 1075°C. These

new peaks were identified as sanidine (ICDD: 00-025-0618). After 1097°C these peaks disappeared leaving cubic leucite peaks.

Representative patterns of all glasses corresponding to room temperature, crystallisation start, crystallisation maxima, intermediate and crystallisation end temperatures are shown in Figures 5.17 – 5.23.

Table 5.3: High Temperature XRD results for all experimental glasses.

Glass	Crystallisation start (°C)	Crystallisation maxima (°C)	Crystallisation end (°C)	Coexistence of cubic leucite – sanidine (°C)
B	750	880	-	
B1	663	793	1205	
B2	728	902	1227	
B3	750	880	1205	
B4	728	793	1249	
B5	728	815	1162	
C	771	858	-	836 - 1075

5.1.4.3 Peak crystallisation temperature selection using HTXRD

An alternative method for peak crystallisation temperature selection was attempted for glass B5 based on HTXRD data due to the absence of T_p in all the B5 DSC plots (Figure 5.9). The main cubic leucite peak height and peak area (peak at 26.527 2θ°, baseline corrected and integrated in Excel) of glass B5 were plotted against temperature. Both plots showed maxima at 820°C (Figure 5.24) and this temperature was used for the crystallisation heat treatments of this glass series.

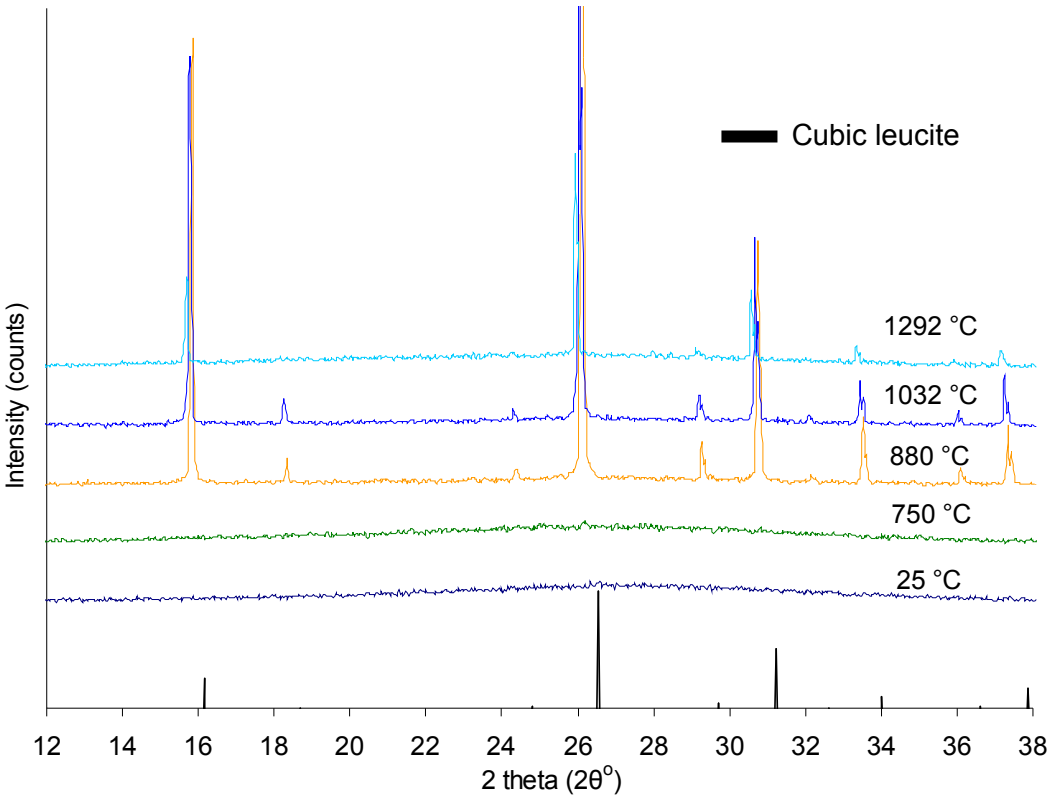

Figure 5.17: High temperature XRD patterns of the glass B.

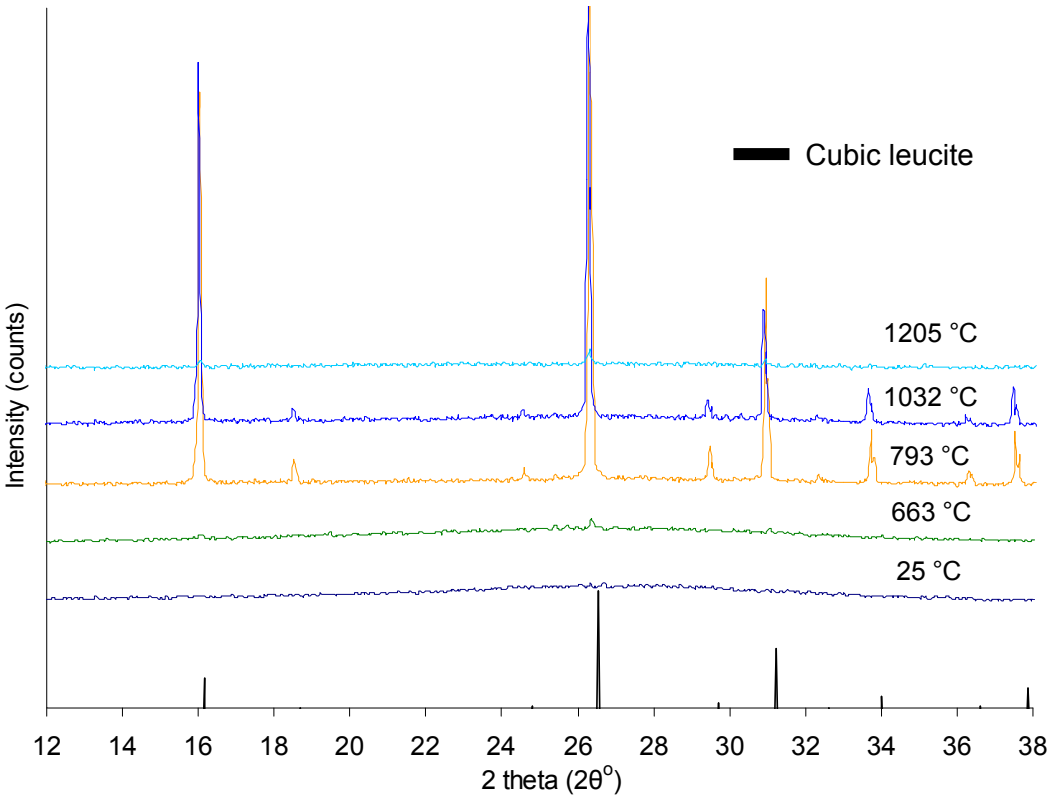

Figure 5.18: High temperature XRD patterns of the glass B1.

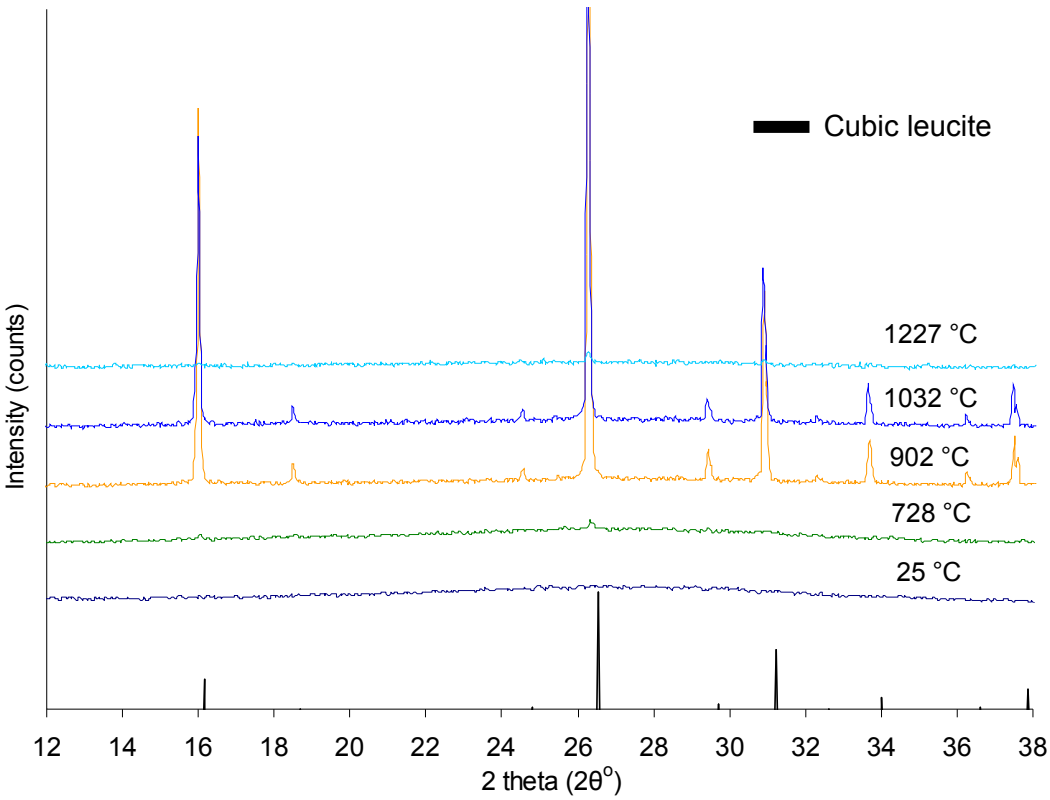

Figure 5.19: High temperature XRD patterns of the glass B2.

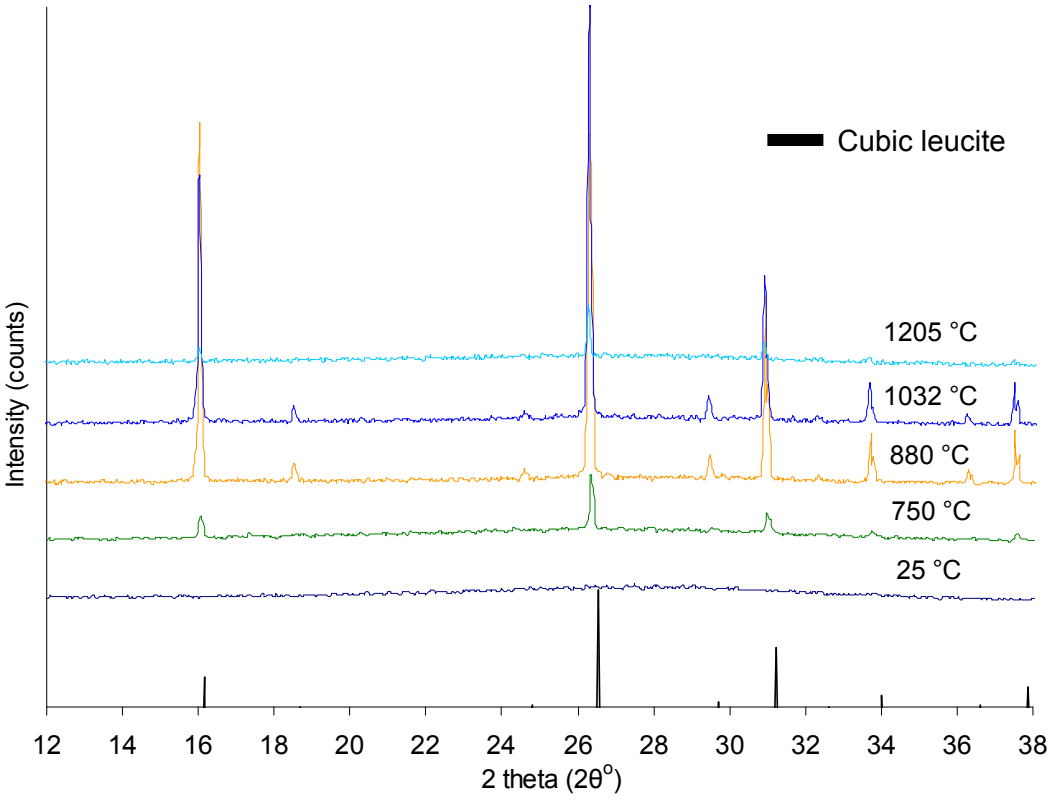

Figure 5.20: High temperature XRD patterns of the glass B3.

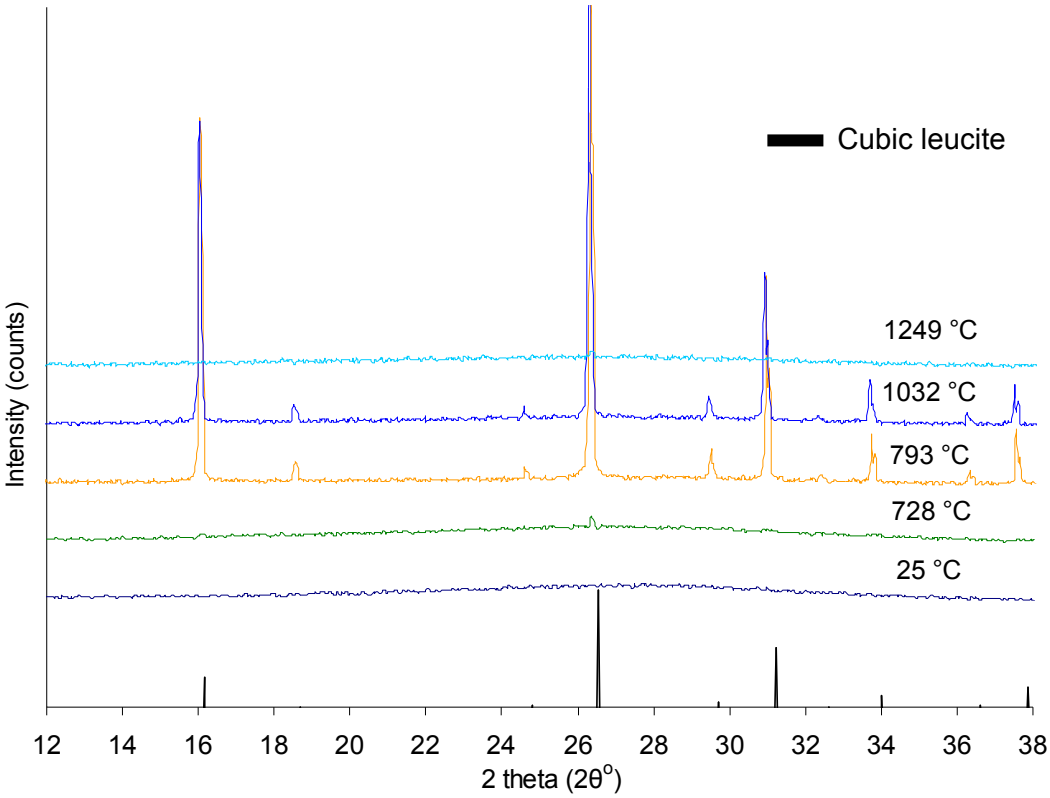

Figure 5.21: High temperature XRD patterns of the glass B4.

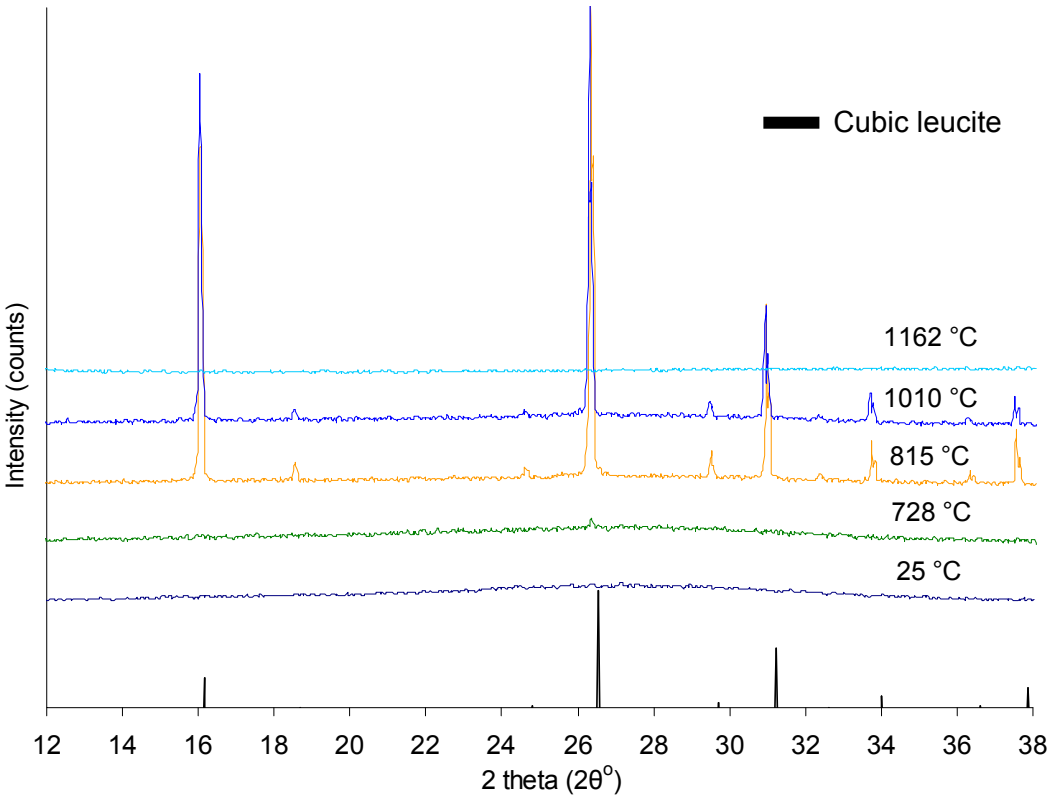

Figure 5.22: High temperature XRD patterns of the glass B5.

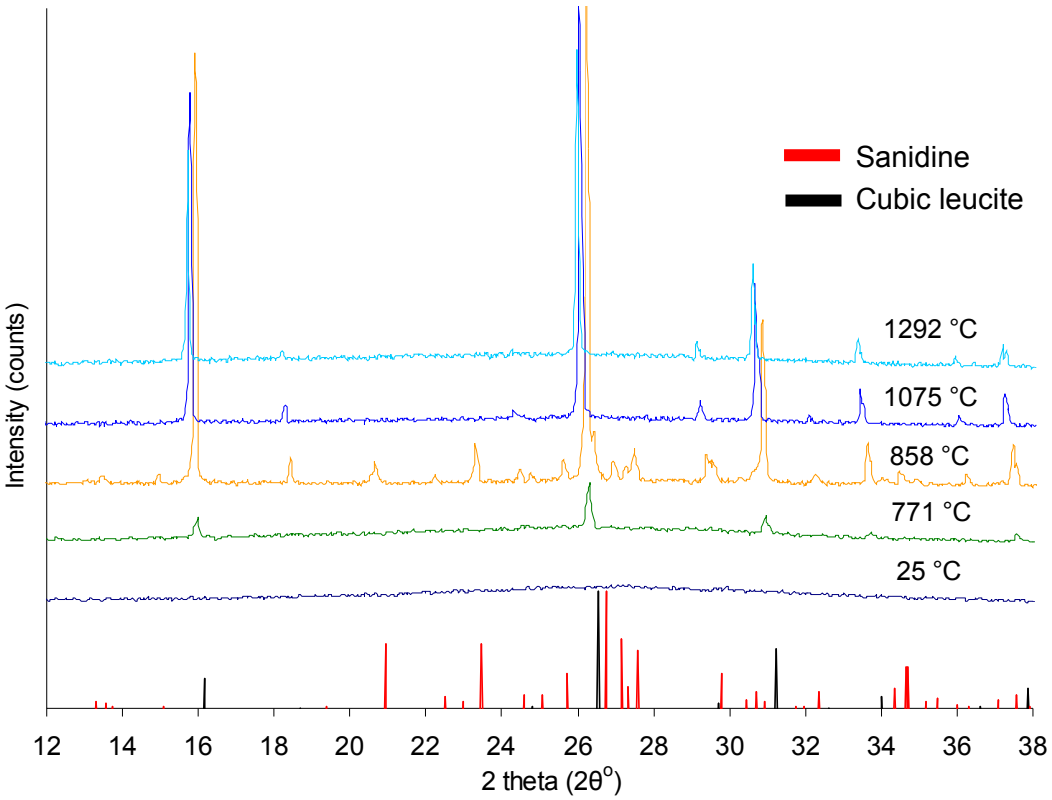

Figure 5.23: High temperature XRD patterns of the glass C.

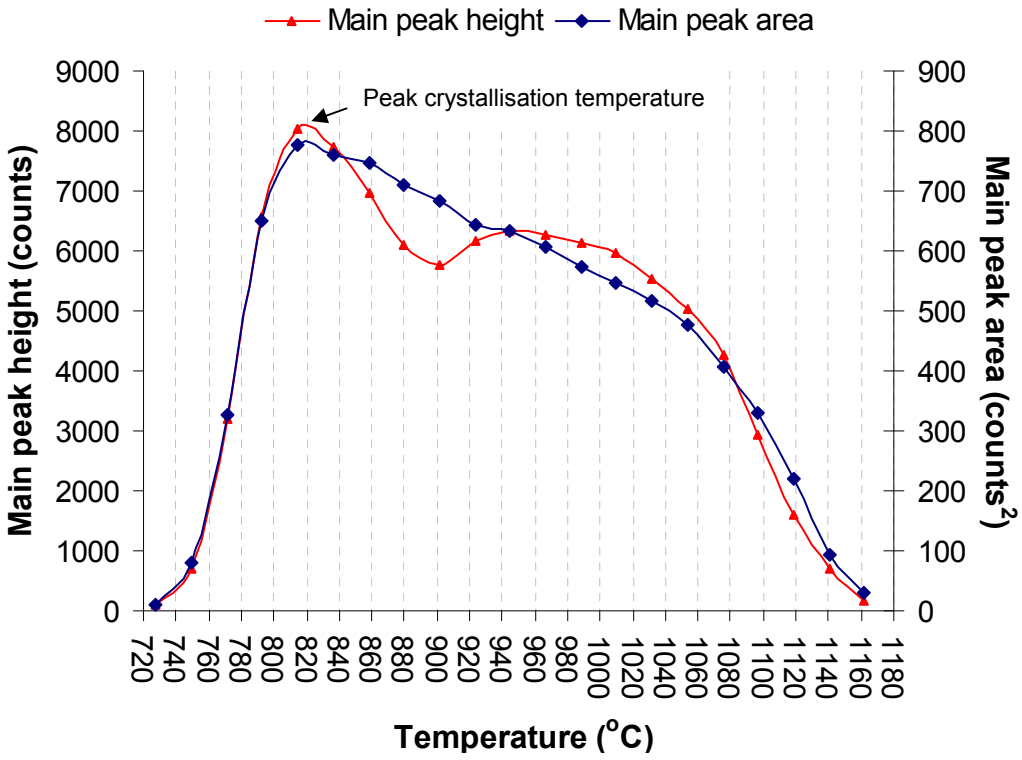

Figure 5.24: Glass B5 peak crystallisation temperature selection using a plot of the main cubic leucite peak height and peak area against temperature.

5.1.4.4 XRD Results for the glass-ceramics

The room temperature XRD patterns of the commercial and the experimental glass-ceramics were all matched to tetragonal leucite (ICDD: 00-038-1423) (Figure 5.25 - Figure 5.30). The results of the mean unit cell dimensions can be seen in Table 5.4.

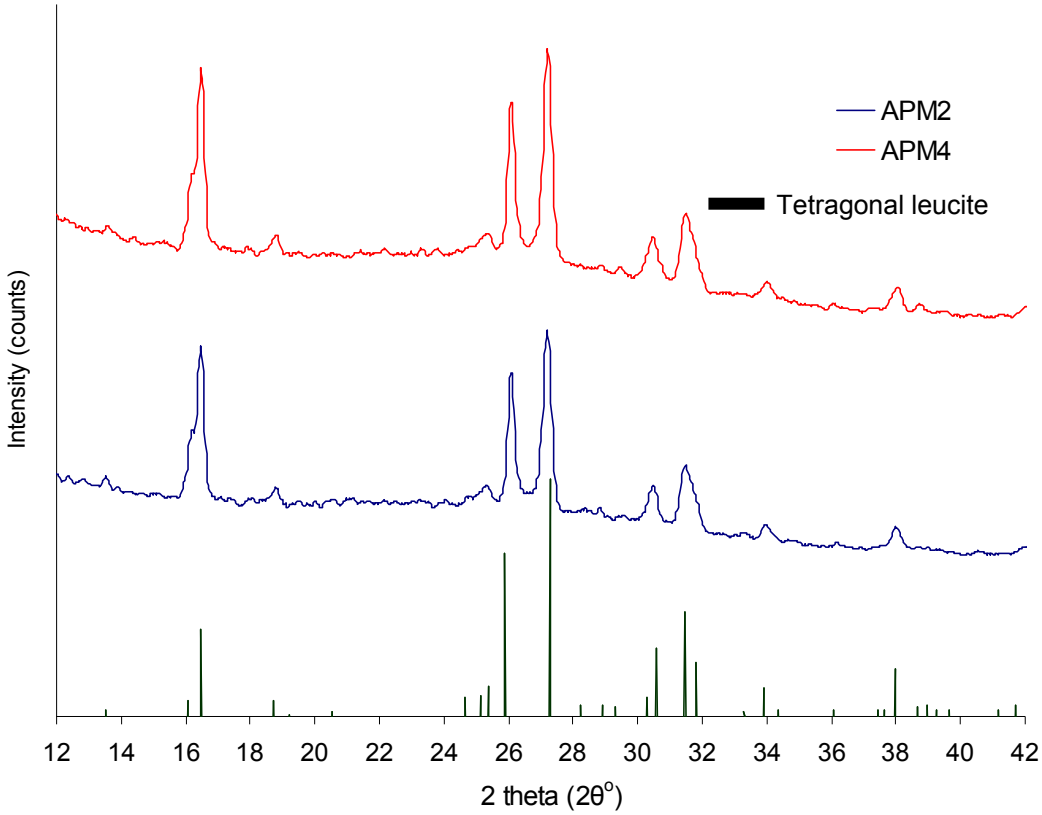

Figure 5.25: XRD patterns of the glass-ceramics APM2 and APM4 showing the presence of tetragonal leucite.

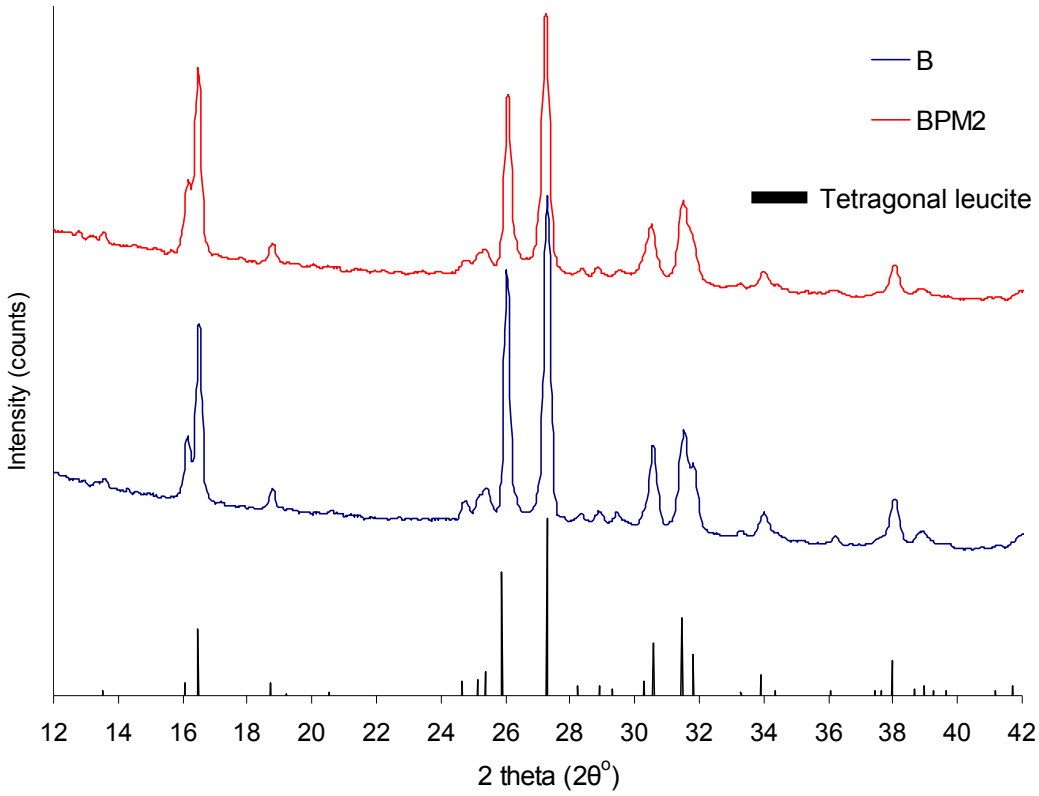

Figure 5.26: XRD patterns of the glass-ceramics B and BPM2 showing the presence of tetragonal leucite.

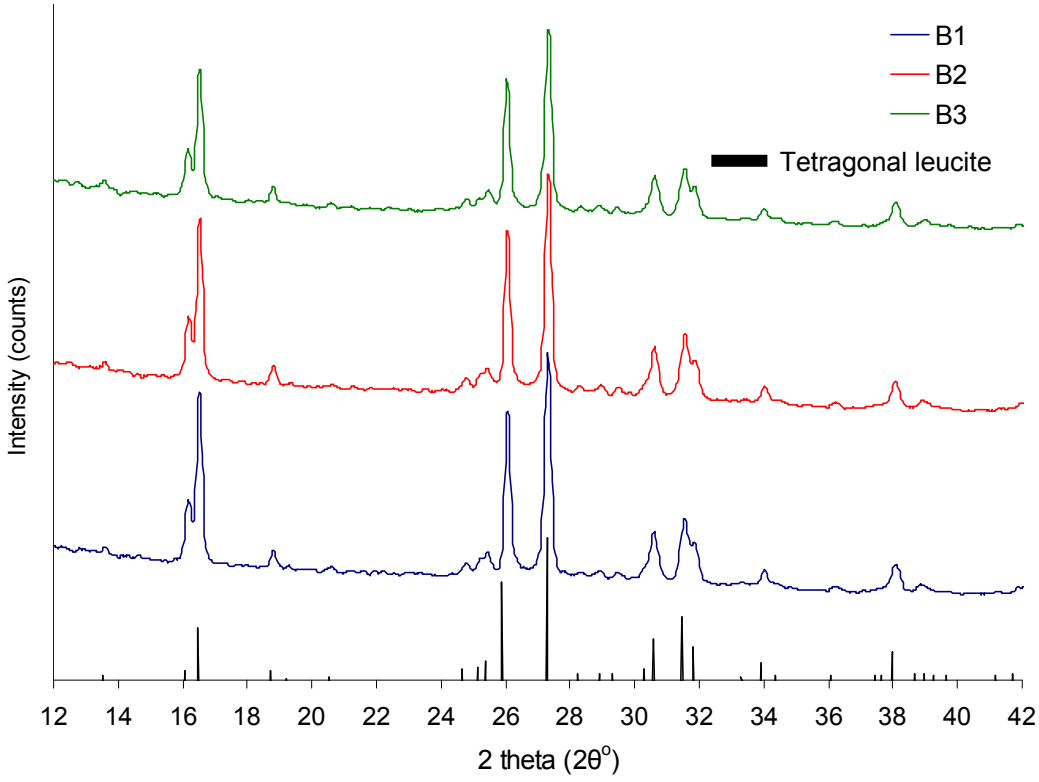

Figure 5.27: XRD patterns of the glass-ceramics B1, B2 and B3 showing the presence of tetragonal leucite.

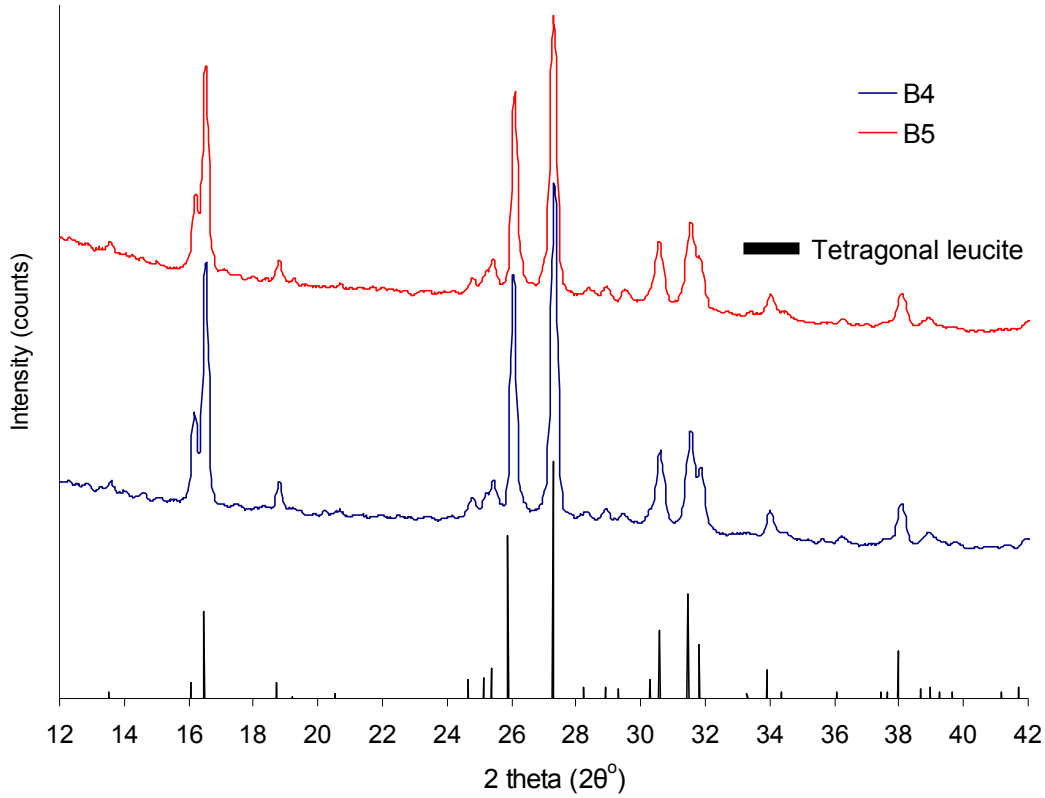

Figure 5.28: XRD patterns of the glass-ceramics B4 and B5 showing the presence of tetragonal leucite.

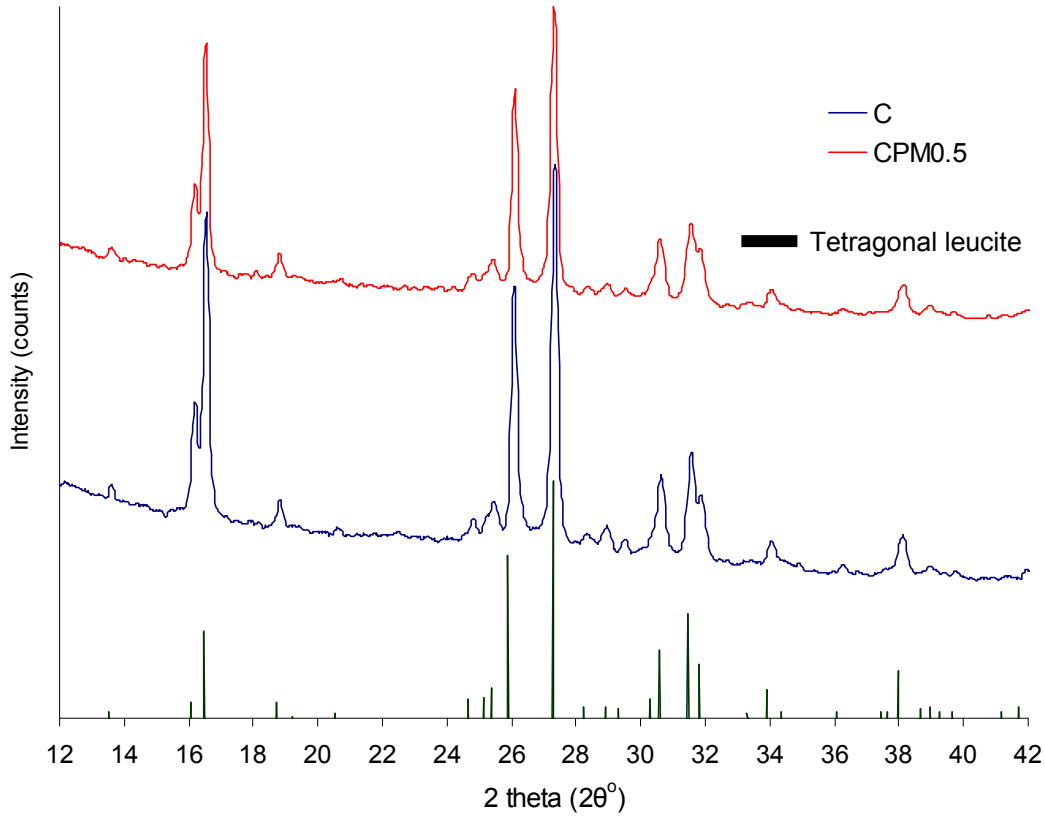

Figure 5.29: XRD patterns of the glass-ceramics C and CPM0.5 showing the presence of tetragonal leucite.

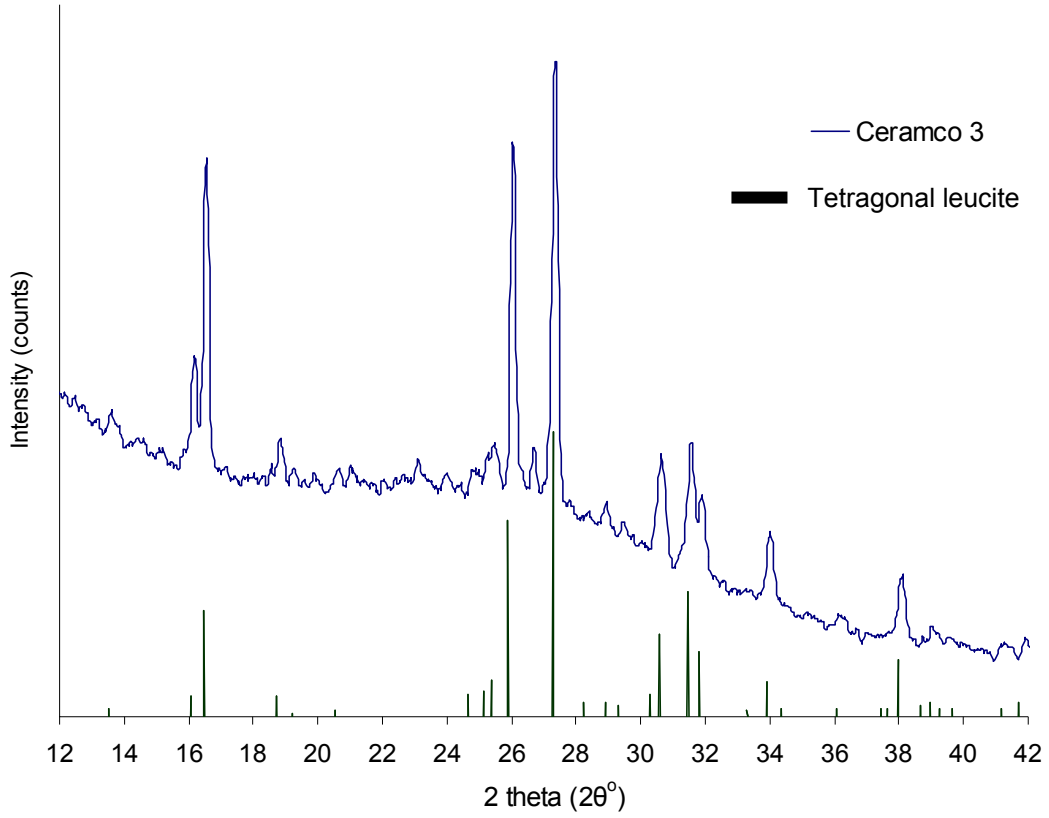

Figure 5.30: The Ceramco 3 commercial glass-ceramic XRD pattern showing the presence of tetragonal leucite.

Table 5.4: The tetragonal leucite mean unit cell dimensions for the experimental and commercial glass-ceramics.

	Mean *a*-axis Unit Cell dimension Å (SD)	Mean *c*-axis Unit Cell dimension Å (SD)	Mean Unit Cell volume $Å^3$ (SD)
APM2	13.1658 (0.0009)	13.7100 (0.0002)	2376.44 (0.39)
APM2 HP	13.1481 (0.0014)	13.7072 (0.0008)	2369.59 (0.34)
APM4	13.1594 (0.0009)	13.7093 (0.0015)	2374.01 (0.37)
AAM4 HP*	13.1343 (0.0007)	13.6869 (0.0012)	2363.19 (0.64)
B	13.1024 (0.0004)	13.7171 (0.0007)	2354.86 (0.17)
BPM2	13.1265 (0.0006)	13.6991 (0.0010)	2360.41 (0.25)
B1	13.1082 (0.0005)	13.7205 (0.0009)	2357.50 (0.21)
B2	13.1016 (0.0005)	13.7248 (0.0008)	2355.89 (0.20)
B3	13.1009 (0.0006)	13.7319 (0.0009)	2356.88 (0.22)
B4	13.1041 (0.0005)	13.7256 (0.0008)	2356.92 (0.19)
B5	13.1153 (0.0006)	13.7049 (0.0009)	2357.39 (0.23)
B5PM0.5	13.1257 (0.0006)	13.7055 (0.0010)	2361.23 (0.25)
C	13.0965 (0.0005)	13.6988 (0.0009)	2349.58 (0.20)
CPM0.5	13.1068 (0.0006)	13.7026 (0.0009)	2353.95 (0.23)
Ceramco 3	13.0874 (0.0007)	13.7320 (0.0012)	2352.02 (0.31)

*result from (Chen, 2009)

5.2 Glass - ceramic Secondary Electron Imaging results

5.2.1 Glass A crystal size optimisation results

5.2.1.1 Glass A powder particle size analysis results

The results of the particle size analysis of the different milling intervals for the high speed milled glass A can be found in Table 5.5. The d_{50} value is plotted against milling time in Figure 5.31. A major reduction in particle size was noted within the first 30 minutes of milling. The particle size distributions were multimodal and positively skewed and an example can be found in Appendix 3.

Table 5.5: Particle size analysis results of the high speed milled Glass A.

Milling time (min)	Particle size (µm)			Span
	d_{10}	d_{50}	d_{90}	
0	3.448	22.03	62.16	2.665
2	0.431	2.445	5.075	1.899
6	0.356	1.163	2.443	1.794
10	0.301	0.640	1.477	1.838
16	0.275	0.550	1.950	3.045
30	0.253	0.475	4.569	9.086
46	0.247	0.541	9.203	16.555
60	0.232	0.548	9.701	17.279
120	0.245	0.583	9.042	15.089
240	0.212	0.692	8.023	11.288

d_{10}: 10% below, d_{50}: 50% below, d_{90}: 90% below

Span = $(d_{90}-d_{10})/d_{50}$

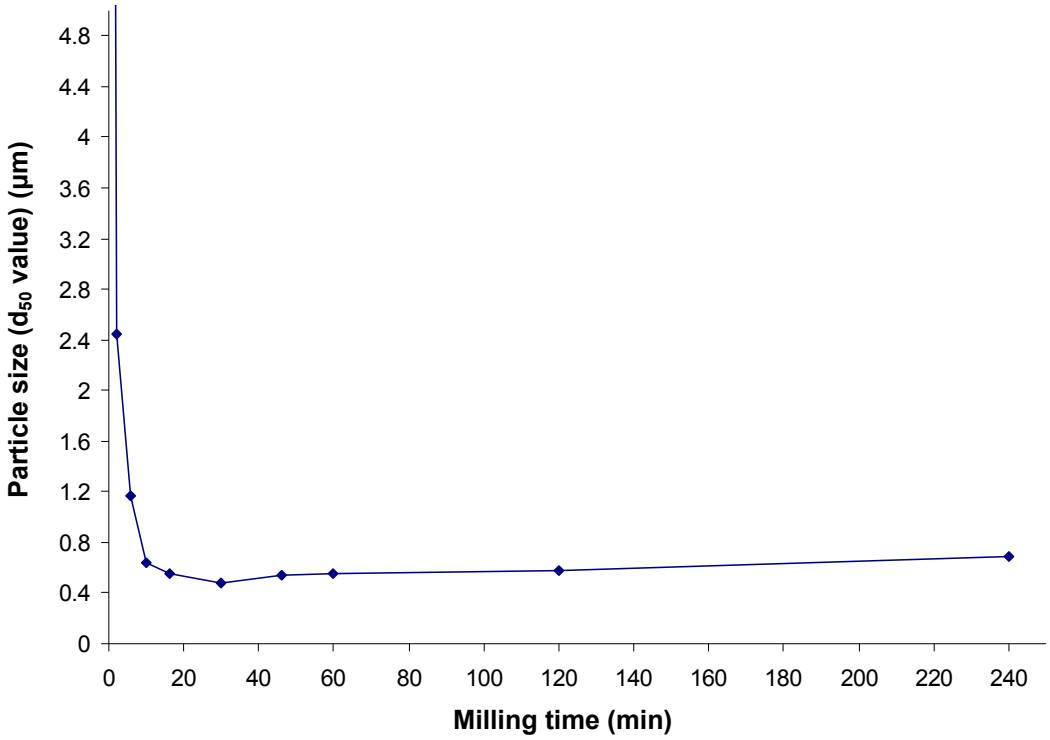

Figure 5.31 : Relationship of glass particle size with milling time for the high speed milled glass A.

5.2.1.2 Glass-ceramic A series SEI and crystal measurements results

The results of the SEI for the glass-ceramic A series specimens are presented in Figures 5.33 - 5.38. Crystallisation data based on quantitative image analysis of the micrographs is presented in Table 5.6. There is a major increase in crystal number as the milling time increases for the high speed milled glass A. There is also an increase in crystal number when comparing the A-AM4 glass-ceramic (Attritor milled) and the 0.5 hours high speed milled glass A (Planetary milling). The median crystal area falls to the nanoscale level beyond 0.5 hours of milling time with statistical differences ($p < 0.001$, Dunn's multiple comparisons test) detected between all groups tested apart from APM1 and APM2 glass-ceramics ($p > 0.001$).

The Histogram in Figure 5.32 shows the positive skewness in the crystal area distributions exhibited in all planetary milled two step heat treated A glasses. The particles become more rounded with milling time according to the increase in the shape factor (Table 5.6). The crystal particle size reduction is evident as the milling time progresses. A uniform dispersion of leucite crystals and minimal or no micro-cracking of the crystals/ glass matrix is also noted in all images. Microcracking was limited to the leucite crystals of starting glass A (Figure 5.33).

Table 5.6: Crystallisation data for the glass A series.

Milling time (h)	Area fraction (%)	Median Crystal area (μm^2) (Q1,Q3)	Crystal number	Particle Size range (μm^2)	Mean Shape Factor (SD)
0 (glass A)	33.2	0.836 [a] (0.589,1.190)	75	0.150 - 6.161	0.752 (0.066)
4 (A-AM4)#	29.3	0.185 [b] (0.119,0.271)	488	0.019 - 0.787	0.827 (0.052)
0.5 (APM0.5)*	24.1	0.085 [c] (0.055,0.127)	790	0.006 - 0.647	0.879 (0.048)
1 (APM1)*	22.3	0.055 [d] (0.038,0.086)	1076	0.009 - 0.506	0.870 (0.061)
2 (APM2)*	25.2	0.055 [d] (0.036,0.081)	1315	0.003 - 0.467	0.886 (0.051)
4 (APM4)*	27.8	0.048 [e] (0.030,0.070)	1718	0.005 - 0.278	0.894 (0.052)

* Planetary milling, # Attritor milling, Q1, Q3: 25th and 75th percentiles

Different superscript letters indicate significant differences between groups.

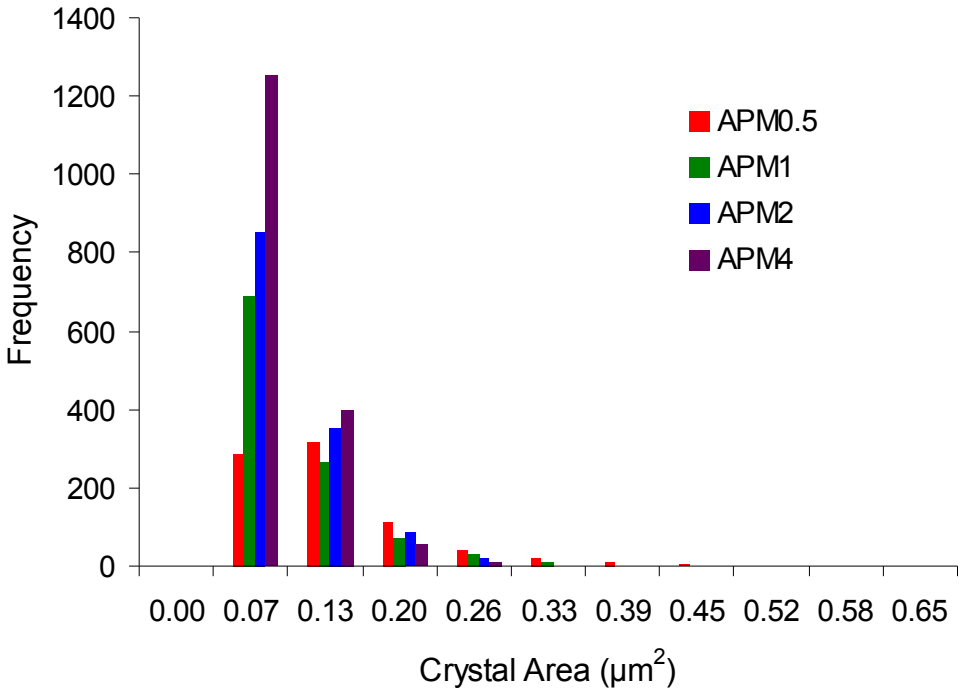

Figure 5.32: Histogram of crystal area values for the experimental planetary milled A samples showing the positive skew of all distributions.

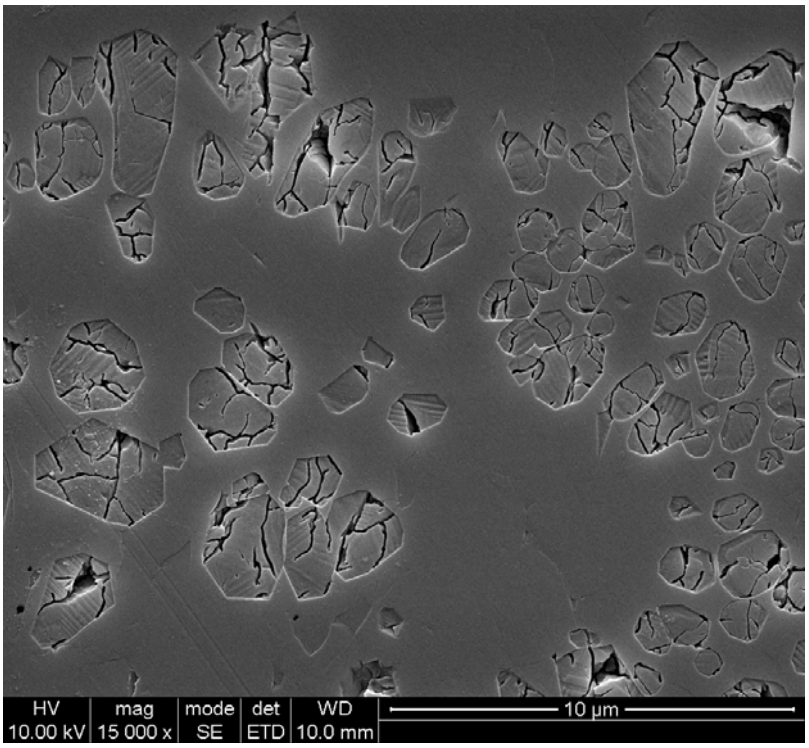

Figure 5.33: SEI of the two step heat - treated starting glass A showing irregular and non-uniform tetragonal leucite crystals and crystal microcracking (x15000).

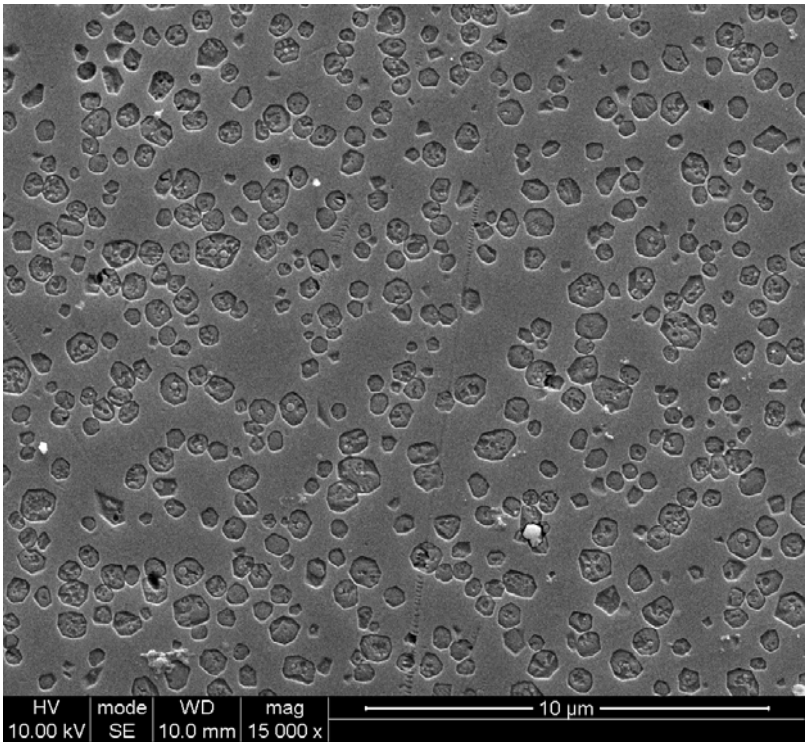

Figure 5.34: SEI of the two step heat - treated glass A-AM4 showing a uniform dispersion of fine (0.185 µm^2 median area) tetragonal leucite crystals (x15000).

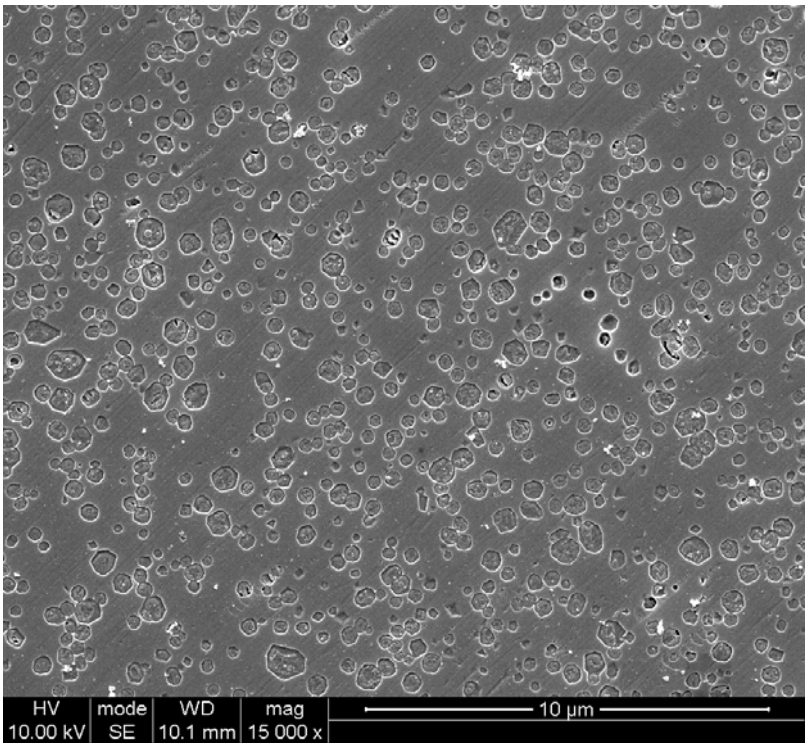

Figure 5.35: SEI of the two step heat - treated glass APM0.5 showing a uniform dispersion of fine (0.085 µm^2 median area) tetragonal leucite crystals (x15000).

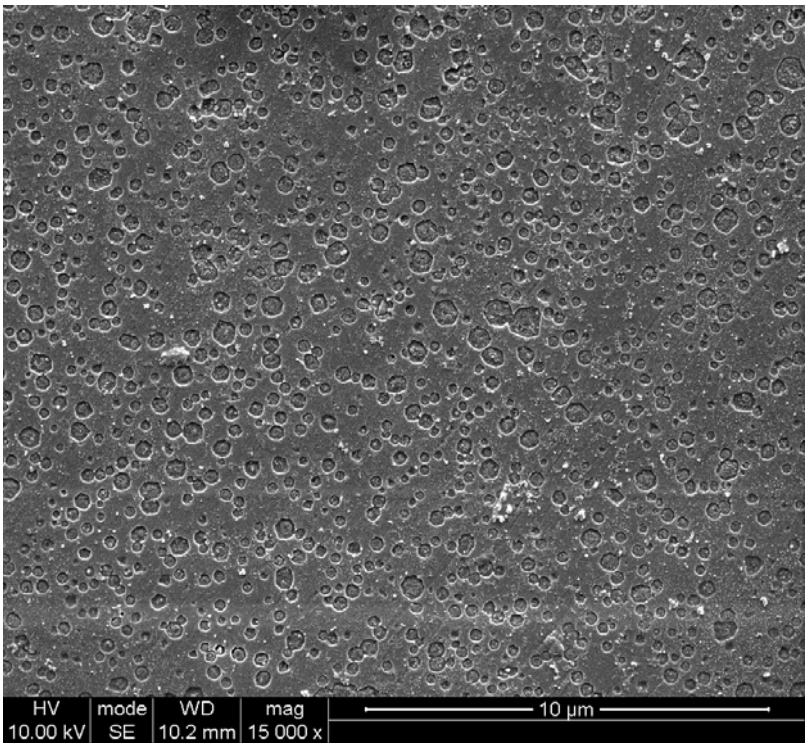

Figure 5.36: SEI of the two step heat - treated glass APM1 showing a dense dispersion of fine (0.055 µm^2 median area) tetragonal leucite crystals (x15000).

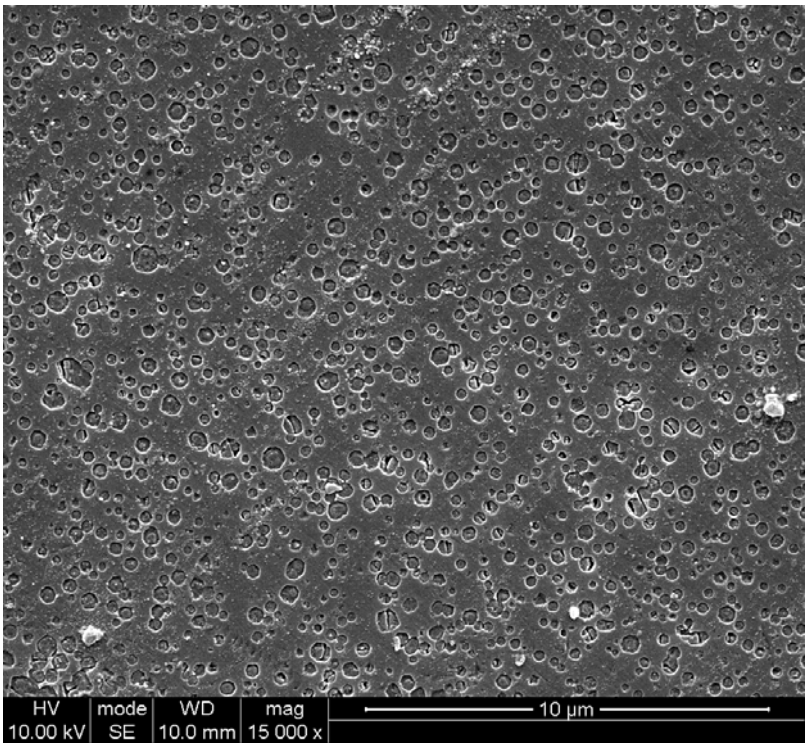

Figure 5.37: SEI of the two step heat - treated glass APM2 showing a dense dispersion of nanoscale (0.055 µm^2 median area) tetragonal leucite crystals (x15000).

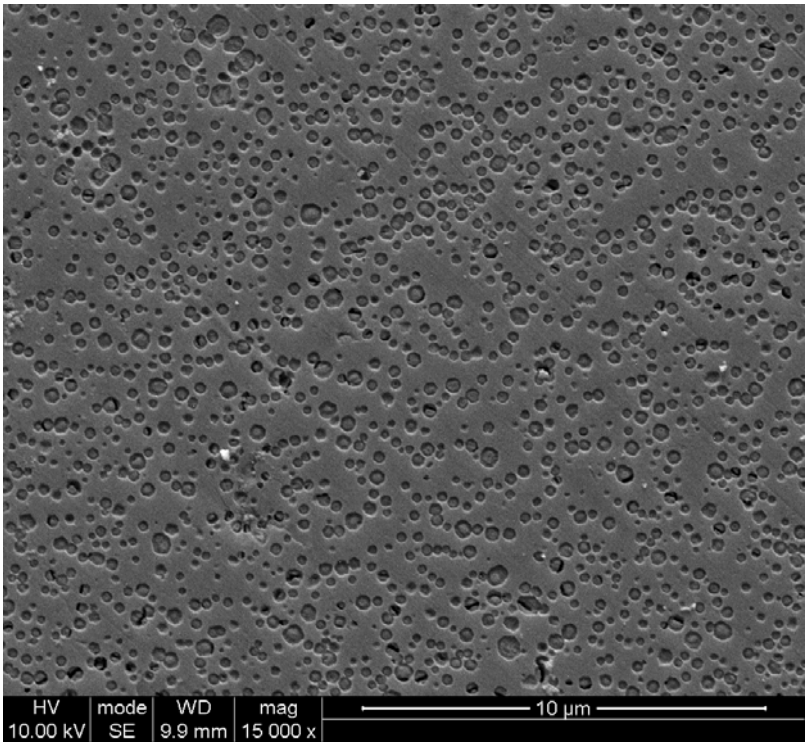

Figure 5.38: SEI of the two step heat - treated glass APM4 showing a dense dispersion of regular nanoscale (0.048 µm^2 median area) tetragonal leucite crystals (x15000).

5.2.2 Glass-ceramic B crystal size optimisation results

The results of the SEI for the glass-ceramic B series specimens are presented in Figures 5.39 – 5.43. Crystallisation data based on quantitative image analysis of the micrographs is presented in Table 5.7. The crystal number in respect to the starting B material slightly drops during the 1st hour of milling and increases during the 2nd hour. All high speed milled materials have significantly smaller median crystal area than the starting B sample ($p < 0.001$, Dunn's multiple comparisons test). The median crystal area drops to about half that of the starting B after 2 hours of milling time. There is however no statistical difference detected between the BPM0.5 and BPM2 groups. The intermediate group BPM1, has a higher median crystal area than the BPM2 sample ($p < 0.001$) while it has no significant difference with the BPM0.5. The Histogram in Figure 5.44 shows the positive skewness in the crystal area distributions exhibited in all planetary milled two step heat treated B glasses. There is a distinct microstructural change in the leucite crystals for all high speed milled two step heat treated B glasses. The mixed high tetragonal leucite area fraction microstructure of rounded and fibre-like conformations present in starting B sample evolves to an "embroidery" like interconnected tetragonal leucite structure as the milling progresses. Minimal or no micro-cracking of the glass matrix is also noted in all images while some crystal microcracking is present in the milled samples apart from the BPM2 two step heat treated glass.

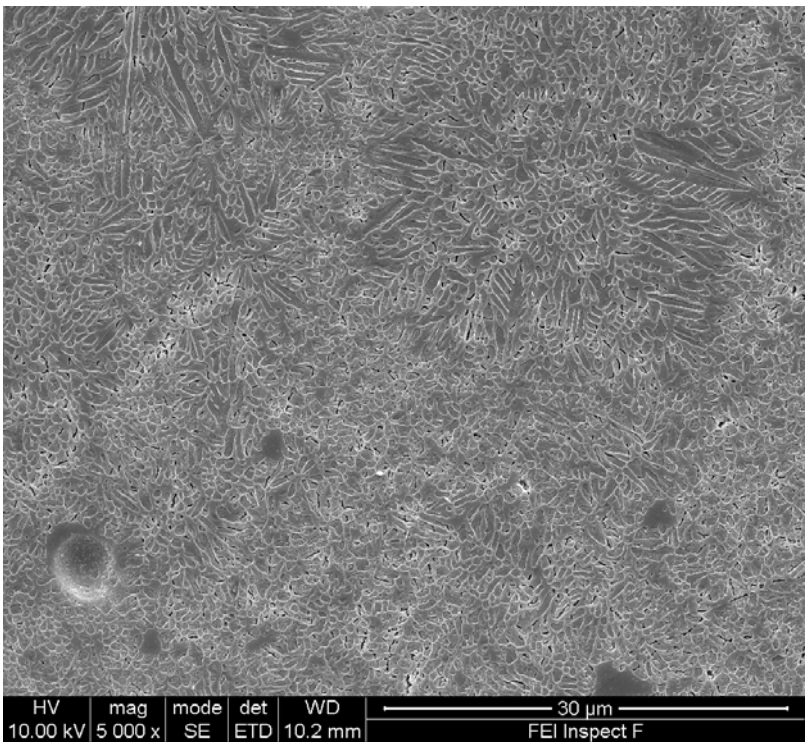

Figure 5.39: SEI of the glass-ceramic B specimen showing a high tetragonal leucite area fraction and coexistence of rounded and fibre-like conformations (x 5000).

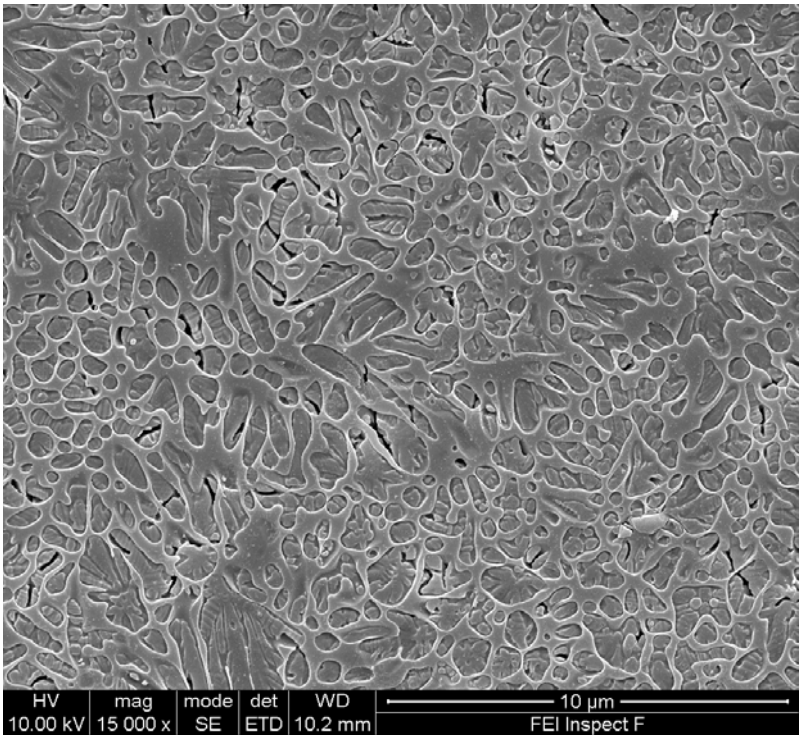

Figure 5.40: SEI of the glass-ceramic B specimen showing a high tetragonal leucite area fraction and coexistence of rounded and elongated conformations (x 15000).

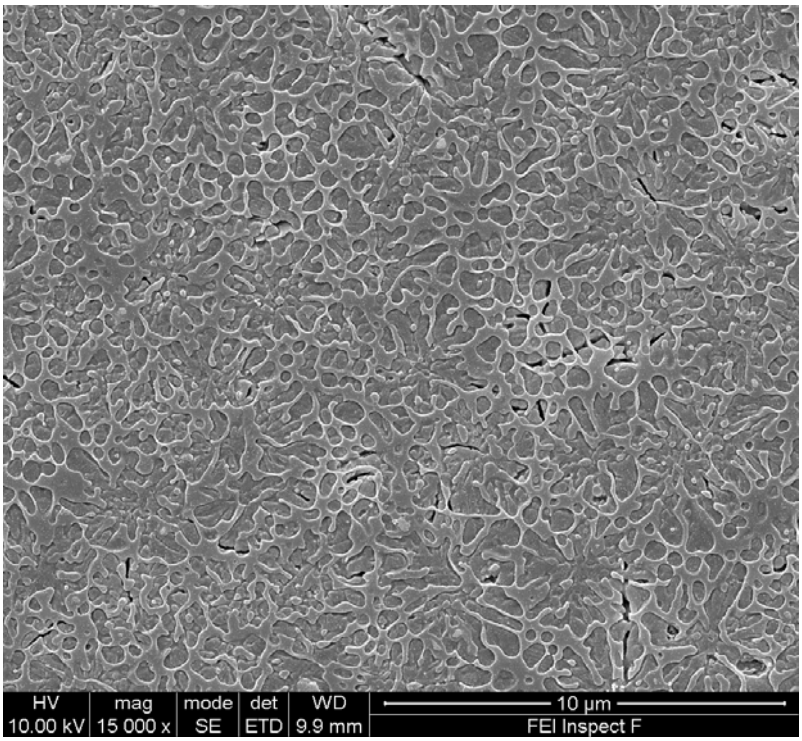

Figure 5.41: SEI of the glass-ceramic BPM0.5 showing a mixed microstructure with agglomerates, fibres and rounded crystal conformations of tetragonal leucite (x 15000).

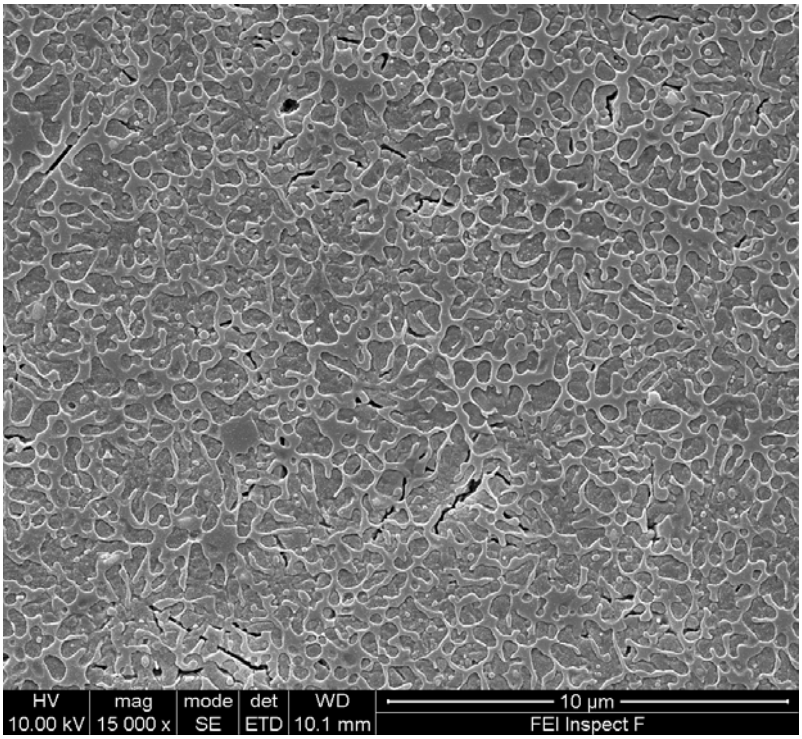

Figure 5.42: SEI of the glass-ceramic BPM1 showing a more uniform but more interconnected microstructure of tetragonal leucite crystals (x 15000).

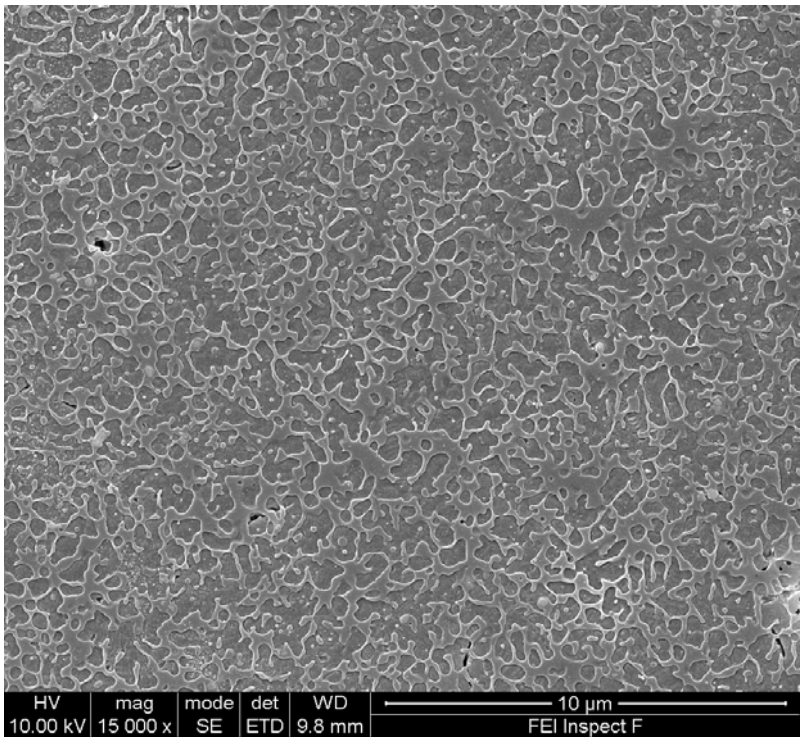

Figure 5.43: SEI of the glass-ceramic BPM2 showing an "embroidery" like interconnected tetragonal leucite crystal structure free of crystal/matrix microcracking (x 15000).

Table 5.7: Crystallisation data for the glass B series.

Milling time (h)	Area fraction (%)	Median Crystal area (µm^2) (Q1,Q3)	Crystal number	Particle Size range (µm^2)	Mean Shape Factor (SD)
0 (glass B)	59.7	0.361^a (0.198,0.695)	423	0.014 – 13.797	0.684 (0.191)
0.5 (BPM0.5)	63.0	0.151^{b,c} (0.066,0.338)	384	0.012 – 14.083	0.654 (0.243)
1 (BPM1)	63.1	0.180^b (0.088,0.495)	380	0.008 – 11.152	0.611 (0.264)
2 (BPM2)	59.7	0.136^c (0.063,0.388)	564	0.008 – 3.716	0.625 (0.246)

Different superscript letters indicate significant differences between groups.

Q1, Q3: 25th and 75th percentiles.

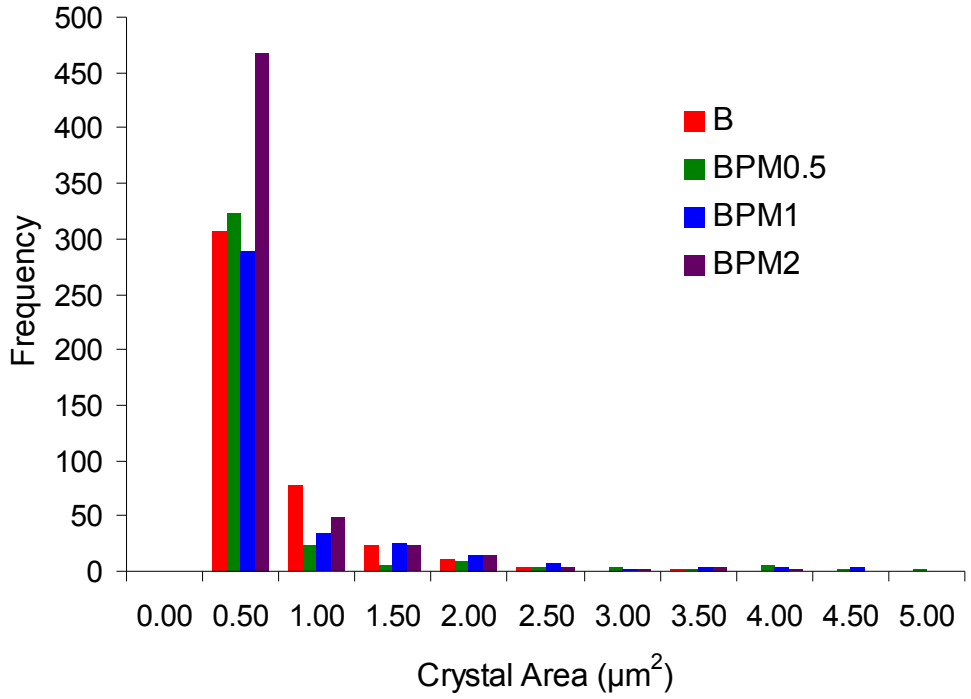

Figure 5.44: Histogram of the crystal area values for the experimental starting and planetary milled B samples showing the positive skew of all distributions.

5.2.3 Results of the SEI study for the B1, B2 and B3 glass-ceramics

The SEI results for the systematic Ca/Ti addition to glass B composition are presented here. The two step heat - treatments of the experimental glasses B1, B2 and B3 at their corresponding maximum crystallisation temperatures, resulted in the microstructures depicted in Figures 5.45 – 5.47. Glass-ceramic B1 (Figure 5.45) demonstrates a largely uniform microstructure, with mostly rounded and few fibre-like tetragonal leucite crystals present. Glass-ceramics B2 (Figure 5.46) and B3 (Figure 5.47) appear to have an increasing fibre-like tetragonal leucite content along with spherulitic and cross shaped structures also being present (Figure 5.48). The crystals appear larger in all dimensions from B1→B2→B3 and this is confirmed by

the crystal measurement results shown in Table 5.8 where the crystal size significantly ($p < 0.001$, ANOVA, Dunn's multiple comparisons test) increases as the content of Ca/Ti in the glass composition increases. Concurrently, the amount of crystals per image area is reduced while the area fraction remains constant.

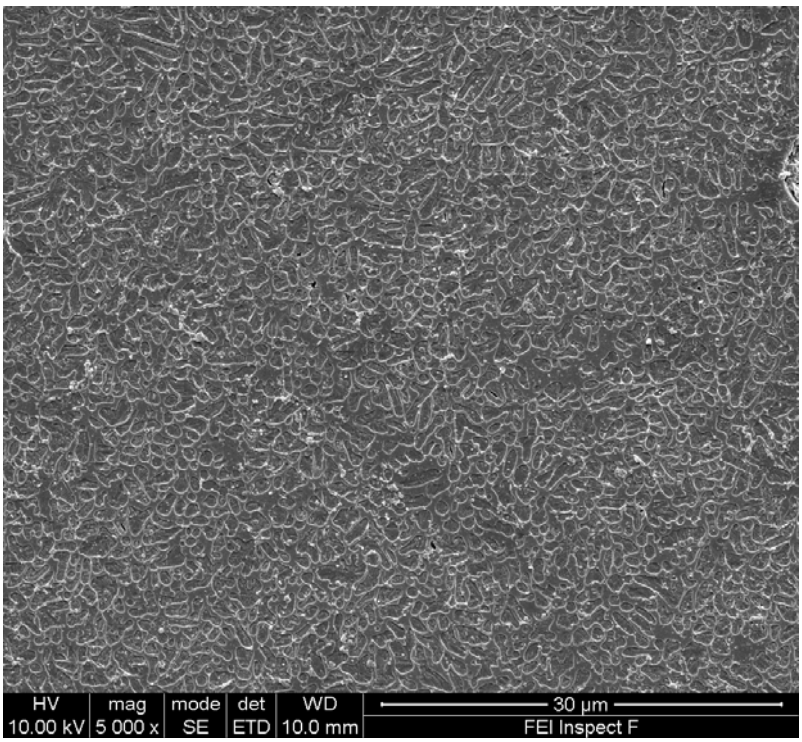

Figure 5.45: SEI of the glass-ceramic B1 (x 5000).

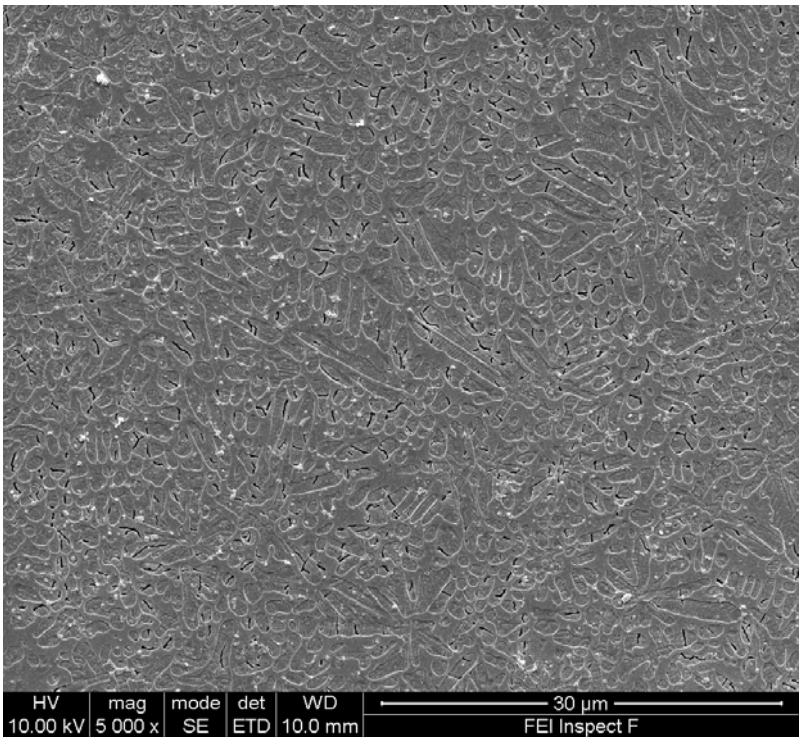

Figure 5.46: SEI of the glass-ceramic B2 with signs of elongated tetragonal leucite crystals (x 5000).

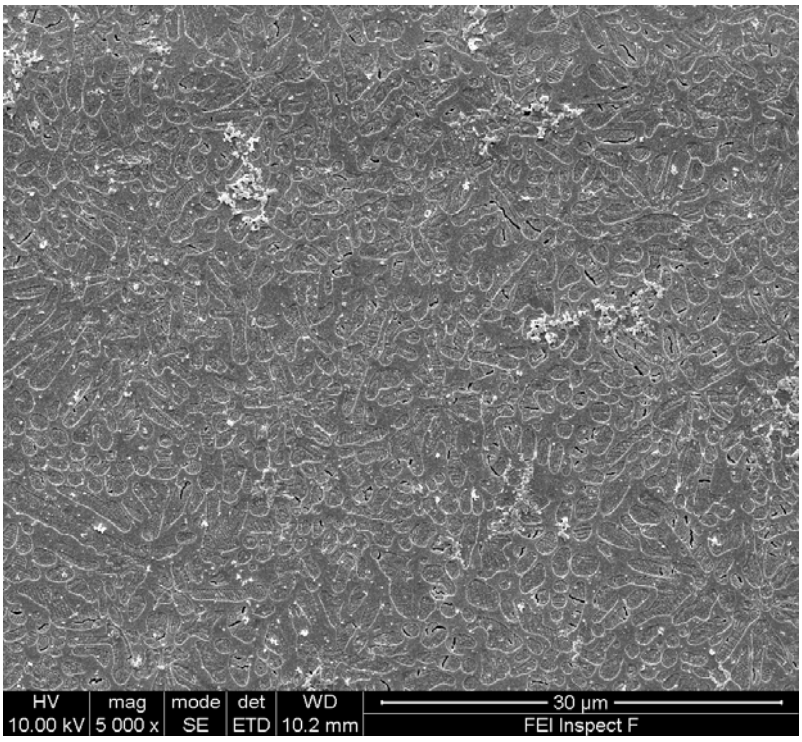

Figure 5.47: SEI of the glass-ceramic B3 showing larger, elongated tetragonal leucite crystals (x 5000).

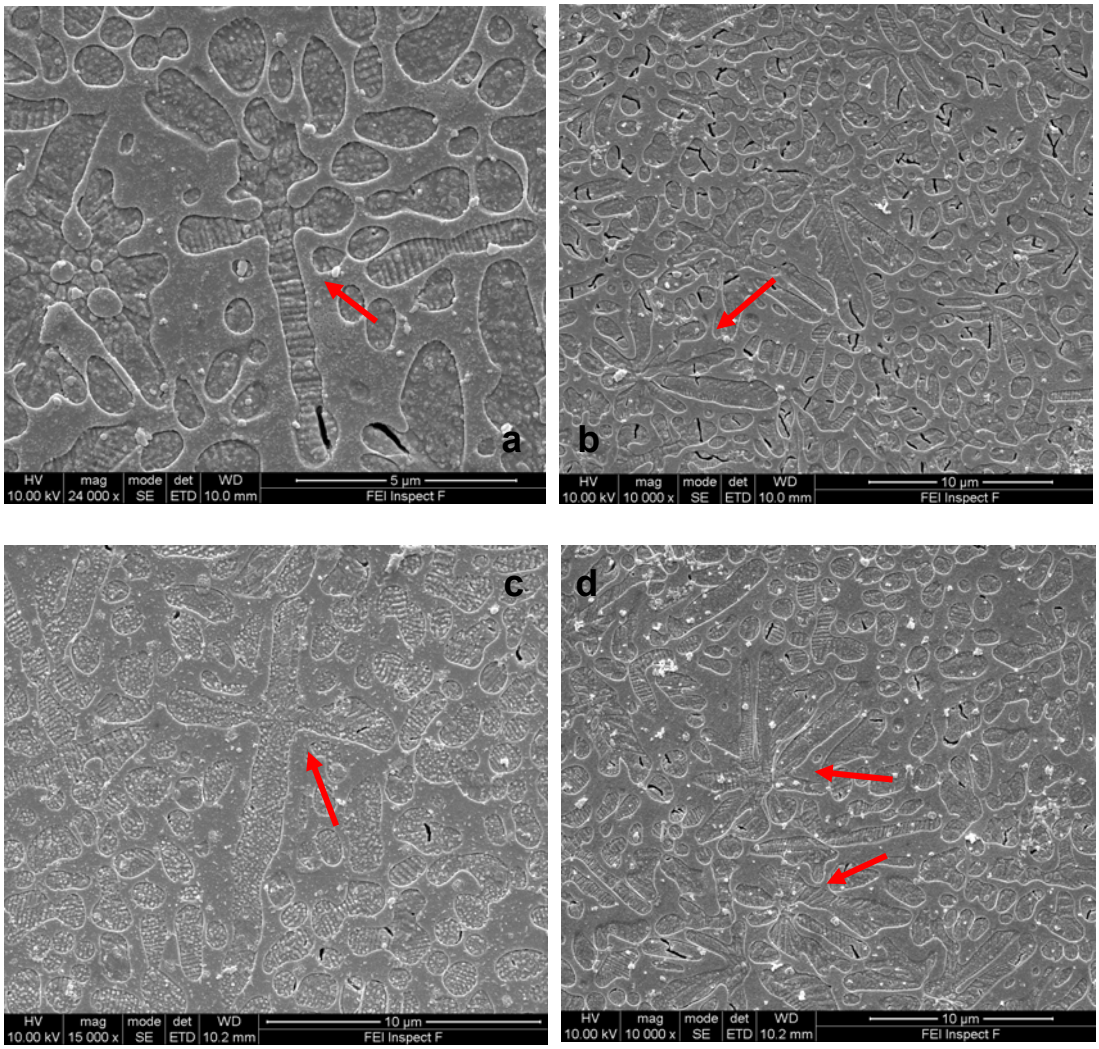

Figure 5.48: Cross-shaped (left) and spherulitic (right) tetragonal leucite structures in the glass-ceramics (a, b) B2 and (c, d) B3.

Table 5.8: Crystallisation data for the glasses B1, B2 and B3.

Glass Ceramic	Area Fraction (%)	Median Crystal area (μm^2) (Q1,Q3)	Crystal Count	Particle Size Range (μm^2)	Mean Shape Factor (SD)
B	59.7	0.361[a] (0.198,0.695)	2985	0.014 – 13.797	0.684 (0.191)
B1	54.6	0.668[b] (0.347,1.371)	1655	0.031 – 7.547	0.686 (0.178)
B2	54.7	0.947[c] (0.542,1.702)	939	0.065 – 27.729	0.704 (0.194)
B3	54.7	1.213[d] (0.664,2.210)	737	0.068 – 32.465	0.695 (0.196)

Different superscript letters indicate significant differences between groups.

Q1, Q3: 25th and 75th percentiles

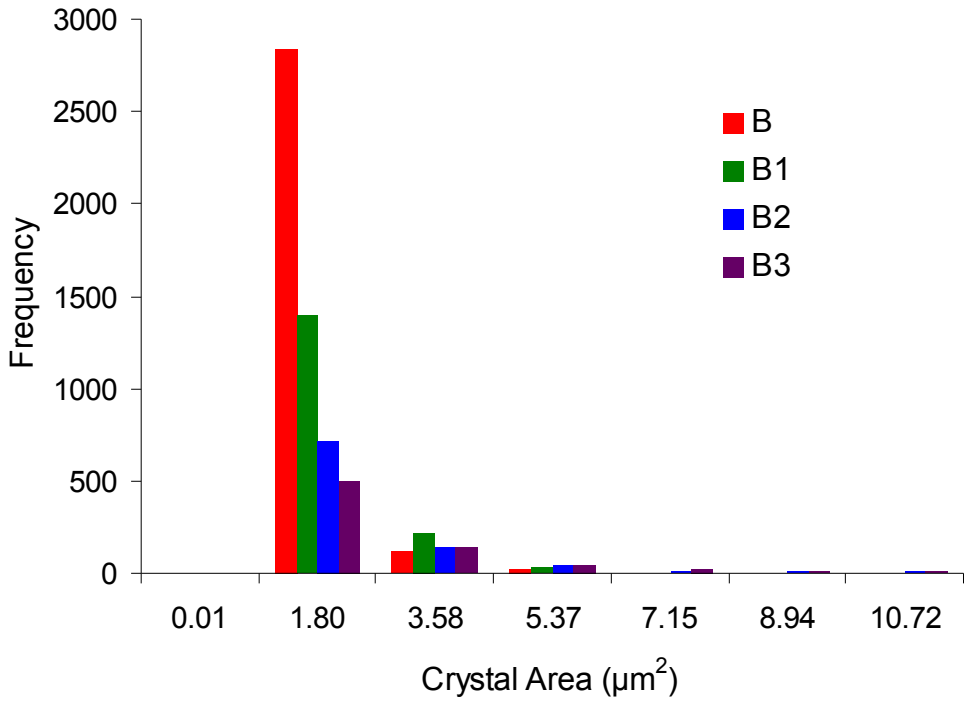

Figure 5.49: Histogram of the crystal area values for the experimental B and B1-B3 glass-ceramics showing the positive skew of all distributions.

5.2.4 Glass-ceramic B4 SEI and crystal measurements results

The results of the SEI for the glass-ceramic B4 specimen are presented in Figures 5.50 and 5.51. Glass-ceramic B4 was found to have a mix of rounded and fibre-like tetragonal leucite crystals dispersed in glassy matrix. The crystallisation data based on quantitative image analysis showed that the glass-ceramic B4 had a lower area fraction, a considerably lower crystal number and a significantly larger ($p < 0.001$) median crystal size than the starting B material (Table 5.9).

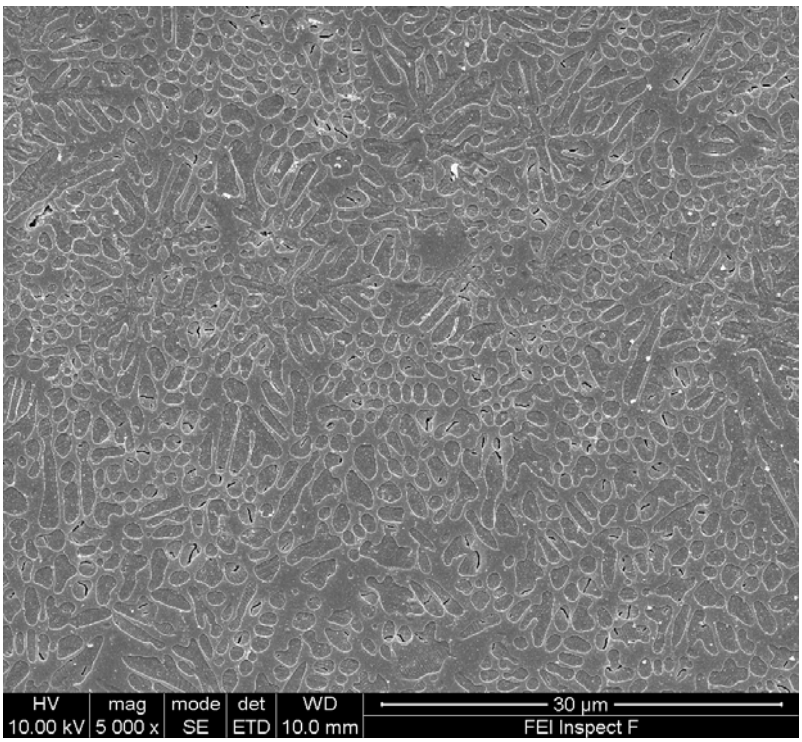

Figure 5.50: SEI of the glass-ceramic B4 showing a mix of rounded, and fibre-like tetragonal leucite crystals dispersed in glassy matrix (x 5000).

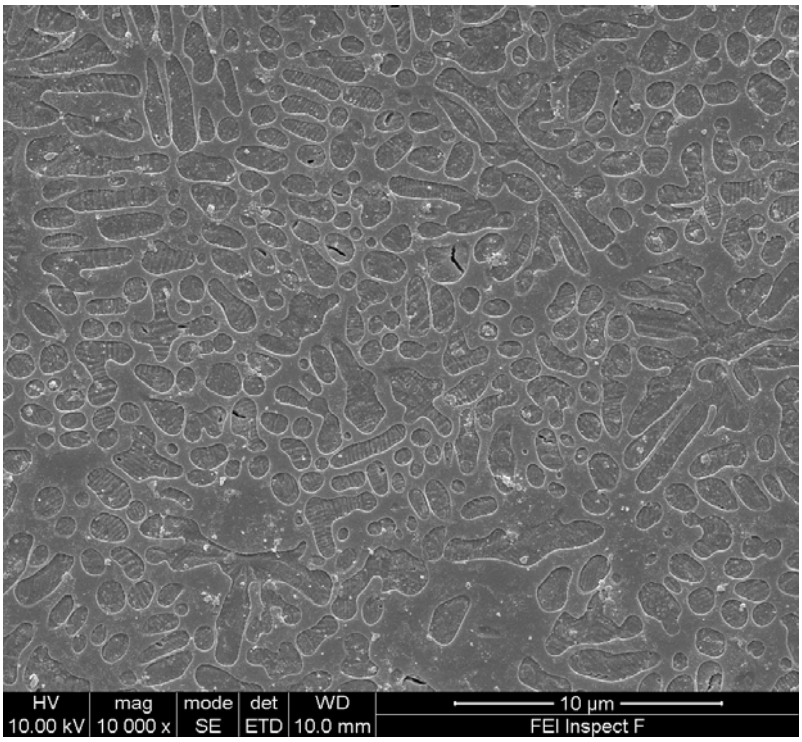

Figure 5.51: SEI of the glass-ceramic B4 (x 10000).

Table 5.9: Crystallisation data for the glass B4.

Glass	Area fraction (%)	Median Crystal area (μm^2) (Q1,Q3)	Crystal number	Particle Size range (μm^2)	Mean Shape Factor (SD)
B	59.7	0.361^a (0.198,0.695)	2986	0.014 – 13.797	0.684 (0.191)
B4	52.5	0.981^b (0.551, 1.730)	909	0.048 – 27.031	0.729 (0.181)

Different superscript letters indicate significant differences between groups.

Q1, Q3: 25th and 75th percentiles.

5.2.5 Glass-ceramic B5 crystal size optimisation results

The results of the SEI for the glass B5 series specimens are presented in Figures 5.52 – 5.57. The starting glass B5 was found to have glassy areas distributed within areas of dense crystalline dispersion (Figure 5.52). The glassy areas in some cases were found to have microcracks (Figure 5.53). The crystalline areas showed varying morphology of tetragonal leucite crystals with dendritic structures, fibres and rounded conformations (Figures 5.53 – 5.55). The high speed milled B5PM0.5 SEI shows the elimination of the glassy areas and microcracking (Figure 5.56) and a uniform distribution of tetragonal leucite crystals (Figure 5.57).

Crystallisation data based on quantitative image analysis of the micrographs is presented in Table 5.10. The median crystal area of the high speed milled two step heat treated B5PM0.5 material was significantly smaller than the starting B5 sample ($p < 0.001$, Dunn's multiple comparisons test) while there was an associated increase in the crystal number and a narrowing of the particle size range. The Histogram in Figure 5.58 shows the positive skewness in the crystal area distributions exhibited in both starting and planetary milled B5 two step heat treated glasses. Starting glass B crystal measurement data is also included for comparison.

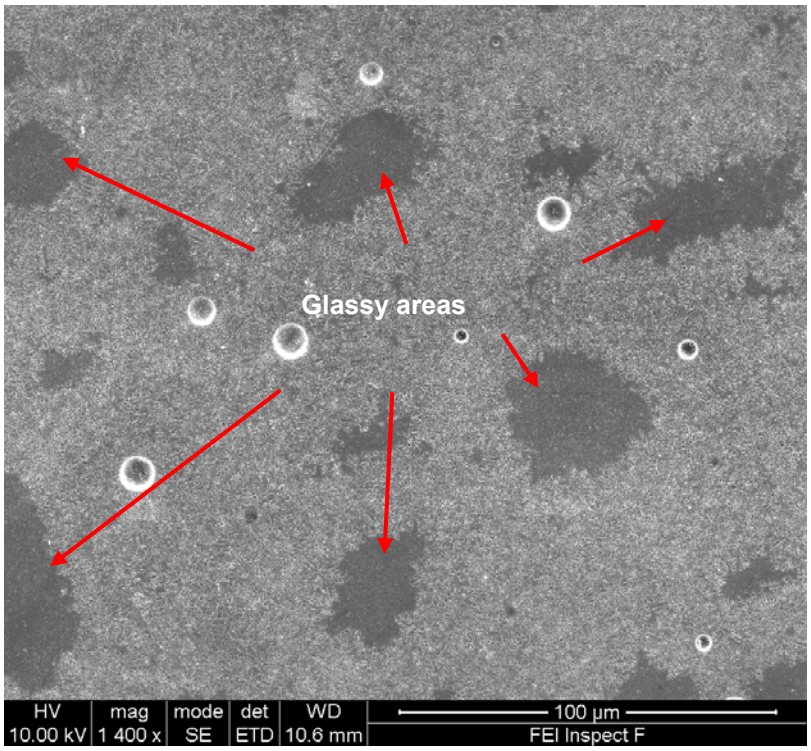

Figure 5.52: SEI of the two step heat - treated starting glass B5 showing distribution of glassy areas within areas of dense crystalline dispersion (x 1400).

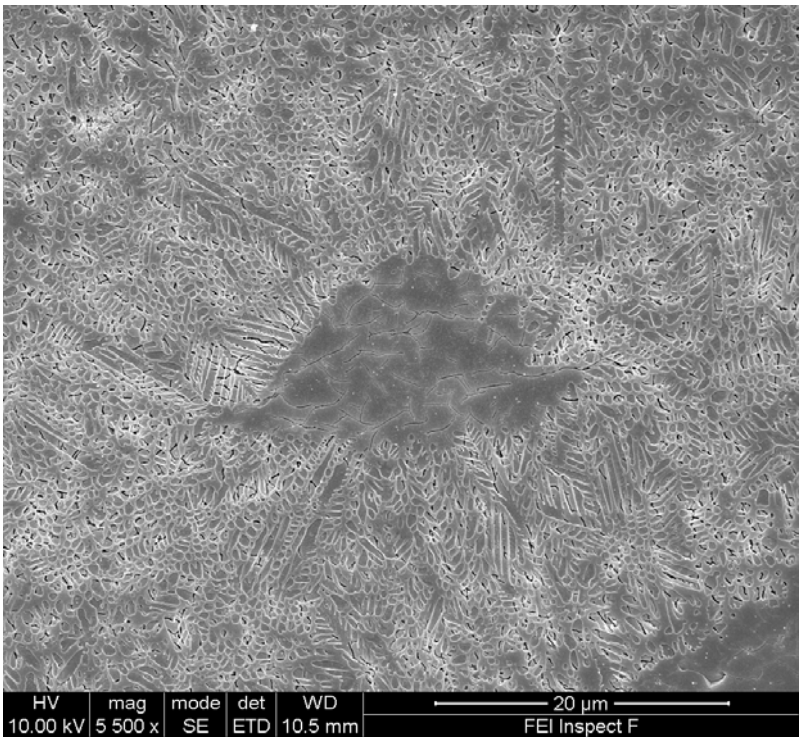

Figure 5.53: SEI of the two step heat - treated starting glass B5 showing a glassy area with microcracks and dendritic, fibre-like and rounded leucite crystals (x 5500).

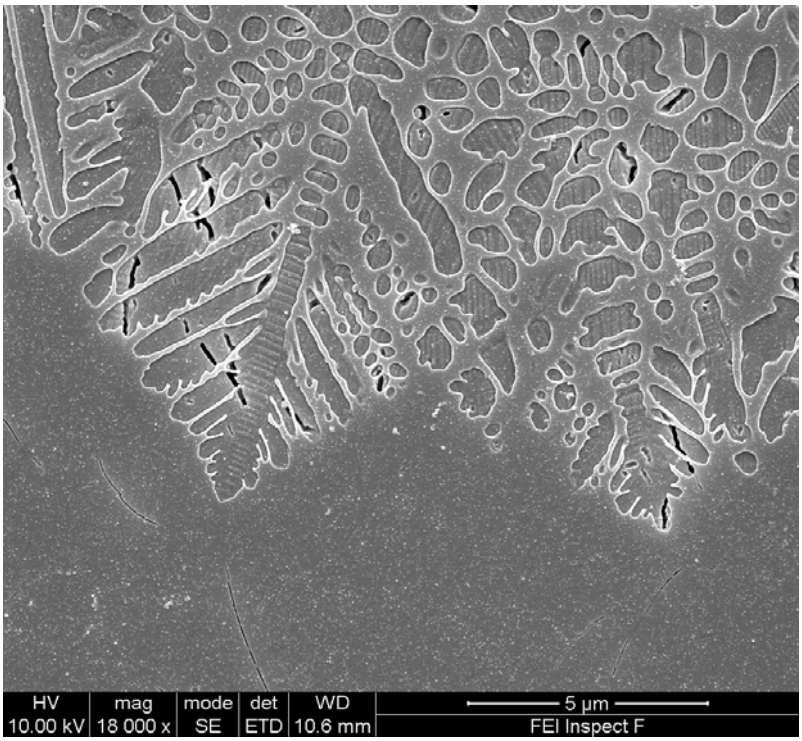

Figure 5.54: High magnification SEI of the dendritic tetragonal leucite structures in the two step heat - treated glass B5 (x 18000).

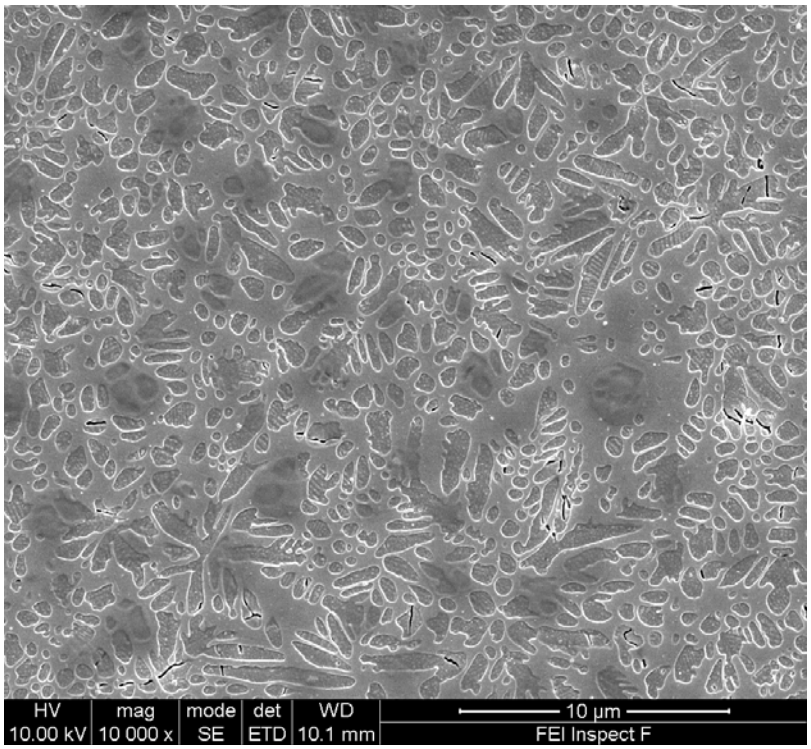

Figure 5.55: SEI of the starting two step heat - treated glass B5 showing dendritic structures, fibres and rounded conformations of tetragonal leucite crystals (x 10000).

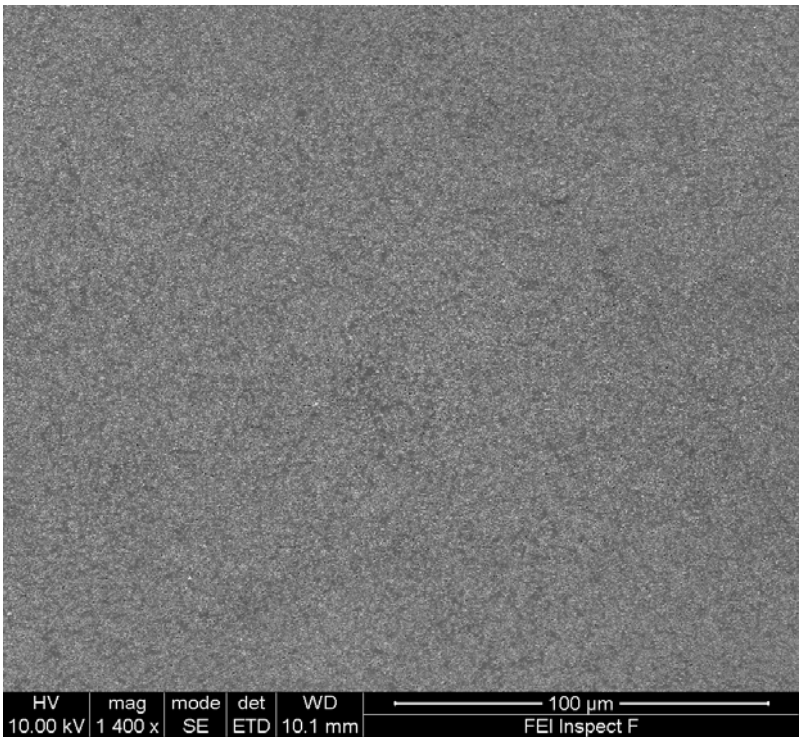

Figure 5.56: SEI of the two step heat - treated glass B5PM0.5 showing elimination of the glassy areas (x 1400).

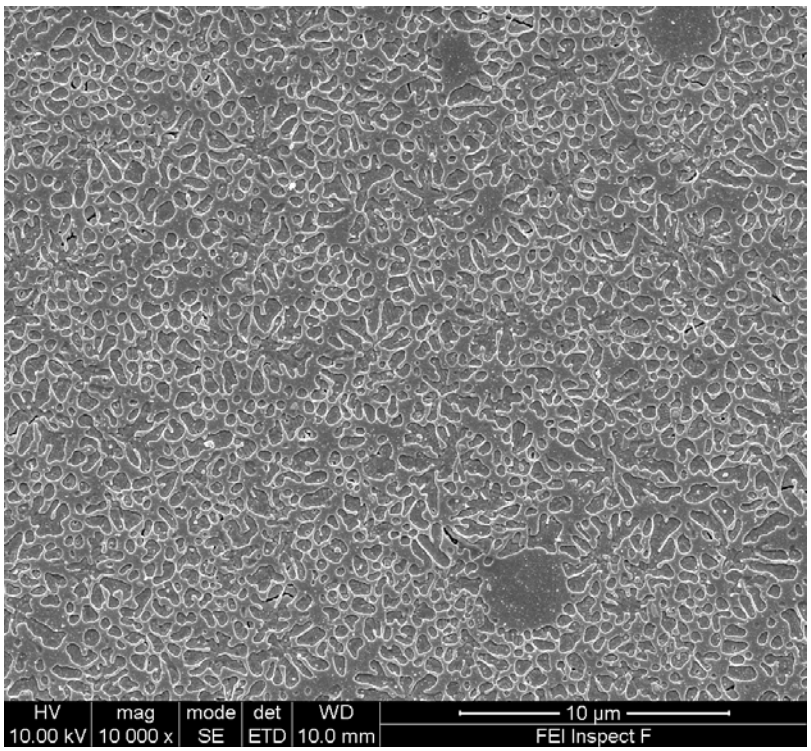

Figure 5.57: SEI of the two step heat - treated glass B5PM0.5 showing a dense, homogenised structure (x 10000).

Table 5.10: Crystallisation data for the glass B5 series.

Glass Ceramic	Area fraction	Median Crystal area (μm^2) (Q1,Q3)	Crystal number	Particle Size range (μm^2)	Mean Shape Factor (SD)
B	59.7	0.361^a (0.198,0.695)	423	0.014 – 13.797	0.684 (0.191)
B5	45.4	0.262^b (0.121,0.556)	319	0.017 – 13.422	0.704 (0.182)
B5PM0.5	49.7	0.164^c (0.087,0.295)	518	0.008 – 6.338	0.694 (0.193)

Different superscript letters indicate significant differences between groups.

Q1, Q3: 25th and 75th percentiles.

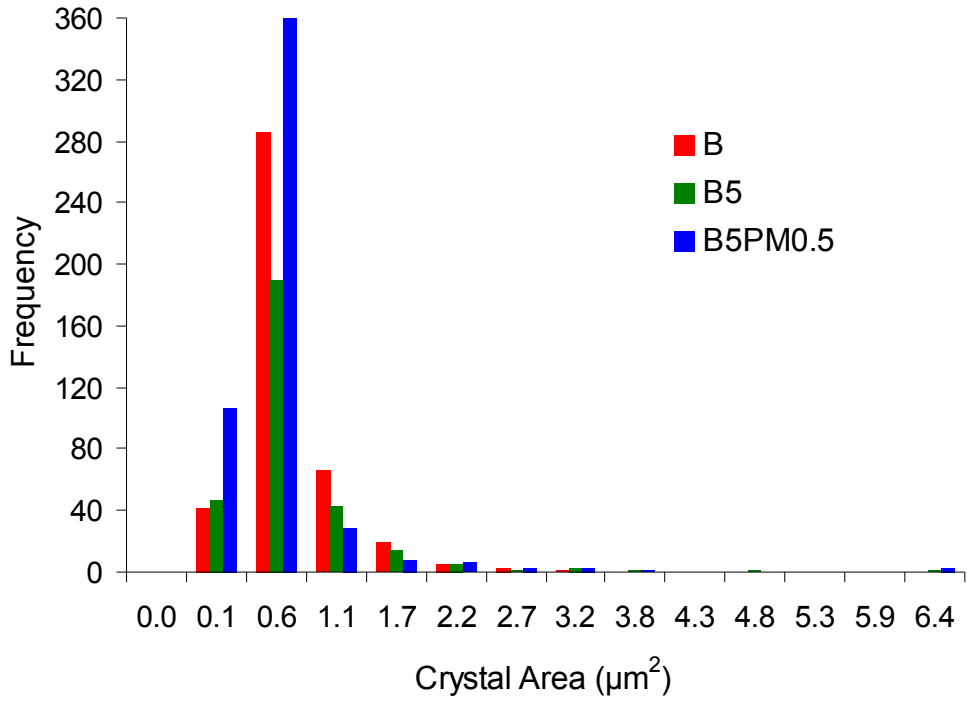

Figure 5.58: Histogram of the crystal area values for the experimental starting B, B5 and the planetary milled B5 samples showing the positive skew of all distributions.

5.2.6 SEI comparison of optimised B and B5 glass-ceramics

The crystal size optimised two step heat treated B, B5 series of glasses from the previous sections (5.2.2 and 5.2.3) are collectively compared here. The B5 group (Figure 5.60) shows reduced area fraction and crystal interconnectivity when compared to the B counterparts (Figure 5.59).

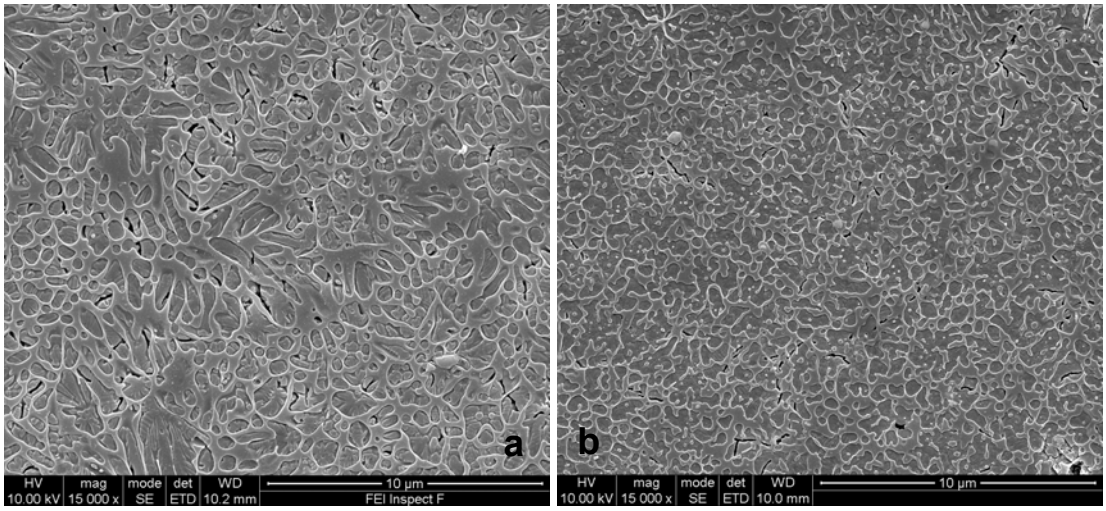

Figure 5.59: SEI of the (a) glass-ceramic B and (b) glass-ceramic BPM2. A high tetragonal leucite area fraction is present in both materials while BPM2 presents an interconnected crystal structure (x 15000).

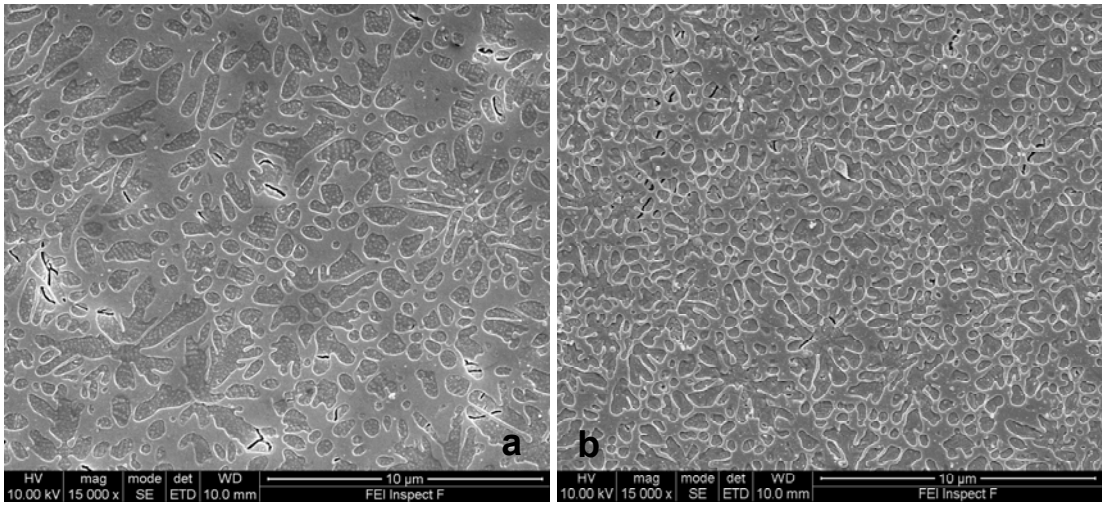

Figure 5.60: SEI of the (a) glass-ceramic B5 and (b) glass-ceramic B5PM0.5. Reduced tetragonal leucite area fraction and crystal interconnectivity is evident in both materials in comparison to the B and BPM2 materials (x 15000).

5.2.7 Glass-ceramic C crystal size optimisation results

The results of the SEI for the glass-ceramic C series specimens are presented in Figures 5.61 – 5.63. The two step heat - treated glass C was found to have a mix of rounded and elongated tetragonal leucite crystals dispersed in glassy matrix (Figures 5.61, 5.62) and signs of predominantly crystal microcracking (Figure 5.63). The two step heat - treated high speed milled CPM0.5 was characterised by the lack of fibre-like tetragonal leucite crystals (Figure 5.65). Only rounded crystals were found to be dispersed in a microcrack free glassy matrix. Based on the quantitative image analysis results in Table 5.11, the crystal number of the high speed milled C material doubled within the 0.5 h milling time, while the median crystal area was significantly smaller than the starting C material ($p<0.001$, Dunn's multiple comparisons test). The histogram in Figure 5.66 shows the positive skewness in the crystal area distributions exhibited in both starting and planetary milled C two step heat treated glasses.

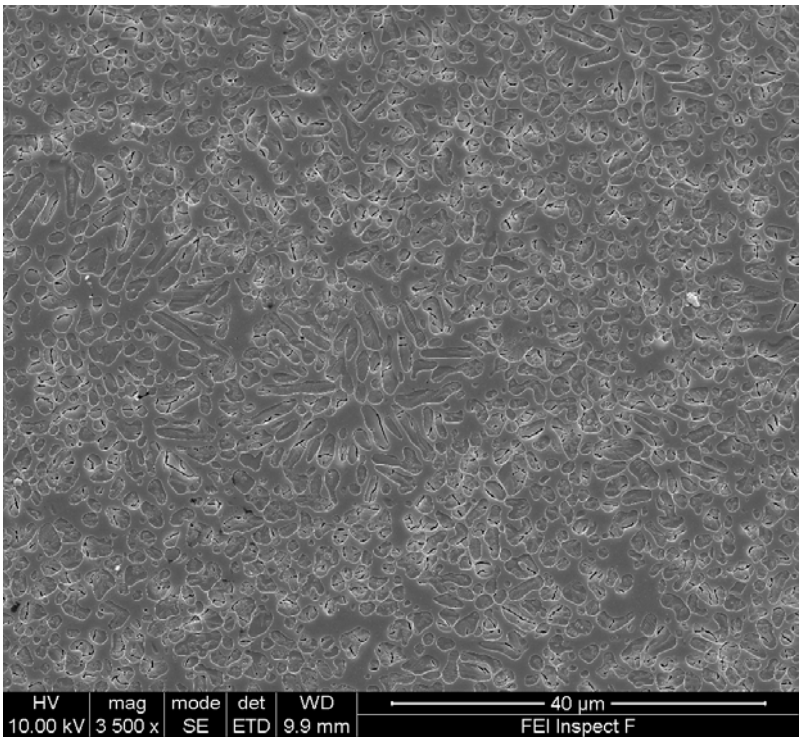

Figure 5.61: SEI of the two step heat - treated glass C showing a mix of rounded and elongated tetragonal leucite crystals dispersed in glassy matrix (x 3500).

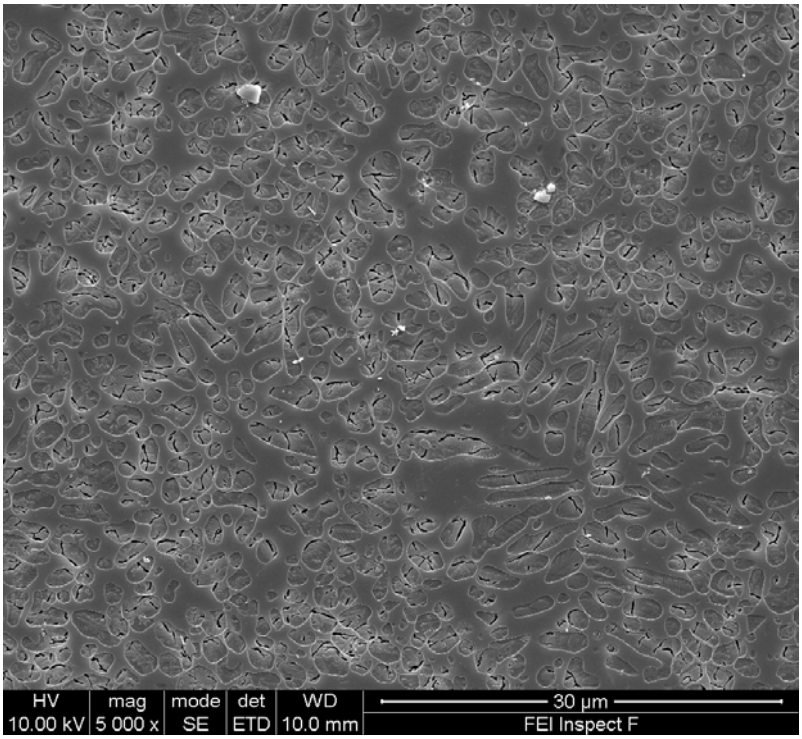

Figure 5.62: SEI of the two step heat - treated glass C showing a mix of rounded and elongated tetragonal leucite crystals dispersed in glassy matrix (x 5000).

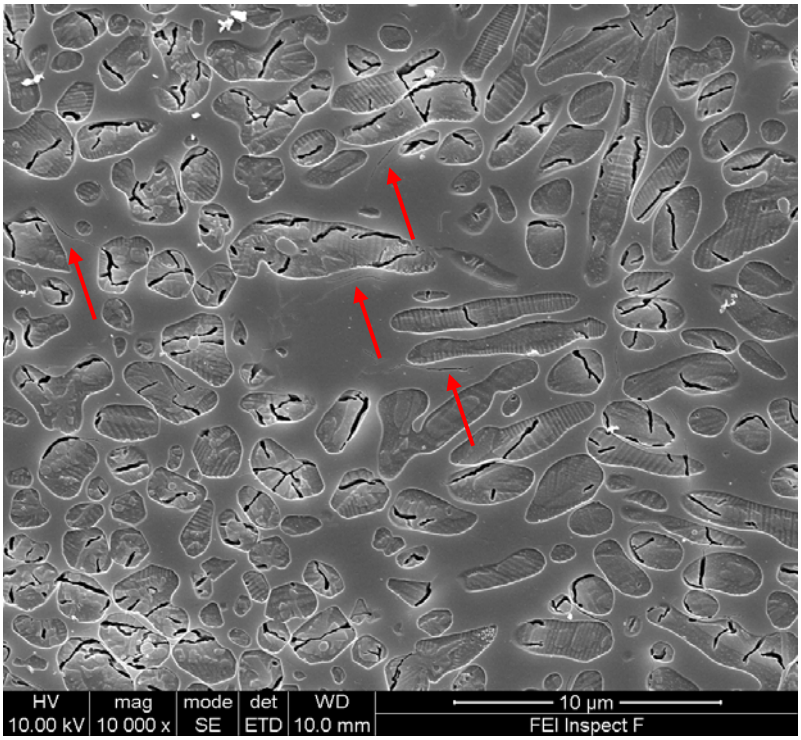

Figure 5.63: SEI (magnified detail from Figure 5.62) of the two step heat - treated glass C showing some elongated crystals and signs of microcracking (x 10000).

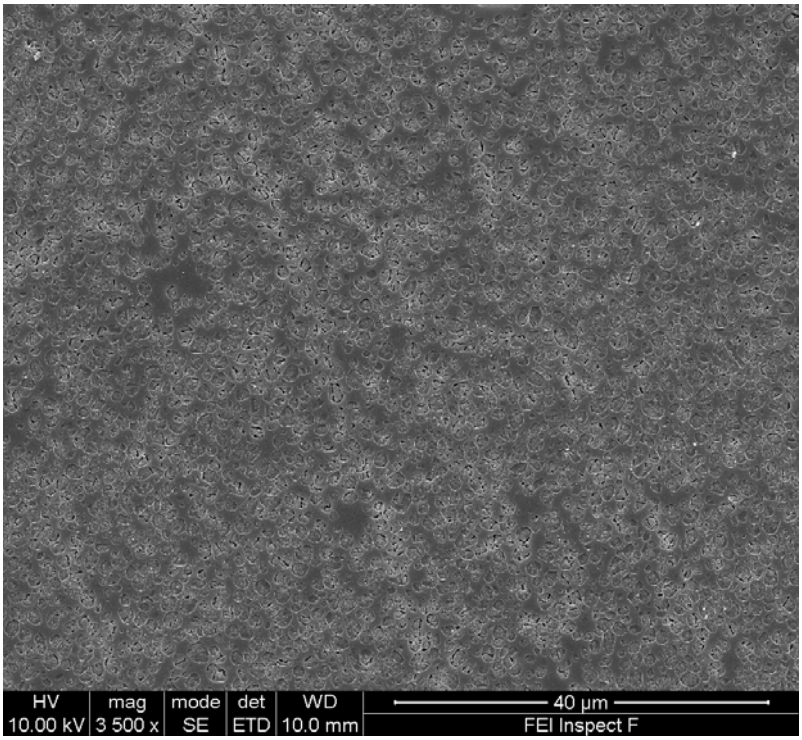

Figure 5.64: SEI of the two step heat - treated glass CPM0.5 showing an even distribution of fine, rounded tetragonal leucite crystals (x 3500).

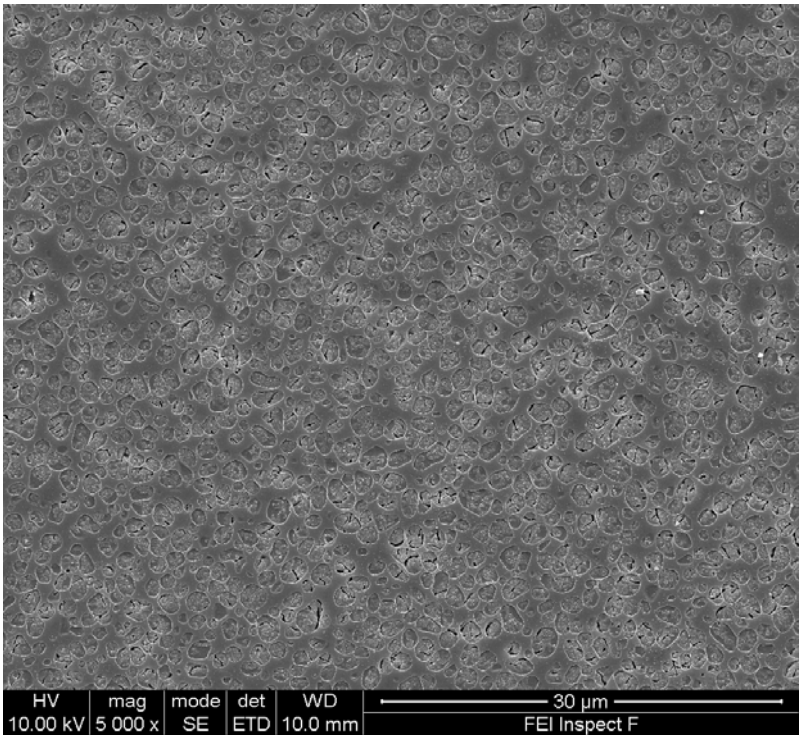

Figure 5.65: SEI of the two step heat - treated glass CPM0.5 showing an even distribution of fine, rounded tetragonal leucite crystals (x 5000).

Table 5.11: Crystallisation data for the glass C series.

Milling time (h)	Area fraction (%)	Median Crystal area (μm^2) (Q1,Q3)	Crystal number	Particle Size range (μm^2)	Mean Shape Factor (SD)
Feed (glass C)	54.0	1.843^a (0.883,3.376)	629	0.044 – 21.145	0.723 (0.152)
0.5 (PM 0.5)*	55.9	1.114^b (0.600,1.774)	1307	0.048 – 6.162	0.804 (0.117)

Different superscript letters indicate significant differences between groups.

Q1, Q3: 25th and 75th percentiles.

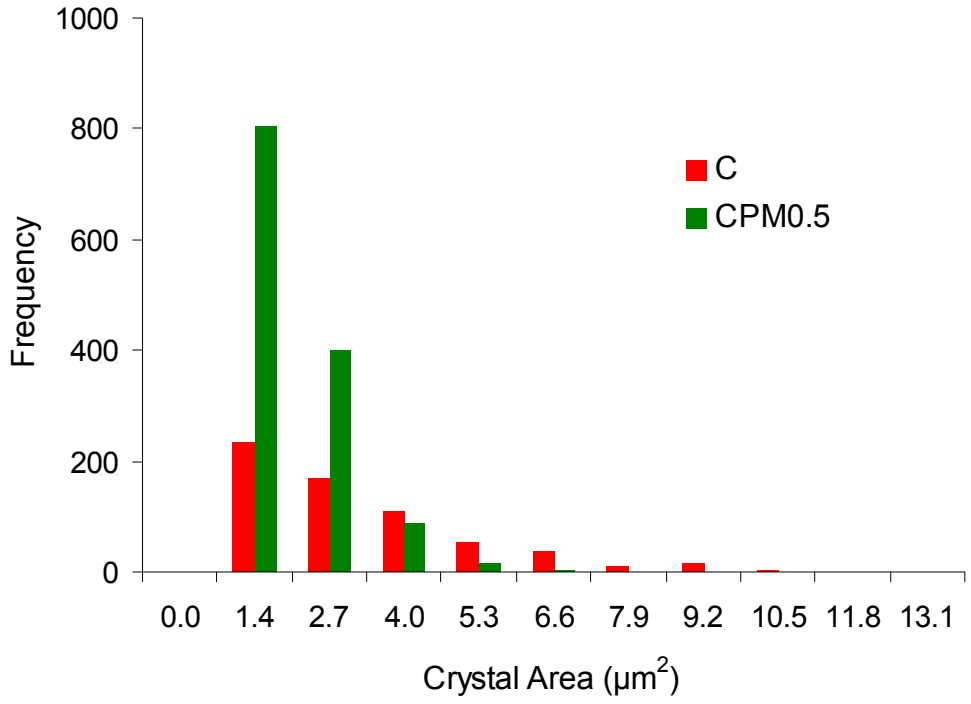

Figure 5.66: Histogram of the crystal area values for the experimental starting and planetary milled C samples showing the positive skew of both distributions.

5.3 Ion-exchange experiments results

5.3.1 Ion-exchange of starting glass A results

5.3.1.1 FTIR Result

Figure 5.67 shows the attenuated total reflectance transmission FTIR spectra for the washed glass A/KNO_3 (red line), glass A/H_2O (blue line) powders and the 1M KNO_3 solution (green line). The trough at 1346.73 cm^{-1} of the 1M KNO_3 solution was associated with the presence of NO_3^- (Grube et al., 2006). There was no trough detected for NO_3^- in the washed glass A/KNO_3 and glass A/H_2O powders. The washing was thus considered efficient in terms of KNO_3 removal. Water associated bands were found in all tested samples in the typical regions 3000 - 3800 cm^{-1}, 1900 - 2400 cm^{-1} and 1550 - 1750 cm^{-1} (Venyaminov and Prendergast, 1997).

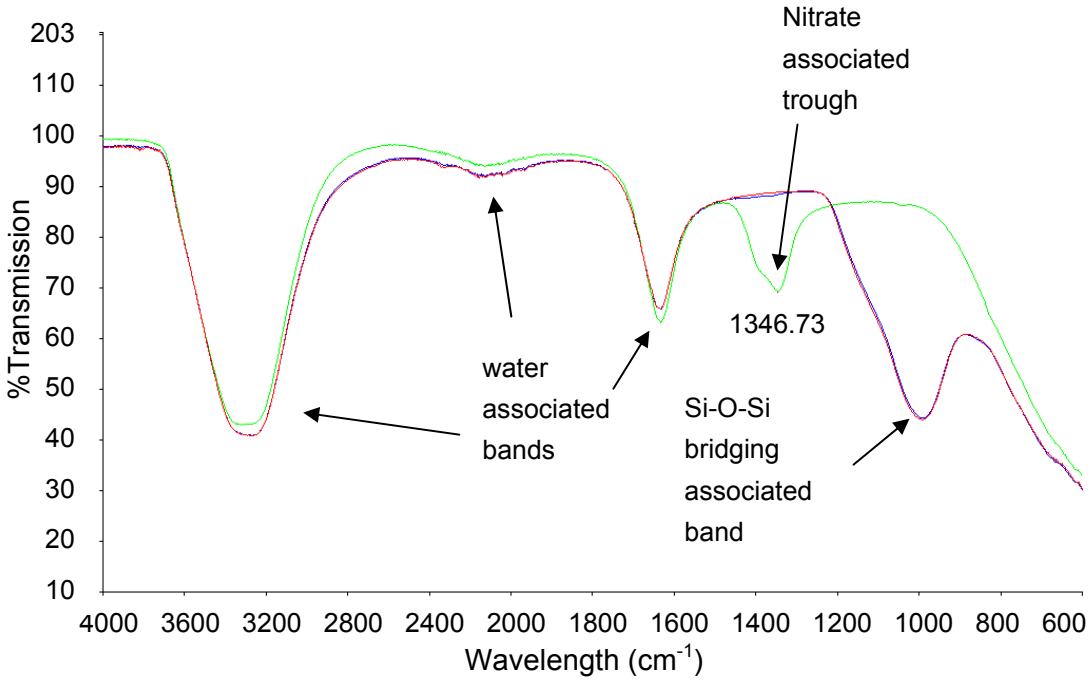

Figure 5.67: FTIR spectra for the washed glass A/KNO_3 (red) and glass A/H_2O (blue) powders and the 1M KNO_3 solution (green).

5.3.1.2 Ion-exchange Chromatography results

Figure 5.68 shows the calibration curves for K^+ and Na^+ as generated by the ion-exchange chromatography (IEC) module using the prepared standards. The IEC quantitative elemental concentration results for the glass A, the glass A/KNO_3 and the glass A/H_2O are found in Table 5.12. The potassium content of the control glass A was very close to the expected value of 452 ppm (calculated assuming 10.9% K_2O in the glass A powder). The sodium content of the control glass A is reduced in relation to the expected 159 ppm (calculated assuming 4.3% Na_2O in the glass A powder). The results for both glass A/KNO_3 and glass A/H_2O digested samples showed a reduction in both K^+ and Na^+ concentrations compared to the control glass A. The lowest value for K^+ was recorded for the glass KNO_3 sample.

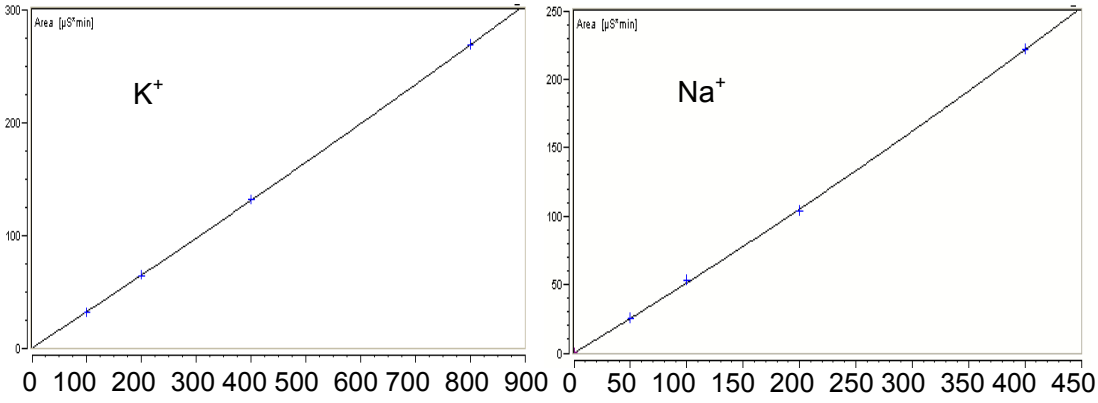

Figure 5.68: Calibration curves for K^+ and Na^+ as generated by the ion-exchange chromatography module using the prepared standards.

Table 5.12: Ion-exchange chromatography results.

	K (ppm)	**Na (ppm)**
Glass A	447.17	138.00
Glass H_2O	402.38	70.18
Glass KNO_3	302.25	81.52

5.3.2 Ion-exchange of glass-ceramic A-AM1.5

The SEI results of the H_2O, Rb and A-AM1.5 (control) samples are shown in Figures 5.69 – 5.71. The SEI of the control sample (Figure 5.69) shows the presence of fine leucite crystals dispersed in glassy matrix. Both planetary milled samples (H_2O and Rb), also show the presence of a distribution of white particles (Figures 5.70 and 5.71). The XRD showed the presence of tetragonal leucite (ICDD: 00-038-1423) in all samples while tetragonal zirconia (ICDD: 50-1089) was also found in both milled samples (Figure 5.76). The EDS analysis of the areas in sample H_2O (Figure 5.72) and Rb (Figure 5.73) showed the presence of zirconium (Figures 5.74, 5.75 and Table 5.13). The Rubidium sample also had Rb^+ present and a concurrent reduction of the K^+ and Na^+ content when compared to the H_2O sample.

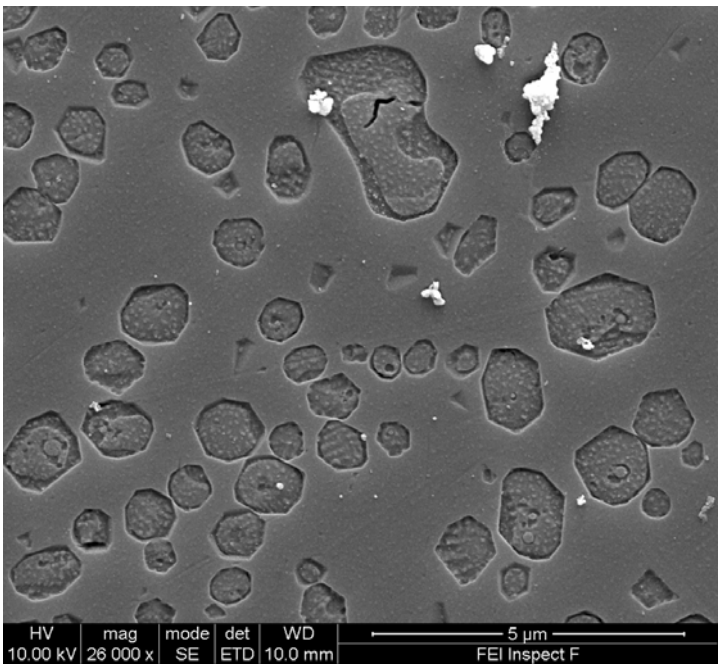

Figure 5.69: SEI of the A-AM1.5 control glass ceramic sample.

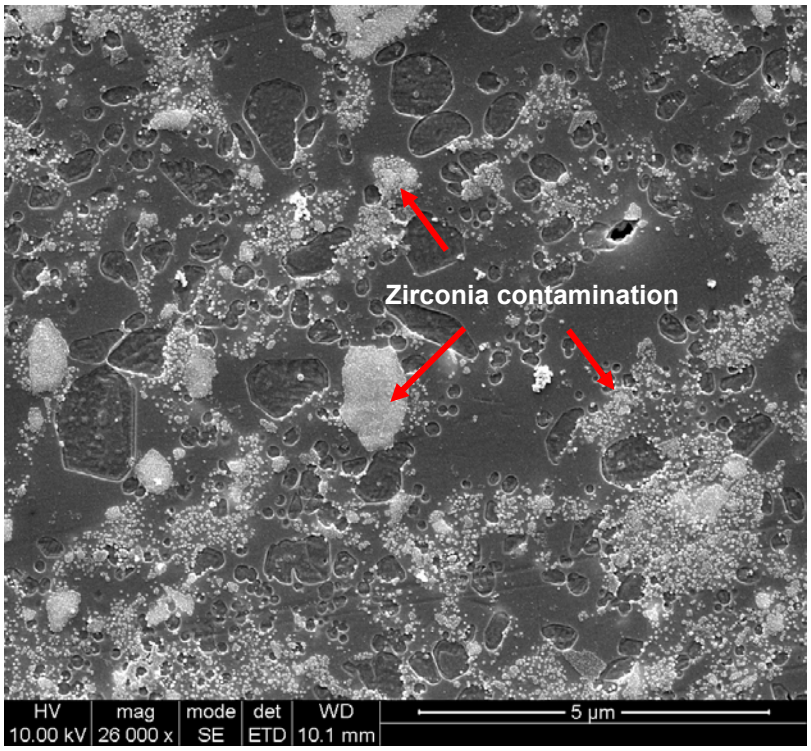

Figure 5.70: SEI of the H_2O exchange glass-ceramic sample showing the presence of tetragonal leucite crystals and particulate zirconia contamination.

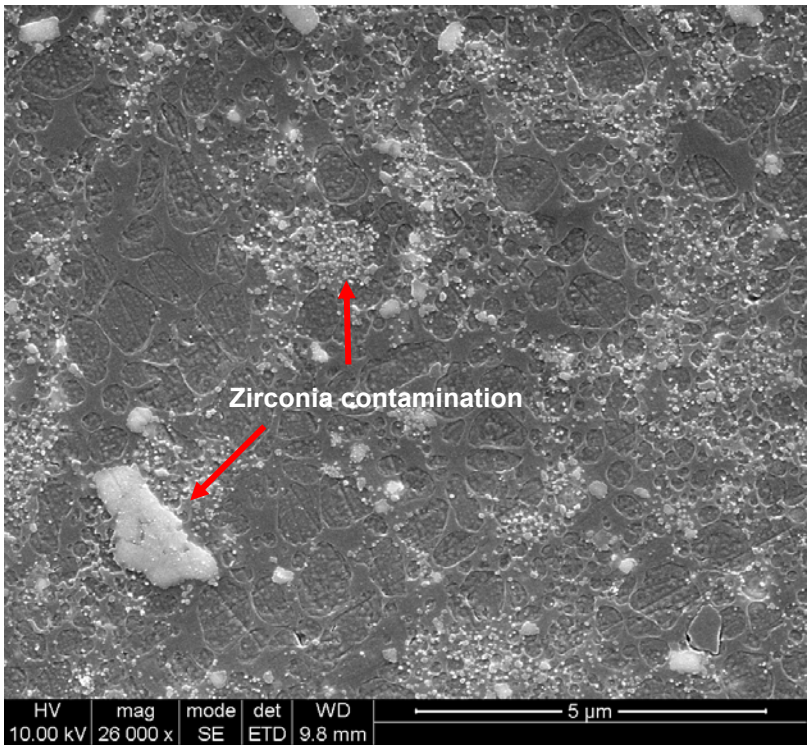

Figure 5.71: SEI of the Rb exchange glass-ceramic sample showing the presence of tetragonal leucite crystals and particulate zirconia contamination.

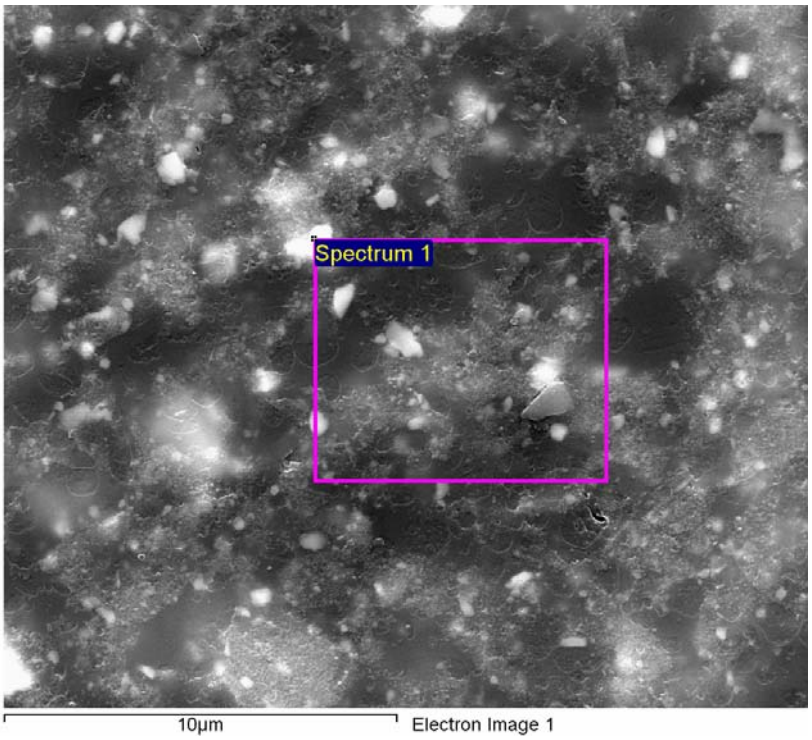

Figure 5.72: Area on the H_2O sample analysed with EDS at 30 KV.

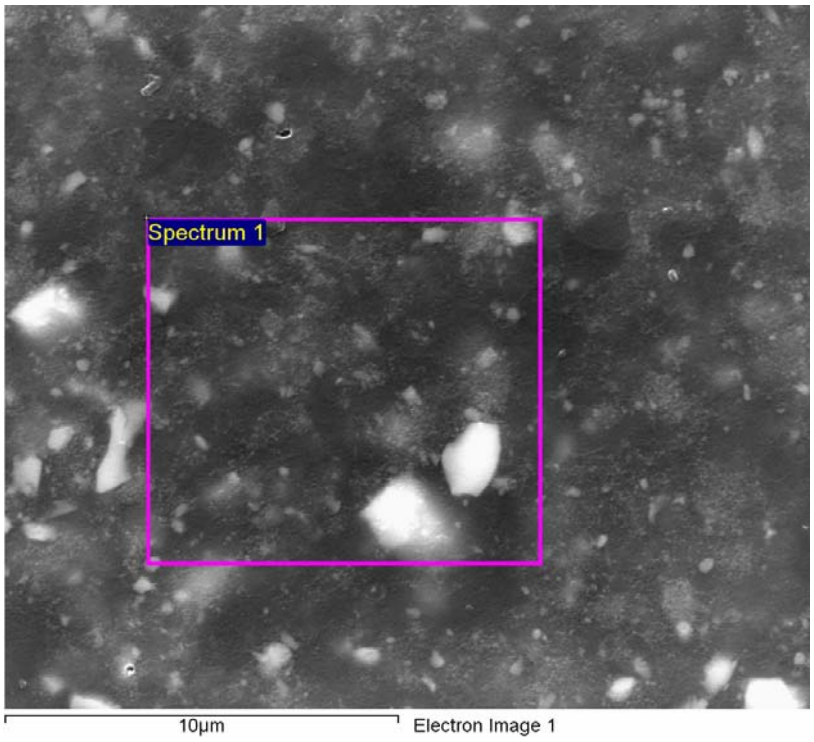

Figure 5.73: Area on the Rb sample analysed with EDS at 30 KV.

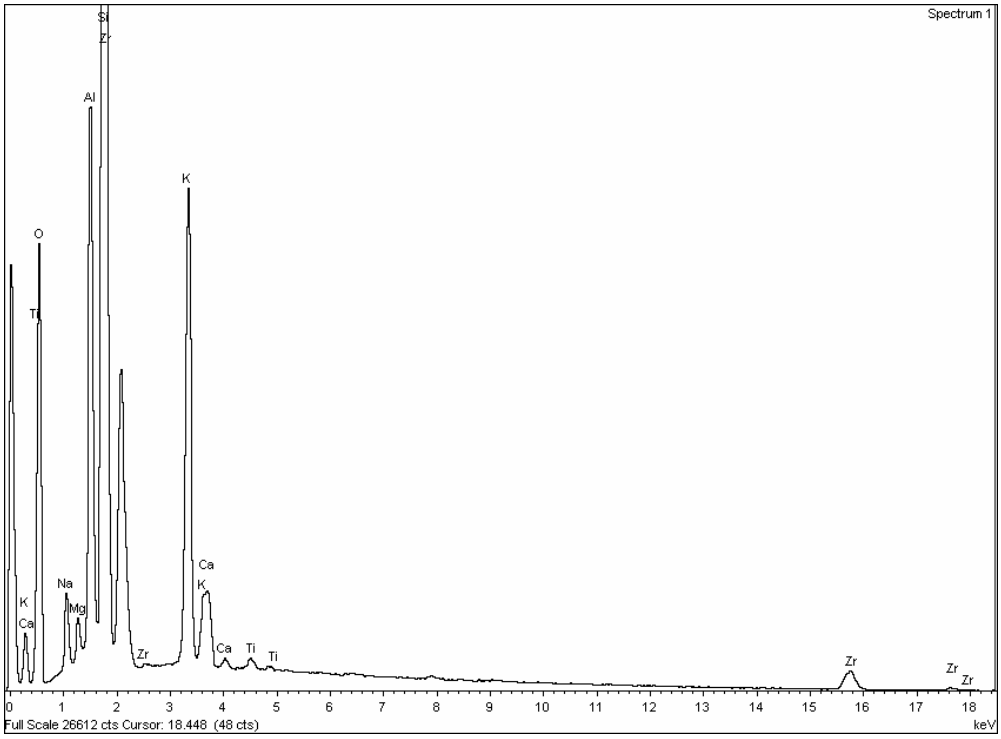

Figure 5.74: Spectrum of the area analysed on the H_2O sample showing peaks for zirconium present.

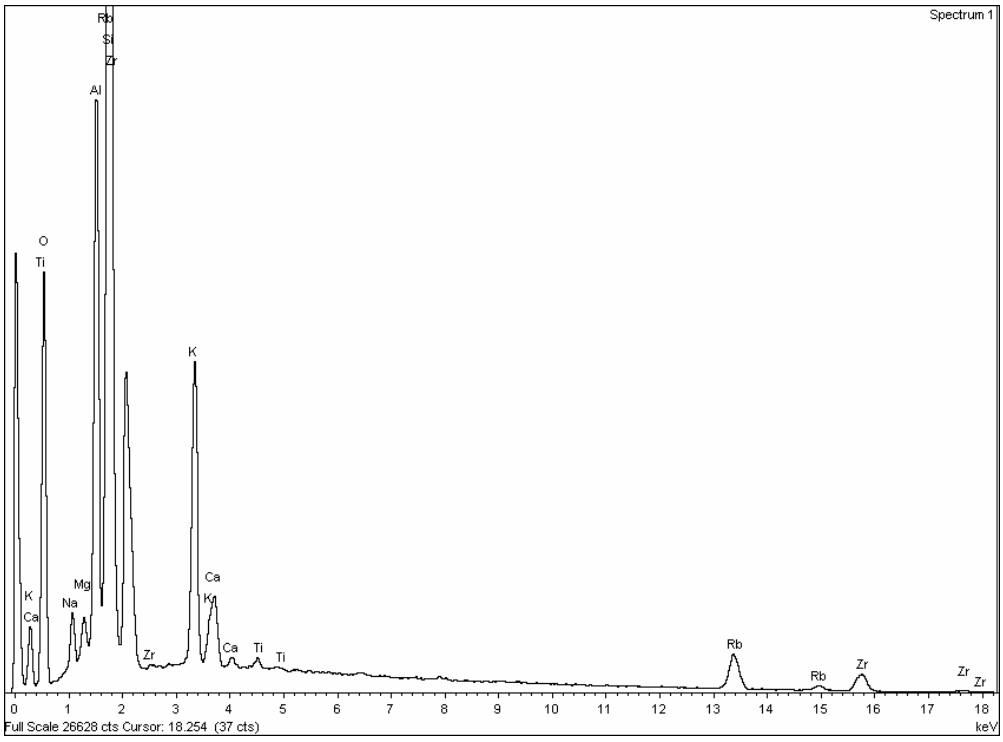

Figure 5.75: Spectrum of the area analysed on the Rb sample showing peaks for zirconium and rubidium present.

Table 5.13: Elemental analysis of the Rb Exchange samples.

	H_2O	Rb
Element	Atomic %	Atomic %
O K	67.63	66.94
Na K	1.91	1.38
Mg K	0.63	0.55
Al K	5.32	5.25
Si K	17.44	17.83
K K	3.75	2.58
Ca K	0.54	0.54
Ti K	0.07	0.08
Zr L	2.70	2.98
Rb K	-	1.87
Totals	100.00	100.00

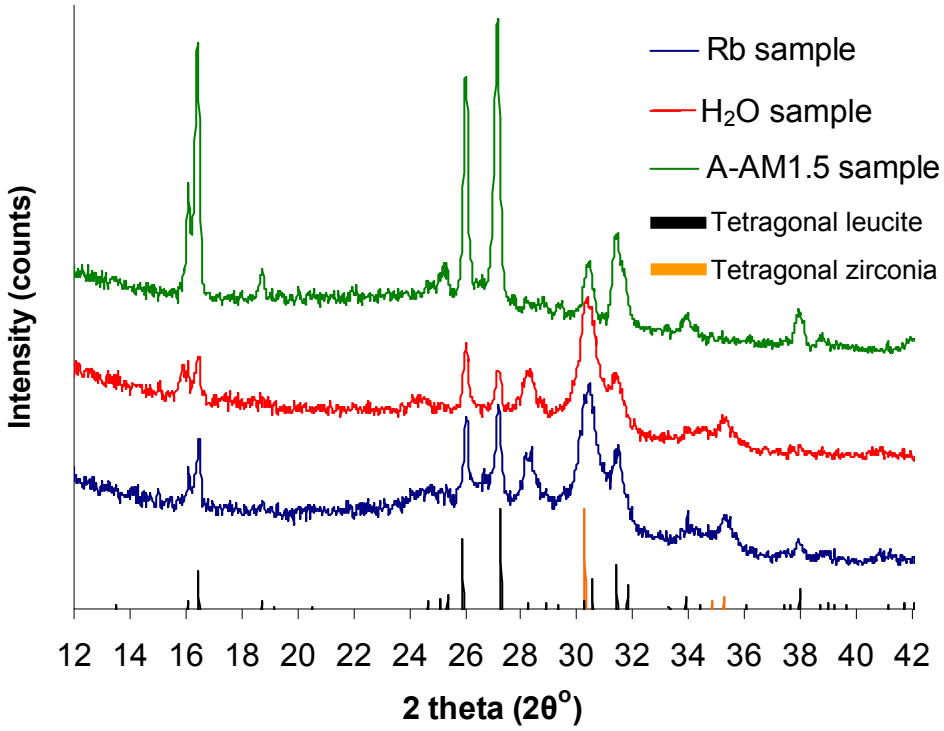

Figure 5.76: XRD plots of the glass-ceramic samples A-AM1.5, Rb and H_2O.

5.4 Biaxial Flexural Strength testing results

The biaxial flexural strength testing results of all experimental glass-ceramic groups were compared to two commercial reference glass-ceramics: the IPS Empress Esthetic (Ivoclar-Vivadent) (results from Chen, 2009, personal communication) and Ceramco 3 (Dentsply, UK). All the strength test data were analysed using ANOVA on ranks (F test; $p < 0.001$). The differences in the median ranks were found to be highly significant ($p \leq 0.001$). The significant differences were next identified by performing multiple comparisons tests (Student-Newman-Keuls method, $p > 0.05$).

5.4.1 Glass-ceramics A series BFS results

The biaxial flexural strength testing results of the A series of glass-ceramics are shown in Tables 5.14 and 5.15. The IPS Empress Esthetic glass-ceramic had a statistically higher median biaxial flexural strength than the Ceramco 3 material glass-ceramic ($p < 0.05$). Both commercial glass-ceramic groups were found to have significantly ($p < 0.05$) lower median biaxial flexural strength than all experimental A series glass-ceramics in Table 5.14. There was no significant difference ($p > 0.05$) found between the APM2 HP and APM4 glass-ceramics, they were however both significantly ($p < 0.05$) different from the A-AM4 HP and APM2 glass-ceramics. The A-AM4 HP and APM2 glass-ceramics were also found to have the highest median BFS and were not significantly ($p > 0.05$) different from each other. The same significant differences that were identified for the median BFS were found for the characteristic strength values according to the overlap of the double sided confidence intervals amongst the tested groups. Ceramco 3 had the highest

Weibull m value compared to the test groups ($p < 0.05$), except for the A-APM4 glass-ceramic ($p > 0.05$) according to the overlap of the double sided confidence intervals. Weibull m values for A-APM4 HP, APM2 groups were not significantly different ($p > 0.05$). All other groups tested (IPS Empress Esthetic, APM2 HP, APM4 and APM2) were found to have no significant difference in the Weibull m values ($p > 0.05$).

Figures 5.77 – 5.79 show the Weibull regression fit on the transformed BFS data of the APM2 HP, APM4 and APM2 groups. A cumulative probability of failure plot for these three groups is shown in Figure 5.80. The APM2 HP and APM4 groups are found to have almost identical cumulative probability functions.

Table 5.14: Results of the BFS test for the glass-ceramics A series.

Test groups	Median BFS MPa (Q1,Q3)	Mean BFS MPa (SD)	Coefficient of Variation (%)
Ceramco 3 glass-ceramic	73.9[a] (71.3, 79.6)	75.7 (6.8)	9.0
IPS Empress Esthetic glass-ceramic[#]	164.4[b] (146.5, 188.6)	165.5 (30.6)	18.5
Glass-ceramic APM2 HP	223.2[c] (201.2, 251.8)	224.0 (38.0)	16.9
Glass-ceramic APM4	230.6[c] (187.4, 249.9)	225.4 (41.8)	18.6
Glass-ceramic A-AM4 HP[#]	249.5[d] (227.1, 260.0)	245.0 (24.3)	9.9
Glass-ceramic APM2	256.4[d] 229.1, 270.7)	255.0 (35.0)	13.7

*significant differences indicated by different superscript letters, [#]results from Chen (2009).

Q1, Q3: 25th and 75th percentiles.

Table 5.15: Results of the Weibull regression analysis for the glass-ceramics A series.

Test groups	m value	C.i. for m (95%)	$\sigma_{0.01}$ (MPa)	$\sigma_{0.1}$ (MPa)	σ_0 (MPa)	C.i. for σ_0 (95%)	r^2
Ceramco 3 glass-ceramic	13.9[a]	11.5 – 17.0	55.9	66.2	77.8[a]	76.0 – 79.6	0.92
IPS Empress Esthetic glass-ceramic[#]	6.3[b]	5.0 – 7.9	85.8	124.4	177.5[b]	168.8-186.6	0.98
Glass-ceramic APM2 HP	7.1[b]	5.7 – 8.8	124.8	173.8	238.9[c]	228.4 – 249.8	0.97
Glass-ceramic APM4	6.8[b]	5.6 – 8.3	122.7	173.0	240.5[c]	229.4 – 252.0	0.92
Glass-ceramic A-AM4 HP[#]	11.9[a,c]	9.3 – 15.1	173.3	211.3	255.5[d,c]	248.8 – 262.4	0.98
Glass-ceramic APM2	8.7[b,c]	7.0 – 10.8	158.4	207.7	269.3[d]	259.6 – 279.3	0.97

*significant differences indicated by different superscript letters, m = Weibull modulus, C.i. = Confidence intervals, σ_0 = Characteristic strength, $\sigma_{0.01}$, $\sigma_{0.1}$ = 1% and 10% probabilities respectively.

[#]results from Chen (2009).

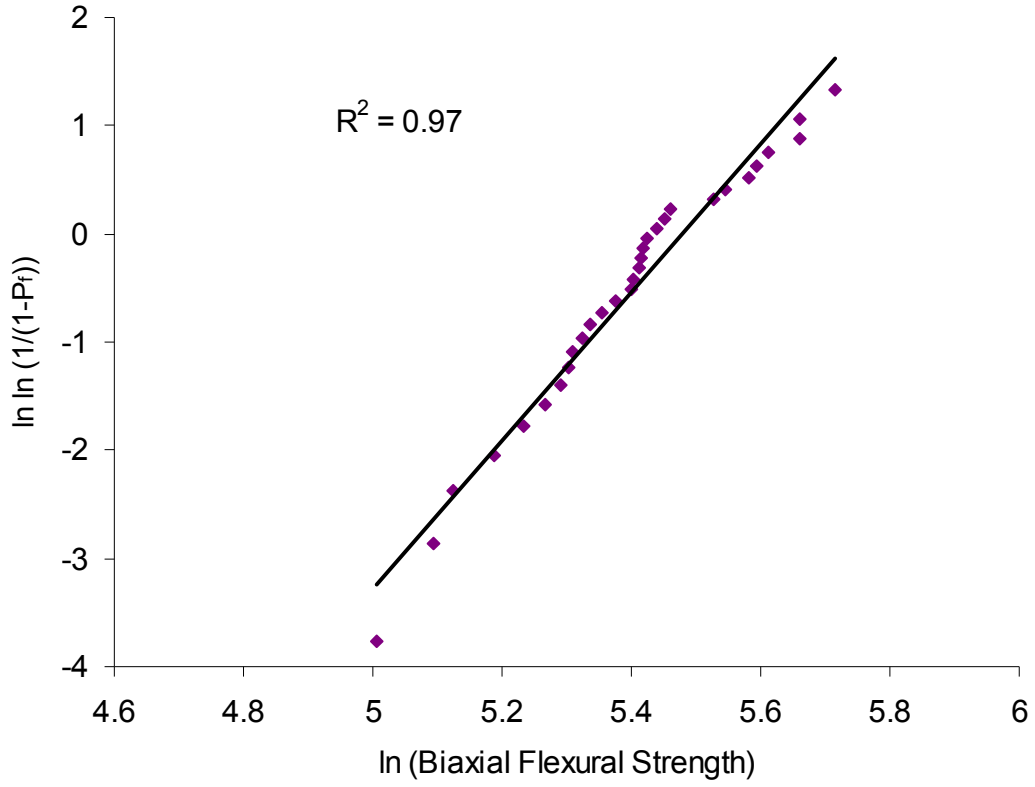

Figure 5.77: Weibull plot for the glass-ceramic APM2 HP group.

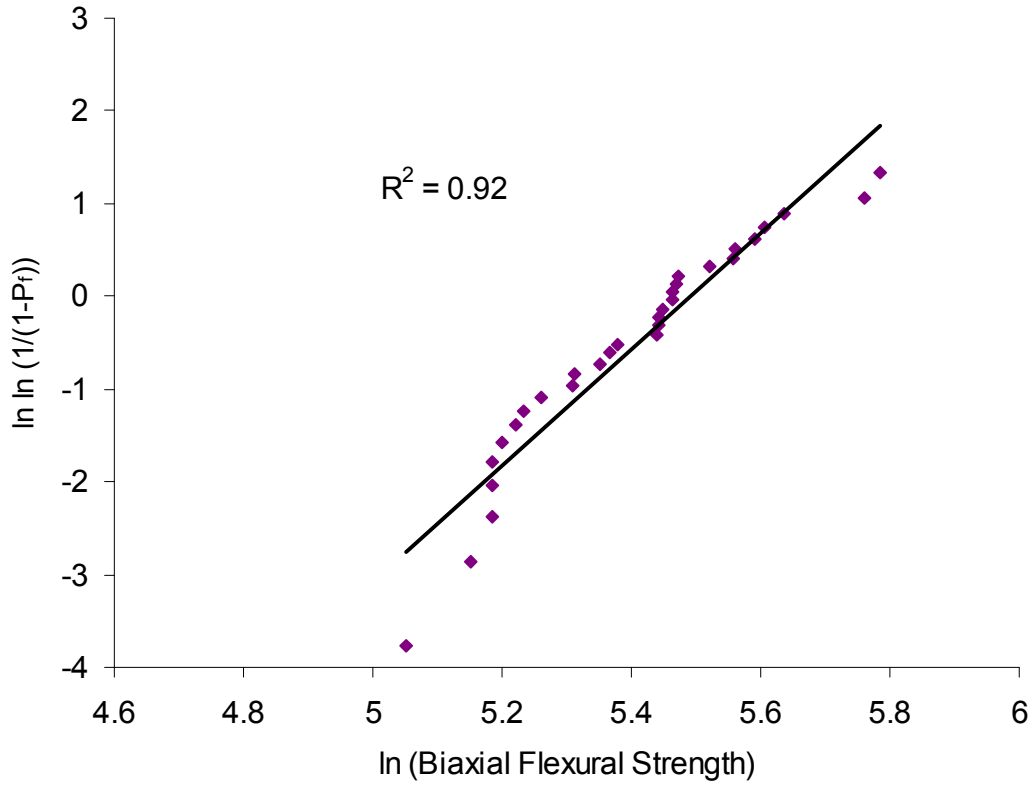

Figure 5.78: Weibull plot for the glass-ceramic APM4 group.

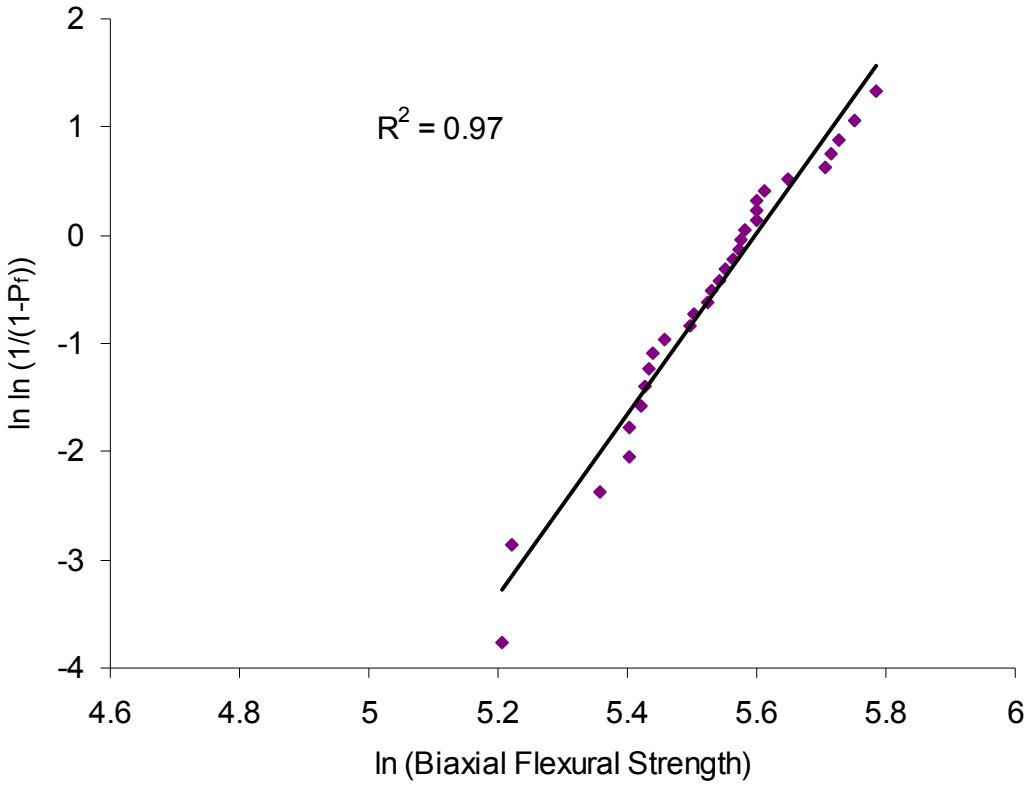

Figure 5.79: Weibull plot for the glass-ceramic APM2 group.

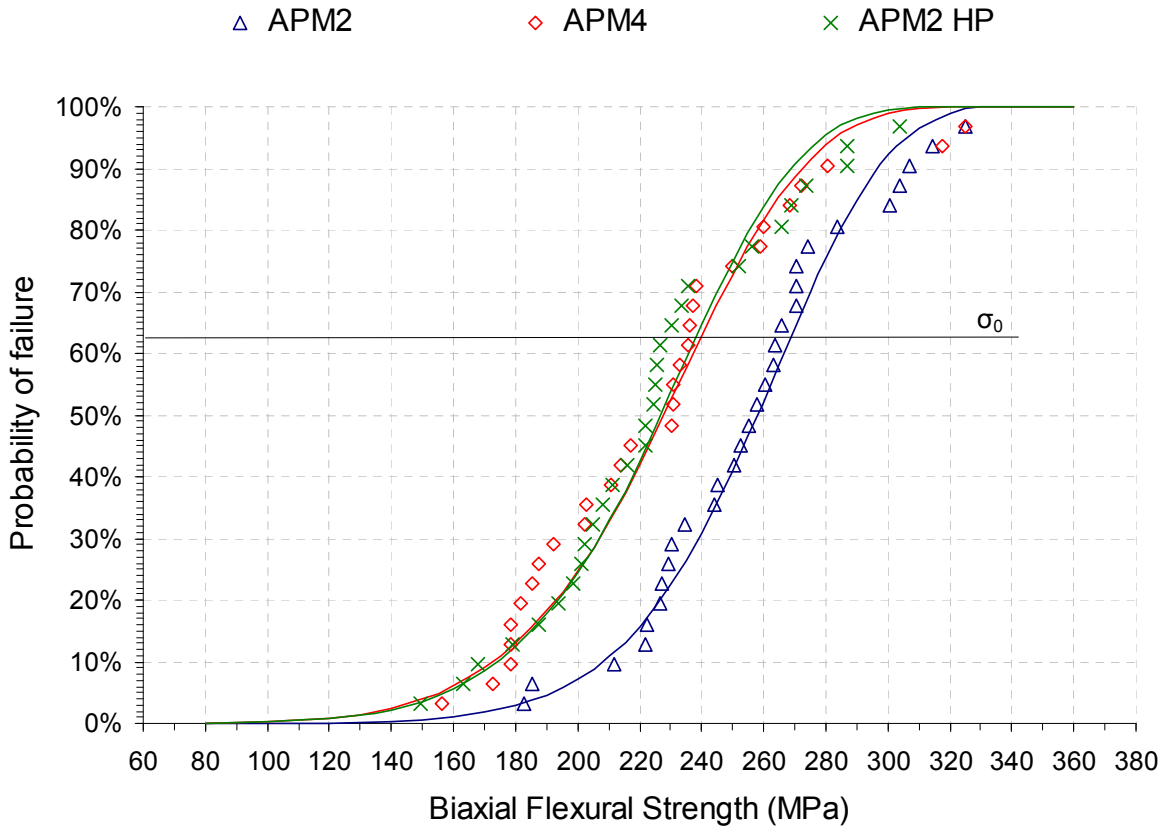

Figure 5.80: Probability of failure plots for the experimental glass-ceramics A series.

5.4.2 Glass-ceramics B, C series BFS results.

The biaxial flexural strength testing results of the B and C series of glass-ceramics are shown in Tables 5.16 and 5.17. The C glass-ceramic exhibited the highest BFS than all compared test groups ($p < 0.05$). The B, the B5PM0.5 and the C glass-ceramics were significantly stronger than both commercial glass-ceramics ($p < 0.05$). The BPM2 glass-ceramic exhibited a significantly ($p < 0.05$) higher median BFS than the Ceramco 3 glass-ceramic group. All B series glass-ceramics' median strengths were not significantly different ($p > 0.05$) to each other. The same significant differences that were identified for the median BFS were found for the characteristic strength values according to the overlap of the double sided confidence intervals amongst the tested groups. Ceramco 3 had the highest Weibull m value from all other groups ($p < 0.05$). All other groups tested were found to have no significant difference in the Weibull m values ($p > 0.05$).

Figures 5.81 – 5.83 show the Weibull regression fit on the transformed BFS data of the BPM2, B5PM0.5, B and C groups. A cumulative probability of failure plot for these four groups is shown in Figure 5.85. The probability of higher strength increases in the order of BPM2→B5PM0.5→B→C according to the positive shift of the respective curves. The B plot however is less tilted than the other three indicating a potentially higher reliability which however failed to differentiate ($p > 0.05$) in the statistical analysis of the m values above.

Table 5.16: Results of the biaxial flexural strength test glass-ceramics B series.

Test groups	Median BFS MPa (Q1,Q3)	Mean BFS MPa (SD)	Coefficient of Variation (%)
Ceramco 3 glass-ceramic	73.9[a] (71.3, 79.6)	75.7 (6.8)	9.0
IPS Empress Esthetic glass-ceramic	164.4[b] (146.5, 188.6)	165.5 (30.6)	18.5
Glass-ceramic BPM2	192.9[b,c] (162.9, 213.8)	192.5 (44.0)	22.8
Glass-ceramic B5PM0.5	205.1[c] (180.2, 234.0)	204.7 (38.4)	18.8
Glass-ceramic B	202.2[c] (184.8, 239.0)	210.6 (33.8)	16.1
Glass-ceramic C	227.4[d] (200.7, 262.8)	229.7 (40.4)	17.6

*significant differences indicated by different superscript letters

Q1, Q3: 25th and 75th percentiles.

Table 5.17: Results of the Weibull regression analysis for the glass-ceramics B series.

Test groups	m value	C.i. for m (95%)	$\sigma_{0.01}$ (MPa)	$\sigma_{0.1}$ (MPa)	σ_0 (MPa)	C.i. for σ_0 (95%)	r^2
Ceramco 3 glass-ceramic	13.9[a]	11.5 – 17.0	55.9	66.2	77.8[a]	76.0 – 79.6	0.92
IPS Empress Esthetic glass-ceramic	6.3[b]	5.0 – 7.9	85.8	124.4	177.5[b]	168.8-186.6	0.98
Glass-ceramic BPM2	5.5[b]	4.5 – 6.8	90.4	138.1	207.5[b,c]	195.6 – 220.2	0.93
Glass-ceramic B5PM0.5	5.9[b]	4.6 – 7.5	101.1	150.6	220.6[c]	209.1 - 232.8	0.99
Glass-ceramic B	8.1[b]	6.6 – 10.0	126.5	168.9	222.7[c]	214.0 – 231.6	0.87
Glass-ceramic C	6.7[b]	5.3 – 8.5	123.4	175.4	245.7[d]	234.3 – 257.5	0.98

*significant differences indicated by different superscript letters, m = Weibull modulus, C.i. = Confidence intervals, σ_0 = Characteristic strength, $\sigma_{0.01}$, $\sigma_{0.1}$ = 1% and 10% probabilities respectively.

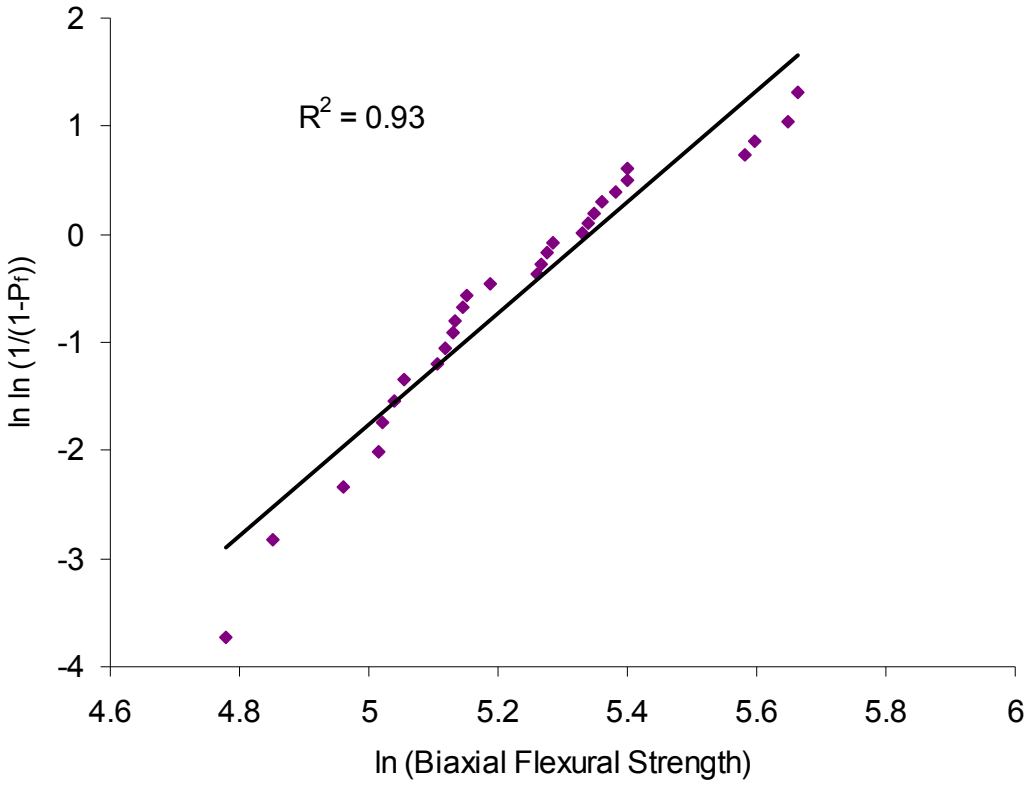

Figure 5.81: Weibull plot for the glass-ceramic BPM2 group.

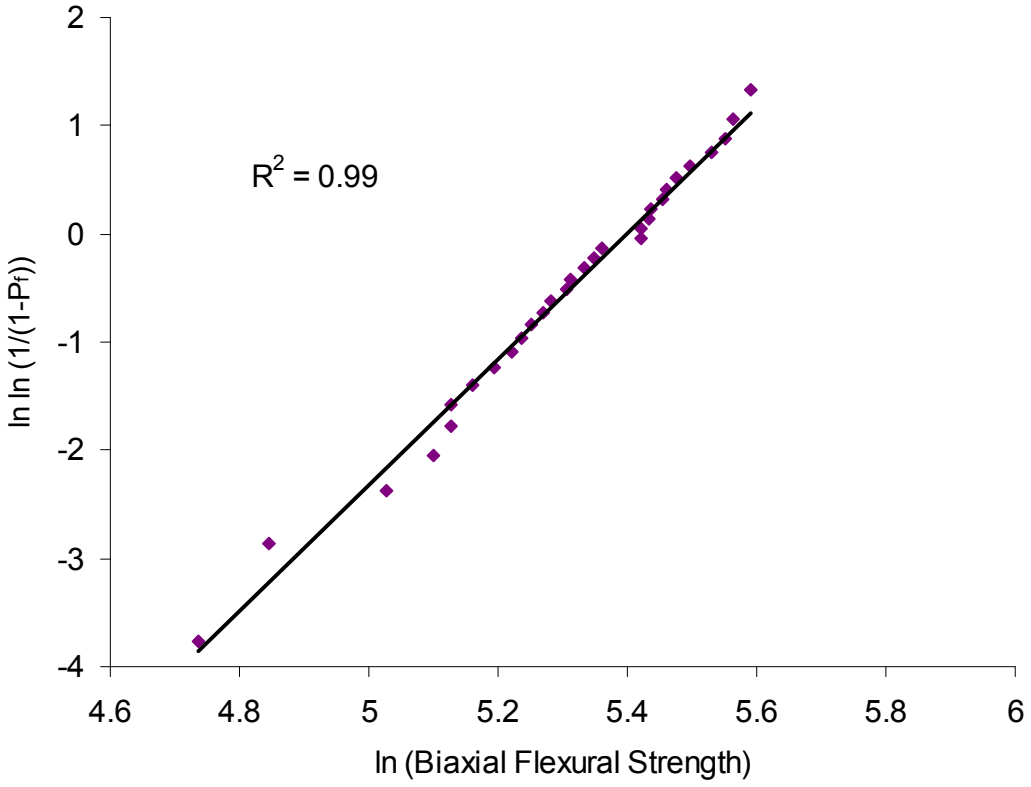

Figure 5.82: Weibull plot for the glass-ceramic B5PM0.5 group.

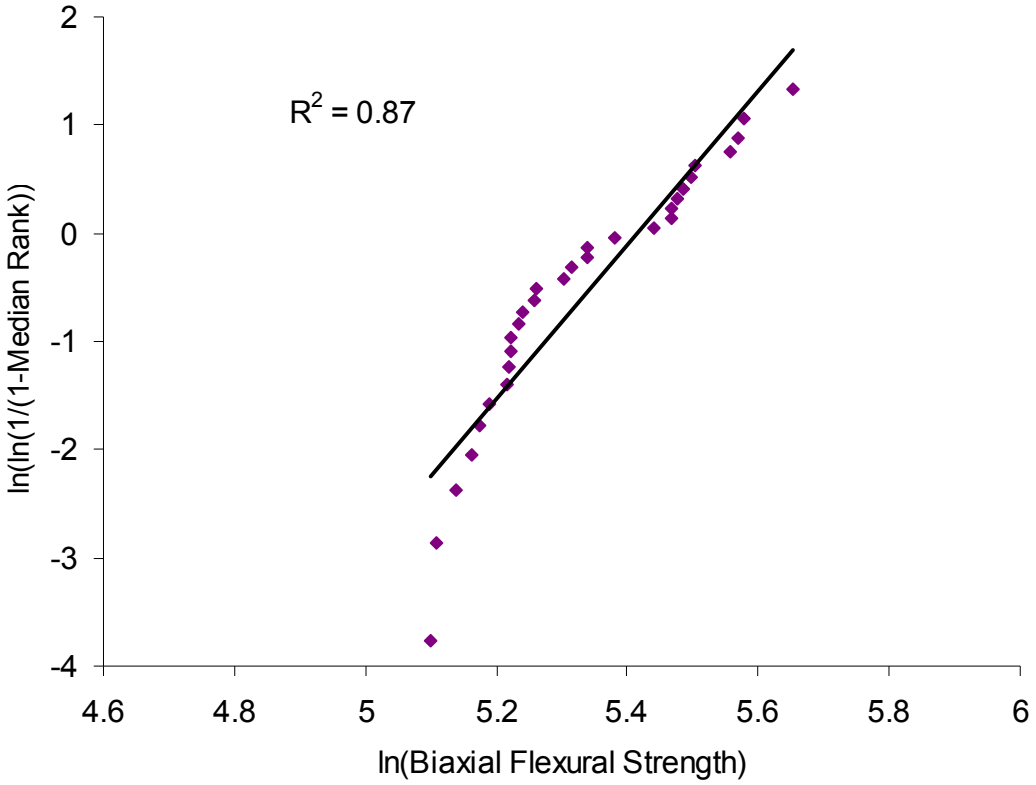

Figure 5.83: Weibull plot for the glass-ceramic B group.

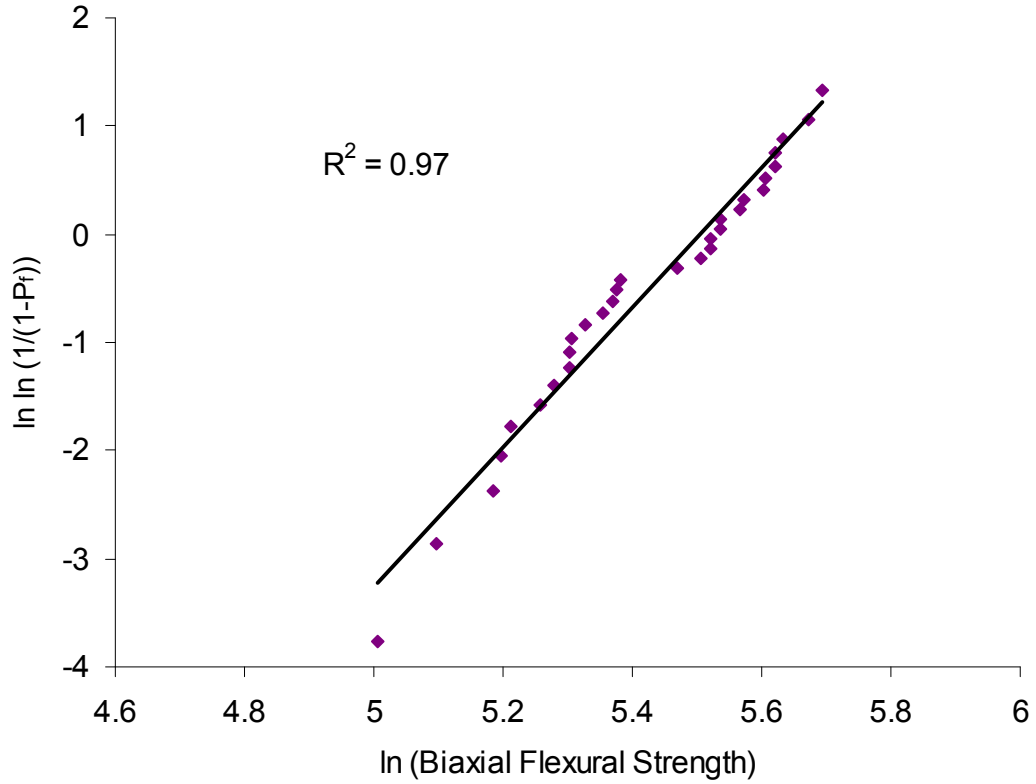

Figure 5.84: Weibull plot for the glass-ceramic C group.

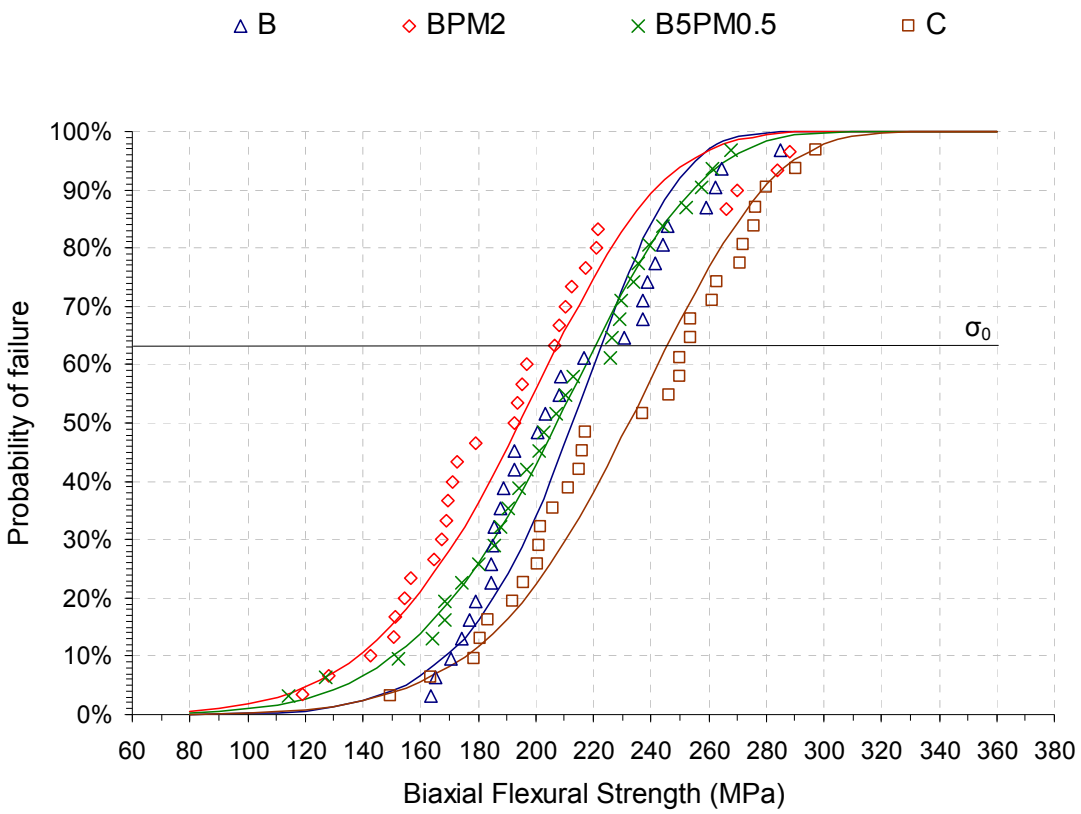

Figure 5.85: Probability of failure plot for the experimental glass-ceramics B and C series.

5.4.3 Comparison of highest BFS groups from all glass-ceramics series

The strength data of the groups exhibiting highest BFS from all series of experimental glass-ceramics, that were previously found significantly ($p < 0.05$) stronger than the commercial glass-ceramics, are compared in this section. The highest ($p < 0.05$) median BFS was exhibited from the APM2 glass-ceramic group. Glass-ceramic C exhibited a significantly ($p < 0.05$) higher median BFS than both B and B5PM0.5 glass-ceramics. The B and B5PM0.5 glass-ceramic groups were not significantly different from each other ($p > 0.05$). The same significant differences that were identified for the median BFS were found for the characteristic strength values according to the overlap of the double sided confidence intervals amongst the tested groups. The Weibull m values of all tested groups were not significantly different ($p > 0.05$).

The cumulative probability plots of the highest BFS groups identified are compared to the plot of the IPS Empress Esthetic material in Figure 5.86. A significant strength improvement and similar reliability for the experimental glass-ceramics versus the commercial glass-ceramic is illustrated.

Table 5.18: Highest BFS groups comparative results.

Test groups	Median BFS MPa (Q1,Q3)	Mean BFS MPa (SD)	Coefficient of Variation (%)
Glass-ceramic B5PM0.5	205.1[a] (180.2, 234.0)	204.7 (38.4)	18.8
Glass-ceramic B	202.2[a] (184.8, 239.0)	210.6 (33.8)	16.1
Glass-ceramic C	227.4[b] (200.7, 262.8)	229.7 (40.4)	17.6
Glass-ceramic APM2	256.4[c] (229.1, 270.7)	255.0 (35.0)	13.7

*significant differences indicated by different superscript letters

Table 5.19: Highest BFS groups comparative Weibull regression analyses.

Test groups	m value	C.i. for m (95%)	$\sigma_{0.01}$ (MPa)	$\sigma_{0.1}$ (MPa)	σ_0 (MPa)	C.i. for σ_0 (95%)	r^2
Glass-ceramic B5PM0.5	5.9[a]	4.6 – 7.5	101.1	150.6	220.6[a]	209.1 - 232.8	0.99
Glass-ceramic B	8.1[a]	6.6 – 10.0	126.5	168.9	222.7[a]	214.0 – 231.6	0.87
Glass-ceramic C	6.7[a]	5.3 – 8.5	123.4	175.4	245.7[b]	234.3 – 257.5	0.97
Glass-ceramic APM2	8.7[a]	7.0 – 10.8	158.4	207.7	269.3[c]	259.6 – 279.3	0.97

*significant differences indicated by different superscript letters, m = Weibull modulus, C.i. = Confidence intervals, σ_0 = Characteristic strength, $\sigma_{0.01}$, $\sigma_{0.1}$ = 1% and 10% probabilities respectively.

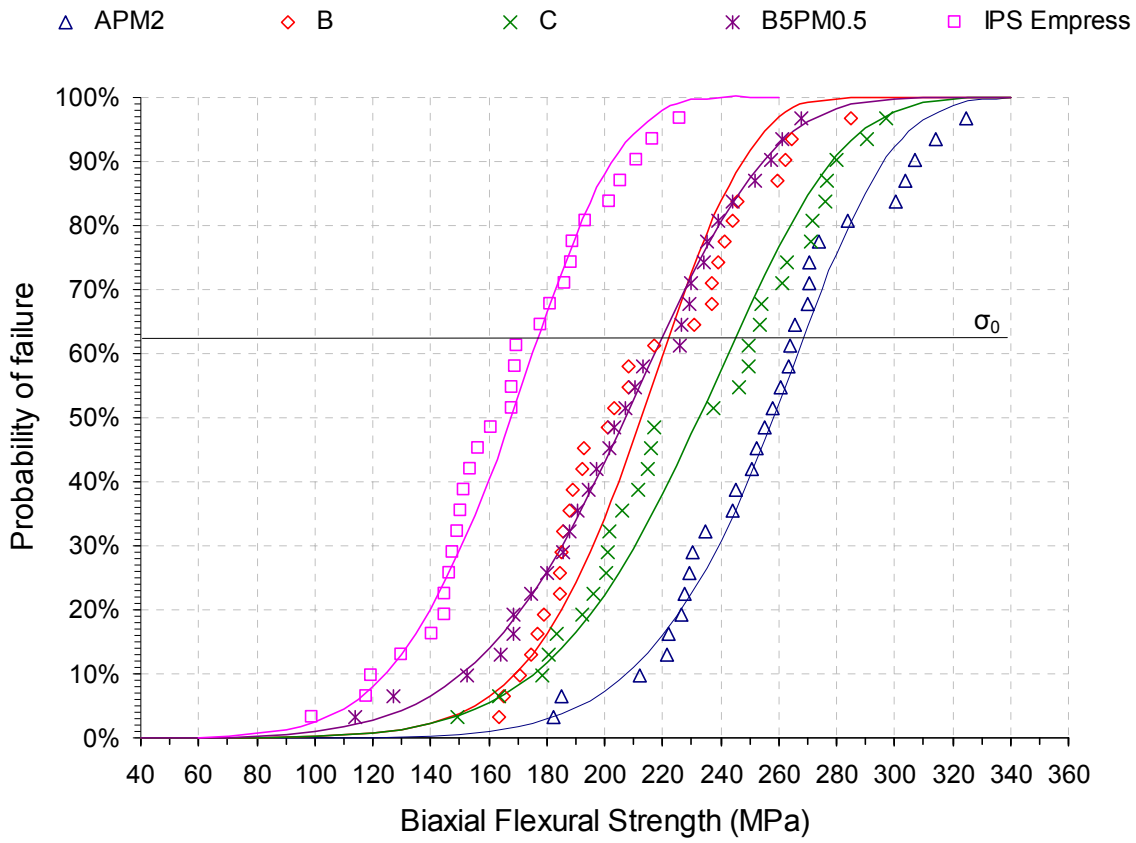

Figure 5.86: Probability of failure plot for the highest BFS experimental glass-ceramics and the IPS Empress Esthetic material.

5.5 Wear Testing

5.5.1 Wear Testing results

Figure 5.87 is a sample oscilloscope trace of the load (blue line) and angle (red line) waveforms phasing at the start of an MTS wear test. The load waveform produced, was a symmetrical square wave.

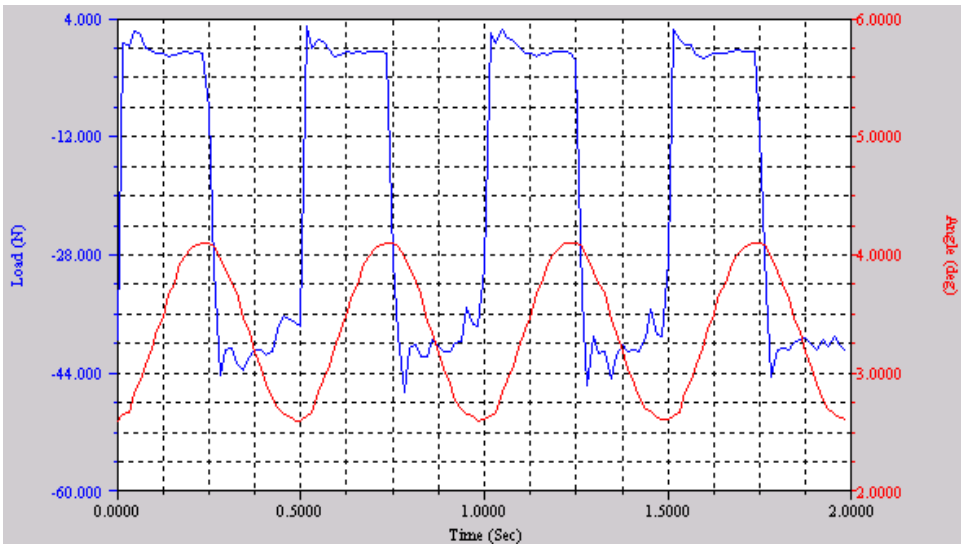

Figure 5.87: Sample oscilloscope trace of the load (blue line) and angle (red line) waveforms phasing at the start of an MTS wear test.

The results of wear quantification for Ceramco 3, A-AM4 HP and APM2 HP glass-ceramic groups can be found in Table 5.20. The wear quantification data failed the normality/ equal variance criteria in some cases and a non-parametric test was selected for the analysis (One - Way ANOVA on Ranks, Sigma stat, version 2.03, SPSS Inc.). The results of the Kruskal-Wallis One - Way ANOVA on ranks indicated significant differences in the median values ($p < 0.05$). A multiple comparison procedure was used (All-pairwise, Student-Newman-Keuls Method). The significant ($p < 0.05$) differences are indicated by different superscript letters in Table 5.20. Values represent medians with the respective 25th (Q1) and 75th (Q3) percentiles.

Both experimental groups were found to exhibit significantly ($p < 0.05$) less antagonistic enamel loss than the commercial glass-ceramic in all three parameters tested (volume, height and mean-height loss). The APM2 HP experimental group was found to exhibit significantly ($p < 0.05$) less antagonistic enamel loss compared to the A-AM4 HP experimental group in both height and mean-height. The APM2 HP group was also found to exhibit significantly ($p < 0.05$) less combined mean-height loss than both the Ceramco 3 material and the A-AM4 HP experimental material. Glass-ceramic material loss was not statistically ($p > 0.05$) different among all three groups for all parameters tested. Ceramco 3 produced significantly ($p < 0.05$) higher enamel than glass-ceramic material loss when compared in height and mean-height parameters. No difference ($p > 0.05$) was however found for Ceramco 3 glass-ceramic versus tooth volume loss. A-AM4 HP produced significantly ($p < 0.05$) less enamel than glass-ceramic material volume loss. APM2 HP was found to create significantly ($p < 0.05$) less enamel than glass-ceramic material volume and height loss. No significant difference ($p > 0.05$) was found for glass-ceramic material versus tooth mean-height loss for both A-AM4 HP and APM2 HP groups. The median (Q1, Q3) results of volume and mean-height loss are also graphically presented in Figures 5.88 and 5.89. The larger data scatter acquired for the Ceramco 3 material versus the experimental A-AM4 HP and APM2 HP materials is demonstrated.

Table 5.20: Results of the wear testing.

Parameter tested	Ceramco 3 glass-ceramic	A-AM4 HP glass-ceramic	APM2 HP glass-ceramic
Disc Volume loss (mm^3)	0.164 [a, #] (0.158 , 0.217)	0.190 [a, #] (0.154 , 0.214)	0.175 [a, #] (0.148 , 0.204)
Tooth Volume loss (mm^3)	0.208 [a, #] (0.127 , 0.252)	0.126 [b, ▲] (0.110 , 0.151)	0.112 [b, ▲] (0.074 , 0.149)
Combined* Volume loss (mm^3)	0.367 [a] (0.287 , 0.480)	0.311 [a] (0.261 , 0.352)	0.283 [a] (0.212 , 0.349)
Disc Height loss (µm)	128.1 [a, #] (117.5 , 150.6)	142.5 [a, #] (127.9 , 162.5)	142.1 [a, #] (128.9 , 151.2)
Tooth Height loss (µm)	226.9 [a, ▲] (167.5 , 259.3)	186.3 [b, ▲] (156.8 , 215.2)	130.9 [c, ▲] (122.5 , 176.0)
Disc Mean-Height loss (µm)	61.8 [a, #] (55.2 , 72.0)	67.9 [a, #] (60.0 , 72.5)	65.0 [a, #] (56.8 , 70.5)
Tooth Mean-Height loss (µm)	88.3 [a, ▲] (69.8 , 103.0)	65.7 [b, #] (56.0 , 77.5)	49.9 [c, #] (43.5 , 70.7)
Combined* Mean-Height loss (µm)	152.5 [a] (124.8 , 164.6)	135.1 [a] (119.1 , 165.4)	122.6 [b] (103.9 , 132.0)

*combined tooth + disc measurements.

Values represent medians and the Q1, Q3 quartiles.

Different superscript letters indicate significant differences between groups in the same row.

Different superscript symbols indicate significant differences in the tested variable within groups in the same column.

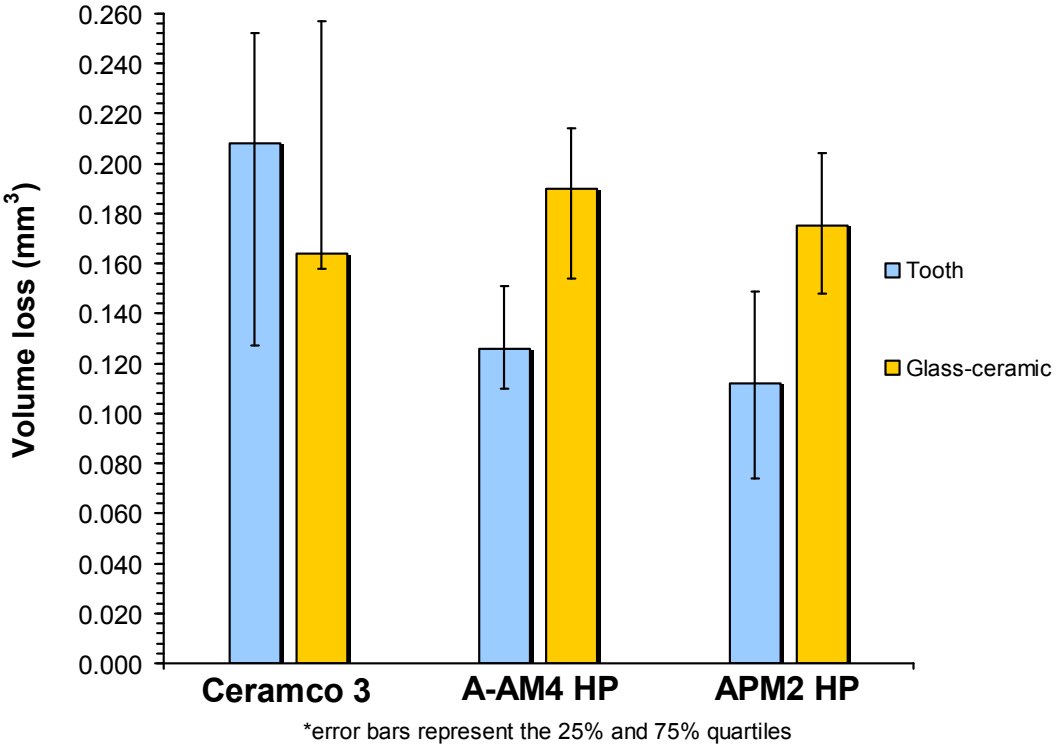

Figure 5.88: Graphical comparison of the median tooth and glass-ceramic disc volume loss for the tested groups.

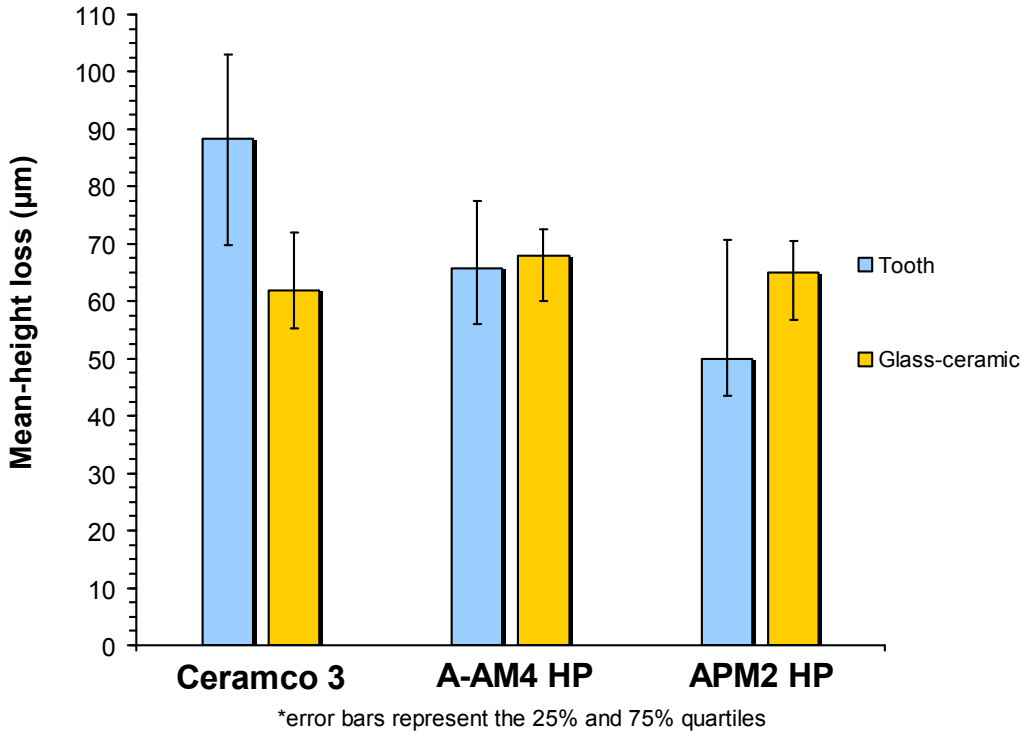

Figure 5.89: Graphical comparison of the median tooth and glass-ceramic disc mean-height loss for the tested groups.

5.5.2 Operator uncertainty and scanning repeatability results

The results for operator uncertainty produced a mean (SD) difference between measured volume loss values of 0.0013 (0.0007) mm^3 for the glass-ceramic disc and of 0.0040 (0.0023) mm^3 for the tooth specimen. The result for scanning repeatability produced a mean (SD) volume difference between scans of 0.0024 (0.0007) mm^3 for the tooth specimen (compared area 1.6 x 1.4 mm^2) and of 0.0030 (0.0015) mm^3 for the disc specimen (compared area 3 x 3 mm^2). Comparing the acquired repeatability and operator induced errors with the mean volume values of the experimental protocol measurements (Table 5.21), we obtain errors ranging 1.25 - 2.08% for teeth and 0.7 – 1.63% for discs.

5.5.3 Automated and Experimental wear quantification results

The results of the measurements acquired by the Automated and Experimental methodologies are shown in Table 5.21. The Automated software measurements adequately calculated disc volume loss and for that reason the mean values measured using the Automated and Experimental protocols were equal. A mean volume loss overestimation of 6.83% was measured when applying the Automated protocol on teeth; however no statistically significant difference ($p > 0.05$) between Automated and Experimental values was identified. There was a significant difference between the means for both tooth ($p < 0.05$) and glass-ceramic disc ($p < 0.001$) mean-height loss values between Automated and Experimental measurements.

Table 5.21: Automated and Experimental wear quantification results

Measurement	Automated Mean (SD)	Experimental Mean (SD)	% Difference
Volume loss mm^3 (SD) teeth	0.206 (0.072)^a	0.192 (0.066)^a	6.83
Volume loss mm^3 (SD) glass-ceramic discs	0.184 (0.042)^a	0.184 (0.042)^a	0
Mean-height loss µm (SD) teeth	48.42 (16.63)^a	65.50 (20.58)^b	27.9
Mean-height loss µm (SD) glass-ceramic discs	19.85 (5.58)^a	67.62 (21.01)^b	69.4

Different superscript letters indicate significant ($p < 0.05$) differences between mean values tested.

5.5.4 Surface topography and roughness results

The results of the SEM and profilometry surface topography images from the wear test groups are presented in Figures 5.90 – 5.97. The worn surfaces of the Ceramco 3 glass-ceramic disc/tooth group appear to have surfaces with increased waviness and damage in comparison to the A-AM4 HP and APM2 HP glass-ceramic disc/tooth groups, both in the SEM and profilometric images (Figures 5.90 – 5.97). The colour gradient (profilometry images) illustrates height gradient. The different colour schemes are chosen for visualisation enhancement.

The surface roughness (R_a parameter) and wave height results can be seen in Table 5.22. All recorded values for A-AM4 HP and APM2 HP glass-ceramic disc/tooth group were lower than the Ceramco 3 group. The APM2 HP group however had higher values than the A-AM4 HP group. The Ceramco 3 glass-ceramic disc specimens had lower mean y than x values. A vertical orientation of the wear grooves parallel to the y-axis of scanning was observed for the Ceramco 3 glass-ceramic group in Figures 5.90 a and 5.96 a. The R_a values for A-AM4 HP for both tooth/ glass-ceramic are the same in both x and y directions. A non-oriented wear pattern was observed for the A-AM4 HP glass-ceramic disc/tooth group (Figure 5.93 and Figure 5.96 c, d). The values for the A-AM4 HP glass-ceramic are the same in both x and y directions for disc R_a and tooth wave height. While both the glass-ceramic disc and tooth samples of the APM2 HP group do not appear to have an oriented wear pattern (Figures 5.94 and 5.95), some marked wear pattern is depicted on the tooth sample when in the closer profilometric view (Figure 5.96 f)

when compared to the A-AM4 HP group tooth sample (Figure 5.96 d). The observations for the SEI in Figure 5.97 show the same trends as the profilometric images in Figure 5.96.

Table 5.22: Profilometry results.

	Ceramco 3		**A-AM 4**		**APM2 HP**	
Parameter	**Mean* x (µm)**	**Mean* y (µm)**	**Mean* x (µm)**	**Mean* y (µm)**	**Mean* x (µm)**	**Mean* y (µm)**
Tooth **R_a**	7.0	7.3	3.7	3.7	4.2	4.5
Disc **R_a**	4.7	4.1	2.7	2.7	2.6	2.6
Tooth **wave height**	30	24	18	17	22	22
Disc **wave height**	37	24	19	20	18	16

* Mean of 501 line profiles

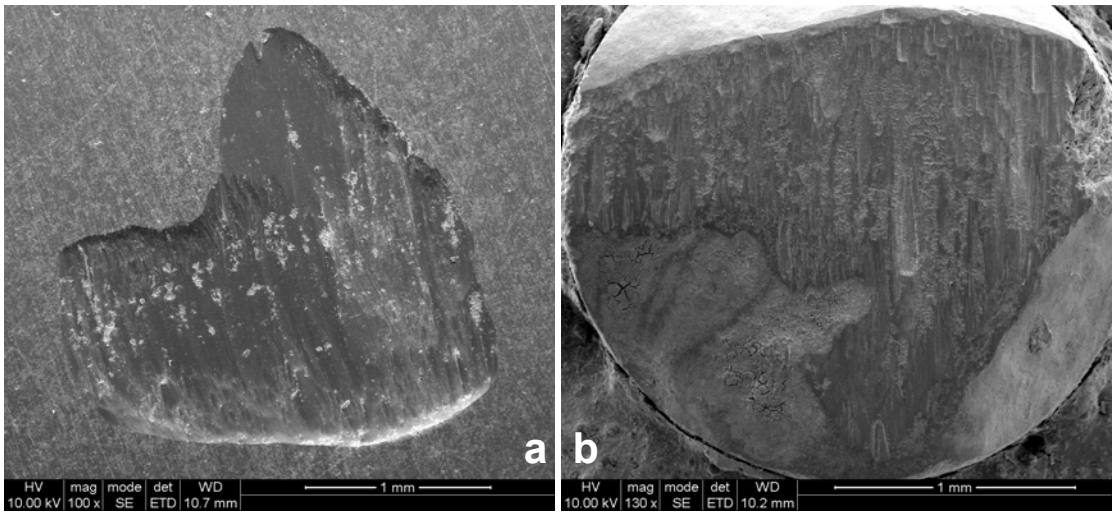

Figure 5.90: SEI of the: (a) Ceramco 3 glass-ceramic disc and (b) tooth antagonist following wear testing.

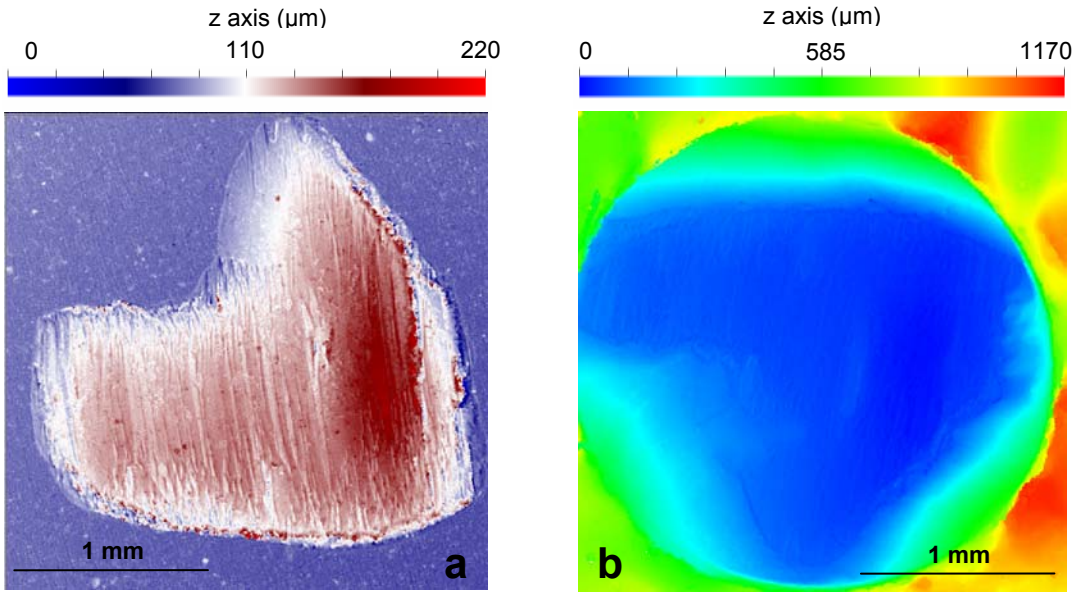

Figure 5.91: Profilometry images of the: (a) Ceramco 3 glass-ceramic disc and (b) tooth antagonist following wear testing.

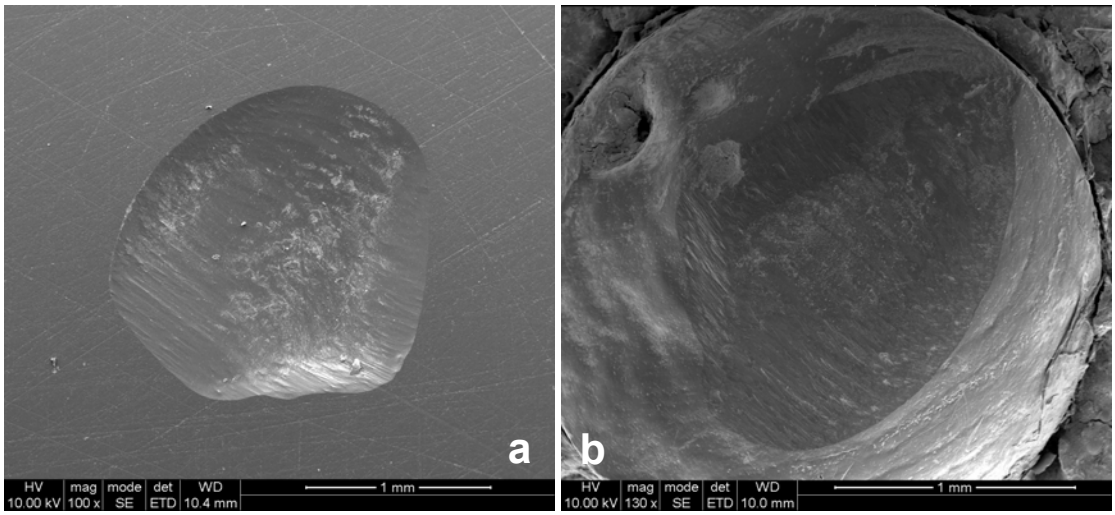

Figure 5.92: SEI of the: (a) A-AM4 HP glass-ceramic disc and (b) tooth antagonist following wear testing.

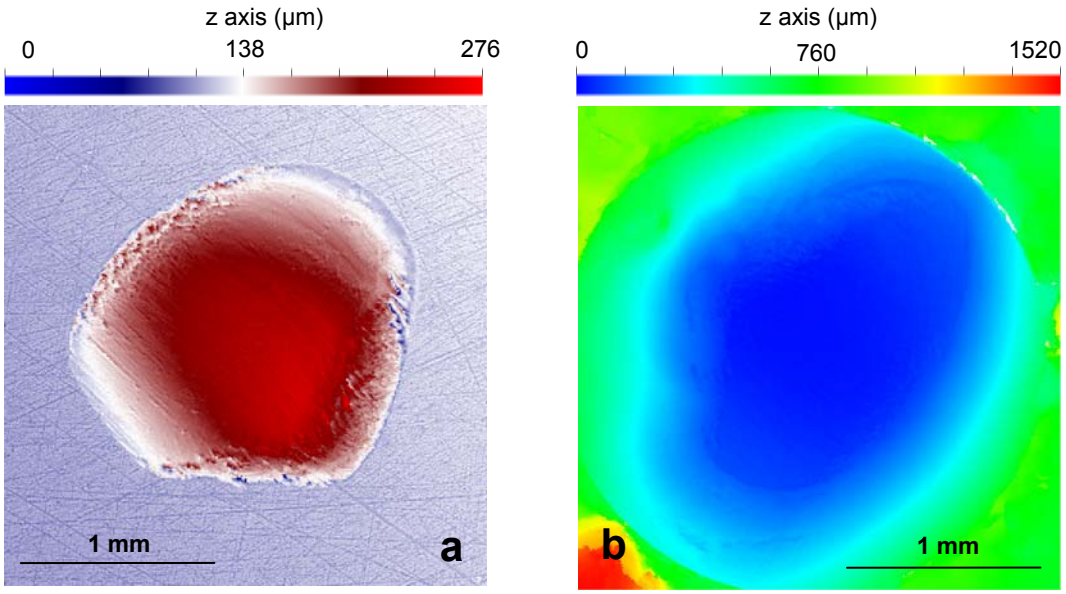

Figure 5.93: Profilometry images of the: (a) A-AM4 HP glass-ceramic disc and (b) tooth antagonist following wear testing.

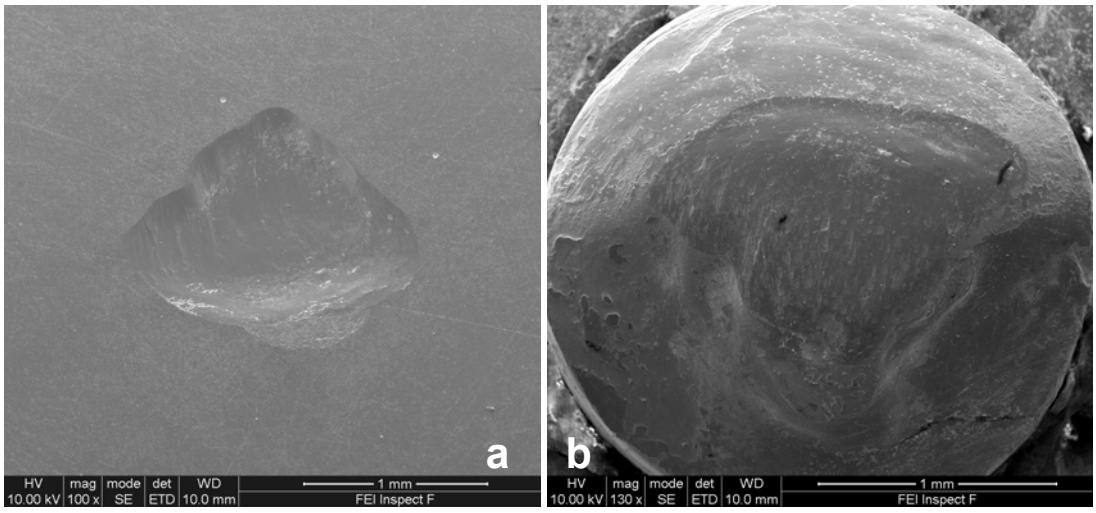

Figure 5.94: SEI of the: (a) APM2 HP glass-ceramic disc and (b) tooth antagonist following wear testing.

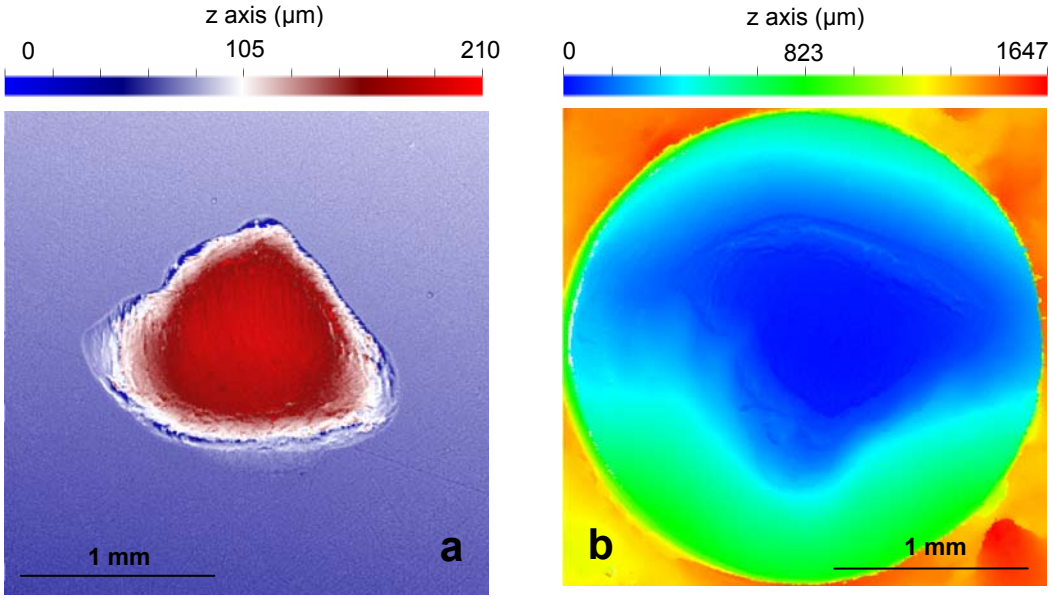

Figure 5.95: Profilometry images of the: (a) APM2 HP glass-ceramic disc and (b) tooth antagonist following wear testing.

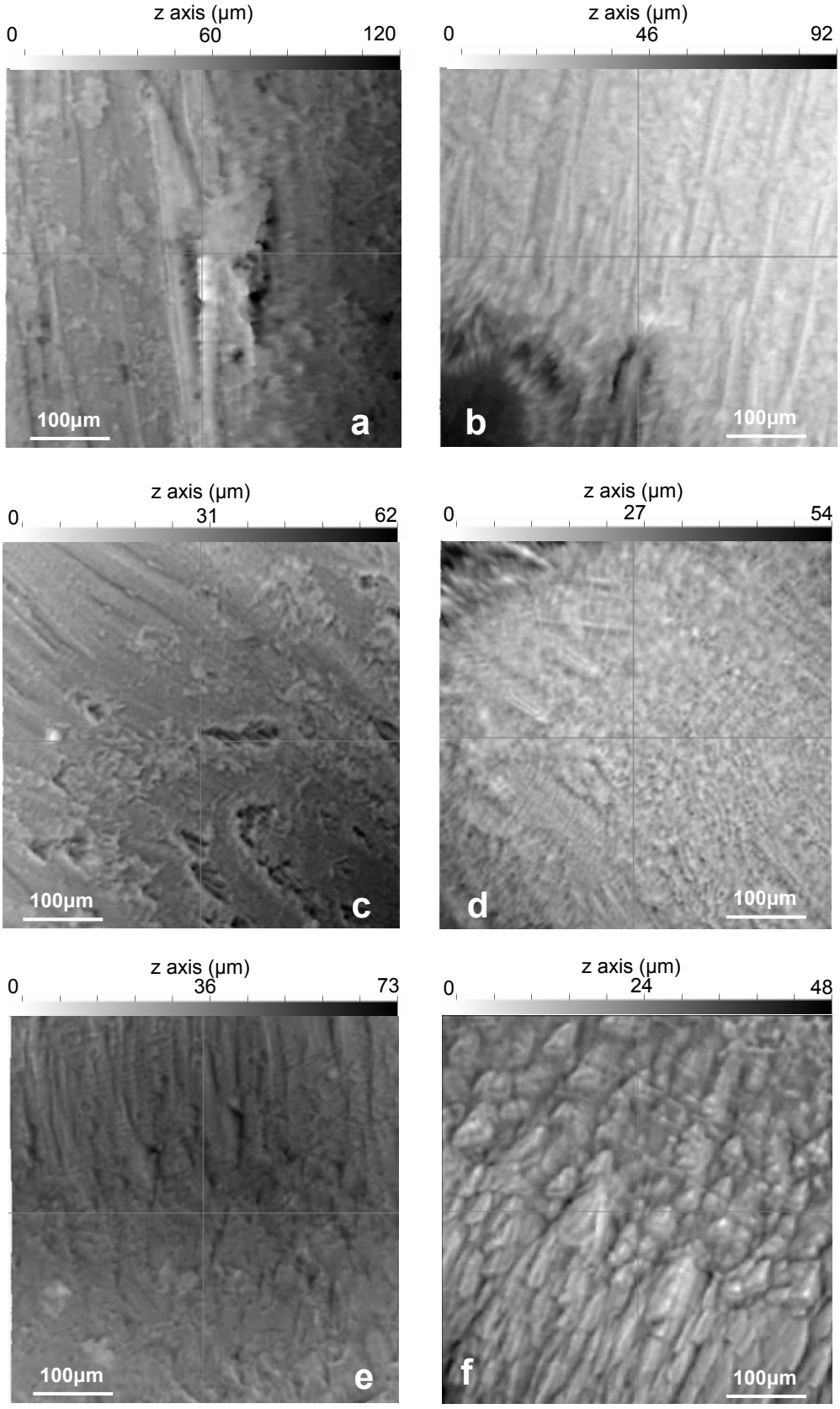

Figure 5.96: Profilometry image of the surface topography within the worn areas of the Ceramco 3 (a) glass-ceramic disc and (b) the tooth antagonist, the A-AM4 HP (c) glass-ceramic disc and (d) the tooth antagonist and the APM2 HP (e) glass-ceramic disc and (f) the tooth antagonist.

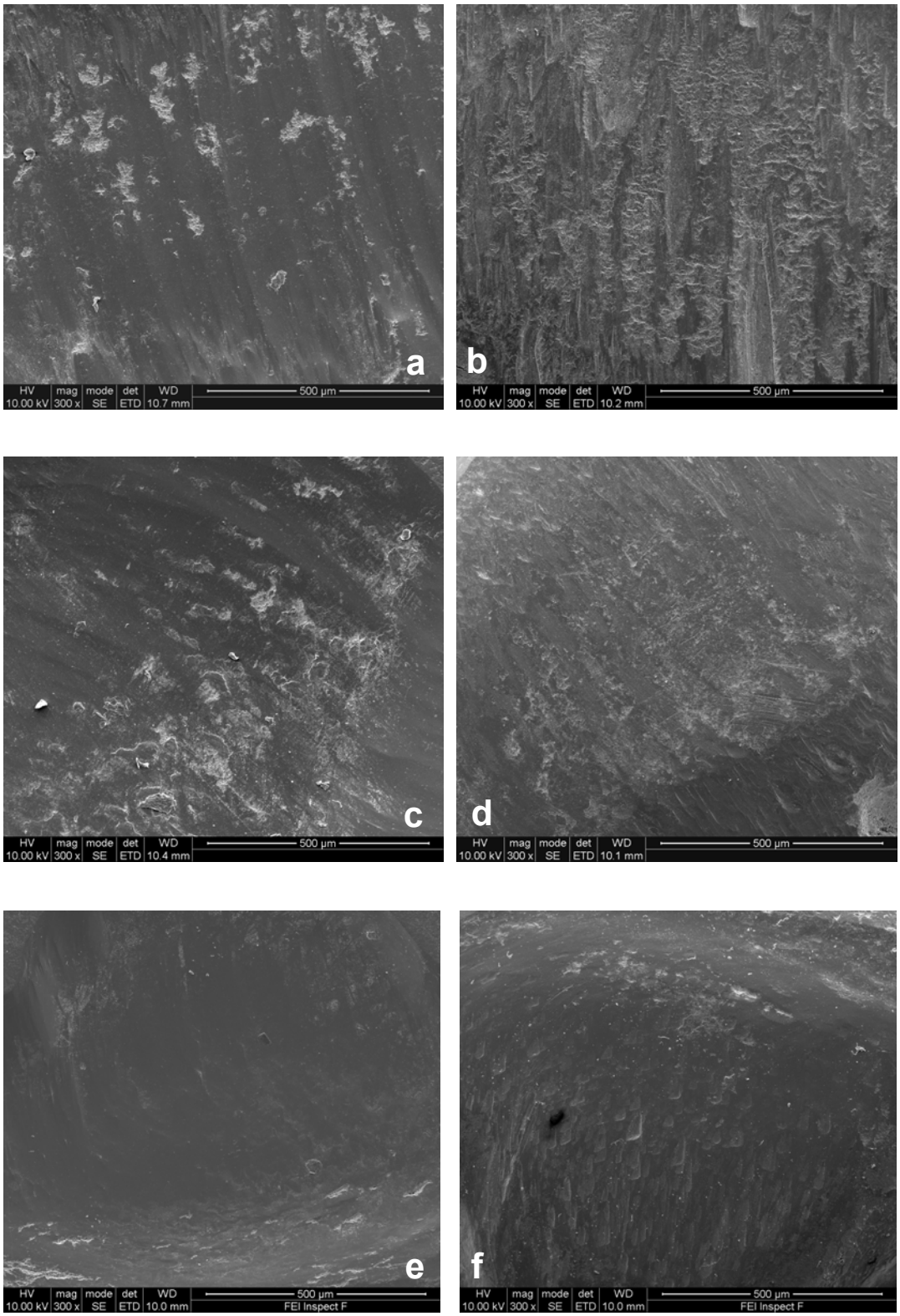

Figure 5.97: SEI of the surface topography within the worn areas of: a Ceramco 3 (a) glass-ceramic disc and (b) the tooth antagonist, an A-AM4 HP (c) glass-ceramic disc and (d) the tooth antagonist and an APM2 HP (e) glass-ceramic disc and (f) the tooth antagonist.

5.5.5 Microstructure of the glass-ceramic wear specimens

The microstructure of the glass-ceramic wear specimens is depicted here to illustrate the very coarse, irregular tetragonal leucite crystals of the Ceramco 3 material (Figure 5.98a) against the fine grained tetragonal leucite crystal structure of the A-AM4 HP experimental material (Figure 5.98b) and the nanoscale tetragonal leucite crystal structure of the APM2 HP material (Figure 5.98c).

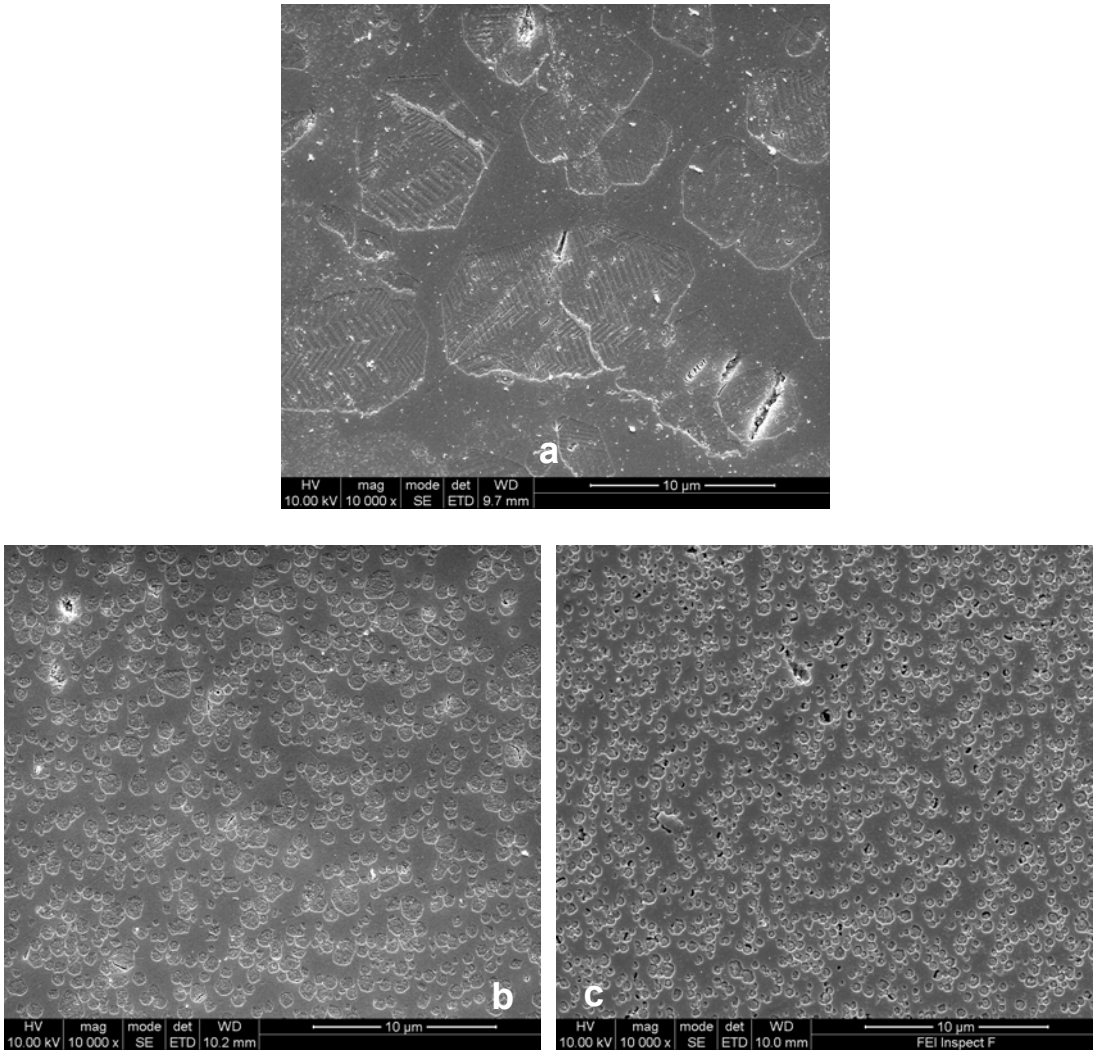

Figure 5.98: Microstructure of the (a) Ceramco 3, (b) A-AM4 HP and (c) APM2 HP specimens showing the crystal size/shape differences.

6. DISCUSSION

6.1 Glasses heat treatment selection

The dilatometry plots provided clear transition steps and were preferred for the T_g determination (Figures 5.1 – 5.3) over the DSC plots (Figures 5.5 – 5.10). A temperature of 30°C above the determined T_g was selected as the nucleation temperature based on McMillan (1979). DSC provided the peak crystallisation temperatures as clear exothermic events in glasses A, B, B1 – B4 and C (Figures 5.5 – 5.8, 5.10), however no clear exothermic peak was identified for glass B5 (Figure 5.9). The DSC determined peak crystallisation temperature (T_p) was used as the crystal growth hold temperature, unless High Temperature X-ray Diffraction (HTXRD) data indicated phase changes other than leucite (Table 5.3). Glass B is an exception as a pilot nucleation study at different crystallisation temperatures, indicated that the onset of the crystallisation peak (804°C) produced a larger crystal number and a more homogenous microstructure than a heat treatment at the DSC T_p. Two crystal phase systems with different thermal expansions (e.g. leucite and sanidine) were avoided (Mackert et al., 2000) as they could lead to compromised properties due to deleterious microcracking (Cattell et al., 2005). For the glass B5, where no clear T_p was identified (Figure 5.9), the growth heat treatment temperature was selected based on HTXRD data (see 5.1.4.3). This alternative method provided the temperature (820°C, Figure 5.24) that was used for the subsequent heat treatments, on the starting glass B5 and the high speed milled glass B5PM0.5. The heat treatment temperatures for the glass A series were chosen based on optimised nucleation – crystallisation heat treatments on the same glass by Chen (2009). The XRD results of all experimental glass-ceramics confirmed the presence of a single

crystal phase of tetragonal leucite at room temperature (ICDD: 00-038-1423, Figure 5.25 - Figure 5.29) as a result of the temperature dependant cubic to tetragonal phase transformation of leucite (Mackert, 1988).

6.2 Activation energies

A higher concentration of nuclei (surface and/or bulk) in a heat treated glass promotes crystallisation and therefore results in a negative shift in T_p (Xu et al., 1991). A tendency towards obtaining a surface nucleated system can be evidenced by a negative shift in the T_p with decreasing particle size (PS) (Aronne et al., 1995, Clifford and Hill, 1996, Romero et al., 1999), as smaller particles provide more surface area, thus it may be easier to overcome the thermodynamic barrier to nucleation. The HTXRD data for glass B (Table 5.3, Figure 5.17) indicate the presence of a cubic leucite phase at the temperature range where the DSC crystallisation peaks occurred (845.7 – 855.5 °C, Figure 5.6). Glass B shows a positive shift of T_p below 45 μm PS. This may be an indication of lower nuclei concentration and a bulk leucite nucleation mechanism present at this PS range. The crystallisation peaks for glass B, are however quite sharp for all particle sizes examined and this is also consistent with a bulk nucleation mechanism (Kingery, 1976, Marotta et al., 1980). The experienced peak shift may therefore not be significant. In addition, Tošić et al., (2000) found particle size dependant shifts of bulk to surface leucite crystallisation for glass particle sizes below 75 μm. The DSC results for glass C are similar to B (sharp peaks, minor T_p shift [6 – 7 °C] for PS<45 μm). Glass C has however shown to develop cubic leucite and sanidine phases at the

peak crystallisation range of 857.4 – 866.0 °C (Figure 5.10) according to the HTXRD results (Table 5.3, Figure 5.23). The two phases may be crystallising by different mechanisms. A two crystal phase leucite – sanidine system is also present at the peak crystallisation range of the A series (860.6 – 904.5 °C) (Figure 5.5) as evidenced by HTXRD between 760 – 1000 °C (Chen, 2009). The DSC crystallisation peaks of glass B4 were broad, possibly indicating a surface crystallisation mechanism (Marotta et al., 1980, Laudisio et al., 1998) of cubic leucite (Table 5.3, Figure 5.21). The peak at the 300 – 125 μm PS range, would however be expected to shift positively even further than the 125 – 45 μm PS range peak, if a surface crystallisation mechanism was present (Aronne et al., 1995, Clifford and Hill, 1996, Romero et al., 1999). Glass B5 did not produce any clearly discernible DSC crystallisation peaks (Figure 5.9) for the crystallisation of cubic leucite (Table 5.3, Figure 5.22). The Kissinger (1956) equation was used for the calculation of the activation energies as a crystallisation mechanism assumption-free method. Due to the absence of DSC crystallisation peaks for glass B5 and two crystalline phases present in glasses A and C the activation energies for the crystallisation of these glasses were not calculated.

An activation energy value of 125 KJ·mol^{-1} was found by Zhang et al., (2007) who crystallised a leucite precursor using a sol-gel process. A higher activation energy value of 319 KJ·mol^{-1} was found by Tošić et al., (2000) for leucite crystallising in a fluorine containing glass. The calculated activation energies of 213.3 KJ·mol^{-1} for glass B and 176.6 KJ·mol^{-1} for glass B4 (Table 5.2) are within this range of reported values. The glass B4 composition was designed after taking into

account quantitative SEM image analysis data of glass B for the leucite area fraction. This area fraction was translated into weight fraction using the glass B and leucite densities. The corresponding quantities of K_2O, Al_2O_3 and SiO_2 for the leucite were then subtracted from the initial glass B composition. The alumina content of the residual composition was then further reduced, theoretically bringing the composition closer to the leucite stoichiometry. The amounts of K_2O, Al_2O_3 and SiO_2 (for leucite) that were subtracted initially were then added back in to provide the B4 glass composition. The lower activation energy of the B4 glass in respect to B may be consistent to this alteration in composition being closer to the leucite stoichiometry. The drop in T_g from 580 °C for glass B, to 567 °C for glass B4 (Table 5.1) is also consistent with the compositional changes. Reducing alumina in aluminosilicate glasses with alumina to modifier content ratio of 1 or less further reduces this ratio. This, in turn, reduces network connectivity by creating more non-bridging oxygens in the network (de-polymerisation) (Shelby, 2005b) lowering T_g (Sadhukhan et al., 1999) and activation energy. Glass B4 was the intermediate step between B and B5. When designing glass B5, all theoretically remaining alumina in the residual glass was deducted after the corresponding oxide amounts for crystallised leucite had been subtracted, potentially further limiting the capacity of leucite crystallisation. Glass B5 has an even lower T_g than glass B4 (558 °C, Table 5.1) and this may imply an even lower activation energy according to the previous argument about alumina reduction and de-polymerisation of the glass network. No activation energy however could be calculated for glass B5 due to the absence of DSC crystallisation peaks. The copious leucite crystallisation (45.4% area fraction,

Table 5.10) and the absence of crystallisation peaks may indeed suggest even lower activation energy for glass B5. The absence of DSC exothermic peaks may also be an indication of relatively small structural rearrangements taking place during crystallisation of this glass involving small energy exchanges with the environment. A nanocrystalline glass structure could potentially be responsible for this, beyond the detection limit of XRD. Future nuclear magnetic resonance and/or transmission electron microscopy studies could verify this view.

6.3 Effect of Ca/Ti synergy on nucleation of B1– B3 glasses

Cattell et al., (2009) witnessed the presence of a Ca and Ti rich domains possibly associated with leucite and sanidine crystallisation in aluminosilicate glasses. Glasses B1, B2 and B3 were formulated to have 1:1, 2:2 and 3:3 molar percent (Table 4.2) of Ca/Ti content versus the non equal molar content (2.7:0.5) present in the glass B (Table 4.1). This would potentially determine the Ca/Ti synergy in leucite crystallisation. Glass transition temperatures of the glasses increased with increasing Ca and Ti content (Table 5.1). The T_g increase indicates changes in the network connectivity towards more linked configurations (Shelby, 2005). Increases in the coordination of the network former (Sadhukhan et al., 1999) with associated reduction in non bridging oxygen availability can be responsible for these changes. Coordination changes of 4-fold to 6-fold for silicon did not impose a barrier to nucleation in a silicon phosphate glass (Weeding et al., 1985) confirming Zachariasen's (1932) idea that a 6-fold coordination would induce octahedral configuration leading to crystallisation (see Table 2.1). In order however for a similar claim to be raised for the current B1 - B3 glass compositions, Magic Angle Spinning – Nuclear Magnetic Resonance (MAS-NMR) studies would have to be carried out to discern the potential changes in silicon and aluminium coordination numbers. The activation energies calculated (Table 5.2, Figure 5.11) also increase in line with glass transition temperatures (Table 5.1), crystallisation peaks (Figure 5.7) and with Ca and Ti content. This potentially indicates a non favourable crystallisation behaviour, where the amount of nuclei formation is decreased (Xu et al., 1991) rather than increased. The increasing amount of Ca/Ti, while having little effect on

the leucite area fraction of the acquired glass-ceramics (see Table 5.8), seems to effect crystal coalescence and microstructural changes. An increasing fibre-like tetragonal leucite content (Figures 5.45 – 5.47) along with spherulitic and cross shaped structures appear in the microstructure (Figure 5.48). The crystal size significantly increases ($p < 0.001$) with Ca and Ti content increase. Concurrently, the crystal number decreases considerably from 1655/3080 crystals/μm^2 for the glass-ceramic B1 to 737/3080 crystals/μm^2 for the glass-ceramic B3 (Table 5.8). The significant ($p < 0.001$) increase in crystal size and decrease in crystal number between the B and B1 glass-ceramics is also not desirable (Table 5.8). The histogram of the crystal area values (Figure 5.49) further indicates the dramatic decrease in the frequency of smaller crystal area values (positive skew progressively less prominent in the B→B1→B2→B3 direction) consistent with Ca, Ti concentration increase.

Tošić et al., (2000) described the ripening and thickening of leucite crystals when neighbouring fibril tips meet at the diffusion fields (crystallisation fronts). It is possible that the Ca/Ti synergy has actually worked towards producing more sites for nucleation. The progressively higher crystallisation temperatures and thus potentially lower viscosities may however have encouraged copious crystal growth. This claim remains to be investigated in a future study. If there is a synergy of Ca and Ti in the intended 1:1 fashion (e.g. forming a Calcium titanate $CaTiO_3$), the total amount of alkali/alkaline earth glass content is considerably reduced in all the B1-B3 glasses in respect to the glass B composition (Table 4.1 - Table 4.2). In the glass B composition, only a 0.5 molar amount of Ca would be bound to Ti leaving an excess

of 2.2 mole %. This may also be a factor in the T_g – network connectivity increase as a result of reduced availability of modifier cations (Shelby, 2005). Raman spectroscopy may aid the investigation of any early precipitated nucleation-promoting phase as it has been used to quantitatively characterise the nuclei formation and crystallisation in Ti (Sprengard et al., 1998) and Ti/Zr doped aluminosilicate glass-ceramics (Gabel et al., 2004).

6.4 Crystal size optimization

6.4.1 Glass A series

6.4.1.1 Nanoscale powders – crystals

The currently employed high speed ball milling process, after 60 minutes of milling time, yielded glass powder sizes (Table 5.5) that enabled the crystallisation of nanoscale (0.048 μm^2 median area) tetragonal leucite. Bottom-up processes that can produce nano-particles from liquid or gas phases such as sol-gel (Schmidt, 2001), high temperature aerosol (Pratsinis and Vemury, 1996) and plasma reactors (Vollath et al., 1997) may not be feasible, due to the complex multi-elemental composition of glasses (Vital et al., 2008). Sol-gel has however been used to synthesize nanosized leucite powders (0.077 μm), for dispersion in low expansion dental glasses to improve the mechanical properties (flexural strength, fracture toughness) (Yang and Wu, 2003). A glass-ceramic containing 25% volume fraction of this nanoscale leucite yielded a flexural strength of 106 MPa (Yang et al., 2005). In comparison, the smallest sized experimental glass-ceramic APM4 (while not the strongest in this study as discussed in 6.4.1.3) produced a considerably higher mean (SD) biaxial flexural strength of 225.4 (41.8) MPa, at a 27.8% leucite area fraction. Current leucite glass-ceramics in the market present a range of mean biaxial flexural strength values of 88 - 175 MPa (Cattell, 1997b, Albarky et al., 2003, Yilmaz et al., 2007). Rouf et al., (1978) crystallised fine tetragonal leucite crystals (0.1-1 μm) in white-ware alumino-silicate glasses with high modulus of rupture values (200 to 300 MPa) which have only recently been reported for dental leucite glass-ceramics (Chen, 2010). The formulations by Rouf et al., (1978) however had

both high viscosity and opacity that would complicate processing and limit aesthetics if considered for dental applications.

6.4.1.2 High speed milling and leucite crystallisation

The high speed milled glass A powders particle size analysis results show a rapid size reduction for up to 30 minutes milling (Table 5.5). This produced a typical milling time - powder particle size curve (Figure 5.31) (McLaughlin, 1999). Submicron particle interactions during analysis can cause dispersing difficulties of the finer powder sizes (Vital et al., 2008). The slight gradual increase in particle size after 30 minutes milling may be an artefact attributed to such difficulties. Agglomeration is known to happen in milling experiments especially after long milling times (Suryanarayana, 2004). This is a result of the fact that the Van der Waals and electrostatic forces for powder sizes below 100 μm will exceed the single particle weight (Visser, 1989). For fine grinding, wet milling has been suggested to provide better results than dry milling, due to adsorption of the solvent molecules on the surface of newly formed powder particles. This results in a reduction of their surface energy, enabling achievement of finer sizes. Less agglomeration is also reported as an advantage in wet milling (Dolgin et al., 1986).

Agglomeration in the final dry product can also be a result of the drying process employed. Freeze drying was the method of choice for drying, as it has been reported to reduce agglomeration and enhance sintering properties when compared to oven drying (Luan et al., 1998). In this respect, the particle size analysis results provided important complementary information to the actual crystal measurements

in deciding the way forward.

The crystal measurement results from the crystallised milled glass A at the selected milling intervals (0.5 to 4 hours) show a drastic decrease in the median tetragonal leucite crystal area by almost two orders of magnitude, from the starting glass-ceramic A material to the APM4 milled material. In particular, the starting glass-ceramic A presented a crystal median (Q1, Q3) area of 0.836 (0.589, 1.190) μm^2 while the APM4 glass-ceramic reached a nanoscale median (Q1, Q3) crystal area of 0.048 (0.030, 0.070) μm^2 (Table 5.6). Of particular interest is the narrowing of the crystal size range and the uniformity of microstructure (Table 5.6, Figures 5.33, 5.38). The histogram in Figure 5.32 shows a progressively more positive skew in the frequency distributions of the crystal area values from 0.5→1→2→4 hours milling time with the 4 hour planetary milled material (APM4) retaining almost 75% of its crystals below 0.07 μm^2. Homogeneity is also apparent in the dispersion of the crystals in the glassy matrix, the latter showing minimal or no microcracking (Figures 5.34, 5.38). This supports the work of Mackert (2001) where minimised microcracking is effected for a mean leucite crystal diameter of less than 4 μm. The lack of microcracking may also suggest a well matched CTE of the leucite phase with the residual glass phase (Mackert et al., 1994, Denry et al., 1996). On cooling after firing, the high temperature (low CTE) cubic leucite transforms to the low temperature (high CTE) tetragonal phase by expanding along the c-axis and contracting along the a-axis (Mackert, 1988). This leads to the formation of tangential compressive stresses around the crystals which has been linked to significant strengthening in leucite glass-ceramics (Denry et al., 1996). This

transformation is also responsible for the characteristic twinning of leucite (Mazzi et al., 1976, Palmer et al., 1988) which may cause crystal microcracking (Mackert, 1988) observed in the starting A material (Figure 5.33). A combination of favourable CTE glass-crystal matching and tangential compressive stress formation within the microcrack free glassy matrix as a result of reduced crystal sizes, may have synergistically contributed to the significant improvement in flexural strength for the milled A series glasses.

There was also a marked increase in the crystal number as the milling time progressed; from 75/342 crystals/μm^2 for the starting A to 1718/342 crystals/μm^2 for the APM4 (Table 5.6). Particle size changes and induction of sharp edges in large numbers due to the milling, may further minimise the thermodynamic barrier to nucleation enhancing surface crystallisation results (Müller et al., 2000). Surface nucleation of leucite may be difficult to control (Höland et al., 1995). The results of the current study however, strongly support that controlled leucite surface crystallisation via particle size reduction is achievable and in agreement with Cattell et al., (2006) and Chen et al., (2010). The currently applied planetary milling regime proved to be more efficient in size reduction than the attritor milling regime used previously, as it produced significantly ($p < 0.001$) smaller crystallites in 0.5 hours (APM0.5 group) than the attritor produced in 4 hours (A-AM4 group)(Table 5.6). Planetary milling in this glass system enabled successful control over the crystallisation of uniform nanoscale materials.

6.4.1.3 Biaxial Flexural Strength and reliability

The homogeneity of leucite reinforced dental ceramic materials has been shown to correlate with high fracture strengths (Shareef et al., 1994, Assmann et al., 2000). Material homogeneity was evident in all attritor/ planetary milled A series glass-ceramics (Figures 5.34 – 5.38). Zhang et al., (2008) has suggested that sub-micrometer sized leucite particles cannot further improve the reliability of dental porcelain as surface defects and inevitable porosity will determine strength in the absence of microcracks. The results of the current study indicated no significant ($p > 0.05$) differences in the reliability between the planetary milled groups and the IPS Empress Esthetic material. Similar flaw type populations may thus be present in these materials which need to be verified by fractographic analysis (Quinn and Quinn, 2010). The IPS Empress Esthetic material is a current generation commercial market leader and is a heat pressed material. The manufacturer claims its biaxial flexural strength (ISO 6872) to be at 160 MPa (IPS Empress, 2006) and this is in agreement with the results in Table 5.14 (165.5 MPa). The Ceramco 3 material, although highly reliable with an m value that was significantly ($p < 0.05$) higher than all other tested materials apart from the A-AM4 HP, was of significantly ($p < 0.05$) lower strength [Mean (SD): 75.7 (6.8) MPa], suggesting a minimal reinforcement by the presence of crystalline tetragonal leucite. The large crystal sizes, in-homogeneity of leucite crystals dispersion, the presence of significant microcracks (Figure 5.98 a) along with a potential crystal – matrix CTE mismatch may account for this result (Assmann et al., 2000, Mackert et al., 2001, Sınmazışık and Öveçoglu, 2006, Cattell et al., 2006). Sınmazışık and Öveçoglu (2006) found a

mean (SD) BFS of 66.02 (4.95) MPa for Ceramco 3. Ceramco 3 is a market leader sintered material that was chosen because of its microstructure and method of fabrication as a commercial reference material. Heat pressing when compared to sintering has been shown to increase the flexural strength and reliability of dental glass-ceramics (Cattell et al., 2001). This may account for the high reliability of the A-AM4 HP (heat pressed) group which was however not significantly different to the reliability of the highest mean (SD) BFS test group APM2 at 255.0 (35.0) MPa (Table 5.15) which was sintered. The APM2 HP group however, was of similar ($p > 0.05$) reliability and significantly ($p < 0.05$) lower BFS than its sintered counterpart (APM2) while it was of similar ($p > 0.05$) BFS with the APM4 material. Fractographic analysis of the test specimens and especially the low failures may further elucidate these findings. The longer milling time of the APM4 material, may however also be related to the presence of zirconia, yttria and hafnium contamination introduced during milling (Suryanarayana et al., 2001, Kong et al., 2001), since both media and milling pots are made of yttria stabilised zirconia. Chen (2010) experienced similar contamination related reliability/ strength drops in the same glass-ceramic system after long attritor milling. Some ion mobility may be present during wet milling as evidenced by the ion-exchange experiments of the glass A/H_2O (section 6.6) and the glass-ceramic A-AM0.5/ $RbNO_3$ (section 6.7) carried out in the current thesis. Zirconium has been shown to change its coordination state and take part in glass networks (Farges et al., 1991). The exact phenomenon is however not elucidated by the results of the current study. Media contamination is a known issue in ball milling experiments (Boldyrev and Tkácová, 2000). Wet milling may be responsible for

more contamination of the milled powder when compared to dry milling. Depending on the application, contamination may be a disadvantage, although in some cases it can be removed if for example the contaminant is magnetic (Suryanarayana, 2004). In the case of zirconia however, no practical solution is applicable that could supply us with a clean milled glass powder.

The APM2 and A-AM4 materials produced glass-ceramics with significantly different median crystal areas ($p < 0.001$) (Table 5.6). This made them the ideal choice for wear testing as they could potentially show the effect of reducing crystal size on wear (discussed in 6.8). The fact that they were both produced from the same parent glass eliminated any composition related wear factors.

6.4.2 Glass B series

6.4.2.1 High speed milling and leucite crystallisation

The high speed milling had a distinct microstructural effect on the crystallisation of the B series glasses. Initially there was a 10% crystal number drop after the first hour of milling, accompanied by a 50% drop in crystal size ($p < 0.001$, Table 5.7). After 2 hours of milling however, the crystal number increased by 25% in respect to the starting B, accompanied by a further reduction in crystal size to a final median (Q1, Q3) of 0.136 (0.063, 0.388) μm^2 (Table 5.7). The histogram in Figure 5.44 shows a general similarity in the distributions of the starting B and the high speed milled BPM0.5 and BPM1 materials, while the BPM2 has a distinct increase in the frequency of the smallest sizes. The evolution of the microstructure from a mixed rounded and fibre-like tetragonal leucite structure (Figures 5.39, 5.40) to an

interconnected “embroidery”- like morphology (Figure 5.43), may imply a glass particle size dependant crystallisation mechanism. Tošić et al., (2000) described the presence of particle size dependant shifts of bulk to surface leucite crystallisation for particle sizes below 75 μm in an aluminosilicate glass.

As explained in detail in section 6.2, Glass B5 was designed based on the B composition but with a reduced alumina amount to reduce the area fraction of crystallising leucite. This method produced a 15% reduction in the leucite area fraction (Table 5.10). The microstructure of the glass-ceramic B5 however had large glassy areas (Figure 5.52), interspersed within areas of dense crystalline dispersion. The latter presented a mixed morphology of tetragonal leucite crystals (Figure 5.54). While no microcracking was observed within the glassy matrix that interpenetrated the crystalline leucite network (Figure 5.55), microcracking was present within the un-reinforced glassy areas (Figure 5.53). The leucite reinforced areas, have a CTE intermediate to that of the glass or the leucite. During cooling of the heat treated glass-ceramic, the higher CTE leucite reinforced areas will tend to contract more than the lower CTE glassy areas. The microcracking in the large glassy areas is therefore the result of the presence of tensile stresses due to this CTE difference (Mackert et al., 1994). The high speed milling had a profound homogenising effect on the microstructure resulting in the elimination of the glassy areas and accompanying microcracking (Figure 5.56, Figure 5.57). The reduction in the leucite area fraction and in the crystal interconnectivity was evident in both the B5 and B5PM0.5 materials when compared to their B starting and BPM2 high speed milled counterparts (Figures 5.59, 5.60). The B5PM0.5 material also had 40% more crystals than the starting B5

material. A similar increase was not achieved in the B glass-ceramic even after 2 hours of milling, possibly due to crystal coalescence (Tošić et al., 2000).

The B4 material, which was an intermediate step between the B and B5 materials, also showed a leucite area fraction reduction. The considerable (~70%) decrease in crystal number and the significant ($p < 0.001$) increase in median crystal area in comparison to the starting B glass-ceramic (Table 5.9), did not however make it a promising candidate for optimisation. Alumina content reduction in aluminosilicate glasses with alumina to modifier content ratio of 1 or less reduces this ratio and in turn network connectivity (de-polymerisation) (Shelby, 2005). The considerably higher heat treatment temperature compared to the glass-ceramic B (924 versus 804°C) may have contributed towards higher growth rates by reducing the viscosity. An Ostwald (1896) ripening mechanism where larger crystals grow at the expense of smaller maintaining a constant volume fraction (Höland et al., 2000) could be responsible.

6.4.2.2 Biaxial Flexural Strength and reliability

Zhang et al., (2009) did compressive testing of dental leucite glass-ceramics with varying leucite volume fraction and found a threshold of 50% leucite volume fraction above which significant reductions of compressive strength occurred. Cesar et al., (2006) indicated that porcelains can benefit in terms of characteristic BFS from high volume fractions of leucite, only if it is homogenously distributed and of low particle size. Mackert et al., (2001) suggested that the crystal size threshold below which matrix microcracking disappears, is 4 μm. Beham (2003) however claims a three-point bending strength of 200 MPa for a very high leucite volume fraction (90%) needle and rod shaped dental glass-ceramic material. Glass B had fibre-like leucite structures with long axis sizes reaching a maximum of 15 μm and a significant crystallite amount having sizes above 4 μm in at least one dimension (Figure 5.39). At the same time, it exhibited a microcrack-free matrix containing the highest leucite area fraction measured in the current study (59.7%, Table 5.7), in a mixed morphological distribution. The ability of the glass to be thermally matched to the crystal phase achieving glass compression (Denry et al., 1996), may have led to its high mean (SD) BFS of 210.6 (33.8) (Table 5.16). Optimisation of its properties was explored in the current study by attempting both compositional and processing adjustments. All glass-ceramics tested from the B series (B, BPM2 and B5PM0.5) were found to have no significant differences in BFS ($p > 0.05$) (Table 5.16). The starting glass-ceramic B and the high speed milled B5PM0.5 were found to have significantly higher ($p < 0.05$) median/ characteristic BFS than both commercial glass-ceramics (IPS Empress Esthetic, Ceramco 3). The BPM2 was found to have

significantly higher ($p < 0.05$) strength than the Ceramco 3 group, while no significant difference ($p > 0.05$) was found against the IPS Empress Esthetic. It appears that the microstructural changes observed after milling in both the BPM2 and B5PM0.5 did not provide benefits towards strength increases. The results however are promising as the flexural strengths achieved are higher than the commercial glass-ceramics tested and other current commercial leucite containing glass-ceramics (88 - 175 MPa) reported in the literature (Cattell et al., 1997a, Albakry et al., 2003, Yilmaz et al., 2007). Metzler et al., (1999) indicated that finer grained leucite glass-ceramics caused less wear to enamel antagonists than coarser grained varieties. This finding is supported by the findings of the current study as significantly ($p < 0.05$) lower enamel loss (volume and mean-height) was found against both fine and nanosized experimental glass-ceramics (A-AM4 HP, APM2 HP) compared to the coarser grained Ceramco 3 material (discussed in detail in 6.8). The optimised morphologies achieved for the high speed milled B and B5 materials should also be wear tested against human enamel in a future study. The lower area fraction B5PM0.5 material may prove to be beneficial compared to BPM2 in that respect as it could potentially expose less leucite area during function. As it requires considerably less milling time (1.5 hours less) than the BPM2 material it is likely to have less amounts of contaminants (Suryanarayana et al., 2001, Kong et al., 2001). A typical probability of failure s-curve behaviour for the B5PM0.5 glass-ceramic (Figure 5.85) suggests a single type critical flaw population present (Addison et al., 2007, Fleming et al., 2004, Quinn and Quinn, 2010). Glass-ceramic B exhibited an m value of 8.1 and, as a result, a less tilted probability of failure curve

(Figure 5.85). This m value was however not significantly different than both the BPM2 and B5PM0.5 glass-ceramics. The Weibull fit for glass-ceramic B was poor (r^2 = 0.87) as the failure plot had asymmetries (Figure 5.85) that may be attributed to mixed defect mechanisms. Fractographic analysis is however critical to confirm these assumptions (Quinn and Quinn, 2010).

Further microstructural optimisation of the crystal sizes and distributions that were attempted in the glass B composition by Ca/Ti addition (Glasses B1 – B3, discussed in 6.3) were not successful. Future flexural strength testing is necessary to assess the biaxial flexural strength of these glass-ceramics. Increased nucleation may be more beneficial in the B5 glass that is of lower leucite volume fraction in order to avoid crystal impingement and coalescence. Further crystallisation studies should therefore be attempted in modified glass B compositions as its potential is believed to be not fully exploited currently.

6.4.3 Glass C series

Glass C was designed to have a CTE intermediate to that of A and B glasses. The growth heat treatment of glass C had to be limited to 30 minutes (Table 4.4), as pilot crystallisation studies showed the occurrence of increased crystal growth at longer holding times. Glass C contains B_2O_3 in the composition. Boron is a network former and can be three or four fold coordinated into triangles or tetrahedra (Kingery, 1976). Its coordination state may affect glass viscosity due to the glass network connectivity (Du et al., 2004), and in turn the kinetics of the leucite crystal growth. Nuclear magnetic resonance could be a useful tool in quantitatively identifying the

coordination state of Boron (Vogel, 1985b) and other elements (O, Si, Al) to confirm these observations.

Glass-ceramic C had mixed rounded and fibre-like fine [median (Q1, Q3) μm^2: 1.843 (0.883, 3.376)], tetragonal leucite morphology and some matrix microcracking (Figure 5.63). Nevertheless the BFS testing results were promising as a significantly higher ($p < 0.05$) median/ characteristic strength was found compared to both commercial glass-ceramics tested (Tables 5.16, 5.17). The mean BFS strength (229.7 MPa, Table 5.16) was also considerably higher than other leucite containing market materials reported in the literature (Mean BFS values of 88 - 175 MPa (Cattell et al., 1997a, Albakry et al., 2003, Yilmaz et al., 2007)). It is possible that the minimal matrix microcracking experienced was in a size range that was smaller than the critical flaw size (Janssen et al., 2002). The possible presence of competing flaw type populations (Figure 5.84) will be verified in future fractographic analysis (Quinn and Quinn, 2010). The high speed milled CPM0.5 glass-ceramic presented a considerably more homogenised microstructure than the starting C material lacking fibre-like tetragonal leucite crystals and matrix microcracking (Figures 5.61 – 5.65). A doubling in crystal number (from 629/3080 crystals/μm^2 to 1307/3080 crystals/μm^2) and a 40% decrease in crystal size was achieved as a result of the high speed milling. The histogram of the crystal area frequencies also shows the narrowing of the size range and the considerably larger occurrence of smaller crystal sizes (Figure 5.66), in comparison to the starting C material. Since there was also no noteworthy change in the area fraction (Table 5.11), this result may suggest a surface crystallisation mechanism being dominant in this system. Future BFS

testing will be carried out to identify the potential effect of the microstructural changes on the biaxial flexural strength.

6.5 Comparative experimental glass-ceramic BFS studies

The experimental glass-ceramics with the highest BFS values were statistically compared (Tables 5.18 – 5.19). The reliability of all groups was not found to be significantly different ($p < 0.05$). The statistical analysis indicated that the highest median/ characteristic strength group, was the nanoscale material AMP2 with a mean (SD) BFS of 255 (35) MPa. The range of flexural strength values achieved is well within the range first proposed by Rouf et al., (1978) who used nucleating agents to crystallise fine tetragonal leucite crystals (0.1-1 μm) in opaque white-ware alumino-silicate glasses (200 to 300 MPa). The materials produced in this study are of high aesthetic potential due to their inherent translucency. Interestingly the BFS values achieved are over a range of considerably different microstructures and leucite area fractions. Microstructures span from mixed rounded, elongated fibre-like (B, C glass-ceramics, Figures 5.39, 5.40, 5.61, 5.62) and spherulitic shapes (B5PM0.5 glass-ceramic, Figure 5.57) to rounded nanosized crystallites (APM2 glass-ceramic, Figure 5.37). The leucite area fractions range from 28 – 60% (Tables 5.6, 5.10, 5.11) with the lowest area fraction APM2 material giving the highest biaxial flexural strength (Tables 5.18 – 5.19). The strengthening mechanism of leucite in a glass-ceramic is multifactorial and may explain these findings. The temperature dependant cubic to tetragonal transformation of leucite (Deer et al., 1969) and the associated discontinuous unit cell volume change (Mackert et al.,

1986) are responsible for the generation of tangential compressive stresses around the leucite crystals (Denry et al., 1996). These stresses can strengthen the surrounding glassy matrix, as they further alter crack trajectories (Denry et al., 1996), by enhancing crack pinning/ deflection mechanisms present in composite systems (Lange, 1970, 1971). Strain calculations using the unit cell dimensions in Table 5.4 as per Chen et al. (2010), can provide insight for the nature and extent of these stresses in respect to those present in the commercial materials. Stresses that result in matrix microcracking formation can deplete the elastic stored strain energy and thus limit any strengthening effect (Denry et al., 1996). The tangential compressive stresses are developed during cooling of the heat treated material through the transformation temperature to room temperature. Alleviation of these stresses by suppressing the transformation as a result of ion-exchange, significantly reduced strength in a caesium containing leucite glass-ceramic (Denry et al., 1996). The relationship of the glass matrix T_g with the leucite transformation temperature is also key to the development and maintenance of these stresses (Lee et al., 1997). While the transformation can also cause microcracking especially along the expanding c-axis and crystal-matrix de-bonding (Mackert, 1988), crystal-matrix thermal matching can suppress this effect (Lee et al., 1997). Incorporation of small rather than large crystallites in the glassy matrix, especially at sizes below 4 μm (Mackert et al., 2001), also leads to microcracking minimisation with accompanied strength improvements in composite systems (Davidge and Green, 1968, Shareef et al., 1994). The compositional range explored in this study is thus within a “window” that permits the development of the attained high strength microcrack-free glass-

ceramics as a result of both thermal and microstructural characteristics.

The cumulative failure probability plot in Figure 5.86 may suggest a generally typical s-curve behaviour for all tested groups. A tendency of the starting groups (B and C) to exhibit more interrupted P_f patterns than the optimized groups (APM2, B5PM0.5) is noted, however no significant ($p > 0.05$) differences amongst m values was detected (Tables 5.18, 5.19). The P_f curve of the IPS Empress Esthetic material is included in this plot to accentuate the significantly ($p < 0.05$) lower strength of a material that is amongst the strongest current commercial leucite glass-ceramic products. Concurrently, its P_f distribution can be considered comparable with the experimental groups tested (especially the optimised APM2 and B5PM0.5 groups) in terms of the agreement between the modelled curve (based on calculated Weibull m and characteristic strength σ_0) and the actual P_f level of the failed specimens (based on their median BFS ranking and the number of specimens tested, eq. 25, pg 89). Fractographic analysis would be useful in further evaluation of the flaw types associated with failure (Quinn and Quinn, 2010) and will be performed in a future study. The BFS results indicate the strong potential of the developed materials to prove beneficial if commercially developed.

6.6 Ion exchanging of starting glass A

The milling experiment of starting glass A powder with the 1M KNO_3 solution was done in an attempt to saturate the surface of the glass grains with K^+ ions as a result of alkali ion-exchange (e.g. Li^+ and Na^+). This could influence the reactivity of the glass powder to promote nucleation (Rouf et al., 1978). It was hoped that, during subsequent heat treatment stages, excess potassium could be provided at the surface, close to nucleation sites such as interfacial boundaries between grains.

The elimination of KNO_3 from the powders after milling was verified by the FTIR result (Figure 5.67), as no nitrate associated absorption band was detected in the spectrum of the washed glass A/KNO_3 powder. The detection limit for the instrument was 1% (Personal communication, Perkin Elmer UK). The absorption bands found in both glass A/KNO_3 and glass A/H_2O washed powder samples in the region around 1000 cm^{-1} are attributed to the Si-O-Si bridging found in dental aluminosilicate glasses (Gritco et al., 2005).

The quantitative results of the ion-exchange chromatography (Table 5.12) showed that, in both the control powder milled in deionised water (glass A/H_2O) and the powder milled with the KNO_3 solution (glass A/KNO_3), K^+ and Na^+ ions were leached. No uptake of K^+ was detected in the glass A/KNO_3 with more K^+ leached from the glass A/KNO_3 than the control (A/H_2O). It is assumed that a hydrolysis effect was more intense than any ion exchanging effect. Dental glasses, although generally quite inert, are known to leach ions when in contact with water or aqueous solutions (Jakovac et al., 2006). Static leaching experiments are employed to study the dissolution of elements from glasses in aqueous environments with given pH,

temperature and defined time (Farges et al., 2007). In the dynamic environment of a high speed ball mill, fresh particle surfaces are constantly exposed bringing more glass surface in contact with water thus potentially accelerating dissolution effects. Milling in a KNO_3 solution close to saturation may have to be employed to suppress this elution and encourage ion-exchange. It may also however be possible that the energy supplied in the current milling regime was not sufficient for the ion-exchange to occur.

6.7 Ion exchanging of glass-ceramic A-AM1.5

The milling experiment of glass-ceramic A-AM1.5 powder with the 2.5M $RbNO_3$ solution was done in an attempt to ion-exchange Rb^+ for smaller sized alkali ions (e.g. K^+ or Na^+), from interstitial sites in the structure of the leucite present in the glass-ceramic. This could stabilise the cubic variety of leucite to room temperature (Denry et al., 1998), leading to reduced glass-ceramic thermal expansion (Hermansson and Carlsson, 1976, Rouf et al., 1978). The objective was to produce a nano-sized leucite glass-ceramic veneering material thermally compatible (CTE-matched) with zirconia substrates used in Dentistry.

An exchange process of Rb^+ with Na^+ and K^+ ions was evidenced in the material milled with the $RbNO_3$ solution by EDS (Table 5.13, Figure 5.75) as a reduction in Na^+ and K^+ was accompanied by the appearance of Rb^+ in the sample compared to the H_2O milled control. The XRD plots however identified the presence of only tetragonal and not cubic leucite in both milled samples (Figure 5.76). Therefore the exchange process occurred only within the residual glass phase without stabilising

any fraction of leucite present (or at least not more than 1% which is the detection limit of the XRD technique) to its cubic variety. More importantly however, the milling experiment produced significant amounts of zirconia contamination in both milled materials as evidenced by all techniques used (SEM, EDS, XRD) to characterise the samples (Figures 5.70 – 5.75). This suggests that the current milling regime is not optimised for these glass-ceramic powders. The milling speed used for this experiment was at the limits recommended by the planetary mill manufacturer for the specific media size used. Lower speed would provide even less energy for the exchange to proceed according to Eq. 18 (Kano et al., 1999) (pg. 64) and this would not be favourable according to the current results. Therefore the reactive ball milling approach was regarded as not feasible for the intended purpose in this case. Melt methods have been used to crystallise cubic leucite in rubidium or caesium aluminosilicate glass systems (Brodkin and Panzera, 2000). Similar glasses should be explored in a future study. Such glasses may benefit from the milling regimes applied to the glass systems of the current thesis in manufacturing a nano-sized cubic leucite glass-ceramic.

6.8 Wear Testing

6.8.1 Testing apparatus

The protocol suggested in the study of Magne et al., (1999) was the basis for the experimental setup. Modifications were made to the test method. The MTS 858 used in this study is equipped with one actuator which is capable of both axial and torsional force control in contrast to Magne et al., (1999) setup where the MTS used (812 series) incorporated a horizontal and a vertical actuator. Special jigs were developed that would bear three teeth styli in the form of a tripod as an upper member, so that the load could be evenly distributed. Three glass-ceramic discs were supported from the lower member jig (Figure 4.4 and Appendix 5). In the current setup, both the onset and ending of each loading (lower part of square waveform, Figure 5.87) were synchronized with the onset and ending of each uni-directional sweeping motion of the tooth on the disc surface. This enabled clear unloading during the return of the tooth specimen to its start position over the disc. A similar range of values was recorded in the current thesis with those of the study of Magne et al., (1999). Within the limitations mentioned this finding may act in support of the adopted design and testing regime. The current results may also be considered as considerably more precise, as for the wear evaluation, step sizes of 20 x 20 μm (x,y, teeth) or 30 x 30 μm (x,y, glass-ceramic discs) were used versus 50 x 100 μm (x,y) used by Magne et al., (1999).

6.8.2 Counter sample choice and preparation

Prepared flat human enamel has been used in various wear studies as the reference antagonist material (Hacker et al., 1996, Ramp et al., 1997, Metzler et al., 1999, O'Kray and O'Brien, 2005). Such specimens suffer unrealistic high wear rates as the remaining prepared enamel is thin and the underlying dentin is exposed during testing (Heintze, 2006). In studies where cusps had been prepared and standardized to retain sufficient enamel thickness for the test, less test variation and inconsistency was still reported for unprepared cusps (Krejci et al., 1999, Heintze et al., 2008). The removal of aprismatic enamel during preparation (20 – 100 µm thickness, Whittaker, 1982), may be responsible for these changes in wear properties (Krejci et al., 1999). Other potentially contributing factors can be the changes in enamel properties from its surface towards the amelodentinal junction such as density (Weidmann et al., 1967), elastic modulus, hardness (Zhou and Hsiung, 2007) and fracture toughness (Bajaj and Arola, 2009). The depth-dependant changes in properties have been found to correlate with the local changes in microstructure and more importantly localised composition (Cuy et al., 2002). The use of an enamel substitute (steatite) has been suggested by Wassel et al., (1994) as an attempt to standardize antagonists. Krejci et al., (1999) however rejected its use as clinically irrelevant. Based on the above mentioned literature, unprepared human enamel cusps were the antagonistic material of choice in the current thesis as the more clinically relevant solution. The selection of the tooth cusps was attempted to meet the standards set by Heintze et al., (2008) so that

huge variations of results due to demineralisations, surface defects and most importantly pointed cusp configurations would be avoided. Pointed configurations have been reported to cause significantly higher rates of both enamel wear (Krejci et al., 1992) and material wear (Condon and Ferracane, 2003), when compared to cupola shaped cusps. This is due to more fatigue stress caused on the material as a result of smaller surface area in contact (Heintze et al., 2008). Deionised water was selected as the conditioning medium of choice to narrow the test parameters, but also because saliva effects on wear cannot be reproduced *in vitro* (Heintze, 2006). Polishing or glazing of a ceramic restoration can influence the wear rate at the onset of wear, however as wear advances no influence is present (Metzler et al., 1999, Heintze et al., 2008). Turssi et al., (2005) found no effect of surface finish / roughness on abrasive wear after 100000 simulated masticatory cycles although 300000 cycles were used in the current study. Based on these observations, a simple surface flattening and standardization protocol (P600 grit finish) was adopted for the tested materials in the current thesis since the main interest was to identify the material effect on antagonistic enamel wear.

6.8.3 Wear quantification method

The sensor chosen for the wear quantification measurements in this study was mainly chosen based on its measuring range (3.5 mm) and its high axial resolution (75 nm). The axial distance to be measured on the teeth samples in order to include the tooth cusp, the surface of the embedding resin and the reference marks was a

maximum of 2 mm (Figure 4.3a). Axial resolution in this type of sensors increases as the working range decreases (Cohen-Sabban et al., 2001). Use of a smaller working range sensor would potentially require axially segmented scanning to include the full specimen height without significant gain in resolution. The maximum wear facet depth recorded on the glass-ceramic discs did not exceed 250 μm, thus a lower working distance sensor could have been chosen to increase axial resolution; the same sensor however was used for both glass-ceramic discs and tooth samples to ensure inter-measurement consistency.

The sampling rate of 30 Hz was chosen after a series of scans at all available frequencies (30, 100, 300 and 1000 Hz), which revealed that the slower the sampling rate, the less missing data appeared on the scans. The scans at 30 Hz eliminated missing data almost completely which whenever present were interpolated using the Proscan 2000 software. The slow sampling rate adopted was thus mainly dictated by the reflectivity of glass-ceramic/ tooth samples, both being translucent thus light scattering surfaces (Cohen-Sabban et al., 2001). Remaining missing data generally appeared either in 90° angles (e.g. areas between the embedding resin and the cusp cylindrical walls) or in locally high sloped surfaces. The latter may be attributed to the limitation of the sensor itself as its specifications include a maximum angular slope of 22° for specular surfaces, although this can be increased up to 80° for scattering surfaces (Cohen-Sabban et al., 2001). Laser techniques, although much faster, require either coating the surfaces to be scanned or the fabrication of plaster replicas (Heintze et al., 2006). In contrast to laser

techniques, white light Profilometry enabled the actual specimens' surfaces to be digitised potentially introducing less systematic errors in the acquired measurements.

The S16/3.5 sensors' lateral resolution (x,y) is quoted as 4 μm (STIL-SA, 2008), therefore the step sizes investigated (10, 20, 30, 50 and 100, Appendix 6) were well within the sensor's capabilities. The wear testing setup used in this study and most of the parameters (No of cycles, applied force, cuspal lateral excursion) were based on a setup used previously by Magne et al., (1999), where the artificial oral simulator of De Long et al., (1991) was utilised. De Long et al., (1991) correlated simulated wear results (250000 cycles) in their simulator to 1 year of *in vivo* mastication (Lambrechts et al., 1985, Sakaguchi et al., 1986). Magne et al., (1999) quantified volume and mean-height loss of human enamel and dental glass-ceramics, using a tungsten carbide contact sensor and a considerably lower x,y spatial resolution (50 x 100 μm), with results in the same range as the present study. Kramer et al., (2006) reported that 10 – 25 μm step sizes can lead to reliable results with mechanical (contact) sensors. A resolution of 4 x 4 μm x,y of a white light sensor was found to be in good agreement to a >30 x 30 μm x,y resolution of a laser sensor (Heintze, 2006), when both were applied to quantify volume loss in the same glass-ceramic and composite disc specimens. Hara et al., (2008), used a step size of 10 x 100 μm (Proscan 2000) to investigate the erosive potential of beverages on enamel. The selected step sizes of 20 x 20 μm for tooth and 30 x 30 for glass-ceramic disc samples are therefore within the range of step sizes suggested in the

literature for similar applications and materials.

The Automated measurements (Table 5.21), significantly ($p < 0.05$) under-estimated the mean-height loss in both tooth and glass-ceramic discs, supporting the use of the experimental protocol. In particular, 27.9% less mean-height tooth loss and 69.4% less mean-height disc loss was measured using the Automated regimen. The very satisfactory fit achieved on the disc samples resulted in an (almost) zero difference area around the wear facets (Figure 4.6 b). There was thus no need to delete the area around the disc wear facets for the volume calculation. This explains the absence of difference for the mean volume loss values measured on discs, via both the experimental and automated procedures (Table 5.21). The only difference in procedure is that the automated disc volume loss values were measured by the Proform software and the experimental from the Proscan software. This demonstrates the good agreement between the two different pieces of software. To limit any potentially systematically induced error, our protocol standardisation was limited to a 3 x 3 mm^2 area which was ample to include the wear area. The apparent overestimation of the tooth volume loss by the automated measurements (Table 5.21), failed to differentiate ($p > 0.05$) from the experimental measurements, suggesting that the experimental protocol may not provide an added benefit in the volume loss calculation. In the author's opinion, although no significant difference was detected, exclusion of volume from areas around the area of interest (Figure 4.10) was preferable. A potential error source is the accuracy of the utilized sensor. The accuracy of white light sensors is continuously being

improved to achieve sub-micron levels (tested maximum linearity error for the S16/3.5 sensor is 0.4 μm, (STIL-SA, 2008). The accuracy of measurements is thus much more likely to be affected by systematically induced errors and should therefore be considered in wear quantification protocol designs.

6.8.4 Wear testing results evaluation

The results of the Kruskal-Wallis One Way ANOVA on ranks gave statistically ($p < 0.05$) higher antagonistic tooth volume, height and mean-height loss for the Ceramco 3 commercial glass-ceramic when compared to the experimental A-AM4 HP and APM2 HP groups. The microstructural features of the A-AM4 HP and APM2 HP groups show an even dispersion of rounded leucite crystals with sub-micron and nanoscale sizes (Figure 5.98b, c and Table 5.6). On the contrary, Ceramco 3 has been reported to have a range of leucite crystal sizes of 1 – 7 μm with irregular morphology (Sınmazışık and Öveçoglu, 2006) as can also be seen in Figure 5.98a. The resultant surface after wear on the representative enamel antagonists presented herein appears to have increased abrasion and damage for the Ceramco 3 glass-ceramic disc - tooth group when compared to both experimental glass-ceramic disc - tooth groups (Figures 5.90 – 5.95). This trend was also illustrated by the indicative R_a and wave height values acquired; these were lower for the A-AM4 HP and APM2 HP glass-ceramic disc - tooth groups evaluated (Table 5.22). The A-AM4 HP glass-ceramic disc - tooth group exhibited a smoother, non-oriented wear pattern in contrast to the Ceramco 3 glass-ceramic disc - tooth group that exhibited

a distinct coarse patterned wear profile with parallel grooves. This was supported by both qualitative topographic observations (Figure 5.96 a-d, Figure 5.97 a-d) and by the dissimilar indicative x and y mean R_a and wave height values (Table 5.22). The SEI evaluation of APM2 HP glass-ceramic disc - tooth group also seems to attribute a smoother non-oriented wear profile compared to the Ceramco 3 group (Figure 5.97 a, b, e, f). The closer profilometric examination however revealed some marked wear pattern on the APM2 HP tooth sample (Figure 5.96f). This observation seems to agree with the higher AMP2 HP tooth x and y mean R_a and wave height values in comparison to the A-AM4 tooth (Table 5.22) The values however are still lower than the Ceramco 3 group. These findings may suggest that the coarser microstructure of the Ceramco 3 glass-ceramic material (Figure 5.98) is responsible for increased wear of the enamel antagonists. The experimental A-AM4 HP and APM2 HP glass-ceramics appear to be friendlier to enamel in this respect. Furthermore, the smallest crystal size of the APM2 HP material may be a factor for the significantly less ($p < 0.05$) enamel wear than the A-AM4 HP material in height and mean-height loss (Table 5.22). These findings agree with those of Metzler et al., (1999) who proposed that a coarser microstructure increases the wear of enamel antagonists. Reduced enamel wear is certainly a matter of clinical importance (Hacker et al., 1996). Maintaining natural enamel reduces the need for further patient treatment due to pain as a result of dentine exposure (Anderson, 1975, Bartlett and Smith, 2000) or due to aesthetic and/or functional reasons (McIntyre, 2000). The glass-ceramic material loss between all groups did not

however produce statistically significant differences ($p > 0.05$) in the variables tested (Table 5.20). The multi factorial nature of wear may be in support of this result as microstructure in isolation cannot determine the wear behaviour of a material (Chinnasamy et al., 2001). The interesting and promising outcome is that both experimental materials wear the antagonistic enamel less than the commercial material, and at the same time they themselves do not wear faster than the commercial material.

When comparing the relative wear of the tooth versus its antagonistic material (Table 5.20) there is a trend for the tooth to wear more than the glass-ceramic material in the case of Ceramco 3. In the case of the experimental groups however, the opposite trend where the tooth wears less than the glass-ceramic is found. These trends are shown graphically in Figures 5.88 – 5.89. These trends fail to differentiate in the case of volume loss for Ceramco 3 and of mean-height loss for both experimental groups. This may be due to the largely overlapping data populations in the mentioned cases as can partly be seen in Figures 5.88 – 5.89. Nevertheless, significantly ($p < 0.05$) more enamel than disc mean-height loss is recorded for Ceramco 3 while significantly ($p < 0.05$) less enamel than disc volume loss is recorded for both experimental groups. These findings may have clinical importance as it can be suggested that the experimental materials will wear at either equal or higher rate than the opposing enamel. In an *in vivo* situation restoration wear rate should approximate that of enamel (Seghi et al., 1991). This is to benefit patients as it is more desirable to replace a restoration than to restore tooth

structures. Clinical trials are however necessary to confirm the *in vitro* results discussed. Taking into account the *in vitro* limitations of the study, the findings of this study can be of clinical importance as they could support the use of the APM2 HP and in turn the A-AM4 HP glass-ceramic materials to achieve reduced rates of cuspal structure loss and, ultimately, facial height loss (Pintado et al., 1997, Chacona, 2003).

7. Conclusions

Nanosized (median crystal area: 0.048 μm^2) tetragonal leucite glass-ceramics with uniform microstructures and minimal or no microcracking were successfully synthesized. A nanosized experimental material (median crystal area: 0.055 μm^2) produced the highest ($p < 0.05$) mean (SD) biaxial flexural strength [255.0 (35.0) MPa] amongst all experimental and commercial glass-ceramics. This may help to address problems with brittle fracture of dental all-ceramic restorations.

A range of experimental glass-ceramics (B, B5, C series) with significantly higher ($p < 0.05$) mean (SD) BFS values [192.5 (44.0) – 229.7 (40.4)] than commercial materials were synthesized. These materials produced a wide variety of microstructures (spheres, fibres) and leucite volume fractions and minimal or no matrix microcracking. The processing of all the synthesized experimental materials was achieved using conventional dental porcelain furnaces. Further optimisation of these materials could provide a range of useful Dental restorative products.

A new method for crystal growth temperature selection by utilisation of HTXRD data in the absence of DSC crystallisation peaks (e.g. glass B5) was proposed and successfully applied. This method may be useful for the exploration of the crystallisation behaviour of similar glass systems.

A new wear quantification methodology for dental glass-ceramics and human enamel using white light profilometry was designed. The new method was proven to provide repeatable results and could be beneficial for similar applications and

materials in Medicine and Dentistry.

The regimen used during the reactive ball milling regimes did not prove beneficial in ion-exchanging the glass and glass-ceramic powders investigated. Stabilisation of cubic leucite by this route was not achieved.

The fine and nano-sized experimental leucite glass-ceramics synthesized in the current study produced significantly ($p < 0.05$) lower enamel wear than a commercial material containing larger and more irregular leucite crystals. Within the *in vitro* limitations of this study, these findings may be of clinical importance as these materials could be used to achieve reduced wear rates of antagonistic human enamel.

8. Future Work

- The sintered glass ceramics synthesized should be processed using currently available heat pressing techniques. The effects on microstructure/ strength/ reliability and wear against enamel should be then explored. Fracture toughness measurements should also be carried out for all the synthesized materials.
- Fractographic analysis of failed flexural strength tested specimens should be carried out to characterise the fracture process and fracture origins. This may further inform the statistical findings of the Weibull analysis carried out in the current study.
- Strain calculations based on the changes in the leucite unit cell dimensions should be performed. These may inform the development of optimum residual stresses that can be responsible for the significant strengthening encountered in the synthesized materials.
- Systematic crystallisation kinetic studies of intermediate glass compositions from A→B→C should be pursued to further inform the observed microstructural evolution differences between these glasses, in order to identify the effect of subtle compositional changes on strength.
- Magic Angle Spinning – Nuclear Magnetic Resonance (MAS-NMR) studies should be carried out in B1-B3 glass compositions to discern the potential changes in silicon and aluminium coordination numbers and their effects on nucleation. Raman spectroscopy may further aid this investigation for detecting the precipitation of a Ca/Ti nucleation-promoting phase.

- A nuclear magnetic resonance and/or transmission electron microscopy study on glass B5 may be useful in establishing the presence of a nanocrystalline structure. This would cast light on its copious crystallisation behaviour while having no DSC crystallisation peaks.
- Caesium and Rubidium aluminosilicate glasses should be investigated for synthesis of cubic leucite containing glass-ceramics. Such systems may benefit from the milling regimes applied to the glass systems of the current thesis in manufacturing a nano-sized cubic leucite glass-ceramic.

9. APPENDIX

Appendix 1: Appen Factors for glass properties prediction.

Oxides	Thermal Expansion Coefficient (α) Appen Factors (x 10^{-6}/K, 20-400°C)	Fusion Temperature (°C, Winkelmann and Schott)
SiO_2	0.5 to 3.8	6.161
$Al2O_3$	-3.0	34.585
K_2O	46.5 (42.0)	783.92
CaO	13.0	885.046
TiO_2	-1.5 to -3.0	-79.806
Na_2O	39.5	670.233
Li_2O	27.0	
MgO	6.0	1125.698
B_2O_3	-5	

For some Appen Factors , the following remarks apply:

SiO_2: when $67 \le p_{SiO_2} \le 100$, $\alpha_{SiO_2} = 10.5 - 0.1 \cdot p_{SiO_2}$,

when $p_{SiO_2} \le 67$, $\alpha_{SiO_2} = 3.8$,

K_2O: the values in parentheses only apply to glass

with composition of $p_{Na_2O} < 1\%$,

TiO_2: when $50 \le p_{SiO_2} \le 80$, $\alpha_{TiO_2} = 10.5 - 0.15 \cdot p_{SiO_2}$

B_2O_3: when the proportion of

{([Na_2O]+[K_2O]+[BaO])+0.7([CaO]+[SrO]+[CdO]+[PbO])+0.3([Li_2O]+

[MgO]+[ZnO])-[Al_2O_3]}/[B_2O_3] >4, $\alpha_{B_2O_3}$ = -5.0, otherwise, Appen can be

calculated by -1.25 times the above proportion.

The weight percentage of oxides p_i is expressed in mole percentage (Scholze and Lakin, 1991).

Appendix 2: Details of the reagents used for the glass batching.

Reagent	Description	Manufacturer	Lot No
Kasil ® SS Pwd	Potassium silicate (SiO_2/K_2O = 2.50)	The PQ Corporation, Valley Forge, USA	11-904w -112804
SS 20 ® Pwd	Sodium silicate (SiO_2/Na_2O = 3.22)		11-139w -110305
Aluminium oxide	Purity: 99.9%	Fluka, Germany	1270233
Calcium carbonate	Purity: >= 99.0%	Fluka, Italy	21060
Lithium carbonate	Purity: >= 98.0%	Fluka, USA	62372
Titanium (IV) oxide	Purity: >= 99.8%	Sigma-Aldrich, USA	232033 (07119ED)
Magnesium oxide	Desiccant beads, Purity: >= 98.0%	Sigma-Aldrich, USA	220361 (08907BD)
Silica sand		Glassworks service Ltd, UK	
Boric anhydride	Purity: >= 97.0%	Sigma-Aldrich, USA	1231246

Appendix 3: Example of a glass Particle Size Analysis graph showing positive skew and multimodal distribution.

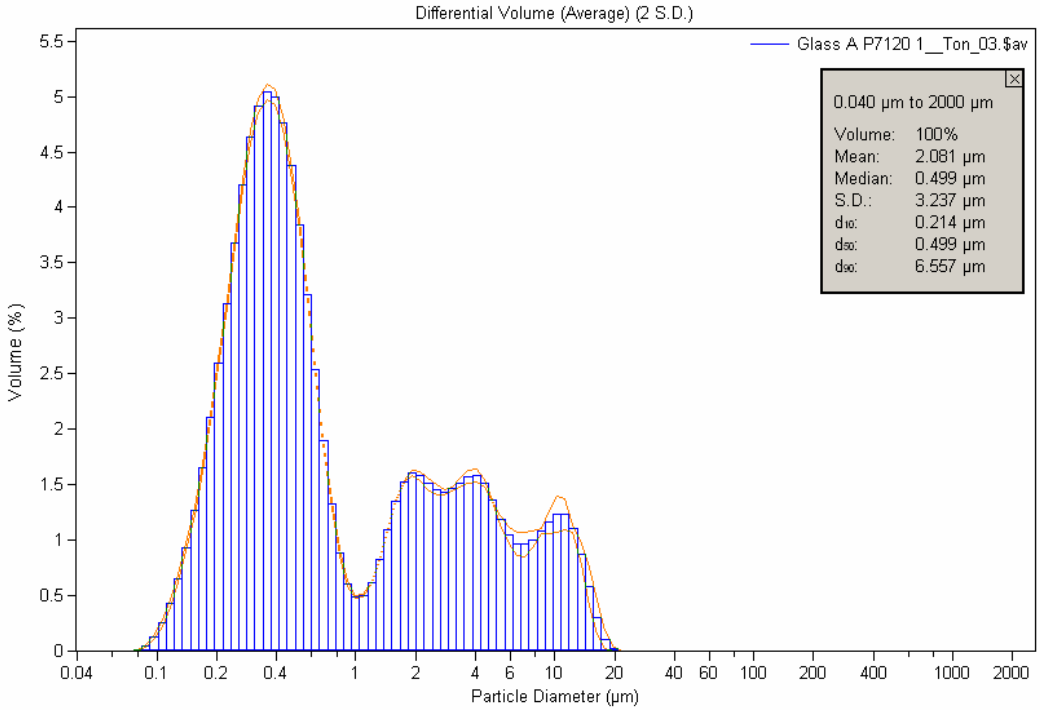

Appendix 4: HTXRD furnace calibration.

The furnace was calibrated by comparing the temperature measured by the Pt/Pt-10% Re thermocouple and that of known highly pure compounds.

- Alfa Aesar Sodium Chloride Puratonic 99.999% pure
- Alfa Aesar Potassium Sulphate Puratonic 99.997% pure
- Alfa Aesar Potassium Iodide Puratonic 99.999% pure
- Alfa Aesar potassium Nitrate Puratonic 99.997% pure
- Optically pure Rock Quartz from Madagascar

The known phase changes or decompositions used were (Weast, 1978):

- KNO_3 phase change at 129°C
- KNO_3 melting point at 334°C
- Quartz phase change at 573°C
- KI melting point at 681°C
- NaCl melting point at 801°C
- K_2SO_4 melting point at 1076°C

The following formulae relating the true temperature to the measured temperature were obtained by least squares fitting for the 6 points used.

$$T(Meas)=0.9211*T(True)+9.6218\ (°C)\ r^2=0.9999 \quad (1)$$

$$T(True)=1.0856*T(Meas)-10.378\ (°C)\ r^2=0.9999 \quad (2)$$

Appendix 5: Wear testing jig design.

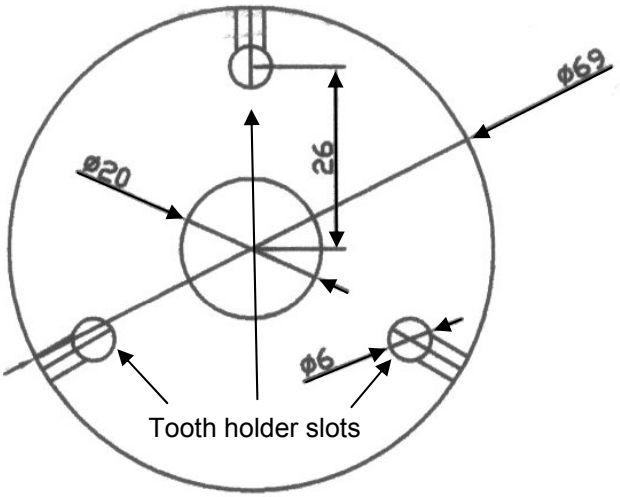

Figure 9.1: Top jig planar view.

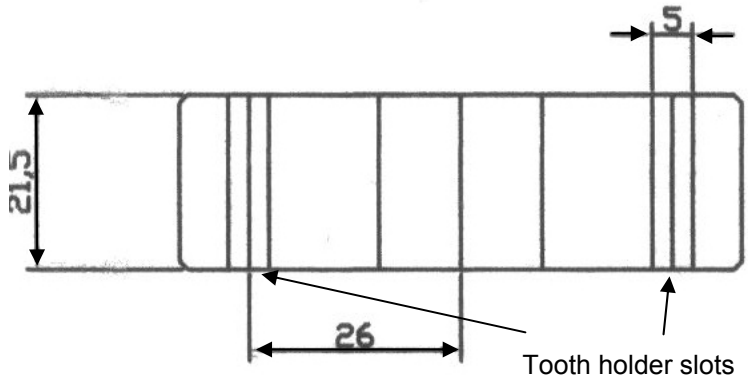

Figure 9.2: Top jig cross section.

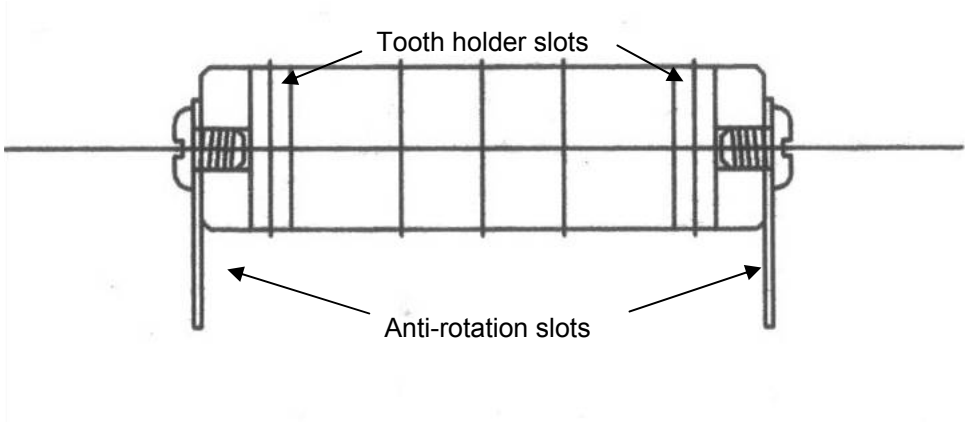

Figure 9.3: Top jig with anti-rotation slots in place.

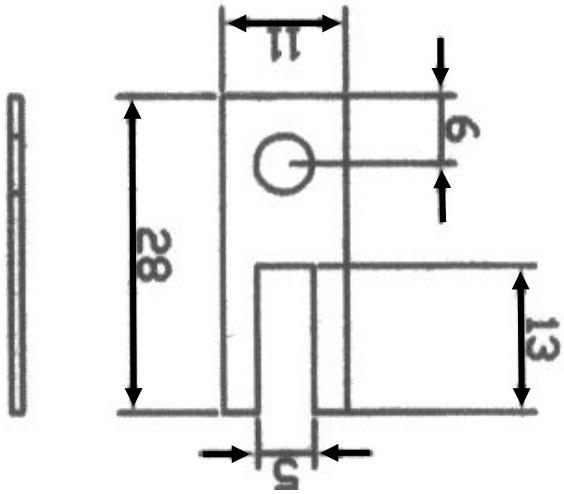

Figure 9.4: Anti-rotation slot.

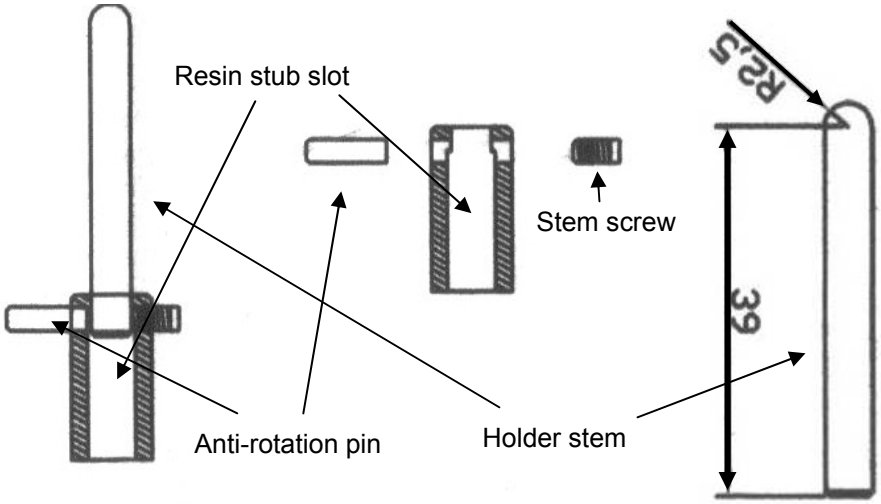

Figure 9.5: Tooth holder.

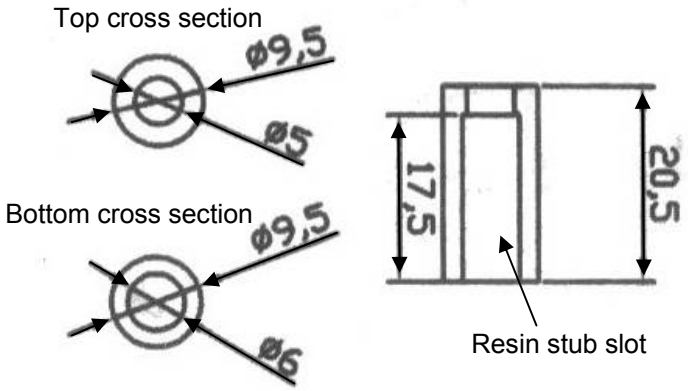

Figure 9.6: Tooth holder cross-sections.

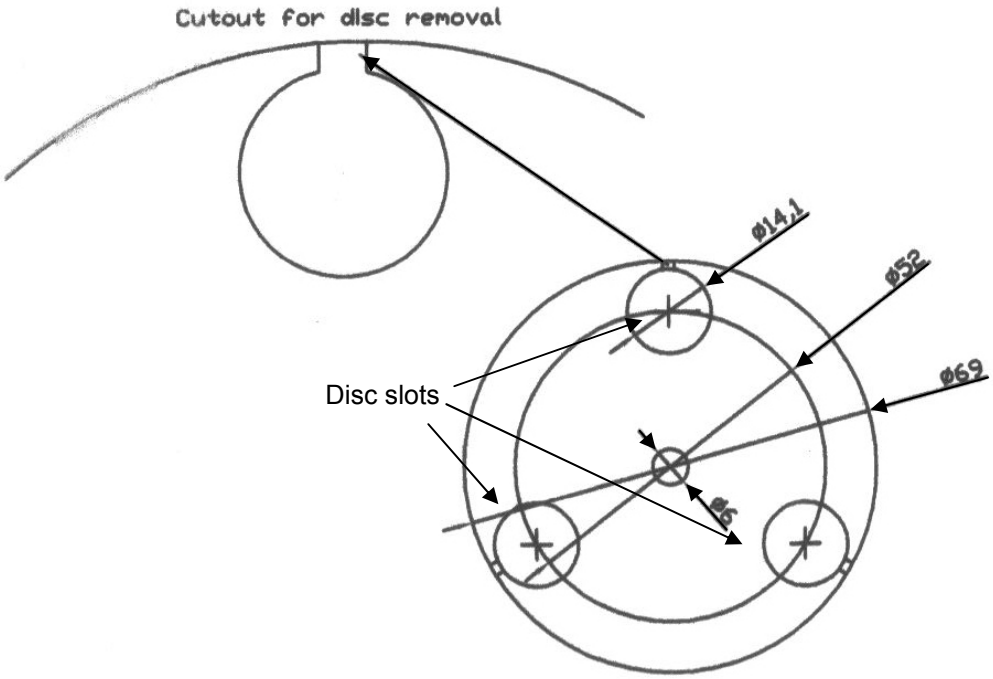

Figure 9.7: Lower jig – 3 disc holder top view with detail for disc removal cut-out.

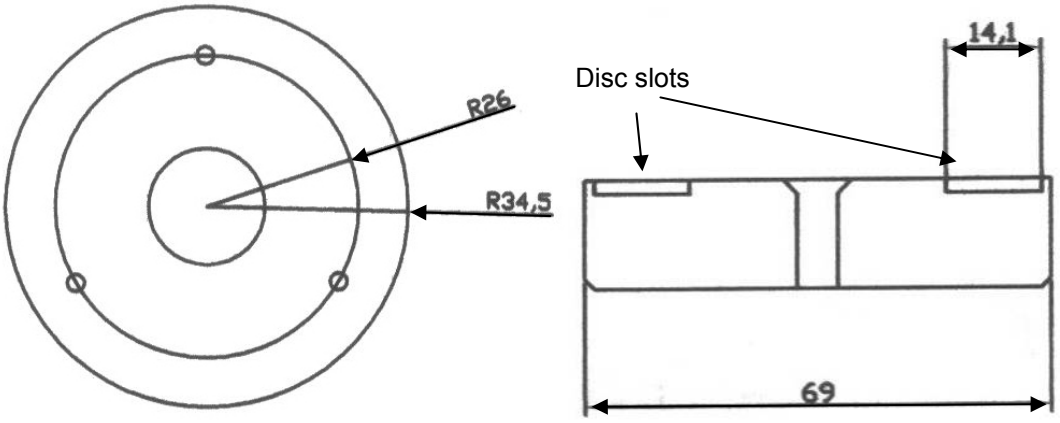

Figure 9.8: Lower jig (a) bottom view and (b) cross section.

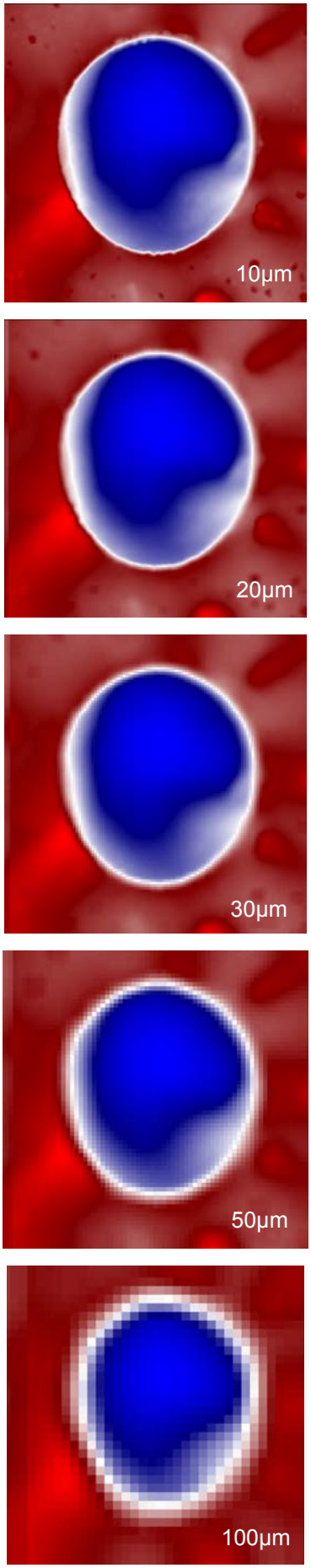

Appendix 6:
Profilometry step size selection scans for the tooth sample (10, 20, 30, 50 and 100 µm).

Appendix 7: Profilometry filters

Warpage filter

This filter is used to remove the surface noise or roughness from the entire scan. The general shape is therefore acquired. The operation of the warpage filter utilises the Rolling Rectangular Filter principle. In the picture below, each circle represents a scan data point. When a warpage filter of 1 is used, the points enclosed by the red line (1 step size away in all directions) are averaged and the result of the averaging is placed into the point shown as black. We next move on to the next point, until all of the scan points have been filtered. For higher warpage filters of 2, 3 etc, the red line extends to 2, 3 etc step sizes to include more points.

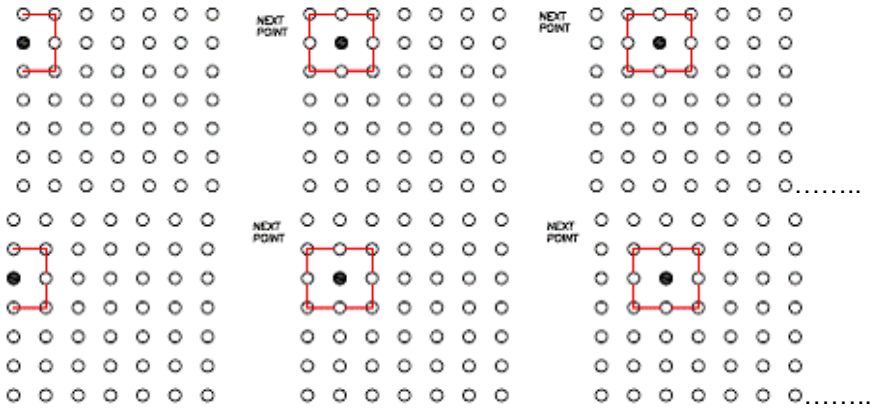

Surface filter

This filter removes the underlying general shape of an object, leaving just the surface features/roughness. The principle is shown in the picture below. It works by applying a warpage filter to the original profile. The warped profile (shape associated information) is then subtracted from the original profile, and the resultant final profile is displayed.

Original scan

Shape associated information

Shape associated information subtracted

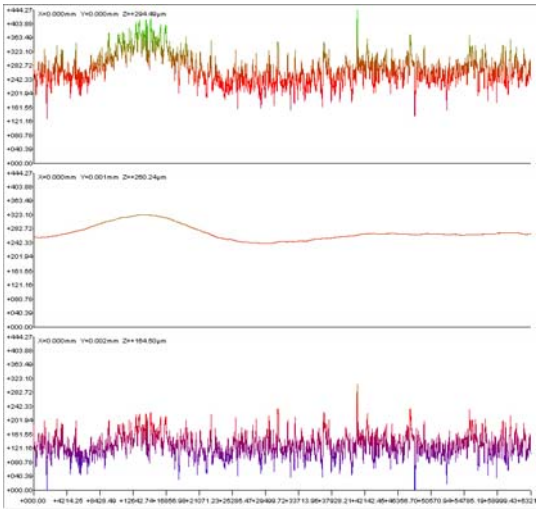

Pictures reprinted with permission from: Scantron Industrial Products Ltd., Taunton, UK.

10 . References

Açil, Y., Mobasseri, A. E., Warnke, P. H., Terheyden, H., Wiltfang, J. & Springer, I. (2005). Detection of mature collagen in human dental enamel. *Calcified Tissue International,* 76**,** 121-126.

Adair, P. J. & Grossman, D. (1984). The castable ceramic crown. *International Journal of Periodontics and Restorative Dentistry* 4**,** 32-46.

Addison, O., Marquis, P. M. & Fleming, G. J. P. (2007). Resin elasticity and the strengthening of all-ceramic restorations. *Journal of Dental Research,* 86**,** 519-523.

Addy, M. & Shellis, R. P. (2006). Interaction between attrition, abrasion and erosion in tooth wear. IN: Lussi, A. (Ed.) *Dental Erosion, Monographs in Oral Science.* Basel, Switzerland, Karger,17-31.

Albakry, M., Guazzato, M. & Swain, M. V. (2003). Biaxial flexural strength, elastic moduli, and X-ray diffraction characterization of three pressable all-ceramic materials. *The Journal of Prosthetic Dentistry,* 89**,** 374-380.

An, J.-S., Park, J.-S., Kim, J.-R., Hong, K. S. & Shin, H. (2006). Effects of Bi_2O_3 and Na_2O on the thermal and dielectric properties of zinc borosilicate glass for plasma display panels. *Journal of the American Ceramic Society,* 89**,** 3658-3661.

Anderson, D. J. (1975). Pain from dentine and pulp. *British Medical Bulletin,* 31**,** 111-114.

Anusavice, K. J., Kakar, K. & Ferree, N. (2007). Which mechanical and physical testing methods are relevant for predicting the clinical performance of ceramic-based dental prostheses? *Clinical Oral Implants Research,* 18**,** 218-231.

Appen, A. A. (1961). Toward the method for calculating the properties of glass. *Glass and Ceramics (Steklo I Keramika),* 18**,** 235-237.

Aronne, A., Catauro, M. & Pernice, P. (1995). Bulk and surface crystallisation of lead tetragermanate glass. A DTA study. *Thermochimica Acta,* 259**,** 269-275.

Arrhenius, S. (1889). *"Uber die reaktionsgeschwindigkeit bei der inversion von rohrzucker durch sauren"* (On the reaction velocity of the inversion of cane sugar by acids). *Zeitschrift für Physikalische Chemie,* 4**,** 226–248.

Arsecularatne, J. A. & Hoffman, M. (2010). On the wear mechanism of human dental enamel. *Journal of the Mechanical Behavior of Biomedical Materials,* 3**,** 347-356.

Assmann, S., Ermrich, M. & Kunzmann, K. (2000). Determination of quantitative leucite content in pressable ceramics compared to conventional dental porcelains. *Journal of Materials Science: Materials in Medicine,* 11**,** 833-835.

ASTM (2005). "Standard Terminology of Glass and Glass Products" C162-05. ASTM International, West Conshohocken, PA, www.astm.org.

Bajaj, D. & Arola, D. D. (2009). On the R-curve behaviour of human tooth enamel. *Biomaterials,* 30**,** 4037-4046.

Baldassarri, M., Margolis, H. C. & Beniash, E. (2008). Compositional determinants of mechanical properties of enamel. *Journal of Dental Research,* 87**,** 645-649.

Ban, S. & Anusavice, K. J. (1990). Influence of test method on failure stress of brittle Dental materials. *Journal of Dental Research,* 69**,** 1791-1799.

Baricco, M., Chierici, E., Battezzati, L., Braglia, M., Dai, G., Kraus, J. & Mosso, S. (2001). Nucleation and growth of crystals in a ZBLYALiPb glass. *Journal of Non-Crystalline Solids,* 289**,** 144-150.

Barreiro, M. M., Riesgo, O. & Vicente, E. E. (1989). Phase identification in dental porcelains for ceramo-metallic restorations. *Dental Materials,* 5**,** 51-57.

Barry, T. I., Clinton, D., Lay, L. A., Mercer, R. A. & Miller, R. P. (1969). The crystallisation of glasses based on eutectic compositions in the system Li_2O-Al_2O_3-SiO_2. *Journal of Materials Science,* 4**,** 596-612.

Bartlett, D. W. & Smith, B. G. N. (2000). Definition, classification and clinical assessment of attrition, erosion and abrasion of enamel and dentine. IN: Addy, M., Embery, G., Edgar, M. & Orchardson, R. (Eds.) *Tooth wear and sensitivity.* London, UK, Martin Dunitz Ltd,87-92.

Basu, B., Tiwari, D., Kundu, D. & Prasad, R. (2009). Is Weibull distribution the most appropriate statistical strength distribution for brittle materials? *Ceramics International,* 35**,** 237-246.

Basudeb, K., Paritosh, K., Sunirmal, J. & Ravindra, N. D. (2002). Crystallization kinetics and mechanism of low-expansion lithium aluminosilicate glass-ceramics by dilatometry. *Journal of the American Ceramic Society,* 85**,** 2572-2574.

Becker, R. (1940). On the formation of nuclei during precipitation. *Proceedings of the Physical Society,* 52**,** 71-76.

Beham, G. (1990). IPS-Empress: A new ceramic technology. *Ivoclar-Vivadent Report* 6**,** 1-13.

Beham, G. (2003). Glass-ceramic material for dental restoration and method for producing same. US Patent 6,527,846 B1.

Berenbaum, R. & Brodie, I. (1959). Measurement of the tensile strength of brittle materials. *British Journal of Applied Physics,* 10**,** 281-287.

Binns, D. (1983). The chemical and physical properties of dental porcelain. IN: McLean, J. W. (Ed.) *Dental Ceramics Proceedings of the First International Symposium on Ceramics.* Chicago, IL, USA, Quintessence Publishing Co.,48-56.

Boldyrev, V. V. & Tkácová, K. (2000). Mechanochemistry of Solids: Past, Present, and Prospects. *Journal of Materials Synthesis and Processing,* 8**,** 121-132.

Boyde, A. (1967). The development of enamel structure. *Proceedings of the Royal Society of Medicine,* 60**,** 923.

Bragg, W. (1928). *An introduction to crystal analyses*. London, G.Bell and Sons, Ltd.,1-19.

Brodkin, D. & Panzera, C. (2000). Cubic leucite-containing dental porcelains. US Patent 6,090,194.

Broughton, J. Q. & Gilmer, G. H. (1983). Molecular dynamics investigation of the crystal-fluid interface. I. Bulk properties. *The Journal of Chemical Physics,* 79**,** 5095-5104.

Burk, B. & Burnett, A. P. (1978). Leucite-containing porcelains and method of making same. US Patent 4,101,330.

Calamia, J.R. & Simonsen, R.J., (1984). Effect of coupling agents on bond strength of etched porcelain. *Journal of Dental Reaserch*, 63**,**179, Abstract 79.

Carrier, D. D. & Kelly, J. R. (1995). In-Ceram failure behaviour and core-veneer interface quality as influenced by residual infiltration glass. *Journal of Prosthodontics,* 4**,** 237-242.

Cattell, M. J., Chadwick, T. C., Knowles, J. C. & Clarke, R. L. (2005). The crystallization of an aluminosilicate glass in the K_2O-Al_2O_3-SiO_2 System. *Dental Materials,* 21**,** 811-822.

Cattell, M. J., Chadwick, T. C., Knowles, J. C. & Clarke, R. L. (2009). The development and testing of glaze materials for application to the fit surface of dental ceramic restorations. *Dental Materials,* 25**,** 431-441.

Cattell, M. J., Chadwick, T. C., Knowles, J. C., Clarke, R. L. & Lynch, E. (2001). Flexural strength optimisation of a leucite reinforced glass ceramic. *Dental Materials,* 17**,** 21-33.

Cattell, M. J., Chadwick, T. C., Knowles, J. C., Clarke, R. L. & Samarawickrama, D. Y. D. (2006). The nucleation and crystallization of fine grained leucite glass-ceramics for dental applications. *Dental Materials,* 22**,** 925-933.

Cattell, M. J., Clarke, R. L. & Lynch, E. J. R. (1997a). The biaxial flexural strength and reliability of four dental ceramics - Part II. *Journal of Dentistry,* 25**,** 409-414.

Cattell, M. J., Clarke, R. L. & Lynch, E. J. R. (1997b). The transverse strength, reliability and microstructural features of four dental ceramics - Part I. *Journal of Dentistry,* 25**,** 399-407.

Cattell, M. J., Knowles, J. C., Clarke, R. L. & Lynch, E. (1999). The biaxial flexural strength of two pressable ceramic systems. *Journal of Dentistry,* 27**,** 183-196.

Cesar, P. F., Yoshimura, H. N., Miranda Jr, W. G., Miyazaki, C. L., Muta, L. M. & Filho, L. E. R. (2006). Relationship between fracture toughness and flexural strength in dental porcelains. *Journal of Biomedical Materials Research Part B: Applied Biomaterials,* 78B**,** 265-273.

Chacona, R. L. (2003). Enamel loss and occlusal vertical dimension. Causes and considerations for treatment. *Dentistry Today,* 22**,** 92-97.

Chadwick, R. G. & Mitchell, H. L. (2001). Conduct of an algorithm in quantifying simulated palatal surface tooth erosion. *Journal of Oral Rehabilitation,* 28**,** 450-456.

Chen, X. (2009). The controlled crystallisation of high strength leucite glass ceramics. *Institute of Dentistry, Barts and The London School of Medicine and Dentistry.* PhD Thesis, London, Queen Mary University of London.

Chen, X., Chadwick, T. C., Wilson, R. M., Hill, R. & Cattell, M. J. (2010) Crystallization of high-strength fine-sized leucite glass-ceramics. *Journal of Dental Research*, 89, 1510-1516.

Cheng, M., Chen, W. & Sridhar, K. R. (2003). Biaxial flexural strength distribution of thin ceramic substrates with surface defects. *International Journal of Solids and Structures,* 40, 2249-2266.

Cheung, K. C. & Darvell, B. W. (2002). Sintering of dental porcelain: effect of time and temperature on appearance and porosity. *Dental Materials,* 18, 163-173.

Chinnasamy, C. N., Narayanasamy, A., Ponpandian, N., Joseyphus, R. J., Chattopadhyay, K., Shinoda, K., Jeyadevan, B., Tohji, K., Nakatsuka, K. & Greneche, J. M. (2001). Ferrimagnetic ordering in nanostructured $CdFe_2O_4$ spinel. *Journal of Applied Physics,* 90, 527-529.

Christian, P. A. & Mao, O. (2002). Mechanochemical synthesis of lithiated manganese dioxide. US Patent 6,403,257 B1.

Clifford, A. & Hill, R. (1996). Apatite-mullite glass-ceramics. *Journal of Non-Crystalline Solids,* 196, 346-351.

Coble, R. L. (1970). Diffusion models for hot pressing with surface energy and pressure effects as driving forces. *Journal of Applied Physics,* 41, 4798-4807.

Cohen-Sabban, J., Gaillard-Groleas, J. & Crepin, P.-J. (2001). Quasi-confocal extended field surface sensing. *Optical Metrology Roadmap for the Semiconductor, Optical, and Data Storage Industries II.* San Diego, CA, USA, SPIE, 178-183.

Condon, J. R. & Ferracane, J. L. (2003). Effect of antagonist diameter on *in vitro* wear of dental composite. *Journal of Dental Research,* 82 (Spec Iss A), Abstract 954.

Creyke, W. E. C., Sainsbury, I. E. J. & Morrell, R. (1982). *Design with non-ductile materials*. Barking, UK, Applied Science Publishers Ltd., 85-87.

Cullity, B. D. & Stock, S. R. (2001). *Elements of X-ray Diffraction,* 3rd ed. Upper Saddle River, NJ, USA, Prentice Hall,89-94, 101-103,106-118,182, 275-280.

Cuy, J. L., Mann, A. B., Livi, K. J., Teaford, M. F. & Weihs, T. P. (2002). Nanoindentation mapping of the mechanical properties of human molar tooth enamel. *Archives of Oral Biology,* 47, 281-291.

Davidge, R. W. & Green, T. J. (1968). The strength of two-phase ceramic/glass materials. *Journal of Materials Science,* 3**,** 629-634.

de Chemant, D. N. (1804). A dissertation on artificial teeth in general. London.

Deer, W. A., Howie, R. A. & Zussman, J. (1969). *An introduction to the rock-forming minerals*. New York, John Wiley and sons Inc., 367-375.

Della Bona, A., Anusavice, K. J. & DeHoff, P. H. (2003). Weibull analysis and flexural strength of hot-pressed core and veneered ceramic structures. *Dental Materials,* 19**,** 662-669.

DeLong, R. & Douglas, W. H. (1983). Development of an artificial oral environment for the testing of dental restoratives: bi-axial force and movement control. *Journal of Dental Research,* 62**,** 32-36.

DeLong, R. & Douglas, W. H. (1991). An artificial oral environment for testing dental materials. *IEEE Transactions on Biomedical Engineering* 38**,** 339-345.

Denry, I. L., Holloway, J. A. & Rosenstiel, S. F. (1998). Effect of ion-exchange on the microstructure, strength, and thermal expansion behaviour of a leucite-reinforced porcelain. *Journal of Dental Research,* 77**,** 583-588.

Denry, I. L., Mackert, J. R., Jr., Holloway, J. A. & Rosenstiel, S. F. (1996). Effect of cubic leucite stabilization on the flexural strength of feldspathic dental porcelain. *Journal of Dental Research,* 75**,** 1928-1935.

Dietzel, A. Z. (1942). ‘‘Die Kationenfeldstarken und ihre Beziehungen zu Entglasungsvorgangen, zur Verbindungsbildung und zu den Schmelzpunkten von Silikaten’’. *Z. Elektrochemie,* 48**,** 9-23.

Dietzel, A. Z. (1983). On the so-called mixed alkali effect. *Physics and Chemistry of Glasses,* 24**,** 172-180.

Dolgin, B. P., Vanek, M. A., McGory, T. & Ham, D. J. (1986). Mechanical alloying of Ni, CO, and Fe with Ti. Formation of an amorphous phase. *Journal of Non-Crystalline Solids,* 87**,** 281-289.

Doremus, R. H. (1973). *Glass science*. New York, NY, USA, Wiley-Interscience, 1, 80-87.

Dorsch, P., Fesseler, A. & Pfeiffer, T. (1994). Influence of test conditions on biaxial strength of dental ceramic. Journal of Dental Research, 73, 980, Abstract 331.

Du, L. S., Allwardt, J. R., Schmidt, B. C. & Stebbins, J. F. (2004). Pressure-induced structural changes in a borosilicate glass-forming liquid: boron coordination, non-bridging oxygens, and network ordering. *Journal of Non-Crystalline Solids,* 337**,** 196-200.

Einstein, A. (1926). *Investigations on the theory of the Brownian movement*. London, Methuen, 68-75.

Elliott, S. R. (1983). *Physics of amorphous materials*. London, UK, Longman, 1984, 5.

Esquivel-Upshaw, J., Young, H., Jones, J., Yang, M. & Anusavice, K. (2006). *In vivo* wear of enamel by a lithia disilicate-based core ceramic used for posterior fixed partial dentures: first-year results. *The International Journal of Prosthodontics,* 19**,** 391.

Etman, M. K., Ferenczi, L. & Woolford, M. J. (2006). Tooth wear and wear of ceramic restorations: Prospective clinical study. *Journal of Dental Research,* 85 (Spec Iss A)**,** Abstract 215.

Etman, M. K., Woolford, M. & Dunne, S. (2008). Quantitative measurement of tooth and ceramic wear: *in vivo* study. *International Journal of Prosthodontics,* 21**,** 245-252.

Farges, F., Etcheverry, M. P., Haddi, A., Trocellier, P., Curti, E. & Brown Jr, G. E. (2007). Durability of Silicate Glasses: An Historical Approach. *X-ray Absorption Fine Structure - XAFS 13,* 882**,** 44-50.

Farges, F., Ponader, C. W. & Brown, G. E. (1991). Structural environments of incompatible elements in silicate glass/melt systems: I. Zirconium at trace levels. *Geochimica et Cosmochimica Acta,* 55**,** 1563-1574.

Fisher, J. C., Hollomon, J. H. & Turnbull, D. (1948). Nucleation. *Journal of Applied Physics,* 19**,** 775-784.

Flegler, S. L., Heckman, J. W. J. & Klomparens, K. L. (1993). *Scanning and transmission electron microscopy: An introduction*. New York, NY, USA, W.H. Freeman and Company, 1-3, 17-19, 65-75.

Fleming, G. J. P., El-Lakwah, S. F. A., Harris, J. J. & Marquis, P. M. (2004). The influence of interfacial surface roughness on bilayered ceramic specimen performance. *Dental Materials,* 20**,** 142-149.

Fleming, G. J. P. & Narayan, O. (2003). The effect of cement type and mixing on the bi-axial fracture strength of cemented aluminous core porcelain discs. *Dental Materials,* 19**,** 69-76.

Frankenheim, M. L. (1835). *"Die Lehre von der Cohäsion, umfassend die Elasticität der Gase, die Elasticität und Cohärenz der flüssigen und festen Körper und die Krystallkunde".* Schulz, Breslau, 389.

Gabel, F., Muller, G., Raether, F., Kiefer, W., Pannhorst, W., Sohr, O. & Sprengard, R. (2004). Quantitative characterisation of nuclei formation by Raman spectroscopy of lithium alumino-silicate glass ceramics doped with titania and zirconia. *Physics and Chemistry of Glasses,* 43**,** 306-310.

Gilard, P. & Dubrul, L. (1937). Calculation of physical properties of glass: III. Index of refraction. *Journal of the Society of Glass Technology,* 21**,** 476-488.

Gill, J. R. (1932) Methods and results in condensation of dental porcelain. *Journal of the American Dental Association,* 19**,** 1147-1154.

Goldschmidt, V. M. (1926). “Geochemische Verteilungsgesetze der Elemente” (The geochemical laws of the distribution of the elements), Oslo: Skrifter Norske Videnskaps Akad. *I. Math. Naturwiss. Kl.,* 8**,** 156.

Granasy, L. & James, P. F. (1998). Nucleation in oxide glasses: Comparison of theory and experiment. *Proceedings: Mathematical, Physical and Engineering Sciences,* 454**,** 1745-1766.

Granazy, L. & James, P. F. (1999). Transient nucleation in oxide glasses: The effect of interface dynamics and subcritical cluster population. *Journal of Chemical Physics,* 111**,** 737-749.

Greene, K., Pomeroy, M. J., Hampshire, S. & Hill, R. (2003). Effect of composition on the properties of glasses in the K_2O–BaO–MgO–SiO_2–Al_2O_3–B_2O_3–MgF_2 system. *Journal of Non-Crystalline Solids,* 325**,** 193-205.

Gritco, A., Moldovan, M., Grecu, R. & Simon, V. (2005). Thermal and infrared analyses of aluminosilicate glass systems for dental implants. *Journal of Optoelectronics and Advanced Materials,* 7**,** 2845.

Grube, M., Lin, J. G., Lee, P. H. & Kokorevicha, S. (2006). Evaluation of sewage sludge-based compost by FT-IR spectroscopy. *Geoderma,* 130**,** 324-333.

Hacker, C. H., Wagner, W. C. & Razzoog, M. E. (1996). An *in vitro* investigation of the wear of enamel on porcelain and gold in saliva. *The Journal of Prosthetic Dentistry,* 75**,** 14-17.

Hara, A. T. & Zero, D. T. (2008). Analysis of the erosive potential of calcium-containing acidic beverages. *European Journal of Oral Sciences,* 116**,** 60.

Harris, D. C. (2007). *Quantitative chemical analysis,* 7th Edition ed. New York, NY, USA, W.H. Freeman and Company, 506-511,589-591.

He, J. & Schoenung, J. M. (2002). Nanostructured coatings. *Materials Science and Engineering A,* 336**,** 274-319.

He, L. H. & Swain, M. V. (2007a). Enamel - A "metallic-like" deformable biocomposite. *Journal of Dentistry,* 35**,** 431-437.

He, L. H. & Swain, M. V. (2007b). Influence of environment on the mechanical behaviour of mature human enamel. *Biomaterials,* 28**,** 4512-4520.

Heintze, S. D. (2006). How to qualify and validate wear simulation devices and methods. *Dental Materials,* 22**,** 712-734.

Heintze, S. D., Cavalleri, A., Forjanic, M., Zellweger, G. & Rousson, V. (2006). A comparison of three different methods for the quantification of the *in vitro* wear of dental materials. *Dental Materials,* 22**,** 1051-1062.

Heintze, S. D., Cavalleri, A., Forjanic, M., Zellweger, G. & Rousson, V. (2008). Wear of ceramic and antagonist - A systematic evaluation of influencing factors *in vitro*. *Dental Materials,* 24**,** 433-449.

Hermansson, L. & Carlsson, R. (1976). High and low temperature forms of leucite. *Proceedings of the 8th International Symposium on the Reactivity of Solids.* Gothenberg, Sweden, Swedish Institute for Silicate Research,541-545.

Hermansson, L. & Carlsson, R. (1978). Crystallization of the glassy phase in whitewares. *Transactions and Journal of the British Ceramic Society,* 77**,** 32-35.

Hoare, M. R. & Barker, J. A. (1977). Tammann revisited: Cluster theories of the glass transition with special reference to soft packings. *The structure of non-crystalline materials.* Cambridge, UK, Taylor & Francis,175-180.

Hobo, S. & Iwata, T. (1985). Castable apatite ceramics as a new biocompatible restorative material II: Fabrication of the restoration. *Quintessence International,* 16**,** 207.

Höhne, G., Hemminger, W. & Flammersheim, H. J. (2003). *Differential scanning calorimetry,* 2nd ed. New York, NY, USA, Springer,1-5.

Höland, W., Frank, M. & Rheinberger, V. (1995). Surface crystallization of leucite in glasses. *Journal of Non-Crystalline Solids,* 180**,** 292-307.

Höland, W., Rheinberger, V., Apel, E., van 't Hoen, C., Höland, M., Dommann, A., Obrecht, M., Mauth, C. & Graf-Hausner, U. (2006). Clinical applications of glass-ceramics in dentistry. *Journal of Materials Science: Materials in Medicine,* 17**,** 1037-1042.

Höland, W., Rheinberger, V., Wegner, S. & Frank, M. (2000). Needle-like apatite-leucite glass-ceramic as a base material for the veneering of metal restorations in dentistry. *Journal of Materials Science Materials in Medicine,* 11**,** 11-17.

Höland, W., Rheinberger, V. & Schweiger, M. (2003). Control of nucleation in glass ceramics. *Philosophical Transactions of the Royal Society of London, Series B,* 361**,** 575-589.

Hormadaly, J. (1986). Empirical methods for estimating the linear coefficient of expansion of oxide glasses from their composition. *Journal of Non-Crystalline Solids,* 79**,** 311-324.

Hu, X., Harrington, E., Marquis, P. M. & Shortall, A. C. (1999). The influence of cyclic loading on the wear of a dental composite. *Biomaterials,* 20**,** 907-912.

Huggins, M. L. & Sun, K.-H. (1943). Calculation of density and optical constants of a glass from its composition in weight percentage. *Journal of the American Ceramic Society,* 26**,** 4-11.

Ibsen, R. L., Chadwick, T. C. & Pritchard, S. A. (1991). Strong dental porcelain and method for its manufacture. US Patent 5,009,709.

Ibsen, R. L., Chen, X., Cattell, M. J., Riddell, J. V. & Chadwick, T. C. (2008). Control of ceramic microstructure. US Patent 4,233,282.

IPS Empress (2006). IPS Empress CAD: Instructions for use - Labside. Ivoclar Vivadent Technical, Schaan, Liechtenstein, 4.

Jakovac, M., Zivko-Babic, J., Curkovic, L. & Aurer, A. (2006). Measurement of ion elution from dental ceramics. *Journal of the European Ceramic Society,* 26**,** 1695-1700.

Janssen, M., Zuidema, J. & Wanhill, R. J. H. (2002). *Fracture Mechanics,* 2nd ed. Delft, The Netherlands, Delft University Press, 15.

Kaidatzis, A., Wachter, J. B., Chrissafis, K., Paraskevopoulos, K. M. & Kanatzidis, M. G. (2008). Crystal/glass phase change in $K_{1-x}Rb_xSb_5S_8$ (x= 0.25, 0.50, 0.75) studied through thermal analysis techniques. *Journal of Non-Crystalline Solids,* 354**,** 3643-3648.

Kaidonis, J. A., Richards, L. C., Townsend, G. C. & Tansley, G. D. (1998). Wear of human enamel: A quantitative *in vitro* assessment. *Journal of Dental Research,* 77**,** 1983-1990.

Kano, J., Mio, H. & Saito, F. (1999). Correlation of size reduction rate of inorganic materials with impact energy of balls in planetary ball milling. *Journal of Chemical Engineering of Japan,* 32**,** 445-448.

Kao, R., Perrone, N. & Capps, W. (1971). Large-deflection solution of the coaxial-ring-circular-glass-plate flexure problem. *Journal of the American Ceramic Society,* 54**,** 566-571.

Kelly, J. R. (1997). Ceramics in restorative and prosthetic dentistry. *Annual Review of Materials Science,* 27**,** 443-468.

Kelly, J. R., Nishimura, I. & Campbell, S. D. (1996). Ceramics in dentistry: historical roots and current perspectives. *Journal of Prosthetic Dentistry,* 75**,** 18-32.

Kelly, J. R., Tesk, J. A. & Sorensen, J. A. (1995). Failure of all-ceramic fixed partial dentures *in vitro* and *in vivo*: Analysis and modelling. *Journal of Dental Research,* 74**,** 1253-1258.

Kelton, K. F. (1991). Crystal nucleation in liquids and glasses. IN: Ehrenreich, H. & Turnbull, D. (Eds.) *Solid State Physics.* Cambridge, MA, USA, Academic Press Inc, 159-161.

Kern, M., Strub, J. R. & Lu, X. Y. (1999). Wear of composite resin veneering materials in a dual-axis chewing simulator. *Journal of Oral Rehabilitation,* 26**,** 372-378.

Kingery, W. D., Bowen, H. K. & Uhlmann, D. R. (1976). *Introduction to ceramics,* 2nd ed. New York, NY, USA, Wiley, 3-6,94,108, 501-503.

Kirstein, A. F. & Woolley, R. M. (1967). Symmetrical bending of thin circular elastic plates on equally spaced point supports. *Journal of Research of the National Bureau of Standards, Sect. C,* 71**,** 1-10.

Kissinger, H. E. (1956). Variation of peak temperature with heating rate in differential thermal analysis. *Journal of Research of the National Bureau of Standards,* 57**,** 217–221.

Kohyama, K., Hatakeyama, E., Sasaki, T., Dan, H., Azuma, T. & Karita, K. (2004). Effects of sample hardness on human chewing force: a model study using silicone rubber. *Archives of Oral Biology,* 49**,** 805-816.

Kong, L. B., Ma, J., Zhu, W. & Tan, O. K. (2001). Reaction sintering of partially reacted system for PZT ceramics *via* a high-energy ball milling. *Scripta Materialia,* 44**,** 345-350.

Kotrla, M. (1996). Numerical simulations in the theory of crystal growth. *Computer Physics Communications,* 97**,** 82-100.

Kramer, N., Kunzelmann, K. H., Taschner, M., Mehl, A., Garcia-Godoy, F. & Frankenberger, R. (2006). Antagonist enamel wears more than ceramic inlays. *Journal of Dental Research,* 85**,** 1097-1100.

Krejci, I., Albert, P. & Lutz, F. (1999). The influence of antagonist standardization on wear. *Journal of Dental Research,* 78**,** 713-719.

Krejci, I., Lutz, F. & Zedler, C. (1992). Effect of contact area size on enamel and composite wear. *Journal of Dental Research,* 71**,** 1413-1416.

Kuczynski, G. C. & Zaplatynskyj, I. (1956). Sintering of glass. *Journal of the American Ceramic Society,* 39**,** 349.

Laird, B. B. & Haymet, A. D. J. (1992). The crystal/liquid interface: structure and properties from computer simulation. *Chemical Reviews,* 92**,** 1819-1837.

Lambrechts, P., Vuylsteke, M., Vanherle, G. & Davidson, C. L. (1985). Quantitative *in vivo* wear of posterior dental restorations. Four-year results. *Journal of Dental Research,* 64**,** 370, Abstract 1759.

Land, C. H. (1893). Illustrated epitome of the Land system of dental practice: devoted to the act of restoring the dental organs to their natural appearance. Detroit

Lange, F. F. (1970). The interaction of a crack front with a second-phase dispersion. *Philosophical Magazine,* 22**,** 983 - 992.

Lange, F. F. (1971). Fracture energy and strength behavior of a sodium borosilicate glass - Al_2O_3 composite system. *Journal of the American Ceramic Society,* 54**,** 614-620.

Laudisio, G., Catauro, M. & Aronne, A. (1998). The non-isothermal devitrification of $Li_2TiGe_3O_9$ glass. *Thermochimica Acta,* 321**,** 123-126.

Lebedev, A. A. (1921). Polymorphism and annealing of glass. *Trudy Cossud. Opt. Inst.,* 2**,** 1–20.

Lee, H. H., Kon, M. & Asaoka, K. (1997). Influence of modification of Na_2O in a glass matrix on the strength of leucite-containing porcelains. *Dental Materials Journal,* 16**,** 134-143.

Lee, S. K. & Stebbins, J. F. (2000). Al-O-Al and Si-O-Si sites in framework aluminosilicate glasses with Si/Al=1: quantification of framework disorder. *Journal of Non-Crystalline Solids,* 270**,** 260-264.

Levi, A. C. & Kotrla, M. (1997). Theory and simulation of crystal growth. *Journal of Physics: Condensed Matter,* 9**,** 299-344.

Litwin, D., Galas, J. & Blocki, N. (2006). Variable wavelength profilometry. *Proceedings of the Symposium on Photonics Technologies for 7th Framework Program.* Wroclaw 476-479.

Luan, W.-l., Gao, L. & Guo, J.-k. (1998). Study on drying stage of nanoscale powder preparation. *Nanostructured Materials,* 10**,** 1119-1125.

Mackert, J. J. R. (1988). Effects of thermally induced changes on porcelain-metal compatibility. *Perspectives in dental ceramics, Proceedings of the 4th international symposium on ceramics.* Chicago, Quintessence Pub. Co.,53-64.

Mackert, J. J. R., Butts, M. B. & Fairhurst, C. W. (1986). The effect of the leucite transformation on dental porcelain expansion. *Dental Materials,* 2**,** 32-36.

Mackert, J. J. R., Rueggeberg, E. A., Lockwood, P. E., Evans, A. L. & Thompson, W. O. (1994). Isothermal anneal effect on microcrack density around leucite particles in dental porcelain. *Journal of Dental Research,* 73**,** 1221-1227.

Mackert, J. J. R., Twiggs, S. W., Russell, C. M. & Williams, A. L. (2001). Evidence of a critical leucite particle size for microcracking in dental porcelains. *Journal of Dental Research,* 80**,** 1574.

Mackert, J. J. R., Williams, A. L., Ergle, J. W. & Russell, C. M. (2000). Water-enhanced crystallization of leucite in dental porcelain. *Dental Materials,* 16**,** 426-431.

Mackert, J. R. J. & Russell, C. M. (1996). Leucite crystallization during processing of a heat-pressed dental ceramic. *International Journal of Prosthodontics,* 9**,** 261-265.

Magne, P., Oh, W.-S., Pintado, M. R. & DeLong, R. (1999). Wear of enamel and veneering ceramics after laboratory and chairside finishing procedures. *Journal of Prosthetic Dentistry,* 82**,** 669-679.

Málek, J. (1995). The applicability of Johnson-Mehl-Avrami model in the thermal analysis of the crystallization kinetics of glasses. *Thermochimica Acta,* 267**,** 61-73.

Marotta, A., Buri, A. & Branda, F. (1980). Surface and bulk crystallization in non-isothermal devitrification of glasses. *Thermochimica Acta,* 40**,** 397-403.

Maslyuk, V. T., Doinikov, L. I. & Puga, P. P. (2001). Myuller's structural models in statistical thermodynamics of glasses I. *Glass Physics and Chemistry,* 27**,** 428-434.

Matusita, K. & Sakka, S. (1980). Kinetic study of crystallization of glass by differential thermal analysis -criterion on application of Kissinger plot. *Journal of Non-Crystalline Solids,* 38**,** 741-746.

Matusita, K. & Sakka, S. (1981). Kinetic study of non-isothermal crystallization of glass by thermal analysis. *Bulletin of the Institute for Chemical Research, Kyoto Univ,* 59**,** 159-171.

Matusita, K., Sakka, S. & Matsui, Y. (1975). Determination of the activation energy for crystal growth by differential thermal analysis. *Journal of Materials Science,* 10**,** 961-966.

Maurer, R. D. (1962). Crystal nucleation in a glass containing titania. *Journal of Applied Physics,* 33**,** 2132-2139.

Mazzi, F., Galli, E. & Gottardi, G. (1976). The crystal structure of tetragonal leucite. *American Mineralogist,* 61**,** 108-115.

McCabe, J. F. & Carrick, T. E. (1986) A statistical approach to the mechanical testing of dental materials. *Dental materials: official publication of the Academy of Dental Materials,* 2**,** 139.

McIntyre, F. (2000). Restoring esthetics and anterior guidance in worn anterior teeth: A conservative multidisciplinary approach. *Journal of the American Dental Association,* 131**,** 1279-1283.

McKinney, K. R. & Herbert, C. M. (1970). Effect of surface finish on structural ceramic failure. *Journal of the American Ceramic Society,* 53**,** 513-516.

McLaughlin, J. R. (1999). Bead size and mill efficiency. *Ceramic Industry***,** 34-40.

McLean, J. W. (2001). Evolution of dental ceramics in the twentieth century. *The Journal of Prosthetic Dentistry,* 85**,** 61-66.

McLean, J. W. & Hughes, T. H. (1965). The reinforcement of dental porcelain with ceramic oxides. *British Dental Journal,* 119**,** 251.

McMillan, P. W. (1979). *Glass-ceramics,* 2nd ed. London, Academic Press, 1-13, 57-59, 61.

Mehl, A., Gloger, W., Kunzelmann, K. H. & Hickel, R. (1997). A new optical 3-D device for the detection of wear. *Journal of Dental Research,* 76**,** 1799-1807.

Metzler, K. T., Woody, R. D., Miller, A. W. & Miller, B. H. (1999). *In vitro* investigation of the wear of human enamel by dental porcelain. *Journal of Prosthetic Dentistry,* 81**,** 356-364.

Mio, H., Kano, J., Saito, F. & Kaneko, K. (2002). Effects of rotational direction and rotation-to-revolution speed ratio in planetary ball milling. *Materials Science and Engineering A,* 332**,** 75-80.

Mitchell, H. L. & Chadwick, R. G. (1998). Mathematical shape matching as a tool in tooth wear assessment - development and conduct. *Journal of Oral Rehabilitation,* 25**,** 921-928.

Moore, C. & Addy, M. (2005). Wear of dentine *in vitro* by toothpaste abrasives and detergents alone and combined. *Journal of Clinical Periodontology,* 32**,** 1242-1246.

Muller, P. (1994). Glossary of terms used in physical organic chemistry (IUPAC Recommendations 1994). *Pure and Applied Chemistry,* 66**,** 1147.

Müller, R., Zanotto, E. D. & Fokin, V. M. (2000). Surface crystallization of silicate glasses: nucleation sites and kinetics. *Journal of Non-Crystalline Solids,* 274**,** 208-231.

Munakata, Y., Tsuji, M. & Kasai, S. (1991). Occlusal force pattern during rhythmic human tapping movement. *Journal of Oral Rehabilitation,* 18**,** 265-272.

Nanci, A. (2003). *Ten Cate's Oral histology,* 6th ed. St. Louis, MO, USA, Mosby, 5, 145-191.

Nathanson, D. (1994). Principles of porcelain use as an inlay/onlay material. IN: Garber, D.A., Goldstein, R.E., (Eds), *Porcelain and composite inlays and onlays, esthetic posterior restorations*. Carol Stream, IL, USA, Quintessence Pub. Co. Inc., 32-6.

Nixon, W. C. (1969). Scanning Electron Microscopy. *Contemporary Physics,* 10**,** 71-96.

Nyquist, G. & Owall, B. (1968). Masticatory load registrations during function. A methodological study. *Odontologisk Revy,* 19**,** 45.

O'Kray, H. P. & O'Brien, W. J. (2005). *In vitro* human enamel wear by a hydrated high-alkali porcelain. *Quintessence International,* 36**,** 617-622.

Oh, W., DeLong, R. & Anusavice, K. J. (2002). Factors affecting enamel and ceramic wear: A literature review. *The Journal of Prosthetic Dentistry,* 87**,** 451-459.

Ohnesorge, R., Löwen, H. & Wagner, H. (1994). Density functional theory of crystal-fluid interfaces and surface melting. *Physical Review E,* 50**,** 4801.

Ostwald, W. (1896). "Lehrbuch der Allgemeinen Chemie" (Textbook of general chemistry). 2, Part 1**,** Leipzig, Germany, W. Engelmann.

Palmer, D. C., Dove, M. T., Ibberson, R. M. & Powell, B. M. (1997). Structural behavior, crystal chemistry, and phase transitions in substituted leucite: High-resolution neutron powder diffraction studies. *American Mineralogist,* 82**,** 16-29.

Palmer, D. C., Putnis, A. & Salje, E. K. H. (1988). Twinning in tetragonal leucite. *Physics and Chemistry of Minerals,* 16**,** 298-303.

Pauling, L. (1927). The sizes of ions and the structure of ionic crystals. *Journal of the American Chemical Society,* 49**,** 765-790.

Pauling, L. (1929). The principles determining the structure of complex ionic crystals. *Journal of the American Chemical Society,* 51**,** 1010-1026.

Pauling, L. (1932). The nature of the chemical bond. IV. The energy of single bonds and the relative electronegativity of atoms. *Journal of the American Chemical Society,* 54**,** 3570-3582.

Pauling, L. (1960). *The nature of the chemical bond and the structure of molecules and crystals,* 3rd ed. ed. Ithaca, NY, USA, Cornell University Press, 98.

Piche, P. W., O'Brien, W. J., Groh, C. L. & Boenke, K. M. (1994). Leucite content of selected dental porcelains. *Journal of Biomedical Materials Research,* 28**,** 603-609.

Piddock, V., Marquis, P. M. & Wilson, H. J. (1987). The mechanical strength and microstructure of all-ceramic crowns. *Journal of Dentistry,* 15**,** 153-158.

Pintado, M. R., Anderson, G. C., DeLong, R. & Douglas, W. H. (1997). Variation in tooth wear in young adults over a two-year period. *Journal of Prosthetic Dentistry,* 77**,** 313-320.

Pratsinis, S. E. & Vemury, S. (1996). Particle formation in gases: A review. *Powder Technology,* 88**,** 267-273.

Price, G. J. (1998). *Thermodynamics of chemical processes*. New York, NY, USA, Oxford University Press Inc., 1-3, 7-9.

Priven, A. I. (2004). General method for calculating the properties of oxide glasses and glass forming melts from their composition and temperature. *Glass Technology,* 45**,** 244-254.

Priven, A. I. & Mazurin, O. V. (2003). Comparison of methods used for the calculation of density, refractive index and thermal expansion of oxide glasses. *Glass Technology,* 44**,** 156-166.

Qualtrough, A. J. E. & Piddock, V. (1997). Ceramics update. *Journal of Dentistry,* 25**,** 91-95.

Quinn, J. B. & Quinn, G. D. (2010). A practical and systematic review of Weibull statistics for reporting strengths of dental materials. *Dental Materials,* 26**,** 135-147.

Rak, M., Izdebski, M. & Brozi, A. (2001). Kinetic Monte Carlo study of crystal growth from solution. *Computer Physics Communications,* 138**,** 250-263.

Ramp, M. H., Suzuki, S., Cox, C. F., Lacefield, W. R. & Koth, D. L. (1997). Evaluation of wear: Enamel opposing three ceramic materials and a gold alloy. *The Journal of Prosthetic Dentistry,* 77**,** 523-530.

Rao, K. J. (2002). *Structural chemistry of glasses*. Amsterdam, The Netherlands, Elsevier, 23-30.

Rasmussen, S. T., McLaren, C. I. & O'Brien, W. J. (2004). The effect of cesium-containing leucite additions on the thermal and mechanical properties of two leucite-based porcelains. *Journal of Biomedical Materials Research Part B: Applied Biomaterials,* 69B**,** 195-204.

Rawson, H. (1956). The relationship between liquidus temperature, bond strength and glass formation. *Travaux du IVo Congrès International du Verre.* Paris, France, 62-69.

Ray, N. H. (1978). *Inorganic Polymers*. Norwich, UK, Academic Press Inc., 13-16, 95.

Rekow, D. & Thompson, V. P. (2005). Near-surface damage: a persistent problem in crowns obtained by computer-aided design and manufacturing. *Proceedings of the Institution of Mechanical Engineers Part H: Journal of Engineering in Medicine,* 219**,** 233-243.

Rekow, E. D., Erdman, A. G., Riley, D. R. & Klamecki, B. (1991). CAD/CAM for dental restorations - some of the curious challenges. *IEEE Transactions on Biomedical Engineering,* 38**,** 314-318.

Rekow, E. D. & Thompson, V. P. (2007). Engineering long term clinical success of advanced ceramic prostheses. *Journal of Materials Science: Materials in Medicine* 18**,** 47-56.

Robinson, C., Connell, S., Kirkham, J., Shore, R. & Smith, A. (2004). Dental enamel - a biological ceramic: regular substructures in enamel hydroxyapatite crystals revealed by atomic force microscopy. *Journal of Materials Chemistry,* 14**,** 2242-2248.

Rochow, T. G. & Tucker, P. A. (1994). *Introduction to microscopy by means of light, electrons, X-rays or acoustics,* 2nd Ed. New York, NY, USA, Plennum Press, 80-81.

Romero, M., Rawlings, R. D. & Rincón, J. M. (1999). Development of a new glass-ceramic by means of controlled vitrification and crystallisation of inorganic wastes from urban incineration. *Journal of the European Ceramic Society,* 19**,** 2049-2058.

Rouf, M. A., Hermansson, L. & Carlsson, R. (1978). Crystallization of glasses in the primary phase field of Leucite in the K_2O-Al_2O_3-SiO system. *Transactions and Journal of the British Ceramic Society,* 77**,** 36-39.

Rowell, D. L. (1994). *Soil science: Methods and applications*. Harlow, Longman Scientific & Technical, 29.

Sadhukhan, M., Modak, D. K. & Chaudhuri, B. K. (1999). Study of microstructural behavior and nonadiabatic small polaron hopping conduction in $BaTiO_3$ doped lead-vanadate glass and glass-ceramics dispersed with ferroelectric nanocrystals. *Journal of Applied Physics,* 85**,** 3477-3487.

Sadoun, M. (1988). All ceramic bridges with the slip casting technique. *Seventh International Symposium on Ceramics.* Paris.

Sakaguchi, R. L., Douglas, W. H., DeLong, R. & Pintado, M. R. (1986). The wear of a posterior composite in an artificial mouth: a clinical correlation. *Dental Materials,* 2**,** 235-240.

Sarzanini, C. (1999). Liquid chromatography: a tool for the analysis of metal species. *Journal of Chromatography A,* 850**,** 213-228.

Schairer, J. F. & Bowen, N. L. (1955). The system K_2O-Al_2O_3-SiO_2. *American Journal of Science,* 253**,** 681-746.

Schmidt, H. (2001). Nanoparticles by chemical synthesis, processing to materials and innovative applications. *Applied Organometallic Chemistry,* 15**,** 331-343.

Scholze, H. & Lakin, M. J. (1991). *Calculation based on composition. Glass: nature, structure and properties.* London, UK, Springer-Verlag, 189-190.

Schweiger, M., Höland, W., Frank, M., Drescher, H. & Rheinberger, V. (1999) IPS Empress 2: A new pressable high-strength glass-ceramic for esthetic all-ceramic restorations. *Quintessence of Dental Technology,* 22**,** 143-151.

Seghi, R. R., Rosenstiel, S. F. & Bauer, P. (1991). Abrasion of human enamel by different dental ceramics *in vitro*. *Journal of Dental Research,* 70**,** 221-225.

Shareef, M. Y., Noort, R., Messer, P. F. & Piddock, V. (1994). The effect of microstructural features on the biaxial flexural strength of leucite reinforced glass-ceramics. *Journal of Materials Science: Materials in Medicine,* 5**,** 113-118.

Shelby, J. E. (2005). *Introduction to glass science and technology,* 2nd ed. Cambridge, UK, Royal Society of Chemistry, 11, 90-92.

Shetty, D. K., Rosenfield, A. R., Duckworth, W. H. & Held, P. R. (1983). A biaxial-flexure test for evaluating ceramic strengths. *Journal of the American Ceramic Society,* 66**,** 36-42.

Shortall, A. C., Hu, X. Q. & Marquis, P. M. (2002). Potential countersample materials for *in vitro* simulation wear testing. *Dental Materials,* 18**,** 246-254.

Simonsen, R.J. & Calamia, J.R. (1983). Tensile bond strength of etched porcelain. *Journal of Dental Reaserch,* 62, 297, Abstract 1154.

Sınmazışık, G. & Öveçoglu, M. L. (2006). Physical properties and microstructural characterization of dental porcelains mixed with distilled water and modelling liquid. *Dental Materials,* 22**,** 735-745.

Smekal, A. G. (1951). On the structure of glass. *Journal of the Society of Glass Technology,* 35**,** 411.

Smith, B. G. N., Bartlett, D. W. & Robb, N. D. (1997). The prevalence, etiology and management of tooth wear in the United Kingdom. *The Journal of Prosthetic Dentistry,* 78**,** 367-372.

Spears, I. R. (1997). A three-dimensional finite element model of prismatic enamel: A re-appraisal of the data on the Young's modulus of enamel. *Journal of Dental Research,* 76**,** 1690-1697.

Sprengard, R., Fotheringham, U. & Pannhorst, W. (1998). Raman spectroscopic characterisation of nuclei formation in TiO_2 nucleated lithium aluminosilicate glass ceramics. *Proceedings of the 18th International Congress on Glass.* San Francisco, CA, USA, 19-24.

Stanworth, J. E. (1946). The structure of glass. *Journal of the Society of Glass Technology,* 30**,** 54-66.

Stanworth, J. E. (1948A). The structure of glass. *Journal of the Society of Glass Technology,* 32**,** 154-172.

Stanworth, J. E. (1948B). The ionic structure of glass. *Journal of the Society of Glass Technology,* 32**,** 366-372.

STIL-SA (2008). Measurement report, Metrological characteristics for the S16/3.5 contactless optical sensor: Ref. no M08011718, 22/1/08.

Stookey, S. D. (1960). Method of making ceramics and product thereof. US Patent 2,920,971.

Studart, A. R., Filser, F., Kocher, P., Luthy, H. & Gauckler, L. J. (2007). Mechanical and fracture behaviour of veneer-framework composites for all-ceramic dental bridges. *Dental Materials* 23**,** 115-123.

Sun, K. H. (1947). Fundamental condition of glass formation. *Journal of the American Ceramic Society,* 30**,** 277-281.

Suryanarayana, C. (2001). Mechanical alloying and milling. *Progress in Materials Science,* 46**,** 1-184.

Suryanarayana, C. (2004). *Mechanical alloying and milling*. Boca Raton, FL, USA, CRC Press, 37.

Suryanarayana, C., Ivanov, E. & Boldyrev, V. V. (2001). The science and technology of mechanical alloying. *Materials Science & Engineering A,* 304**,** 151-158.

Tarjus, G. & Kivelson, D. (1995). Breakdown of the Stokes-Einstein relation in supercooled liquids. *Journal of Chemical Physics,* 103**,** 3071-3073.

Theocharopoulos, A., Zou, L., Hill, R. & Cattell, M. (2010). Wear quantification of human enamel and dental glass-ceramics using white light profilometry. *Wear,* 269**,** 930-936.

Timoshenko, S. P. & Woinowsky-Krieger, S. (1959). *Theory of plates and shells,* 2nd Ed. New York, NY, USA, McGraw-Hill, 70-71.

Tomozawa, M. (1972). Liquid phase separation and crystal nucleation in Li_2O-SiO_2 glasses. *Physics and Chemistry of Glasses,* 13**,** 161-166.

Tošić, M. B., Mitrović, M. M. & Dimitrijević, R. Ž. (2000). Crystallization of leucite as the main phase in aluminosilicate glass with low fluorine content. *Journal of Materials Science,* 35**,** 3659-3667.

Turnbull, D. (1950). Kinetics of heterogeneous nucleation. *The Journal of Chemical Physics,* 18**,** 198-203.

Turnbull, D. (1956). Phase changes. IN: Seitz, F. & Turnbull, D. (Eds.) *Solid State Physics.* New York, NY, USA, Academic Press Inc., 279-281.

Turnbull, D. (1969). Under what conditions can a glass be formed? *Contemporary Physics,* 10**,** 473-488.

Turnbull, D. & Cohen, M. H. (1958). Concerning reconstructive transformation and formation of glass. *The Journal of Chemical Physics,* 29**,** 1049-1054.

Turnbull, D. & Fisher, J. C. (1949). Rate of nucleation in condensed systems. *The Journal of Chemical Physics,* 17**,** 71-73.

Turnbull, D. & Vonnegut, B. (1952). Nucleation catalysis. *Industrial and Engineering Chemistry,* 44**,** 1292-1298.

Turssi, C. P., Ferracane, J. L. & Serra, M. C. (2005). Abrasive wear of resin composites as related to finishing and polishing procedures. *Dental Materials,* 21**,** 641-648.

Valenkov, N. & Poray-Koshitz, E. (1936). X-ray investigation of the glassy state. *Zeitschrift fur Kristallographie,* 95**,** 195-229.

van Noort, R. (2002). Introduction to Dental Materials. 2nd edition ed. London, UK, Mosby 231 - 246.

Varshneya, A. K. & Seward, T. P. (2001). Inorganic glasses – Structure, composition and properties. IN: Harper, C. A. (Ed.) *Handbook of ceramics, glasses, and diamonds.* New York; London, McGraw-Hill, 5.1.

Vedishcheva, N. M., Shakhmatkin, B. A., Shultz, M. M. & Wright, A. C. (1996). The thermodynamic modelling of glass properties: a practical proposition? *Journal of Non-Crystalline Solids,* 196**,** 239-243.

Venyaminov, S. Y. & Prendergast, F. G. (1997). Water (H_2O and D_2O) molar absorptivity in the 1000-4000 cm^{-1} range and quantitative Infrared Spectroscopy of aqueous solutions. *Analytical Biochemistry,* 248**,** 234-245.

Vieira, A., Overweg, E., Ruben, J. L. & Huysmans, M. (2006). Toothbrush abrasion, simulated tongue friction and attrition of eroded bovine enamel *in vitro*. *Journal of Dentistry,* 34**,** 336-342.

Vines, R. F., Semmelman, J. O., Lee, P. W. & Fonvielle, F. P. (1958). Mechanisms involved in securing dense, vitrified ceramics from preshaped partly crystalline bodies. *Journal of the American Ceramic Society,* 41**,** 304-309.

Visser, J. (1989). Van der Waals and other cohesive forces affecting powder fluidization. *Powder Technology,* 58**,** 1-10.

Vital, A., Zürcher, S., Dittmann, R., Trottmann, M., Lienemann, P., Bommer, B., Graule, T., Apel, E. & Höland, W. (2008). Ultrafine comminution of dental glass in a stirred media mill. *Chemical Engineering Science,* 63**,** 484-494.

Vogel, W. (1985). *Chemistry of glass*. Columbus, Ohio, USA, American Ceramic Society, a: 33-47, b: 50-59.

Volf, M. B. (1988). *Mathematical approach to glass*. Czechoslovakia, Elsevier Science Pub. Comp. Inc, 31-31, 142-146.

Vollath, D., Szabó, D. V. & Hauelt, J. (1997). Synthesis and properties of ceramic nanoparticles and nanocomposites. *Journal of the European Ceramic Society,* 17**,** 1317-1324.

Volmer, M. (1929). "Uber Keimbildung und Keimwirkung als Spezialfalle der heterogen Katalyse". *Zeitschrift fur Elektrochemie,* 35**,** 555-561 in Turnbull, D. & Vonnegut, B. (1952) Nucleation Catalysis. Industrial and Engineering Chemistry, 1944, 1292-1298.

Warren, B. E., Krutter, H. & Morningstar, O. (1936). Fourier analyses of X-ray patterns of vitreous SiO_2 and B_2O_3. *Journal of the American Ceramic Society,* 19**,** 202-206.

Wassell, R. W., McCabe, J. F. & Walls, A. W. (1994). A two-body frictional wear test. *Journal of Dental Research,* 73**,** 1546-1553.

Weast, R. C. (Ed.) (1978). *CRC Handbook of Chemistry and Physics,* West Palm Beach, FL, USA, CRC Press.

Weeding, T. L., de Jong, B. H. W. S., Veeman, W. S. & Aitken, B. G. (1985). Silicon coordination changes from 4-fold to 6-fold on devitrification of silicon phosphate glass. *Nature,* 318**,** 352-353.

Weibull, W. (1951). A statistical distribution function of wide applicability. *Journal of Applied Mechanics,* 18**,** 293-297.

Weidmann, S. M., Weatherell, J. A. & Hamm, S. M. (1967). Variations of enamel density in sections of human teeth. *Archives of Oral Biology,* 12**,** 85-97.

Weinstein, M., Katz, S. & Weinstein, A. B. (1962). Fused porcelain-to-metal teeth. US Patent 3,052,098.

Weyl, W. A. (1951). The significance of the co-ordination requirements of the cations in the constitution of glass II. The effect of temperature and composition on oxidation-reduction equilibria in glasses. *Journal of the Society of Glass Technology,* 35**,** 396.

White, S. N., Luo, W., Paine, M. L., Fong, H., Sarikaya, M. & Snead, M. L. (2001). Biological organization of hydroxyapatite crystallites into a fibrous continuum toughens and controls anisotropy in human enamel. *Journal of Dental Research,* 80**,** 321-326.

Whittaker, D. K. (1982). Structural variations in the surface zone of human tooth enamel observed by scanning electron microscopy. *Archives of Oral Biology,* 27**,** 383.

Wilshaw, T. R. (1968). Measurement of tensile strength of ceramics. *Journal of the American Ceramic Society,* 51**,** 111-112.

Winkelmann, A. & Schott, O. (1894a). Expansion coefficients of glasses. *Annalen der Physik,* 51**,** 730.

Winkelmann, A. A. & Schott, O. (1894b). Dependence of thermal resistance coefficients of glasses on their chemical composition. *Annalen der Physik (Leipzig),* 51**,** 730-746.

Wiskott, H. W. A., Perriard, J., Scherrer, S. S. & Belser, U. C. (2000). A new method to quantify wear using implant supported restorations. *Dental Materials,* 16**,** 218-225.

Wohlwend, A., Schärer, P. & Stub, J. R. (1990). Metalloceramic and full ceramic restorations. *Quintessenz der Zahntechnik,* 41**,** 981-991.

Wunderlich, B. (1994). The nature of the glass transition and its determination by thermal analysis. IN: Seyler, R. J. (Ed.) *Assignment of the glass transition.* Baltimore, MO, USA, ASTM, 17-30.

Xu, X. J., Ray, C. S. & Day, D. E. (1991). Nucleation and crystallisation of $Na_2O \cdot 2\ CaO \cdot 3\ SiO_2$ glass by differential thermal analysis. *Journal of the American Ceramic Society,* 74**,** 909-914.

Yang, J. & Wu, J. (2003). Preparation of high thermal expansion coefficient porcelains fused to metals. *Acta Metallurgica Sinica (English Letters),* 16**,** 256-260.

Yang, J., Wu, J., Rao, P., Xin, C. & Chen, D. (2005). The influence of nanosized leucite on dental porcelain properties. *Key Engineering Materials,* 280**,** 1605-1608.

Yi, C., Yanchun, L. & Yunlong, H. (2008). The correctional kinetic equation for the peak temperature in the differential thermal analysis. *Journal of Thermal Analysis and*

Calorimetry, 93**,** 111-113.

Yilmaz, H., Aydin, C. & Gul, B. E. (2007). Flexural strength and fracture toughness of dental core ceramics. *The Journal of Prosthetic Dentistry,* 98**,** 120-128.

Yu, Y., Chen, D., Wang, Y., Liu, F. & Ma, E. (2007). A new transparent oxyfluoride glass ceramic with improved luminescence. *Journal of Non-Crystalline Solids,* 353**,** 405-409.

Zachariasen, W. H. (1932). The atomic arrangement in glass. *Journal of the American Chemical Society,* 54**,** 3841-3851.

Zarzycki, J. (1965). Coordination numbers in vitreous and crystalline systems. *Proceedings of the International conference on the Physics of non – crystalline solids.* Amsterdam, The Netherlands, North-Holland Publishing Company, 531.

Zarzycki, J. (1991). *Glasses and the vitreous state*. Cambridge, UK, Cambridge University Press, 1, 37-64,228-231.

Zhang, B., Qian, F., Duan, X. & Wu, B. (2009). Relationship between leucite content and compressive strength of K_2O-Al_2O_3-SiO_2 system dental glass ceramics. *Journal of Wuhan University of Technology - Materials Science Edition,* 24**,** 72-74.

Zhang, N.-Z. & Anusavice, K. J. (1999). Effect of alumina on the strength, fracture toughness, and crystal structure of Fluorcanasite glass-ceramics. *Journal of the American Ceramic Society,* 82**,** 2509–2513.

Zhang, Y., Lv, M., Chen, D. & Wu, J. (2007). Leucite crystallization kinetics with kalsilite as a transition phase. *Materials Letters,* 61**,** 2978-2981.

Zhang, Y., Rao, P., Lü, M. & Wu, J. (2008). Mechanical properties of dental porcelain with different leucite particle sizes. *Journal of the American Ceramic Society,* 91**,** 527-534.

Zhou, J. & Hsiung, L. L. (2007). Depth-dependent mechanical properties of enamel by nanoindentation. *Journal of Biomedical Materials Research Part A,* 81**,** 66-74.

Zhou, Z. R. & Zheng, J. (2008). Tribology of dental materials: a review. *Journal of Physics D: Applied Physics,* 41**,** 113001.

Zou, L., Cherukara, G., Hao, P., Seymour, K. & Samarawickrama, D. Y. D. (2009). Geometrics of tooth wear. *Wear,* 266**,** 605-608.

11 . Publication

Wear 269 (2010) 930–936

Contents lists available at ScienceDirect

Wear

journal homepage: www.elsevier.com/locate/wear

Short communication

Wear quantification of human enamel and dental glass–ceramics using white light profilometry

A. Theocharopoulos[a,*], L. Zou[a], R. Hill[b], M. Cattell[a]

[a] Queen Mary University of London, Barts and The London School of Medicine and Dentistry, Institute of Dentistry, Centre for Adult Oral Health, Turner Street, Whitechapel, London E1 2AD, UK
[b] Queen Mary University of London, Barts and The London School of Medicine and Dentistry, Institute of Dentistry, Dental Physical Sciences Unit, Francis Bancroft Building, Mile End Road, London E1 4NS, UK

ARTICLE INFO

Article history:
Received 30 March 2010
Received in revised form 6 August 2010
Accepted 19 August 2010
Available online 9 September 2010

Keywords:
White light profilometry
Wear quantification
Enamel
Dental glass–ceramic
Non-contact chromatic confocal

ABSTRACT

The aim of this study was to develop a protocol for quantifying wear using white light profilometry. Human molar cusps and glass–ceramic disc (Ceramco-3, Ceramco, USA) surfaces were digitised using a non-contact profilometer (Proscan-2000, Scantron, UK) with an S16/3.5 white light sensor (Stil-S.A., France), before and after *in vitro* wear testing. Digitised images were superimposed using the dedicated software (Proform, Scantron, UK). Superimposed images were further processed in Proscan-2000 software to eliminate interferences with calculation of wear quantification parameters (volume, mean-height loss) by isolation of the worn area. Scanning repeatability and operator uncertainty introduced systematic errors that were also evaluated. The elimination of the areas surrounding the wear pattern produced significantly improved results for tooth ($p < 0.05$) and glass–ceramic disc ($p < 0.001$) mean-height loss. Tooth volume loss accuracy was improved by 6.83% while disc volume loss was adequately calculated using the software's automated tool. Operator uncertainty tests produced mean (SD) mm^3 differences of 0.0040 (0.0023) for tooth specimens and 0.0013 (0.0007) for glass–ceramic disc specimens. Scanning repeatability tests produced mean (SD) mm^3 differences of 0.0024 (0.0007) for tooth specimens and 0.0030 (0.0015) for glass–ceramic disc specimens. The improved and repeatable measurements obtained may suggest a similar approach to be beneficial for similar applications and materials.

1. Introduction

Tooth wear is the surface material net loss of a tooth under function. Tooth wear can incorporate different processes frequently occurring in combination that lead to material loss such as erosion, attrition and abrasion [1]. The latter is caused by contact with a material other than tooth [2]. Distinguishing amongst these processes may be difficult in practice and for this reason the term wear is used to describe material loss [3]. Interest in quantification of the material loss (wear quantification) of dental materials and dental hard tissues is evident by the plethora of studies in the literature [4–7]. Wear quantification methods for measuring material loss after *in vivo* or *in vitro* wear tests include measuring weight [8], height [9], mean height, [10,11] and volume [10,12] material loss parameters. Volume and mean height parameters provide the most clinically relevant information as they can be linked to cuspal structure loss and, ultimately, to facial height loss [13]. Wear quantification methodologies that can provide reliable and repeatable results are thus essential. While surface matching and difference detection software are commercially available for *in vitro* wear quantification, algorithms have also experimentally been developed [14] and applied in quantification of erosive wear *in vivo* [5]. Ongoing research highlights that these resources need to be tested and understood before application in dental studies as their infallibility should not be taken for granted [14]. Clinical wear evaluation studies are extremely time consuming and require expertise in patient selection, data collection and analysis [6]. *In vitro* wear evaluation is therefore a useful alternative especially when comparing new materials.

The *in vitro* wear quantification process usually requires the employment of a method that can make an accurate topographical representation of the surfaces of interest before and after wear testing. Methods that have been employed for *in vitro* wear quantification include mainly three types of sensors for scanning and subsequent digitisation of surfaces. These include mechanical sensors (contact) [15], and non-contact sensors such as laser [10] and white light [16]. All three sensor types have been found to be suitable for the quantification of wear facets in a systematic study by

* Corresponding author at: Queen Mary University of London, Dental Physical Sciences, Francis Bancroft Building, Room 2.22.4, Mile End Road, London E1 4NS, UK. Tel.: +44 0 207 882 7723; fax: +44 0 207 882 7979.
E-mail address: a.theocharopoulos@qmul.ac.uk (A. Theocharopoulos).

0043-1648/$ – see front matter © 2010 Elsevier B.V. All rights reserved.
doi:10.1016/j.wear.2010.08.019

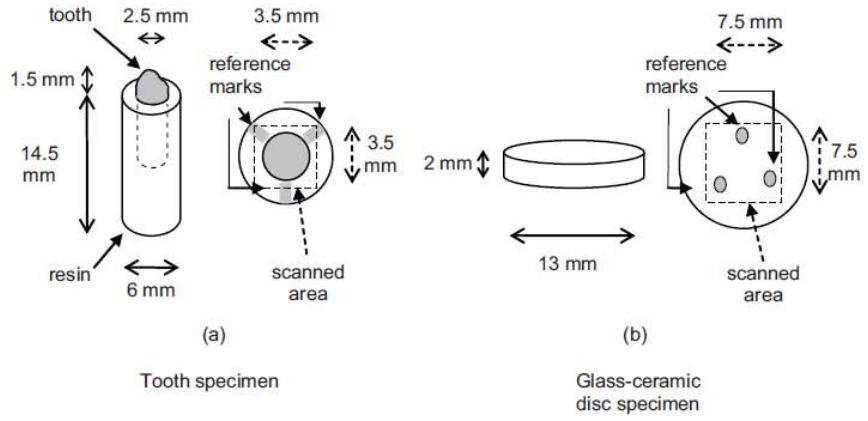

Fig. 1. Schematics of the (a) tooth and (b) glass–ceramic disc specimens.

Heintze et al. [6]. Many studies have used white light non-contact profilometric techniques for quantification of dental wear related phenomena such as erosion [17] and/or abrasion [6,16,18]. The information provided in most of the studies is usually limited to sample type and testing method while parameters used for the scanning (e.g. sensor, sampling rate) and the rationale behind the choice are not discussed.

White light profilometry utilizes accurate distance measuring sensors. These sensors incorporate special lenses that can split the light beam of a polychromatic (white) light source into its constituent wavelengths [19]. Each wavelength can only be sharply focused on a point that lies at a specific distance from the sensor, thus creating a continuum of monochromatic imaging points. The distance sensing ability of the sensor is enabled by matching the central wavelength of the reflected beam to the exact height of the focused point via a spectrometer. A microtopographic image is then constituted by raster scanning across the desired specimen surface [19,20]. Applications of white light sensors include industrial process control, reverse engineering and as high precision research tools. These non-contact sensors can provide analysis of shape and texture, microtopography and microform as well as roughness measurements [21].

The aim of this study was to design a novel protocol for quantification of material loss after wear testing of human enamel versus glass–ceramics using white light profilometry. The protocol was designed to quantify the volume and mean height loss of the enamel and glass–ceramic material as a result of the wear testing, using specialized software. The step size selection process, operator introduced uncertainty and scanning repeatability were investigated. The null hypothesis (Ho) tested was: the Automated measurements generated by the software for volume and mean height loss were not significantly different from the values obtained by the proposed experimental methodology.

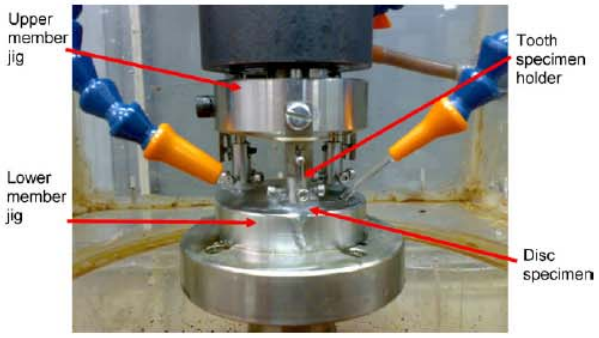

Fig. 2. Wear testing apparatus.

2. Materials and methods

2.1. Wear testing specimen preparation

2.1.1. Tooth specimen preparation

Freshly extracted human adult molar teeth were collected from the Department of Oral and Maxillofacial Surgery (Institute of Dentistry, Barts and The London School of Medicine and Dentistry) and stored in a 30% water/70% ethanol solution in a tissue bank (Medical Ethics REC: 06/Q0603/98). The teeth were visually screened by the same operator under a microscope (Wild M3B, Heerbrug, Switzerland) to exclude those with pointed configurations, demineralisations or surface defects [22]. Eight individual cusps were sectioned in the form of cylinders using a 2.75 mm inner diameter core drill (UKAM Industrial Superhard Tools, Valencia, USA) under water lubrication. The selected tooth cylinders were embedded in photo-curing resin (Palatray, Heraeus Kulzer, UK) using a custom made hollow cylinder PTFE mould (6 mm inner diameter x 14.5 mm height) (Fig. 1a). Three reference marks were made on the top surface of the resin stub containing the embedded tooth (Fig. 1a) by pressing a wax tool tip against the uncured resin. The reference marks acted as reference points for accurate alignment of the digitised surfaces before and after wear testing. The stub was then light cured for 5 min from different directions (3M ESPE Elipar™ Freelight™, Germany).

2.1.2. Glass–ceramic specimen preparation

Eight glass–ceramic disc specimens were constructed by mixing Ceramco 3 (Batch No. 02111576, Dentsply, Ceramco, Burlington, USA) dentine powder (0.96 g) with 0.3 mL of modeling liquid (C.H.B 24066, Vita Zahnfabrik, Germany) and transferring to a hollow cylinder steel mould (16 mm inner diameter) with a plunger. The mould was gently vibrated to remove excess moisture from the slurry and tissue dried (30 s). The powder slurry was compacted at 1 kg × 10^3 for 1 min and then transferred to a dental porcelain furnace (Multimat MCII, Dentsply, Weybridge, UK) and sintered according to manufacturers' instructions using 1 dentine and 1 glaze firing cycle. The disc specimens (2 mm thickness) were then wet lapped on one side with P600 SiC paper to achieve flatness and standardize the test surface. Three hemispherical reference marks forming the points of a triangular area in which the wear test was to be carried out were made on the glass–ceramic disc

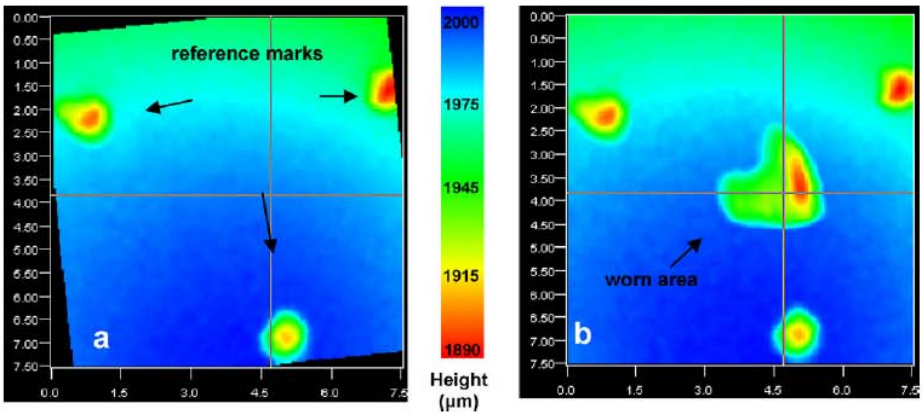

Fig. 3. Digitised glass–ceramic disc surfaces (a) before and (b) after wear testing.

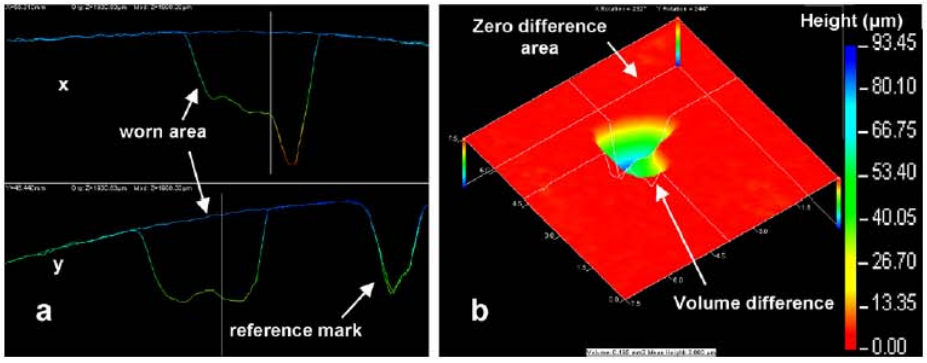

Fig. 4. (a) Digitised glass–ceramic disc cross sectional (x, y) fit overview and (b) superimposed 3D difference view.

surfaces using a pointed dental stone followed by a dental rubber bur (Fig. 1b). Specimens were then cleaned in an ultrasonic bath with aqueous detergent solution (Decon 90, Decon Laboratories Ltd., E. Sussex, UK) for 10 min and then washed with water.

2.1.3. Wear testing

All glass–ceramic disc specimens were stored in deionized water while enamel specimens were stored in a 30% water/70% ethanol solution for 24 h before testing. Glass–ceramic discs and enamel specimens were fixed into specially designed holders (Fig. 2) on the

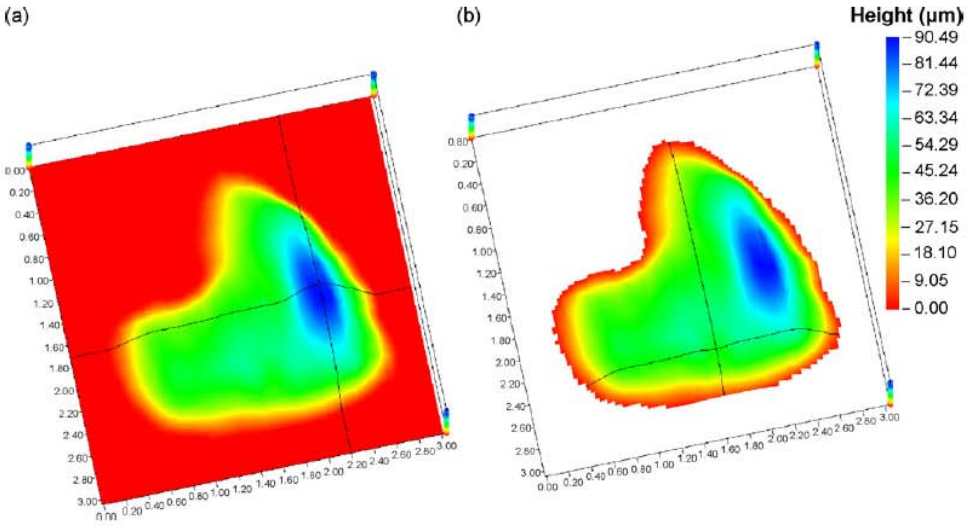

Fig. 5. (a) Cropped difference view for glass–ceramic disc volume loss calculation. (b) Isolated glass–ceramic disc worn area for mean height loss calculation.

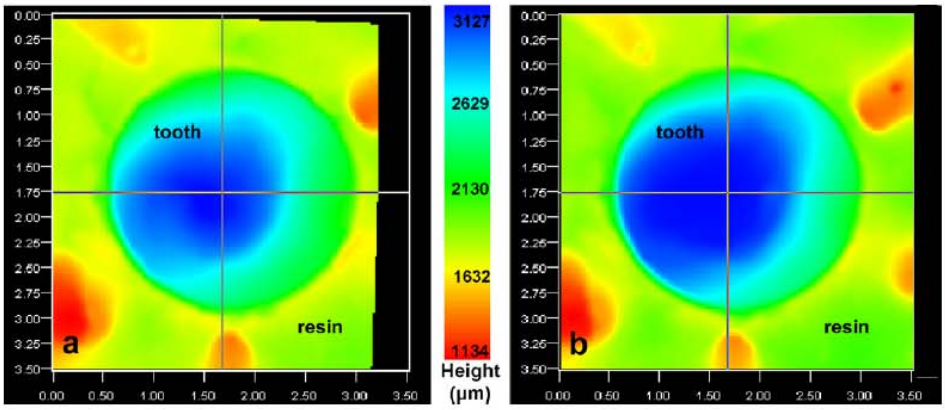

Fig. 6. Digitised tooth surfaces (a) before and (b) after wear testing.

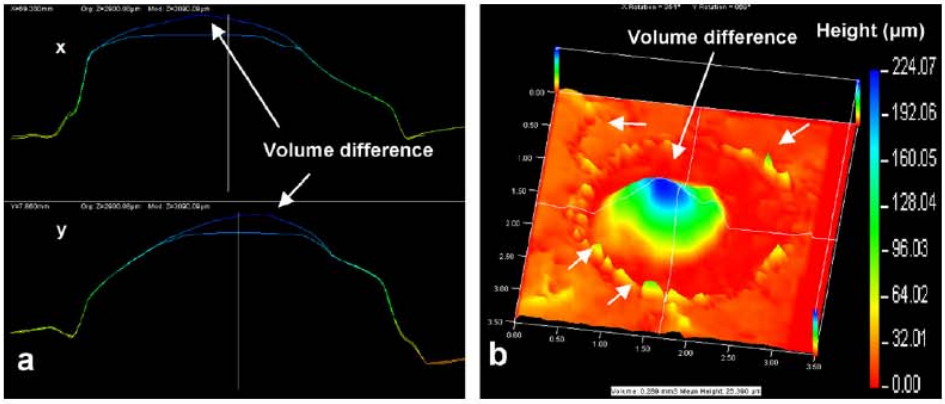

Fig. 7. (a) Tooth cross sectional (x, y) fit overview and (b) superimposed 3D difference view showing irregularities and peaks (arrows) interfering in the volume/mean height loss calculation.

upper and lower members of a servo-hydraulic test frame (Bionix 858, MTS, Minnesota). The opposing glass–ceramic disc and enamel specimens were subjected to 300,000 simulated masticatory cycles at a rate of 2 Hz under a continuous flow of deionized water (37 °C). Specimens were loaded with a load of 13.5 N each, by operating the axial shaft under displacement control on the axial plane. This was followed by a lateral excursion movement exerted by rotating the axial shaft under displacement control by 1.5 degrees. A controlled cuspal contact time (0.25 s) was used to complete a cycle.

2.2. Scanning method development

2.2.1. Scanning equipment and parameters

A non-contact 3D profilometer (Proscan 2000, Scantron, Taunton, UK) and the dedicated software (Proscan 2000, ver.2.1.8.8+ software, Proform ver.1.41 software, Scantron Industrial Products Ltd., Taunton, UK) were used for the tooth and glass–ceramic surface digitisation and the subsequent image analysis. The S16/3.5 Chromatic sensor (Stil S.A., Aix-en-Provence, France) was used for all scans operated at 30 Hz frequency (low scanning speed) through a CHR-150 controller (Stil S.A., Aix-en-Provence, France) that was connected to the Proscan 2000 profilometer. This sensor has a 3.5 mm measuring range and a 75 nm axial resolution. Dark background measurement was performed prior to each scanning session to ensure maximum sensor sensitivity to reflected light. The step size for the scans was selected according to Section 2.2.2.

2.2.2. Step size selection

A custom made jig was constructed to fit on the Proscan 2000 stage which allowed the repositioning of tooth and glass–ceramic disc specimens before and after wear testing. A series of pilot scans on a tooth and a glass–ceramic disc specimen was conducted. The scanning area of the tooth specimen surface was limited to 3.5 mm × 3.5 mm to include the embedded tooth section (Fig. 1a).

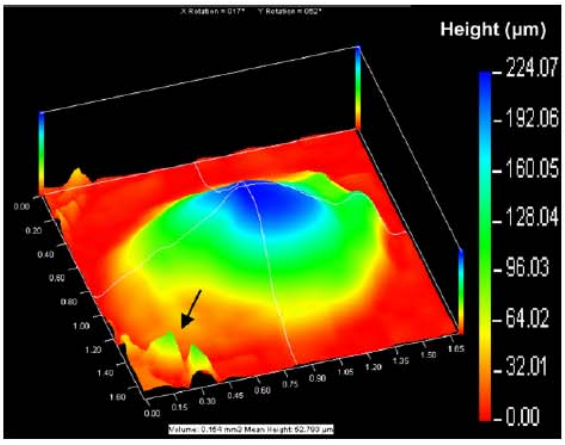

Fig. 8. Cropping of the digitised tooth specimen area with unwanted peaks included.

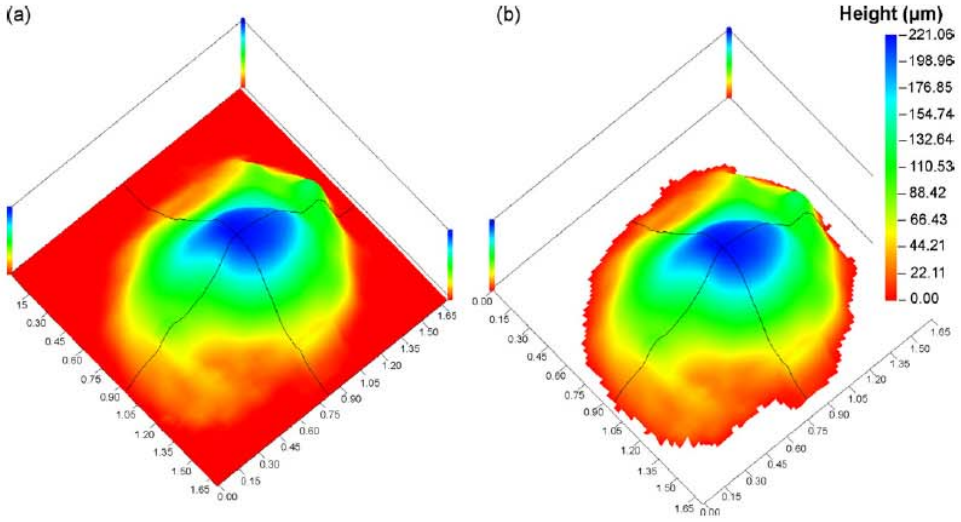

Fig. 9. (a) Peaks eliminated and a zero area inserted around the difference view for tooth volume loss calculation. (b) Isolation of the tooth wear area for mean height loss calculation.

The scanning area on the glass–ceramic disc specimen surface was limited to 7.5 mm × 7.5 mm to include the area to be worn (Fig. 1b). The specified areas of the tooth and the glass–ceramic disc specimens were scanned using five step sizes (10, 20, 30, 50 and 100 μm) in both x and y directions prior to simulated wear testing. The tooth specimen surface was then ground using wet P1000 and P2400 SiC papers on a lapping machine (20 s on each paper, 300 rpm) to simulate the wear process, then washed with water and cleaned with ethanol. The disc specimen was subjected to a pilot wear test (details in Section 2.1.3), then washed with water and surface cleaned with ethanol. Specimens were repositioned on the scanner using the custom jig and the same series of scans were carried out. The resultant digitised images were superimposed using the Proform software (ver.1.41, Scantron, Taunton, UK) to measure the volume loss in respect to varying step size.

2.2.3. Wear quantification method and measurement improvement test

All tooth and glass–ceramic disc specimen test surfaces were scanned before and after wear testing using the optimal step sizes (teeth: 20 μm, glass–ceramic discs: 30 μm) selected previously. The digitised test surfaces before and after wear testing were superimposed (Proform ver.1.41, Proscan 2000 ver.2.1.8.8+ software, Scantron, Taunton, UK) to quantify the total volume and mean height loss. Filters (Proscan 2000 ver.2.1.8.8+ software) were applied to all tooth (warpage 2) and glass–ceramic disc (warpage 3) digitised surfaces. This was performed to separate the long wavelength (low frequency) shape associated information from the short wavelength (high frequency) roughness associated information prior to the superimpositions.

The series of steps followed for the wear quantification of the glass–ceramic disc specimens is shown in Figs. 3–5 namely; before and after wear profile check, superimposition and graphical wear quantification. The shading in all figures illustrates height gradient. The three reference marks made on the disc surface (Fig. 3a and b) were used for alignment of the surfaces before and after testing. The surfaces were superimposed (Fig. 4a and b) and the region with the volume difference was cropped to a square area of 3 mm × 3 mm. At this stage Automated measurements are provided from the software for the volume and mean height loss and these were recorded as the "Automated" set of data. The superimposed file (difference view) was then saved and opened in the Proscan software where the volume tool was used to measure the values. The difference view was then further processed in Proscan software to isolate the worn area (Fig. 5a and b). The file (x, y, z data) was then exported in Excel format and the height values (z values) were averaged to generate the mean height loss for each specimen. These values were recorded as the "Experimental" data set.

For the tooth specimens (Figs. 6 and 7), the difference view from the Proform software was cropped as closely as possible to the worn area (Fig. 8) and the volume/mean height loss measurements provided by the software were recorded as the "Automated" set of data. It was then further processed in the Proscan software to delete unwanted areas around the worn area that interfered with volume calculation (Figs. 7 and 8b). The deleted areas were then replaced with a zero height area (Fig. 9a) to enable the final volume loss determination by the Proscan software. Mean height calculation was then performed as for the disc specimens (Fig. 9b). The values recorded at this stage were recorded as the "Experimental" set of data.

The "Automated" and "Experimental" data sets created for volume and mean height loss of human enamel and glass–ceramic were then compared using individual t-tests to evaluate statistical differences ($p < 0.05$).

2.2.4. Operator uncertainty and scanning repeatability tests

Superimpositions were carried out (5×) following the developed protocol on a tooth/glass–ceramic disc pair, before and after wear testing to evaluate the wear quantification testing process and operator uncertainty. The volume loss values from the individual scans (1–5) were then subtracted in all possible combinations (1–2, 1–3, 1–4, 1–5, 2–3, 2–4, 2–5, 3–4, 3–5, 4–5) and the differences averaged. Scanning repeatability was also evaluated by repeated (5×) scanning of a tooth and a glass–ceramic specimen. The volume difference between the scans was measured by superimposing scans

Table 1
Step size selection results.

Step size (μm)	Tooth volume loss (mm³)	Disc volume loss (mm³)
10	0.226	0.161
20	0.224	0.161
30	0.225	0.161
50	0.218	0.158
100	–	0.151

Table 2
Automated and Experimental wear quantification results.

Measurement	Automated mean (SD)	Experimental mean (SD)	% Difference
Volume loss mm^3 (SD) teeth	0.206 (0.072)[a]	0.192 (0.066)[a]	6.83
Volume loss mm^3 (SD) glass–ceramic discs	0.184 (0.042)[a]	0.184 (0.042)[a]	0
Mean height loss μm (SD) teeth	48.42 (16.63)[a]	65.50 (20.58)[b]	27.9
Mean height loss μm (SD) glass–ceramic discs	19.85 (5.58)[a]	67.62 (21.01)[b]	69.4

Different superscript letters indicate significant ($p < 0.05$) differences between mean values tested.

in all possible combinations (1–2, 1–3, 1–4, 1–5, 2–3, 2–4, 2–5, 3–4, 3–5, 4–5).

3. Results

3.1. Step size choice

The results of the volume loss values as measured at different step sizes on a tooth and a glass–ceramic specimen can be seen in Table 1. For both the tooth and the glass–ceramic disc, there is very little or no difference in the measured volume loss at 10, 20 and 30 μm step sizes. For the glass–ceramic disc specimen the measured volume loss at 50 and 100 μm step sizes shows a reducing trend. For the tooth specimen the measured volume loss at 50 μm was also reduced in respect to the 10, 20 and 30 μm step size measured volume loss. At 100 μm the calculation of the volume loss was not facilitated for the tooth specimen due to insufficient detail to aid the superimposition process and scanning artefacts present. The selected step size for tooth specimens was 20 μm while for the glass–ceramic specimens it was 30 μm.

3.2. Operator uncertainty and scanning repeatability results

The results for operator uncertainty produced a mean (SD) difference between measured volume loss values of 0.0013 (0.0007) mm^3 for the glass–ceramic disc and of 0.0040 (0.0023) mm^3 for the tooth specimen. The result for scanning repeatability produced a mean (SD) volume difference between scans of 0.0024 (0.0007) mm^3 for the tooth specimen (compared area 1.6 mm × 1.4 mm) and of 0.0030 (0.0015) mm^3 for the disc specimen (compared area 3 mm × 3 mm). Comparing the acquired repeatability and operator induced errors with the mean volume values of the experimental protocol measurements (Table 2), we obtain errors ranging 1.25–2.08% for teeth and 0.7–1.63% for discs.

3.3. Automated and Experimental wear quantification results

The results for the measurements acquired via the Automated and Experimental methodologies are shown in Table 2. The Automated software measurements adequately calculated disc volume loss and for that reason the mean values measured via Automated and Experimental protocols were equal. A mean volume loss overestimation of 6.83% was measured when applying the automated protocol on teeth, however no statistically significant difference ($p > 0.05$) between Automated and Experimental values was identified and thus Ho was accepted. There was a significant difference between the means for both tooth ($p < 0.05$) and glass–ceramic disc ($p < 0.001$) mean height loss values between Automated and Experimental measurements. Ho was rejected in this instance.

4. Discussion

The sensor chosen for the wear quantification measurements in this study was mainly chosen based on its measuring range (3.5 mm) and its high axial resolution (75 nm). The axial distance to be measured on the teeth samples in order to include the tooth cusp, the surface of the embedding resin and the reference marks was a maximum of 2 mm (Fig. 1a). Axial resolution in this type of sensors increases as the working range decreases [20]. Use of a smaller working range sensor would potentially require axially segmented scanning to include the full specimen height without significant gain in resolution. The maximum wear facet depth recorded on the glass–ceramic discs did not exceed 250 μm, thus a lower working distance sensor could have been chosen to increase axial resolution; the same sensor however was used for both glass–ceramic discs and tooth samples to ensure inter-measurement consistency.

The sampling rate of 30 Hz was chosen after a series of scans at all available frequencies (1000, 300, 100 and 30 Hz) which revealed that the slower the sampling rate, the less missing data appeared on the scans. The scans at 30 Hz eliminated missing data almost completely which whenever present were interpolated using the Proscan 2000 software. The slow sampling rate adopted was thus mainly dictated by the reflectivity of glass–ceramic/tooth samples both being translucent (scattering surfaces) [20]. Remaining missing data generally appeared either in 90 °C angles (e.g. areas between the embedding resin and the cusp cylindrical walls) or in locally high sloped surfaces. The latter may be attributed to the limitation of the sensor itself as its specifications include a maximum angular slope of 22 °C for specular surfaces, although this can be increased up to 80 °C for scattering surfaces [20]. Laser techniques, although much faster, require either coating the surfaces to be scanned or the fabrication of plaster replicas [6]. In contrast to laser techniques, white light Profilometry enabled the actual specimens' surfaces to be digitised potentially introducing less systematic errors in the acquired measurements.

The S16/3.5 sensors' lateral resolution (x, y) is quoted as 4 μm [23], therefore the step sizes investigated (10, 20, 30, 50 and 100) are well within the sensor's capabilities. The wear testing setup used in this study and most of the parameters (no of cycles, applied force, cuspal lateral excursion) were based on a setup used previously by Magne et al. [15], where the artificial oral simulator of De Long [24] was utilised. De Long [24] correlated wear results over a number of 250,000 cycles in his simulator with 1 year of *in vivo* mastication [25,26]. Magne et al. [15] quantified volume and mean height loss of human enamel and dental glass–ceramics, using a tungsten carbide contact sensor and a considerably lower x, y spatial resolution (50 μm × 100 μm), with results in the same range as the present study. Kramer et al. [11] reported that 10–25 μm step sizes can lead to reliable results with mechanical (contact) sensors. A resolution of 4 μm × 4 μm x, y of a white light sensor was found to be in good agreement to a >30 μm × 30 μm x, y resolution of a laser sensor [6], when both were applied to quantify volume loss in the same glass–ceramic and composite disc specimens. Hara and Zero [17] used a step size of 10 μm × 100 μm (Proscan 2000) to investigate the erosive potential of beverages on enamel. The 10 μm step size on teeth was not selected as it produced images that even after the application of the warpage filter were "noisy" leading to the application of a higher warpage filter to separate the roughness related information. The selected step sizes of 20 μm × 20 μm for tooth and 30 μm × 30 μm for glass–ceramic disc samples are therefore selected and are in the range suggested in the literature for similar applications and materials.

The volume loss figures of glass–ceramic disc specimens (Table 1) could be correlated to weight loss of the specimens using measured glass–ceramic density values. Considerations for varying glass–ceramic density should be then taken into account as a result of varying porosity [27] and a careful calibration protocol could be devised to ensure minimal systematic error involvement (e.g. balance calibration, standardized weighing conditions). This calibration would give a useful check for the data presented in Table 1. A calibration protocol for enamel specimens would however be more problematic. Tooth enamel density varies significantly from one tooth to another and also within the same tooth from the surface towards the amelodentinal junction (3.0–2.84 g/ml) [28]. Standardising weighing conditions (e.g. desiccation) could also influence the integrity and the wear characteristics of the tooth specimens.

The Automated measurements (Table 2), significantly ($p < 0.05$) underestimated the mean height loss in both tooth and glass–ceramic discs, supporting the use of the experimental protocol. In particular, 27.9% less mean height tooth loss and 69.4% less mean height disc loss was measured via the Automated regimen. The very satisfactory fit achieved on the disc samples resulted in an (almost) zero difference area around the wear facets (Fig. 4b). There was thus no need to delete the area around the disc wear facets for the volume calculation. This explains the absence of difference for the mean volume loss values measured on discs, via both the experimental and automated procedures (Table 2). The only difference in procedure is that the automated disc volume loss values were measured by the Proform software and the experimental from the Proscan software. This demonstrates the good agreement between the two different pieces of software. To limit any potentially systematically induced error, our protocol standardisation was limited to a 3 mm × 3 mm area which was ample to include the wear area. The apparent overestimation of the tooth volume loss by the Automated measurements (Table 2), failed to differentiate ($p > 0.05$) from the Experimental measurements, suggesting that the experimental protocol may not provide an added benefit in the volume loss calculation. In the present authors' opinion, although no significant difference was detected, exclusion of volume from areas around the area of interest (Fig. 8) was preferable. A potential error source is the accuracy of the utilized sensor. The accuracy of white light sensors is continuously being improved to achieve sub-micron levels (tested maximum linearity error for the S16/3.5 sensor is 0.4 μm [23]). The accuracy of measurements is thus much more likely to be affected by systematically induced errors and should therefore be considered in wear quantification protocol designs.

5. Conclusions

The proposed methodology was useful in the quantification of material loss after wear testing of human enamel and dental glass–ceramics, by improving the mean height loss calculations compared to Automated measurements. The repeatability of the measurements obtained suggests a similar approach could be beneficial for similar applications and materials in Medicine and Dentistry.

Acknowledgements

The authors acknowledge the financial support from St. Bartholomew's and The Royal London Charitable foundation (RAB05/PJ/06). The authors would also like to express their appreciation to Paul Adams, Tim Tuckey and Adam Henwood (Scantron, UK), Yael Cohen-Sabban (Stil SA, France) for the useful discussions and Bill Godwin and Vins Ford (School of Engineering and Materials Science, QMUL, UK) for their help in the wear jig design and the testing with the MTS 858 Bionix system.

References

[1] D.W. Bartlett, B.G.N. Smith, Definition, classification and clinical assessment of attrition erosion and abrasion of enamel and dentine, in: M. Addy, G. Embery, M. Edgar, R. Orchardson (Eds.), Tooth Wear and Sensitivity, Martin Dunitz Ltd., London, 2000, 87-92.
[2] M. Addy, R.P. Shellis, Interaction between attrition abrasion and erosion in tooth wear, in: A. Lussi (Ed.), Dental Erosion, Monographs in Oral Science, Karger, Basel, 2006, 17-31.
[3] B.G.N. Smith, D.W. Bartlett, N.D. Robb, The prevalence, etiology and management of tooth wear in the United Kingdom, J. Prosthet. Dent. 78 (1997) 367–372.
[4] H.W.A. Wiskott, J. Perriard, S.S. Scherrer, U.C. Belser, A new method to quantify wear using implant supported restorations, Dent. Mater. 16 (2000) 218–225.
[5] R.G. Chadwick, H.L. Mitchell, Conduct of an algorithm in quantifying simulated palatal surface tooth erosion, J. Oral Rehabil. 28 (2001) 450–456.
[6] S.D. Heintze, A. Cavalleri, M. Forjanic, G. Zellweger, V. Rousson, A comparison of three different methods for the quantification of the in vitro wear of dental materials, Dent. Mater. 22 (2006) 1051–1062.
[7] L. Zou, G. Cherukara, P. Hao, K. Seymour, D.Y.D. Samarawickrama, Geometrics of tooth wear, Wear 266 (2009) 605–608.
[8] J.A. Kaidonis, L.C. Richards, G.C. Townsend, G.D. Tansley, Wear of human enamel: a quantitative in vitro assessment, J. Dent. Res. 77 (1998) 1983–1990.
[9] M.K. Etman, M. Woolford, S. Dunne, Quantitative measurement of tooth and ceramic wear: in vivo study, Int. J. Prosthodont. 21 (2008) 245–252.
[10] A. Mehl, W. Gloger, K.H. Kunzelmann, R. Hickel, A new optical 3-D device for the detection of wear, J. Dent. Res. 76 (1997) 1799–1807.
[11] N. Kramer, K.H. Kunzelmann, M. Taschner, A. Mehl, F. Garcia-Godoy, R. Frankenberger, Antagonist enamel wears more than ceramic inlays, J. Dent. Res. 85 (2006) 1097–1100.
[12] K.T. Metzler, R.D. Woody, A.W. Miller, 3rd, B.H. Miller, In vitro investigation of the wear of human enamel by dental porcelain, J. Prosthet. Dent. 81 (1999) 356–364.
[13] M.R. Pintado, G.C. Anderson, R. DeLong, W.H. Douglas, Variation in tooth wear in young adults over a two-year period, J. Prosthet. Dent. 77 (1997) 313–320.
[14] H.L. Mitchell, R.G. Chadwick, Mathematical shape matching as a tool in tooth wear assessment – development and conduct, J. Oral Rehabil. 25 (1998) 921–928.
[15] P. Magne, W.-S. Oh, M.R. Pintado, R. DeLong, Wear of enamel and veneering ceramics after laboratory and chairside finishing procedures, J. Prosthet. Dent. 82 (1999) 669–679.
[16] A. Vieira, E. Overweg, J.L. Ruben, M. Huysmans, Toothbrush abrasion, simulated tongue friction and attrition of eroded bovine enamel in vitro, J. Dent. 34 (2006) 336–342.
[17] A.T. Hara, D.T. Zero, Analysis of the erosive potential of calcium-containing acidic beverages, Eur. J. Oral Sci. 116 (2008) 60.
[18] C. Moore, M. Addy, Wear of dentine in vitro by toothpaste abrasives and detergents alone and combined, J. Clin. Periodontol. 32 (2005) 1242–1246.
[19] D. Litwin, J. Galas, N. Blocki, Variable wavelength profilometry, in: Proceedings of the Symposium on Photonics Technologies for 7th Framework Program (Wroclaw 2006), pp. 476–479.
[20] J. Cohen-Sabban, J. Gaillard-Groleas, P.-J. Crepin, Quasi-confocal extended field surface sensing, Optical Metrology Roadmap for the Semiconductor, Optical, and Data Storage Industries II, SPIE, San Diego, CA, USA, 2001, pp. 178–183.
[21] http://www.stilsa.com/index.htm (accessed 22.03.2010).
[22] S.D. Heintze, A. Cavalleri, M. Forjanic, G. Zellweger, V. Rousson, Wear of ceramic and antagonist-A systematic evaluation of influencing factors in vitro, Dent. Mater. 24 (2008) 433–449.
[23] STIL-SA, Measurement report, Metrological characteristics for the S16/3.5 contactless optical sensor: Ref. no M08011718, 22/1/08.
[24] R. DeLong, W.H. Douglas, An artificial oral environment for testing dental materials, IEEE Trans. Biomed. Eng. 38 (1991) 339–345.
[25] P. Lambrechts, M. Vuylsteke, G. Vanherle and C. L. Davidson, Quantitative in vivo wear of posterior dental restorations. Four-year results, J. Dent. Res. 64 (1985) 370. Abst. No. 1759.
[26] R.L. Sakaguchi, W.H. Douglas, R. DeLong, M.R. Pintado, The wear of a posterior composite in an artificial mouth: a clinical correlation, Dent. Mater. 2 (1986) 235–240.
[27] K.C. Cheung, B.W. Darvell, Sintering of dental porcelain: effect of time and temperature on appearance and porosity, Dent. Mater. 18 (2002) 163–173.
[28] S.M. Weidmann, J.A. Weatherell, S.M. Hamm, Variations of enamel density in sections of human teeth, Arch. Oral Biol. 12 (1967) 85–97.